Western Australia School of Mines: Minerals, Energy, and Chemical Engineering

Reservoir Characterisation of Gas Shale through Sedimentary, Mineralogical, Petrophysical and Statistical Rock Types Evaluation

Muhammad Atif Iqbal

0000-0003-0958-3030

This thesis is presented for the degree of
Doctor of Philosophy
of
Curtin University

(March 2023)

Declaration

To the best of my knowledge and belief, this thesis contains no material previously published by any other person except where due acknowledgment has been made.

This thesis contains no material accepted for awarding any other degree or diploma in any university.

Signature
Date 26/03/2022

ABSTRACT

Shale (mudstone) evaluation of gas shale reservoirs is crucial for exploring and developing large-scale plays. However, shale is a fine-grained heterogeneous sedimentary rock, and it is difficult to understand its heterogeneity through conventional techniques. Understanding reservoir characterisation, particularly shale heterogeneity, is especially critical for successful hydrocarbon exploration in underexplored sedimentary basins such as the Canning Basin, Western Australia. This study provides an integrated characterisation of the organic-rich shale unit of the Ordovician Goldwyer Formation in the Broome Platform and nearby sub-basins of the Canning Basin to assess its potential as an unconventional gas shale reservoir.

A multiscale and systematic workflow was designed to characterise the Goldwyer Formation by first evaluating the different rock types via sedimentary, mineralogical, and petrophysical logs using statistical techniques. The sedimentary facies were identified by integrating core data with high-resolution image logs; petrographic information; Fourier transform infrared (FTIR); and hyperspectral drill core reflectance spectra acquired using a HyLogger3. The petrographic and FTIR data validated the usage of HyLogger3 as a tool to examine high-resolution vertical variations in shale mineralogy. The results indicated that the Goldwyer-III shales are very heterogeneous in terms of sedimentary features, organic richness, and mineral composition. It can be divided into four sedimentary facies based on colour, sedimentary features, mineral composition, and lithology. The facies include thinly laminated siliceous shale (TLSh), concretionary-banded calcareous shale (CSh), massive black shale (MBSh) and heterolithic shale (HSh). The total organic carbon in these lithofacies varies from 0.35 to 4.5 wt% probably due to fluctuation in oxic-anoxic conditions. Typically, the TLSh, MBSh and HSh have a higher TOC value (up to 4.5 wt. %), T_{max} (up to 450 °C), hydrogen index (up to 250 mgHC/g), and brittleness index (>0.4) than the CSh lithofacies. A much better understanding of heterogeneity in Goldwyer-III shale is produced by combining the continuous high-resolution hyperspectral core log data with petrography and conventional core logs.

The hydrocarbon storage and transport capacity of shale reservoirs are dependent on their composition and associated complex pore systems. These have been investigated by various multi-scale techniques including X-ray diffraction, field emission scanning electron microscopy, the TESCAN integrated mineral analyser (TIMA), thin-section optical microscopy, Rock-Eval® pyrolysis, helium porosity, gas adsorption (N_2 and CO_2) and mercury injection capillary pressure (MICP). These methods allow the Goldwyer-III shales to be sub-divided into five main lithofacies based on mineral composition and total organic carbon (TOC) content that corresponds to the log-derived lithofacies, namely: siliceous shale, calcareous shale, heterolithic mixed shale, argillaceous shale, and an additional organic-rich shale.

The organic-rich and siliceous shales have the highest porosity of>10%, whereas porosities decline from the mixed shale to low organic argillaceous shales and in the calcareous shales. Three types of pores occur in Goldwyer-III shales namely: organic, interparticle, and intraparticle. Most of the pores are narrow slit-like or bottle-necked shaped pores. The pore aperture studies showed that mesopores are the most abundant with micropores and macropores less common in the various lithofacies. The volumes and specific surface areas (SSA) of the micropores and mesopores are positively related to TOC for all lithofacies except for the argillaceous shale. In addition, the micro and mesopore pore volumes and SSA have inverse relations with total clay content for all lithofacies except argillaceous shale. This indicates that the TOC and total clay content are the main controlling factors for the pore structure of Goldwyer-III shale. The organic-rich, siliceous, and mixed shales are the most important lithofacies for the control of fluid flow via pore systems due to their high porosity and feasible pore structures. New equations are proposed for estimating the total porosity and water saturation based on well-log analysis to provide continuous information for 3-D modelling across the Canning Basin.

The regional gas shale potential of the Goldwyer-III shale is assessed using a large 3D geological model built using Petrel software. The 3-D models were made for facies, petrophysical and geomechanical properties, including total organic carbon, porosity, water saturation, adsorbed gas, Young's modulus, Poisson's ratio, and brittleness index. Supervised machine learning via existing well logs is used to generate the synthetic curves for wells with missing well logs. Unsupervised machine learning (via K-means clustering) is used to identify the clusters equivalent to lithofacies. The novel approach of defining the mechanical stratigraphy based on the integration of clustering, facies, petrophysical and geomechanical properties provided a new methodology for the development of the gas shale reservoirs. The mapped TOC and mineralogical-derived brittleness cut-offs values allow recognition of the high-quality brittle zones.

This study offers a new overall integrated workflow for rapid, continuous, and accurate recognition of optimum facies for hydraulic fracturing. The approach can improve economic decisions when developing gas shale reservoirs.

PUBLICATIONS AND STATEMENT OF CANDIDATE CONTRIBUTION

This thesis is prepared in parts as a combination of journal papers and work arranged for publication, per Curtin University's regulations regarding Ph.D. degree. The parts of the thesis have been completed during the Ph.D. enrolment at Curtin University and have not been submitted or accepted for a degree previously in any other institute. I certify that the help received during thesis preparation and all sources used have been properly acknowledged.

The bibliographic details for the papers comprising chapters 2, 3, 4, and 5 are hereby set forth.

Paper 1. Iqbal, M. A., Rezaee, R., Laukamp, C., Pejcic, B., & Smith, G. (2022). Integrated sedimentary and high-resolution mineralogical characterisation of Ordovician shale from Canning Basin, Western Australia: Implications for facies heterogeneity evaluation. Journal of Petroleum Science and Engineering, 208, 109347.

Paper 2. Iqbal, M. A., Rezaee, R., Smith, G., & Ekundayo, J. M. (2021). Shale lithofacies controls on porosity and pore structure: An example from Ordovician Goldwyer Formation, Canning Basin, Western Australia. Journal of Natural Gas Science and Engineering, 89, 103888.

Paper 3. Iqbal, M. A., & Rezaee, R. (2020). Porosity and Water Saturation Estimation for Shale Reservoirs: An Example from Goldwyer Formation Shale, Canning Basin, Western Australia. Energies, 13(23), 6294.

Paper 4. Iqbal, M. A., Rezaee, R., Smith, G., Mandal, P. P., & Ceron, G. M. Integrated petrophysical and geomechanical modelling for prospectivity evaluation of heterogeneous gas shale: Geological, mineralogical, and statistical rock typing. Journal of Marine and Petroleum Geology. (Under Submission).

Paper 5. Iqbal, M. A., Rezaee, R., Smith, G., & Mandal, P. P. (2021). Implications of thin laminations on pore structure of marine shale reservoir: Goldwyer Formation case study from Western Australia. The APPEA Journal, 61(1), 205-215.

Book Chapter. Rezaee, R., Iqbal, M.A. (2021). Well-log Analysis of Gas shale Reservoirs. Encyclopedia of Petroleum Geoscience.https.//doi.org/10.1007/978-3-319-02330-4_312-1.

Conference Proceedings 1. Iqbal, M. A., Mandal, P. P., Rezaee, R., Sarout, J., & Smith, G. (2021, October). Integration of mechanical stratigraphy with lithofacies in Goldwyer-III shale for selecting producible and hydraulic fracturing layers. In 82nd EAGE Annual Conference & Exhibition (Vol. 2021, No. 1, pp. 1-5). European Association of Geoscientists & Engineers.

Conference Proceedings 2. Iqbal, M. A., Rezaee, R., Smith, G. (2021). Integration of high-resolution HyLogger3 spectral scanner and TESCAN Integrated Mineral Analyser for mineralogical characterisation of shale. In 3rd Australasian Exploration Geoscience Conference.

ACKNOWLEDGEMENTS

I want to express my gratitude to all who facilitated and guided me throughout the Ph.D. research journey. Firstly, I owe my sincere gratitude to Professor Reza Rezaee, who always helped, guided, supported, and encouraged being the principal and coordinating supervisor for my Ph.D. research. I greatly appreciate the opportunity Reza has provided me to work with him. I still remember and cannot express my feelings when I got his acceptance letter to start Ph.D. research with him. I have learned technical and professional aspects from him that I will carry with me throughout my career. I can never forget the help and cooperation I received from him during the completion of this dissertation. I am also grateful to Professor Gregory Smith for his contribution and valuable reviews to improve the thesis. I always felt relaxed after discussing Geology-related aspects with Greg. He always welcomed new ideas and then helped to conceive them. Many thanks to Carsten, Bobby, and Lionel from CSIRO for fruitful discussions and guidance about HyLogger data interpretation and grain density measurements. For Petrel software training, I appreciate Gonzalo Ceron's guidance and time. I want to acknowledge and appreciate Partha Pratim Mandal for his valuable advice and guidance about Python scripting and for helping to apply machine learning in my work.

My Ph.D. was fully funded by the Punjab Educational Endowment Fund (PEEF): Chief Minister Merit Scholarship (CMMS), Government of Pakistan. Without their support, I could not pursue my Ph.D. at Curtin University; therefore, I would like to acknowledge PEEF for this support. I am grateful to the Western Australia School of Mines, and the Unconventional Gas Research Group at the Department of Petroleum Engineering of Curtin University for providing all the facilities to accomplish my research. Many thanks to the Microscopy and Microanalysis Facility (MMF), John de Laeter Centre, for providing laboratory facilities.

It would have been impossible to conduct my research without data from the Department of Mines, Industry Regulations and Safety (DMIRS), Western Australia. All available datasets in terms of well-logs, seismic and core samples were provided by DMIRS. Many thanks to Schlumberger, Lloyd Register, and easycopy for providing academic versions of Petrel, Techlog, Interactive Petrophysics and easycore software, respectively. Many thanks to Dr. Lukman for his valuable advice and guidance in the start to build a 3-D model in Petrel. Special acknowledgment to Dr. Jamiu for his time to teach me about the methane adsorption experiment and its data analysis.

My valuable and golden time at Curtin University has been brightened by the friendship and goodwill of many people, including Zain, Gonzalo, Partha, Cut Aja, Jamiu, Faaiz, Mohamed, Shoaib, Faranak, Jimmy, Lingping, Zhiqi Zhong, Yujie, Jie, Nilesh, Moantaz, Moshen, and Lukman. I cannot forget the time spent with all these gems during my stay at Curtin. Special thanks to my friends Mudasar, Hasnain, Arif Watto, Hafiz Qaisar, Aqeel, Asim, Rashid, Tahir, Taha, Abdul Salam, and Ayaz for their encouragement and for making my stay in Perth more enjoyable.

Finally, I pay my love, great respect, and most special thanks to my loving Mother "Hanifah Jabeen," Late Father "Muhammad Ishaq" and my very supportive wife "Saman Aziz" for their continuous support and encouragement. I dedicate this thesis to our new lovely family member in our life my daughter "Mirha Atif", she was born on 19th February 2023. I dedicate all my efforts to my loving parents, wife, daughter, brothers (Kashif, Asif, Arif, Amir, and Ahmer,) and sisters (Samina and Saima). They always bestowed affection on me and supported me morally.

Copyright Statement

I have obtained permission from the copyright owners to use any third-party copyright material reproduced in the thesis (e.g., artwork, unpublished letters), or to use any of my own published work (e.g., journal articles, conference proceedings) in which the copyright is held by another party (e.g., publisher, co-author).

Signature................................
Date.......................................

Table of Contents

List of Figures

List of Tables

This page is left blank intentionally.

Chapter 1 Introduction

1.1 Unconventional Energy Resources Overview

The increase in energy demand and depletion of conventional reservoirs places unconventional resources into special focus within the petroleum industry. Natural gas is an essential constituent of the global energy matrix, as recognised by the World Energy Council (2016) (Sieminski & Administrator, 2016). Unconventional gas resources are important in the global quest for the energy resources because they are considered environmentally cleaner fuels. These natural resources are widely spread in various regions, including the United States of America and China. Still, they are only starting to be developed in Australia, as this study focuses on Goldwyer Formation shale from Canning Basin, Western Australia (Leather et al., 2013). Conventional resources occur as discrete accumulations that are part of a larger petroleum system, where oil and gas are trapped by buoyancy within rocks that act exclusively as reservoirs. Standard production methods can extract hydrocarbons stored in these porous and permeable formations.

In contrast, unconventional resources typically exist as more continuous accumulations over a large area mainly due to low permeability trapping mechanisms. Therefore, the commercial production of hydrocarbons from unconventional reservoirs requires specialised extraction techniques and essential investments. Coal, shale, and tight sandstone formations with potentially commercial hydrocarbon volumes all fall under the unconventional reservoir category. Shale may act as both source and trap within a given petroleum system; hence they can be described as “self-sourcing reservoirs.” However, the successful development of gas shale reservoirs is challenging and depends on several processes (P. De Silva et al., 2015; Johnson & Boersma, 2013). These processes are mainly dependent on the reservoir properties of the shale.

Shale is considered an abundant clastic rock in the world. It forms the common source rock in most petroleum systems containing sufficient organic matter

(North, 1985). Although gas shale reservoirs have poor properties (e.g., porosity and permeability), they are typically laterally widespread and thicker than conventional sandstone or carbonate reservoirs. Hence gas shale reservoirs have been assessed worldwide as containing 15,000 to 25,000 trillion cubic feet (Tcf) of gas (Kawata & Fujita, 2001; Rogner, 1997; Sieminski & Administrator, 2016).

The shales in North America, such as Barnett, Haynesville, Marcellus, Woodford, and Fayetteville, have been successfully evaluated and produced by applying the latest techniques and improved systematic workflows (De Silva et al., 2016; Guochang Wang & Timothy R Carr, 2012; Wang & Carr, 2013). The shale plays of North America can provide suitable analogues for the development and production of natural gas from shales in general (Bhattacharya et al., 2016; Wang et al., 2014). However, each gas shale reservoir in other parts of the world is unique regarding source rock and reservoir characteristics (Carr* et al., 2019; Passey et al., 2010). Consequently, the geological, petrophysical, geochemical, and geomechanical assessment of these other shale formations needs to be adapted for each case to identify its potential for gas shale production.

In Australia, there are about fifty to sixty sedimentary basins and sub- basins (Jadoon, 2016; Mackie, 1987). Among all of the basins, the Cooper and Maryborough Basins (in South and East Australia), whereas Perth and Canning Basins (in Western Australia) are considered to have potential gas shale aspects (Administration & Kuuskraa, 2011; Jadoon et al., 2017; Rezaee, 2015; Yuan et al., 2019). Based on an independent assessment, the proposed shale gas-in-place resources in Australia have ranged from 1380 to 2300 Tcf; out of them, 400 Tcf could be technically recovered (Jordan et al., 2013; Sieminski & Administrator, 2016). Production could be feasible from the potential gas shales in Australian Basins by applying the latest analytical techniques and successful technology from the USA in combination with local knowledge of these Australian gas shale resources.

Generally, it is essential to specify and define the gas-shale assessment criteria as the gas-shale productivity mainly depends on the reservoir quality and successful execution of effective hydraulic stimulations (P. De Silva et al., 2015; Zhang et al., 2022). This target can be achieved successfully by considering the characterisation of shale from nano to meter scale in terms of geological and petrophysical prospects. This type of evaluation is very challenging due to heterogeneity and uncertainties in the shale properties. However, these characteristics depend on the depositional environment of the various shale types and this can be used to identify and classify the controlling parameters (e.g. marine, non-marine, lacustrine) (P. De Silva et al., 2015; Zhang et al., 2022).

1.2 Geological and Petrophysical Characteristics of Shale

Shale is a fine-grained fissile sedimentary rock composed of clays, carbonates, and quartz (Sondergeld et al., 2010). The fissile nature is thin parallel layering and bedding formed as the result of the arrangements of clay minerals and their capability to be developed into different structures like plates (Jacobi et al., 2009; Javadpour, 2009; Strahler, 1981). The shale is a source rock as it consists of organic matter that generates hydrocarbon. However, few reservoirs like Montney Formation from Western Canada act as hybrids as they contain shale with higher organic content having interbedded silty layers (Basin et al., 2015). This hybrid nature is due to coastal sand and offshore shale facies. Whatever the situation, it is very important that the organic matter is deposited and preserved in the sediments. Therefore, the potential of gas shale reservoirs is controlled by many geological factors such as organic matter content, thermal maturity, thickness, mineral composition, diagenetic alterations and depositional processes (Jiang et al., 2016). Although some common characteristics exist among conventional and unconventional reservoirs, complex geological characterisation is very challenging in unconventional gas reservoirs due to heterogeneity at different scales (Passey et al., 2010).

The presence of organic matter gives clues about the organic richness of the shale, and its preservation is highly dependent on the depositional settings of the sediments (Chen et al., 2018; P. De Silva et al., 2015; Guochang Wang & Timothy R. Carr, 2012; Zhang et al., 2012). For instance, the algae from the lacustrine environment form type-I kerogen, whereas the type-II kerogen is developed in marine settings. Moreover, kerogen type-III usually results from plants in a continental environment. The analytical techniques usually applied for examining the total organic carbon (TOC) from the core samples or cuttings are Rock-Eval or

Leco TOC (Jarvie et al., 2007). Many techniques and theoretical relationships are well known to find TOC through well-log data. However, the calibration of each method is important to see the variation in lithology and maturity.

Recent studies suggest that the organic-rich shale is thick and heterogeneous even at a finer scale due to variations in depositional settings(Bohacs et al., 2000; P. De Silva et al., 2015; Passey et al., 2010). To introduce a better understanding of heterogeneity, defining the rock types is considered a better solution to remove uncertainties (Kale et al., 2010). However, the different rock types are based on different framework contexts, such as depositional rock type, petrographic rock type, and hydraulic rock type, identified by applying various techniques of different scale levels. Though, all three rock types may also be highly affected by diagenetic processes after deposition. The rock types are generally defined by (Gunter et al., 1997) as "units of rocks deposited under same geological conditions, undergone similar diagenetic processes and resulting in a unique porosity-permeability relationship, capillary pressure profile and water saturations". These distinctive features of rock types are very helpful in recognising suitable producible zones. In conventional reservoirs (e.g. sandstone and carbonates), the rock-typing can be estimated by cross-plotting the porosity-permeability values. The porosity and permeability can be measured directly on a samples as well as some correlations also exist for their estimations as developed by (Swanson, 1981) and (Thomeer, 1983; Thomeer, 1960) for permeability. The values of porosity and permeability are found in a wide range in different parts of the reservoir; therefore, it becomes elementary to identify rock types in conventional reservoirs. A modified perception of the Rock Quality Index (RQI) introduced by (Amaefule et al., 1993) can be assessed by porosity and permeability. On the other hand, Winland and Pitman (1992) suggested another method of rock typing by applying mercury injections extents (capillary curves). The effect of pore throat radius was linked with porosity and permeability measurements.

All these techniques for rock typing classification are utilised based on porosity and permeability measurements and work well for conventional reservoirs as their permeability and porosity are wide. However, these methods do not work for unconventional reservoirs due to ultra-low permeability and the narrow range of porosity in shale (Sondergeld et al., 2010). Although there are many challenges in defining the rock typing of gas shale reservoirs, it can be a very valuable work to divide shale reservoirs into different rock types that may influence gas resource potential and production from shale. The rock types of Barnett Shale had identified by (Kale et al., 2010) by involving mineralogy and TOC with porosity and capillary curves to recognise the sweet spots in the gas shale reservoir. An integrated approach based on well-logs, image logs, and core analysis is always helpful in understanding shale's complex lithofacies system (Jacobi et al., 2007). On the basis of such approach, after analysing the lithofacies according to lithology and mineralogy variation, the favourable and non-favourable zones for hydraulic fracturing can be identified based on computed geomechanical properties and kerogen content (Jadoon et al., 2016; Ross & Bustin, 2008; Rybacki et al., 2016). Therefore, it is required to involve a detailed information for better understanding of rock types in shale that may be helpful to find the gas storage capacity of shale in an accurate way.

Analysing whether a given shale play has enough rock quality and where the favourable sweet spots are located requires a detailed understanding and analysis of available geological and petrophysical data. Understanding the fundamental petrophysical controlling factors is also necessary to successfully evaluate shale (Basin, 2004). The most important petrophysical parameters for determining gas shale potential are thickness, TOC, porosity, pore architecture, permeability, brittleness, irreducible water saturation (clay bound and capillary water), free and adsorbed gas content (Ambrose et al., 2010; Fitch et al., 2015; Jacobi et al., 2009; Mullen, 2010; Ross & Bustin, 2008). These parameters are usually fairly constant; however, in a heterogeneous reservoir (e.g. gas shale), these petrophysical properties can vary significantly. This variation may be handled if petrophysical analyses are carried out at multiscale and by adopting a systematic approach. At the measurement scale, it can be expected that some heterogeneities still exist. Therefore, it is crucial to note that facies that look identical at one scale may show some variation at a finer scale and vice versa (Frykman, 2001; Jennings & Lucia, 2003; Pranter et al., 2005).

1.3 Geological Setting for the Study Area

The Canning Basin is a large basin in the NW part of Australia with an area of about 595,000 km^2 (Carlsen & Ghori, 2005; Iqbal et al., 2022). This basin is bounded by the Pilbara and Musgrave Blocks to the SW, the Kimberley block to the NE, the Roebuck Basin to the west and the Amadeus Basin to the east (Cadman et al., 1993). The Canning Basin is further divided into sub-basins and structural elements, mainly NW-SE structural trends (Apak & Carlsen, 1997) (Figure 1.1).

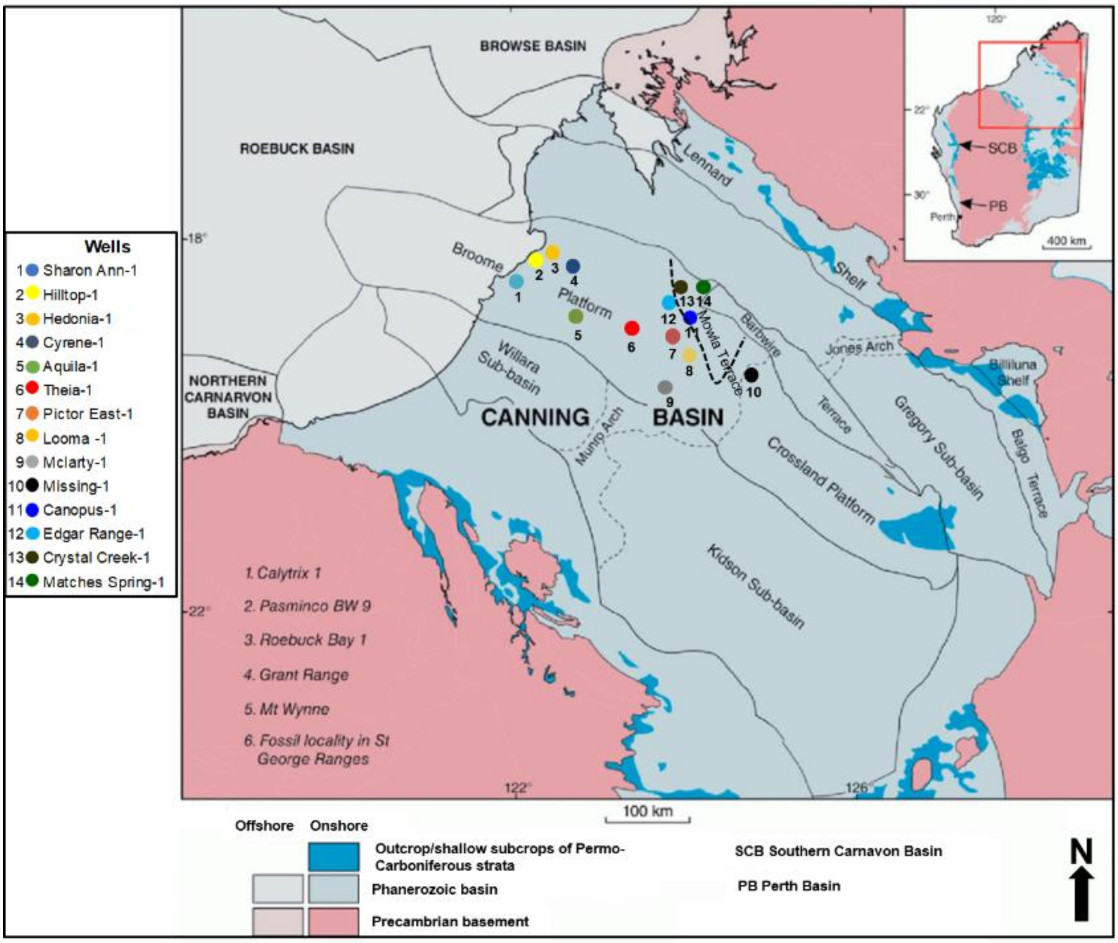

Figure 1.1: Geological map of the study area showing the location of different wells from Broom and Crossland platforms, Canning Basin, Western Australia (Modified from (Taylor et al., 2018) and (Mory, 2010).

The Canning Basin's sedimentary deposits range from the Ordovician to Cretaceous ages (Brown et al., 1984) (Figure 1.2). This research mainly focuses on the Goldwyer Formation of the Lower to Middle Ordovician age (Cadman et al., 1993). The Goldwyer Formation is subdivided into three units as upper shale unit (Goldwyer-I), middle carbonates unit (Goldwyer-II), and lower shale (Goldwyer-III) (Foster et al., 1986; Winchester-Seeto et al., 2000). The Goldwyer Formation's depositional setting is interpreted as open marine based on previous studies (Haines, 2004). The previous research (van Hattum et al., 2019) has suggested that the Goldwyer-III has a good gas shale potential compared to Goldwyer-I shale. Therefore, this study has provided a detailed reservoir characterisation of the Goldwyer-III shale unit. The required dataset, such as borehole logs and core samples for the Goldwyer-III shale unit, are available within different wells drilled in the onshore Canning Basin, Western Australia, as shown in Figure 1.1. Out of the available wells, the Theia-1 well will be used as a crucial well due to the availability of detailed dataset from this well.

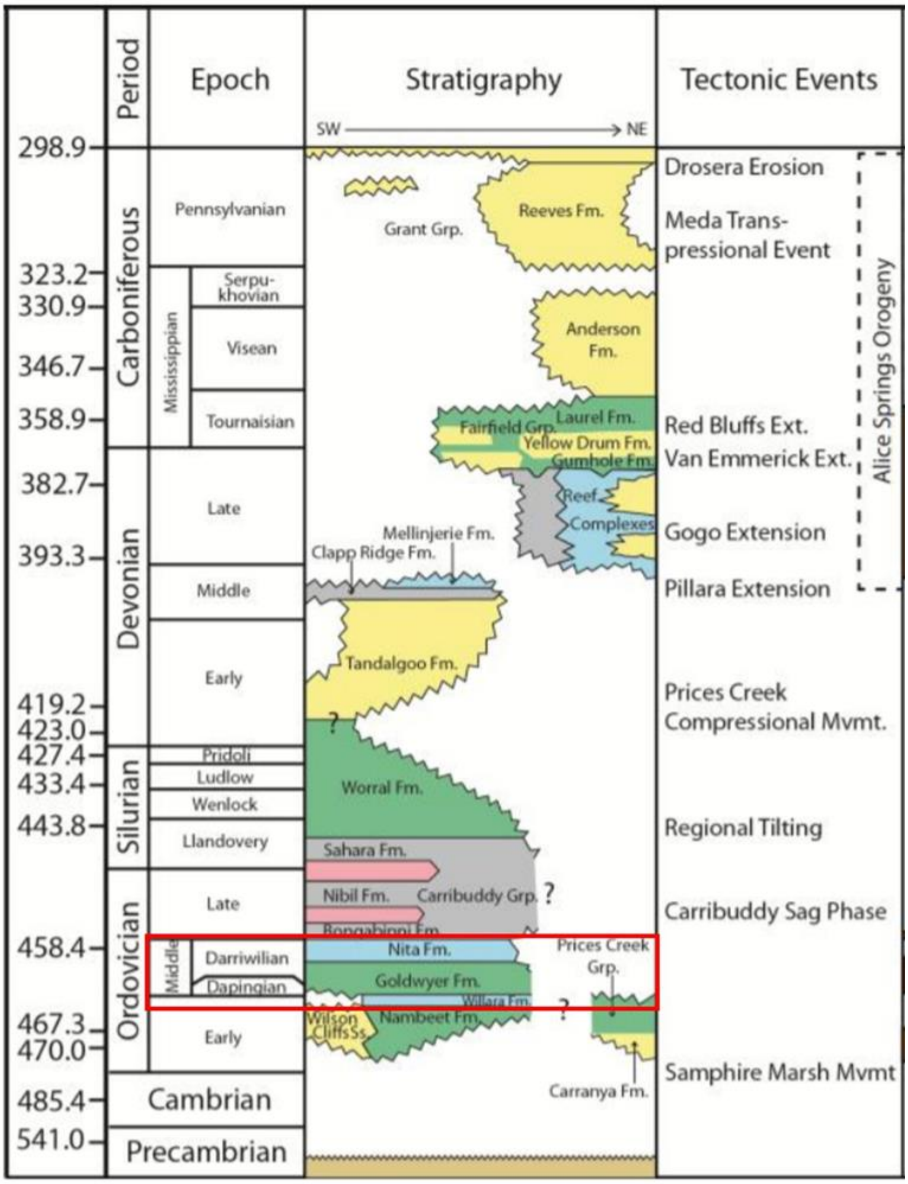

Figure 1.2: Stratigraphic column of early Paleozoic Canning Basin (Adapted from the Department of Mines, Industry Regulation and Safety reports, 2015).

1.4 Project Significance and Research Objectives

The higher demand by the society for energy and environmentally cleaner gas sources mean that gas shale reservoirs are significant exploration targets. The successful exploration of gas shale reservoirs in North America has built confidence to discover these in different regions. However, due to uncertainties and heterogeneities in the reservoir properties of gas shale reservoirs, it is challenging to define an accurate model for gas storage capacity. In Australia and worldwide, rock typing has been carried out based on conventional techniques for conventional reservoirs. However, there exists minimal published work related to rock typing and its effect on the total gas capacity for shale due to many associated challenges.

It is well known that costly techniques are required to explore gas shale reservoirs successfully, so it is crucial to identify suitable production zones from heterogeneous shale units. This research will be significant in solving this problem by introducing a classification scheme for rock typing of shale based on descriptive, analytical, and statistical approaches to reduce uncertainties. Moreover, each rock type unit will determine the free and adsorbed gas contents to examine the impact of different rock typing parameters on gas content in the shale. As a result, this research approach will provide a better understanding of suitable zones for successful gas exploration, and a workflow will be built for it.

Due to the narrow porosity range and heterogeneity in shale, the typical approach of rock typing (e.g., porosity-permeability cross-plot) is not convenient for shale. So, a detailed workflow based on descriptive, analytical, and statistical methods is required to understand the heterogeneity and its impact on the total gas content of gas shale reservoirs which can help know the resource potential. Though, minimal work had been done in previous research on rock typing and its influence on the total gas content of shale.

Hence, the Goldwyer Formation from Canning Basin provides an excellent opportunity (due to the availability of a detailed dataset, e.g., well-logs, image logs, core, and cuttings) to classify the shale intervals into different rock types based on mineral composition, TOC, sedimentary features, porosity ranges, pore size distribution, and capillary curves. Moreover, the accurate estimation of total gas content will also be carried out by considering the effect of rock typing on free and adsorbed gas capacities in the Goldwyer Formation.

This thesis aims to elucidate the influence of different rock types on sedimentary features, mineral compositions, porosity, pore structure, organic richness, brittleness index, and how they are distributed in the Canning Basin. While shales have been the subject of extensive research in recent years, still limited integrated research about shale rock typing has been conducted to date. It used a holistic approach to investigating these rock types and their influence on gas storage and transport mechanisms. In particular, the following key objectives will be addressed in this research work:

i) Rock type identification: To classify the shale into different rock types to understand the heterogeneity by applying descriptive, analytical, and statistical approaches such as sedimentary features, mineral composition, organic richness, porosity, pore size distribution, and clustering based on machine learning.

ii) Estimation of free and adsorbed gases: To estimate the total gas content of gas shale reservoir through well-logs interpretation and experimental tactics:

   a) Free Gas content: Through well-logs analysis and the required porosity determination by lab analysis on the core for validation and accuracy.
   b) Adsorbed Gas content: To determine through experiments on core and well-logs by developing a model based on both techniques.

iii) Identification of suitable layers for gas shale production: The integration of rock typing determination with total gas content in shale to recognize the resource potential of appropriate producible zones and develop a model for total gas content based on different distinctive features of rock typing.

iv) 3-D modelling for prospects evaluation: 3-D modelling of facies, petrophysical and geomechanical properties to understand the heterogeneity for prospects evaluation at the basin scale.

1.5 Materials and Methods

The Canning Basin is an under explored petroleum basin for gas shale exploration and production. Therefore, a limited dataset is available from drilled wells, as shown in Figure 1.1, to characterise the gas shale potential of the Goldwyer Formation. However, an extensive dataset including drilled core, well logs, image logs, and hyperspectral reflectance spectra collected using HyLogger3TM is available for Theia-1 well. This research is focused on the Goldwyer-III shale unit, so an integrated multiscale approach is applied to understand the gas shale potential of this unit (Figure 1.3).

1.5.1 Core Logging and Sampling

A detailed description of the 300m core drilled in the Theia-1 well was carried out to identify the sedimentary features and to select suitable samples for laboratory analyses. A systematic approach was followed to choose the samples at a regular depth interval and from different rock types to cover the whole range of heterogeneities. The core images and HyLogger3TM data were also available from the other five wells. The core description was validated with well logs responses and HyLogger3TM.

1.5.2 Laboratory measurements

Multiscale laboratory analyses were performed on the representative shale samples from the Goldwyer-III unit. The Rock-Eval pyrolysis technique estimated total organic carbon (TOC). The mineral composition was determined based on x-ray diffraction (XRD) on powdered and clay fractions samples; Fourier transform infra-red (FTIR), and mineral distribution mapping was carried out by applying a high-resolution TESCAN integrated mineral analyser (TIMA). The minerals morphology and grain to grain contacts were analysed based on field emission scanning electron microscopy (FESEM).

The porosity was determined based on bulk and grain densities measurements, and the samples were crushed carefully not to lose a single grain to get accurate porosity measurements. The pore morphology was analysed by FESEM analysis. The pore size distributions of micro and mesopores were determined using low-pressure carbon dioxide and nitrogen (LPCO2 and LPN2) adsorptions techniques. Mercury injection capillary pressure (MICP) analysis defined the macropore size distribution. The adsorbed gas was determined by using the data from the high-pressure volume methane adsorption (HPVA-CH4) technique.

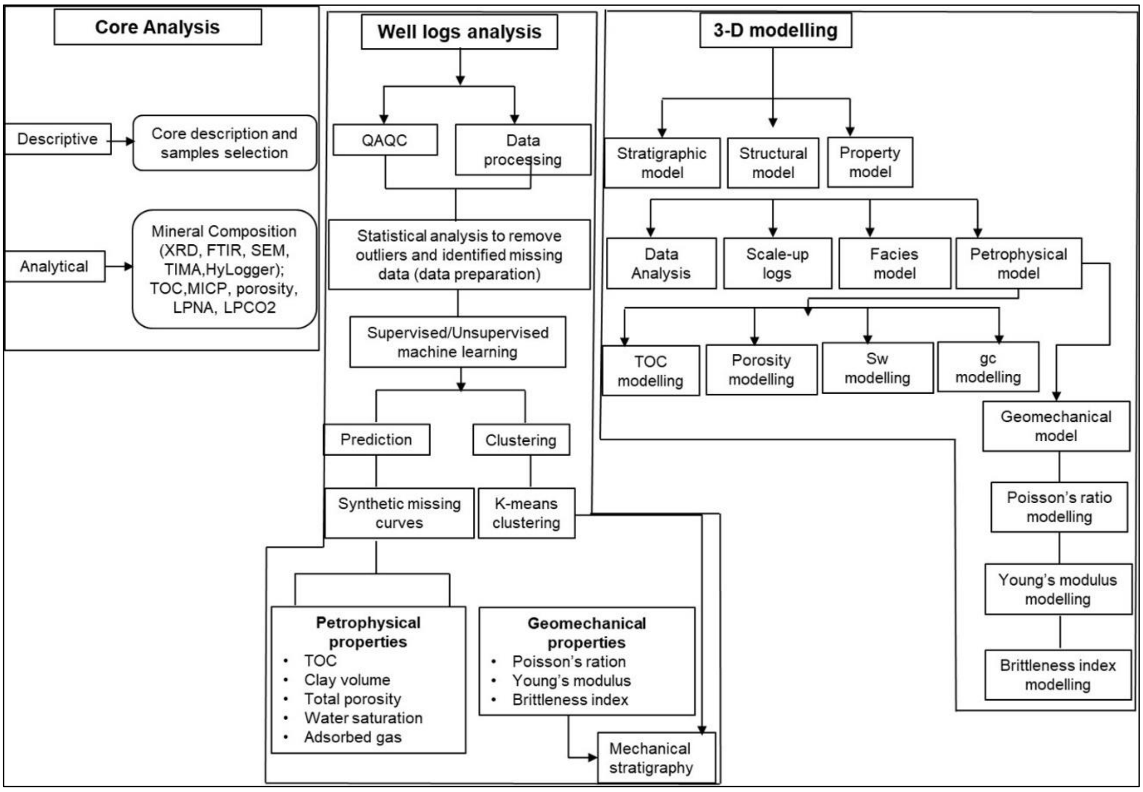

Figure 1.3: A step by step workflow designed for this research to achieve the objectives.

1.5.3 Well Data and 3-D Modelling

Well logs such as Gamma-ray (GR), deep resistivity (LLD), density (RHOB), sonic (DT), and neutron porosity (NPHI) were available for 14 wells from Canning Basin in which the Goldwyer-III shale was drilled. Sonic, density, and neutron logs were missing in a few wells, and their synthetic curves were generated based on machine learning algorithms. The petrophysical properties such as TOC, porosity, shale volume, water saturation, and adsorbed gas content were estimated based on well-logs analysis, and new equations were proposed for porosity and water saturation determination of shale reservoirs. The applied equations were validated and calibrated with the core-based measurements. Similarly, the continuous geomechanical properties (e.g. Poisson's ratio, Young's modulus, and brittleness index) were estimated by applying core-calibrated equations. The rock types in each well were defined based on machine learning-based clustering using well logs, petrophysical, and geomechanical properties as input variables. Mechanical stratigraphy was introduced for shale for the first time by integrating lithofacies (clustering) and geomechanical properties.

After getting the downhole continuous petrophysical and geomechanical properties for all available 14 wells, a 3-D model for facies and all these properties was constructed in Petrel software using the seismic-based polygon covering the area from Broome and Crossland platforms in Canning Basin.

1.6 Thesis Layout

This thesis consists of seven chapters, including this introductory chapter. Chapters 2 to 5 provide the main results of this research and associated discussions, each chapter presenting the key objectives. In the end, Chapter 6 summarises the conclusions of this thesis and Chapter 7 highlights the limitations and recommendations of thesis. The overall structure of the thesis is summarized below:

Chapter 1 provides an overall context of the research topic, basic terminologies, study area, research problem, objectives, and comprehensive methodology addressed in subsequent chapters.

Chapter 2 presents the detailed core description of Goldwyer-III shale and provides a systematic workflow on how different sedimentary facies are identified based on other datasets. A novel approach is introduced by integrating the core description with the image logs and hyperspectral reflectance spectra collected using HyLogger3™. The hyperspectral reflectance spectra were validated with x-ray diffraction and FTIR-based mineralogy. The thin sections and scanning electron microscopy helped to describe the internal structure of each sedimentary facies. Incorporating the HyLogger3TM-based mineralogy, TOC, well logs and brittleness index helped identify the suitable layers for hydraulic fracturing.

Chapter 3 describes how sedimentary facies can be sub-divided into different lithofacies based on defined cut-off values of mineral compositions and TOC contents. The porosity, pore size distribution and pore structure were then determined for each lithofacies. The results allow selection of the producible lithofacies based on defined criteria.

Chapter 4 derives the well log equations for porosity and water saturation calibrated to the core-data. In the previous chapter, the porosity was determined on the representative core samples. However, a well-log-based equation is required to represent the porosity distribution at the basin scale. This is difficult to do because the standard equations for conventional reservoirs do not work accurately for shale reservoirs and usually need to be specific to each shale. Therefore, the proposed equations in this chapter were calibrated and validated with core-based data for the Goldwyer-III shales.

Chapter 5 uses the results from the previous chapter to make a 3-D model of facies, petrophysical and geomechanical properties to understand the regional prospect evaluation of gas shale in the Broome-Crossland Platform area. A new workflow is introduced to define the mechanical stratigraphy by integrating machine learning-based clustering and geomechanical properties to identify the suitable layers for hydraulic fracturing. The mechanical stratigraphy and petrophysical lithofacies are incorporated in the models to recognise the best producible and brittle layers in Goldwyer-III shale. Their distribution across Broome and Crossland platforms is analysed with the help of 3-D modelling by utilising the data from 14 wells.

Chapter 6 summarises the key findings of this thesis and delivers the concluding remarks and recommendations for future research.

Chapter 2 Sedimentary and High-Resolution Mineralogical Characterisation of the Ordovician Goldwyer Formation

Summary

Understanding the nature of the facies heterogeneity is crucial for the successful exploration and development of gas shale reservoirs. However, shale is a very fine-grained sedimentary rock, and it is challenging to understand its heterogeneity through conventional techniques. This chapter addresses this challenge for Ordovician Goldwyer Formation (Goldwyer-III shale) through a unique approach by integrating core data with high-resolution image logs (SCMI); petrographic information; Fourier transform infrared (FTIR); and hyperspectral drill core reflectance spectra acquired using a HyLogger3. The petrographic and FTIR data validate the usage of HyLogger3 as a tool to examine high-resolution vertical variations in shale mineralogy. The results indicate that the Goldwyer-III shale is highly heterogeneous in terms of sedimentary features, organic richness, and mineral composition. The studied shale is divided into four facies based on colour, sedimentary features, mineral composition, and lithology. The facies include thinly laminated siliceous shale (TLSh), concretionary-banded calcareous shale (CSh), massive black shale (MBSh) and heterolithic shale (HSh). The total organic carbon varies from 0.35 to 4.5 wt% due to variation in facies because of fluctuation in oxic-anoxic conditions. The TLSh, MBSh and HSh facies have a higher TOC value (up to 4.5 wt. %), Tmax (up to 450 °C), hydrogen index (up to 250 mgHC/g) and

brittleness index (>0.4) comparatively. Whereas, the CSh facies has least TOC, Tmax, hydrogen index and brittleness index. Continuous high-resolution hyperspectral core log data, combined with petrography and conventional core logging, provides a much better understanding of heterogeneity in Goldwyer-III shale. This study offers a new workflow for rapid, continuous, and accurate recognition of optimum facies for hydraulic fracturing. This approach can improve economic decisions when developing gas shale reservoirs. Based on TOC and mineralogical-derived brittleness index cut-off values, the high-quality brittle zones are recognised in TLSh and HSh facies deposited in medial (proximal to distal) depositional setting.

2.1 Introduction

The development of unconventional resources is vital due to the increase in energy demand and the depletion of conventional reservoirs. Furthermore, unconventional natural gas resources such as gas shale reservoirs are considered environmentally cleaner fuels compared to coal (Jenner & Lamadrid, 2013). These resources are widespread in various regions of the world (Leather et al., 2013). However, the successful extraction of gas shale is very challenging and requires an extensive understanding of the depositional and diagenetic processes behind its occurrence (P. De Silva et al., 2015; Johnson & Boersma, 2013). These processes affect the geological and petrophysical characteristics of the shale as a reservoir. Therefore, it is critical to accurately evaluate the in-situ shale reservoir properties with the progressions in technologies (Weijermars, 2013).

Shale is considered a very complex, fine-grained, anisotropic in nature, fissile rock comprised of different proportions of minerals such as clays, carbonates, and quartz (Ahmad, 2014; Delle Piane et al., 2015; Katahara, 2008; Olgaard et al., 1995; Schieber, 1999; Sondergeld et al., 2010). Recent studies show that organic-rich sediments may be hundreds of meters thick. However, vertical variation in organic richness, sedimentary features, and brittle minerals exists even at a fine vertical scale (Bohacs et al., 2000; P. De Silva et al., 2015; Passey et al., 2010). This vertical heterogeneity can directly connect with changes in geologic and deposition conditions. Even in the same depositional settings, shale is unique to have heterogeneous nature in terms of the colour, mineral composition, porosity, and sedimentary features (Huang et al., 2018; Pawar et al., 2017; Ross & Marc Bustin, 2009; Turner et al., 2016). These features are highly affected by the variation in depositional settings (De Silva et al., 2015). Understanding heterogeneity in shale's reservoir properties plays a vital role in identifying "suitable zones" for reservoir quality and hydraulic fracturing in gas shale reservoirs (Chen et al., 2015; Jiang et al., 2016).

Marine shales have fewer stratigraphic variations over time than lacustrine shales and are widely distributed (Jiang et al., 2016; Suarez-Rivera et al., 2006). Many researchers have introduced geological information, texture and diagenesis, geomechanics, resource potential, and reservoir characterisation workflow for shale reservoirs (P. N. K. De Silva et al., 2015; Delle Piane et al., 2015; Ekundayo & Rezaee, 2019; Guo & Peng, 2019; Iqbal et al., 2018; Josh et al., 2012; Olierook et al., 2014; Rezaee et al., 2007; Rezaee, 2015; Sondergeld et al., 2010; Tang et al., 2017; Yuan et al., 2018; Zou & Rezaee, 2019). However, a detailed and high-confidence workflow for understanding facies heterogeneity in marine shale is still missing. Moreover, as the heterogeneity level varies from micro to macro-scale, there are challenges to having access to suitable sampling methods. Therefore, it is necessary to have high-resolution continuous information to assess the shale vertical heterogeneity. This information is vital to pinpoint appropriate zones for successful gas shale exploration and development.

This chapter presents the recognition of sedimentary facies heterogeneities in the shale unit of Goldwyer Formation (Goldwyer-III shale) deposited in Canning Basin, Western Australia. As suggested by Van Hattum et al., 2019, the Goldwyer-III has more potential as a gas shale reservoir; however, a detailed study of Goldwyer-III facies classification is still missing. Therefore, we focused on Goldwyer-III shale (the third unit known as Goldwyer-III) in this research. The shale is a very fine-grained rock so a multiscale workflow from the core to the microscopic level is applied in this chapter to understand the vertical heterogeneity. Generally, Goldwyer-III shale is considered clay-rich (mainly illite) compared to other global marine shales (Yuan et al., 2019). However, it may have some organic-rich and siliceous layers with higher TOC and brittle minerals content. Without heterogeneity understanding, such suitable layers may be overlooked. Therefore, the continuous high-resolution hyperspectral core log data, combined with FTIR, petrography, and conventional core logging applied in this study, provided a much better understanding of facies heterogeneity in shale. Drill core obtained from the Goldwyer-III offered a unique set of vast information to integrate the conventional approach (core description, petrographic studies, and well logs analysis) of facies identification with high-resolution data. Continuous mineralogical information through HyLogger3 spectra (short wave infra-red, SWIR, thermal infra-red, TIR) leads us to understand the heterogeneity at high resolution. This approach helped us to recognise the "landing points" suitable for hydraulic fracturing. A range of well-logs (Gamma-ray, density, resistivity, sonic, and PEF), TOC, mineral compositions, and brittleness index is defined for each facies. This approach can improve economic decisions when developing gas shale reservoirs.

2.2 Materials and Methods

An extensive dataset including 122 m core, well logs, image logs (slimline compact micro imager: SCMI), and hyperspectral reflectance spectra collected using the HyLogger3TM are investigated for the study of Goldwyer-III shale. A multiscale (m-μm) approach was applied to achieve the objectives of this study as follows:

2.2.1 Core scan and image logs analysis

The sedimentary features were identified at the millimeter to centimeter (m-cm) scale by integrating core scan and image logs data provided by the Department of Mines, Industry Regulation and Safety (DMIRS) for the Theia-1 well. The image log was acquired by Finder Exploration company and processed and interpreted in Techlog software. The processing included depth matching (concerning Gamma-ray log), speed correction, gap filling, and generating normalised dynamic and static images. The integration of image logs and core scan images (collected from DMIRS) was used to recognise different sedimentary features for the characterisation of shale. The spectral gamma-ray log was analysed to understand the distribution of organic matter in different depositional settings. The triple combo logs (Gamma-ray, neutron porosity, density, and resistivity) were interpreted and illustrated in Interactive Petrophysics (IP) software for calibration with core and HyLogger3 data.

2.2.2 HyLogger3 data interpretation

The HyLogger3TM hyperspectral drill core scanner has been developed by the Commonwealth Scientific and Industrial Research Organisation (CSIRO) for fast, non-destructive, and objective mineral spectroscopy (Schodlok et al., 2016). It is a combination of various sensitive reflectance spectrometers that cover the Visible-Near infrared (VNIR), Short-Wave Infrared (SWIR), and Thermal infrared (TIR) wavelengths with the robotic sample. Hyperspectral drill core data were processed by the Geological Survey of Western Australia (GSWA) using The Spectral Geologist software (TSG). It helps to identify different minerals at a spatial resolution of about 10 mm for spectral data and 0.1 mm for RGB images (Hancock & Huntington, 2010). It provides information about mineral assemblages and their compositional variations at the cm scale (Higgs et al., 2015; Huntington et al., 2010). The Spectral Assistant (TSA), a tool in TSG, was used by GSWA to semi-automatically identify the presence of the three most-prominent mineral groups per cm (examples of minerals active in the respective wavelength regions in Table 2.1). The accuracy of this semi-automated mineral identification relies on 1) which minerals are active in which wavelength range, 2) the underlying TSA algorithm (Berman et al., 2017), 3) the range of minerals present in the spectral reference library used for that version of TSA and 4) prior knowledge of the operator processing the hyperspectral data. Example reference spectra are shown in figure 2.1. The TIR and SWIR data were validated and correlated with petrographic information. VNIR data was not used for this project. It should be noted that the TSA-generated result from SWIR spectra does not include any minerals that are not active in the SWIR (for examples quartz or any other non-hydrous silicates). Therefore, any amounts of minerals inferred from TSA results do not represent quantitative mineral abundances.

2.2.3 Fourier Transform InfraRed (FTIR)

Additional infrared spectroscopy studies were performed using a Vertex 70 Fourier transform infrared spectrometer (Bruker). All infrared spectra were collected between 4000 to 400 cm-1 using 32 scans at a resolution of 2 cm-1 and a DLaTGS detector. Attenuated total reflectance (ATR) measurements were made on the rock powders using a Bruker Platinum ATR accessory which comprises a single reflection diamond crystal. All FTIR measurements were undertaken at room temperature (20 ± 2 °C), and the IR spectra have been presented as raw data. This qualitative approach was applied in the CSIRO laboratory for representative powdered samples of Goldwyer-III shale to obtain the spectra. In contrast, the quantitative FTIR data was adopted from Finder Exploration company reports.

TABLE 2.1: The detected minerals at different wavelengths using hylogger33 and TSG software (Higgs et al., 2015; Huntington et al., 2010).

Wavelength region	Wavelength range (nm)	Identified mineralogy
VNIR	400-1100	Iron oxides and hydroxides manganese oxides, rare earths
SWIR	1100-2500	Hydroxyl-bearing minerals (e.g. micas, amphiboles), carbonates, sulphates
TIR	6000-14,500	Carbonates, silicates (including quartz, feldspar, olivine, pyroxene, garnet, mica), sulphates, phosphates

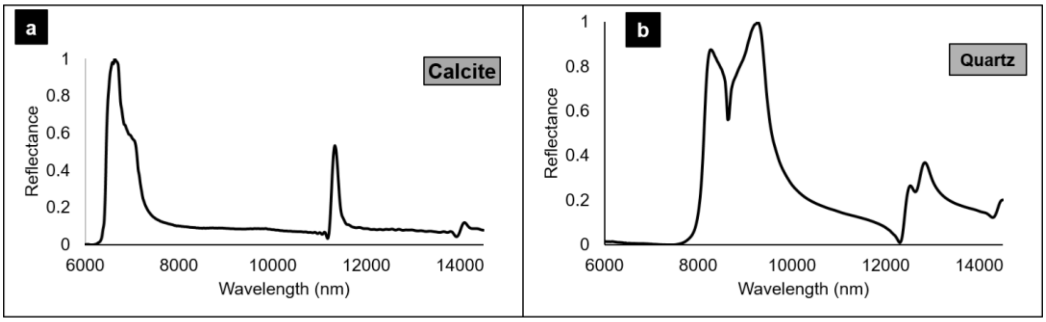

FIGURE 2.1: Mineral reflectance spectra adapted from CSIRO spectral reference library (https://mineralspectrallibraries.csiro.au); a) calcite spectrum with absorption peaks at 6500nm and 11500nm wavelengths, b) quartz mineral spectrum with absorption peaks at 8500nm, 9500nm, and 13500 nm wavelengths.

2.2.4 Total organic carbon and petrography

Total organic carbon was measured on forty powdered bulk samples using Rock-Eval Pyrolysis available in the Unconventional Gas Research Group in the

Department of Petroleum Engineering, Curtin University, Western Australia. This analytical method uses approximately 60-80 mg pulverised shale samples. The sediments were heated under an inert atmosphere of nitrogen, and the emitted organic compounds (S1, S2, S3, and CO_2) were measured during each stage. Pyrolysis provides information on the free, already generated hydrocarbons in the rock (S1) and the hydrocarbons that can be generated from the kerogen by thermal cracking of kerogen (S2) (Espitalie et al., 1985; Espitalie et al., 1977; Tissot & Welte, 2013; Yu et al., 2017). The continuous TOC through well logs was estimated by applying the Δ log R approach (Iqbal et al., 2018; Passey et al., 2010), as shown in Eq. 2.1 and 2.2:

$$\Delta \log Rsonic = \log10\left(\frac{R}{Rbaseline}\right)+0.02(\Delta t- \Delta tbaseline) \quad \text{(Eq. 2.1)}$$

$$TOC = (\Delta \log R)*10(2.297-0.1688*LOM \quad \text{(Eq. 2.2)}$$

Where, Δ log R is the separation between resistivity and sonic log that indicates organic-rich interval, R and Δt are resistivity and travel time from the sonic log, Rbaseline and Δtbaseline are normal resistivity and travel time at the overlay of resistivity and sonic log that represents non-source rock interval. LOM is the level of organic maturity, and its value is taken as 10 that was calculated by (Johnson, 2019; Johnson et al., 2018).

The spectral gamma ray (SGR) data was gathered from the Department of Mines, Industry Regulation and Safety, Western Australia (DMIRS) which was run on the whole core intervals of Goldwyer-III shale by Finder Energy Ltd, Western Australia. This study's SGR data is interpreted to analyse the distribution of organic matter and depositional setting based on Th/K, Th/U, and U/K ratios.

Different petrographic techniques have been applied to recognise facies in Goldwyer Formation (Goldwyer-III shale). Twenty-five impregnated and stained thin sections from Theia-1 well were provided by DMIRS for this study. The thin sections were analysed at mm-μm using transmitted light microscopy in the Department of Geology, Curtin University and Commonwealth Scientific and Industrial Research Organisation (CSIRO), Western Australia. The scanning electron microscopy (SEM) analysis at μm-nm scale was undertaken on representative core chip samples using a Mira-3 Variable Pressure Field Emission Electron Microscopy (VP-FESEM) with energy dispersive x-ray spectroscopy (EDS) and Electron backscattered diffraction (EBSD) located in Microscopic and Microanalysis Facility (MMF), John De Laeter Centre, Curtin University. The samples were polished, and carbon-coated rock blocks were mounted in resin. The imaging was carried out under operating conditions (15 Kev) to provide additional information about the morphology of different minerals and their elemental distribution in each facies.

Semi-quantitative X-ray diffraction (XRD) analysis was carried out on bulk core chip samples. The powdered samples were prepared by crushing and then grinding in Rocklabs swing mill using Tungsten Carbide grinding head. The powders were then scanned on a Bruker D8 Advance diffractometer, from 50 to 900, using a Cu X-ray tube located in XRD laboratory in John De Laeter Centre, Curtin University. The phases of minerals were identified using Bruker Eva Diffracplus software, and the quantification of minerals was estimated by Bruker Topas software. The clay fractions were separated by following USGS and sedimentation method (Iqbal et al., 2019; Poppe et al., 2001). Then three runs (untreated, ethylene glycolated, and heated at 550 ^{o}C) were acquired in Bruker D8 discover diffractometer, from 40 to 350, using a Cobalt X-ray tube.

2.3 Results

2.3.1 Sedimentary Facies

The sedimentary features identified in Goldwyer-III shale are illustrated in Figure 2.2. The thick shale unit in Goldwyer-III is divided into four sedimentary facies distinguished by colour, lithology, sedimentary features, and depositional settings as shown in Figure 2.2 and Figure 2.4. The description of each sedimentary facies is explained below.

2.3.1.1 Thinly laminated siliceous shale (TLSh)

Description: The thinly laminated siliceous shale is dark grey to black and characterised by distinctive interlaminated quartz silt laminae (0.5-2.5 mm thick) (Figure 2.2 to Figure 2.4). The mudstone laminations show deformation around carbonate lenses (siderite on Hylogger), mainly resulting from the early formation of the carbonate concretions and subsequent differential compaction of the mudstone laminae around them. The lenticular bedding is also found in these facies. The silt and clay-rich laminae have scoured base and rippled top (Figure 2.5a). The individual grains within quartz silt laminae are fine-grained, angular to sub-angular shaped, and moderately sorted. Little carbonate cement is locally present. TLSh facies is low to moderate bioturbated, and visual pyrite is also observed (Figure 2.2a).

Overall, TLSh facies is thicker (about 55m thick) as compared to other facies in Goldwyer-III shale drilled in Theia-1 well. Clay minerals in this facies include illite>chlorite>kaolinite>mixed layer illite-smectite. The TLSh facies is composed of about 30% silica minerals (monocrystalline and polycrystalline quartz and feldspar), 55% clay minerals, 12% carbonates (mainly calcite and siderite) and 3% pyrite (Figure 2.7). The ternary diagram illustrates that the thinly laminated shale has a broad range of variations in mineral composition and TOC due to the thin laminations of quartz silt, carbonates, and clay-rich layers (Figure 2.8). Total organic carbon (TOC) averages to 2.5%; however, contrary to TOC values (1.1-3.2 wt%) due to alternating thin layers of organic-rich clay and quartz silt laminae (Figure 2.9). The average thorium to uranium ratio is around 5.5 in this facies, and uranium content is noted as in the range of 1.0-4.5 ppm (Figure 2.10).

Interpretation: The highly interlaminated nature is the most significant sedimentary feature of TLSh facies and it represents the low to moderate energy (mid-ramp) level for this facies and the rarity of fossils as well as minor bioturbation indicate its marine setting within lagoonal area (Flugel & Flügel, 2004; Seyedmehdi et al., 2016). The higher silica minerals content as compared to other facies means the proximal para-sequence (high energy zone); however, the silt and clay-dominated laminations indicate alternating energy regimes and anoxic-dysoxic fluctuations during the deposition (Adnan et al., 2015; Beukes, 1987). Moreover, the organic matter quantity also varies due to variations in transitional to reducing depositional settings that affect the TOC values (Figure 2.10).

2.3.1.2 Concretionary-banded calcareous shale (CSh)

Description: The concretionary-banded calcareous shale is light to dark grey and characterised by interbedded carbonate bands and mudstone bands containing carbonate concretions (Figure 2.2 and Figure 2.3). The mudstone laminations show deformations resulting from the early formation of the carbonate concretions and consequent differential compaction of the mudstone laminae around them (Figure 2.2c and Figure 2.5b). The carbonates occur in bands that are light-coloured and fine-grained or as coarse-grained diagenetic concretions in the darker mudstone bands (Figure 2.3d).

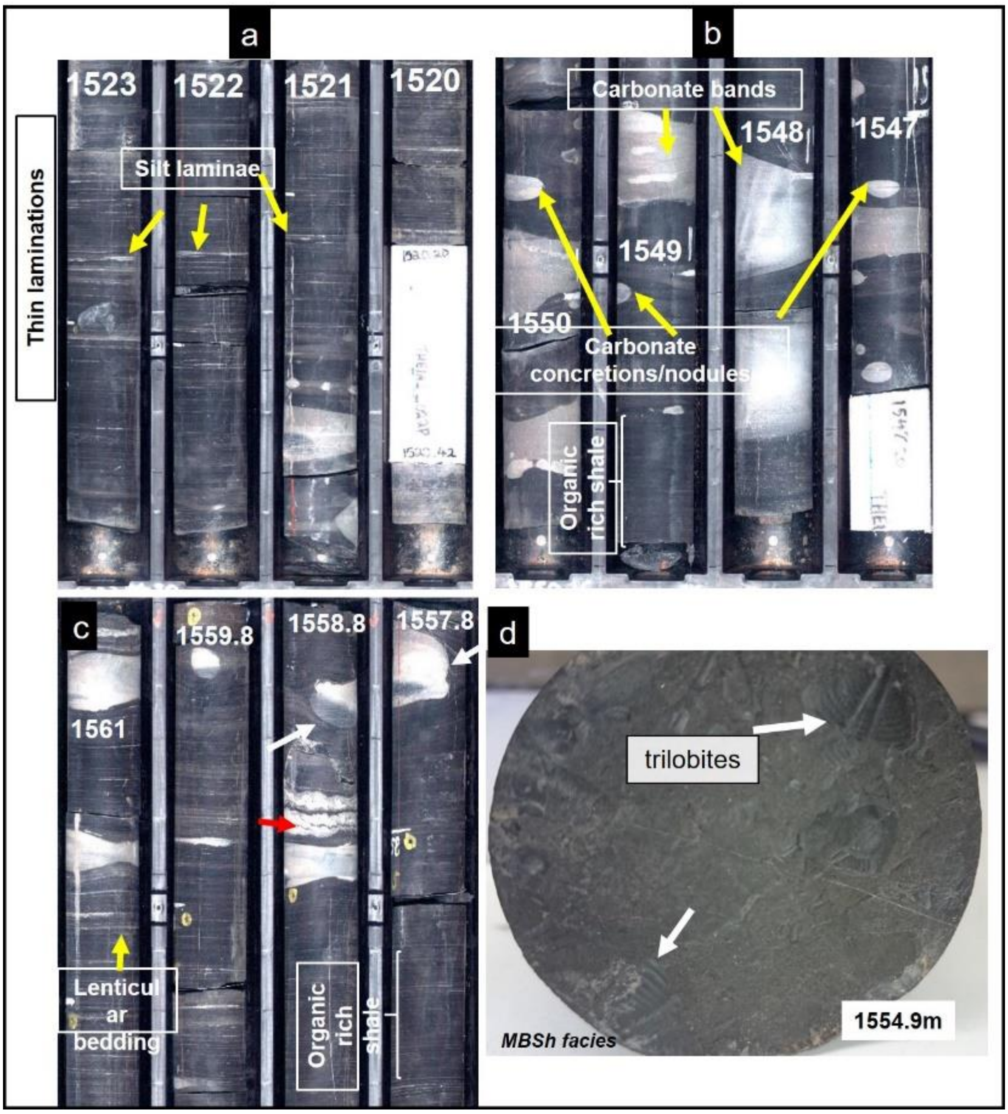

Figure 2.2: Sedimentary features identified in Goldwyer-III shales. Examples from various depths (meters). (a) mm-size quartz silt laminae in thinly laminated shale; (b) carbonate concretions and bands; (c) lenticular bedding in thinly laminated shale, white arrows show the mudstone laminations deformed by the carbonate concretions. The red arrow shows the soft-sediment deformation due

to compaction in concretionary-banded calcareous shale facies; d) Trilobites identified in massive black shale facies.

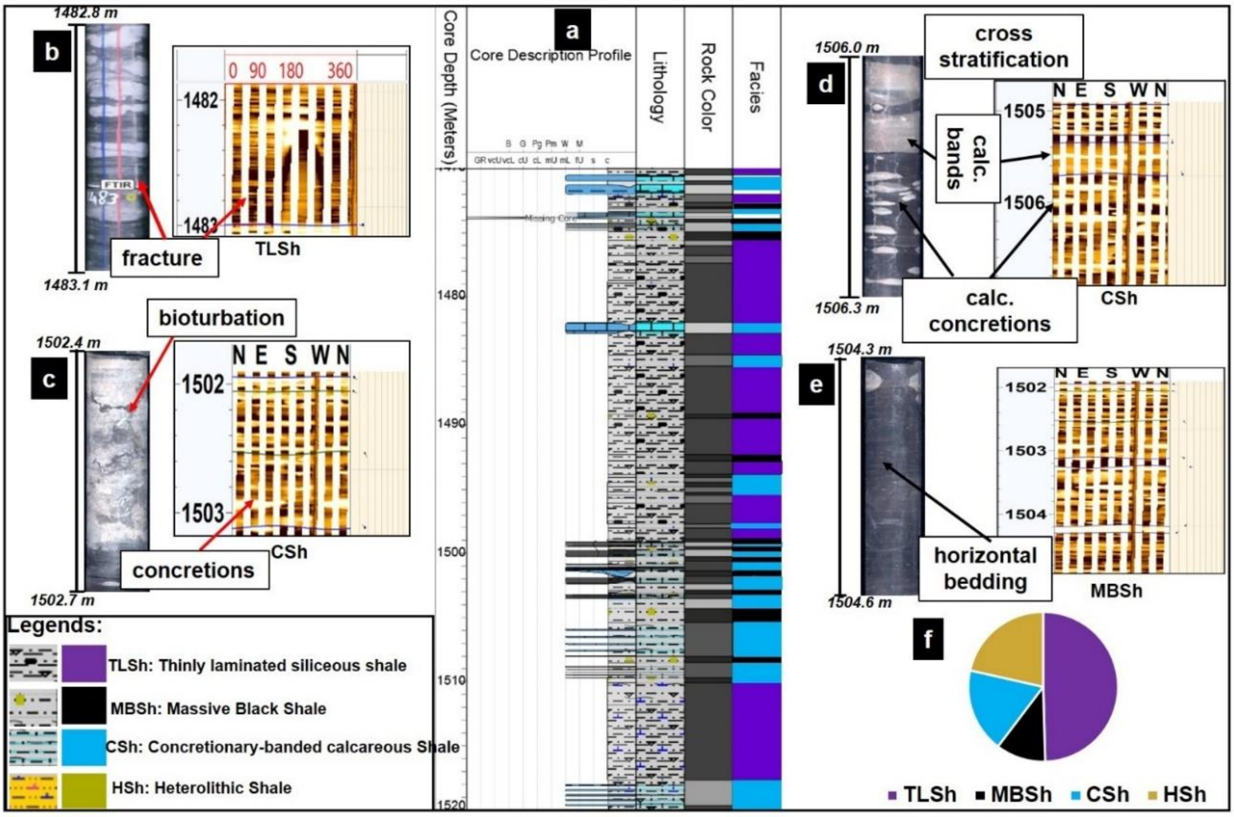

Figure 2.3: The integration of core images and image logs (**depth interval: 1470m-1520m**) to classify various sedimentary facies in Goldwyer-III Shale drilled in Theia-1 well; a) sedimentary facies log: M-lime mudstone; W-wackestone; P-packstone; G-grainstone; B-boundstone; c-clay; s-silt; f-fine; m-medium; c-coarse; Vc-very coarse; GR-gravel, b) fracture identified through core image and image logs in thinly laminated siliceous shale facies, c) bioturbation and concretions in concretionary-banded calcareous shale facies, d) carbonates bands and concretions in CSh facies, e) massive black shale beds in MBSh facies, f) Thickness variation of different facies in Theia-1 well, thinly laminated shale facies is thicker than others.

The laminated silt layers are found sparsely but not very common. This facies is considered as highly bioturbated and has nodular bedding. The individual quartz and calcite grains are fine to medium-grained, sub-angular, and moderately sorted. The calcite cement is observed throughout the facies (Figure 2.6b). The CSh facies is comparatively less thick than other facies. This facies is also comprised of illite as the most abundant clay mineral. The dominant minerals in the concretionary-banded calcareous shale facies are clay minerals with an average amount of about 45%, followed by 35% carbonates.

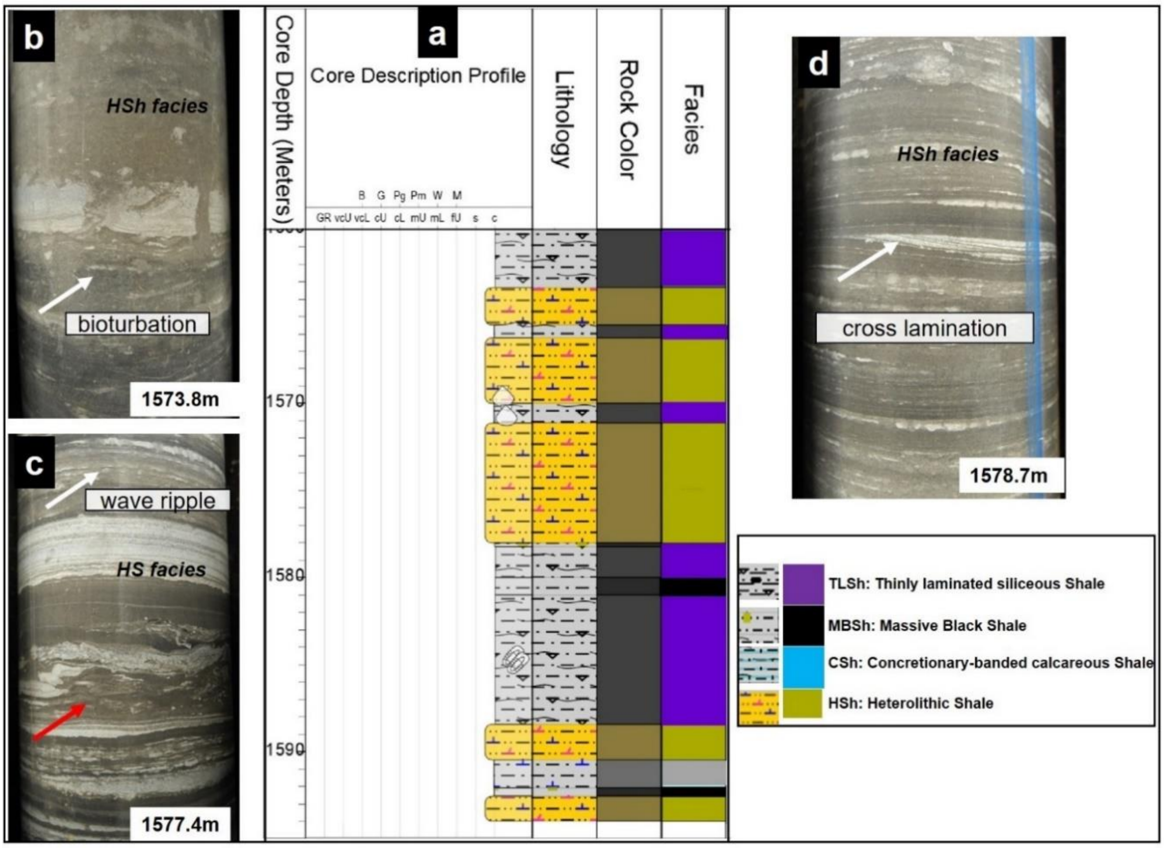

Figure 2.4: Core description (sedimentary facies log: M-lime mudstone; W-wackestone; P-packstone; G-grainstone; B-boundstone; c-clay; s-silt; f-fine; m-medium; c-coarse; Vc-very coarse; GR-gravel) based on core images (depth interval: 1560m-1595m) to identify the repetition of various facies in Goldwyer-III Shale; b) Well-bioturbated with Rosselia, Teichichnus & Planolites; probably bioturbated lenticular bedding in HSh facies, c) wave ripple at the top, soft-sediment deformation (indicated by the red arrow) and bioturbated ripples at the base in HSh facies, d) cross lamination indicated by the white arrow in HSh facies.

Similarly, the average feldspar content is approximately 10% (8% K-feldspar and 2% albite), and the quartz averages about 12%. The pyrite content is even less, with an average amount of almost 1.8%, and few samples contained no pyrite (Figure 2.7). As this facies contains carbonate concretions and bands, in a few samples, the amount of the carbonate minerals reached up to 82% (Figure 2.8). The total organic carbon averaged around 1.7wt% in CSh facies, and the thorium to uranium ratio is estimated to be about 1.7 and uranium content ranging between 0.9 up to more than 5 ppm in this facies (Figure 2.9 and Figure 2.10).

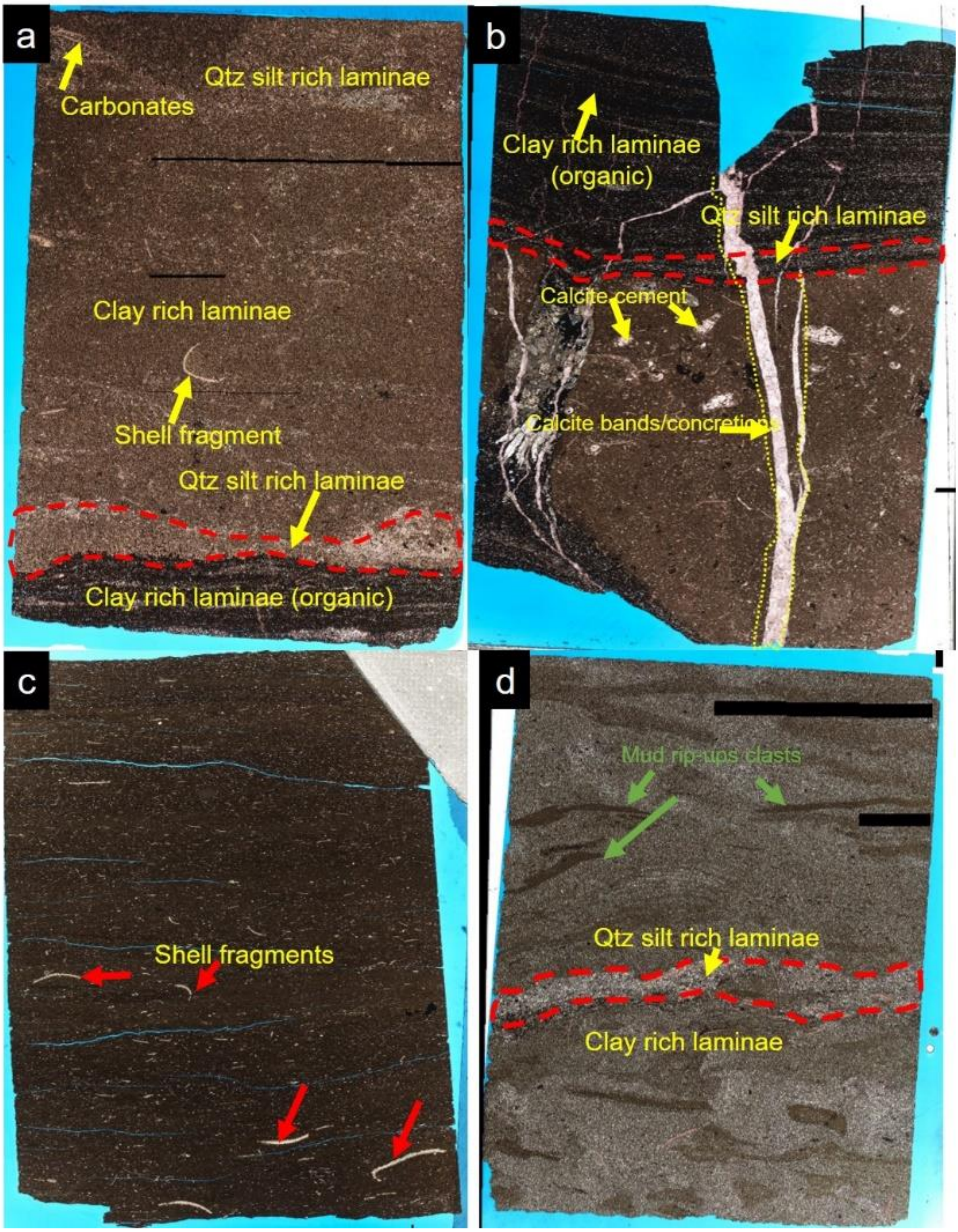

Figure 2.5: Whole thin sections mosaic (2.5X, plane-polarised light) to illustrate various sedimentary features and lithology in different sedimentary facies, such as a) quartz silt rich laminae with scoured base and rippled top in thinly laminated siliceous shale (depth: 1514.27m), b) concretionary-banded calcareous shale (depth: 1546.14m), c) massive black shale (depth: 1499.56m), d) heterolithic shale (1576.5m).

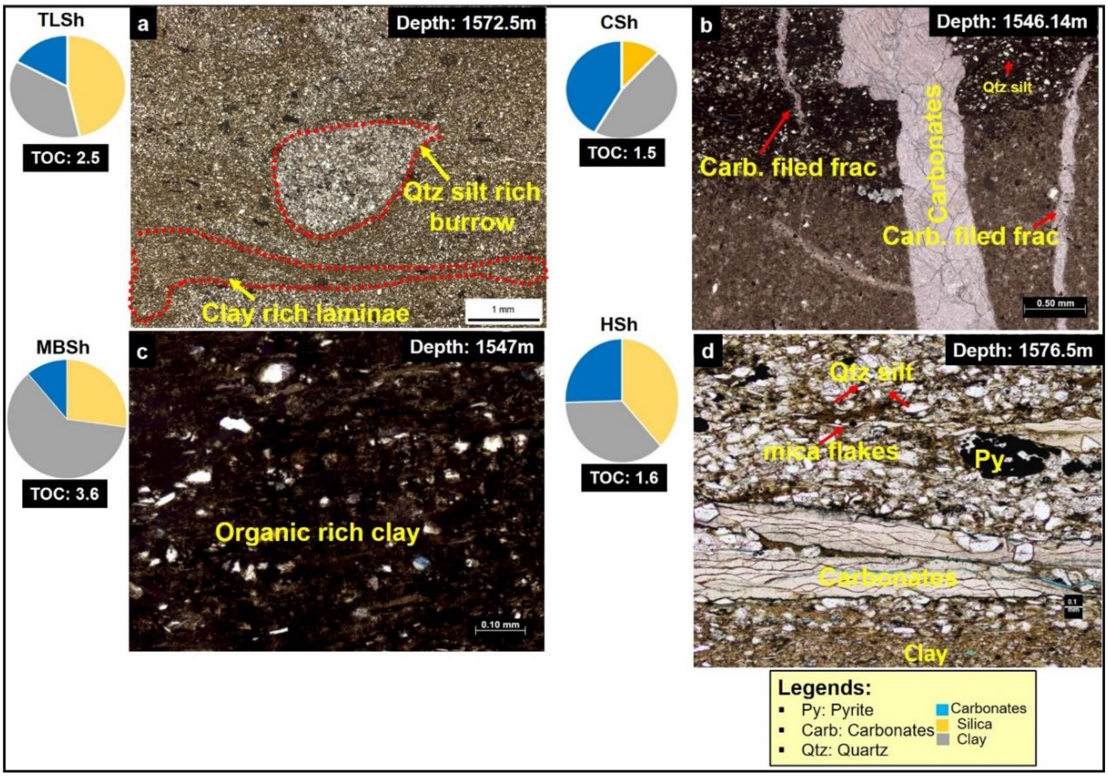

Figure 2.6: Thin section analysis illustrating the rock fabrics in different facies of Goldwyer-III Shale and the pie charts show the major minerals (yellow for quartz and feldspar, blue for carbonates and grey for clays), the average TOC value in each facies is also shown, a) TLSh facies having fine-grained quartz silt rich burrow (white grains) and clay-rich laminae; b) CSh with carbonate filled fractures and bands and other minerals; c) MBSh facies with highest TOC value; d) HSh facies having inter-mixed lithology (carbonates, clays and silica minerals).

Interpretation: The high carbonate content and carbonate concretions/bands are the most distinctive features of CSh facies. This facies is likely to represent a proximal parasequence, medium to high energy, mid and outer ramp, episodic storm and tempestite deposition (Ferguson, 2016; Seyedmehdi et al., 2016). Moreover, this facies illustrates coarsening upward and comparatively maximum grain size and high burrow activity due to its deposition in a shallow water setting (Christ et al., 2012; Colombié & Strasser, 2005). Furthermore, anoxic-dysoxic outer ramp environments with carbonate concretions development at dysoxic/anoxic boundary during periods of reduced sedimentation. Most probably, these concretions formed during late diagenesis due to soft sediment deformations within CSh facies during compaction (Figure

2.2c and Figure 2.4c). TOC is a product of the interplay between productivity and sediment dilution. The ratio of sedimentation to dilution is higher in CSh facies, so it has low TOC (Ibach, 1982).

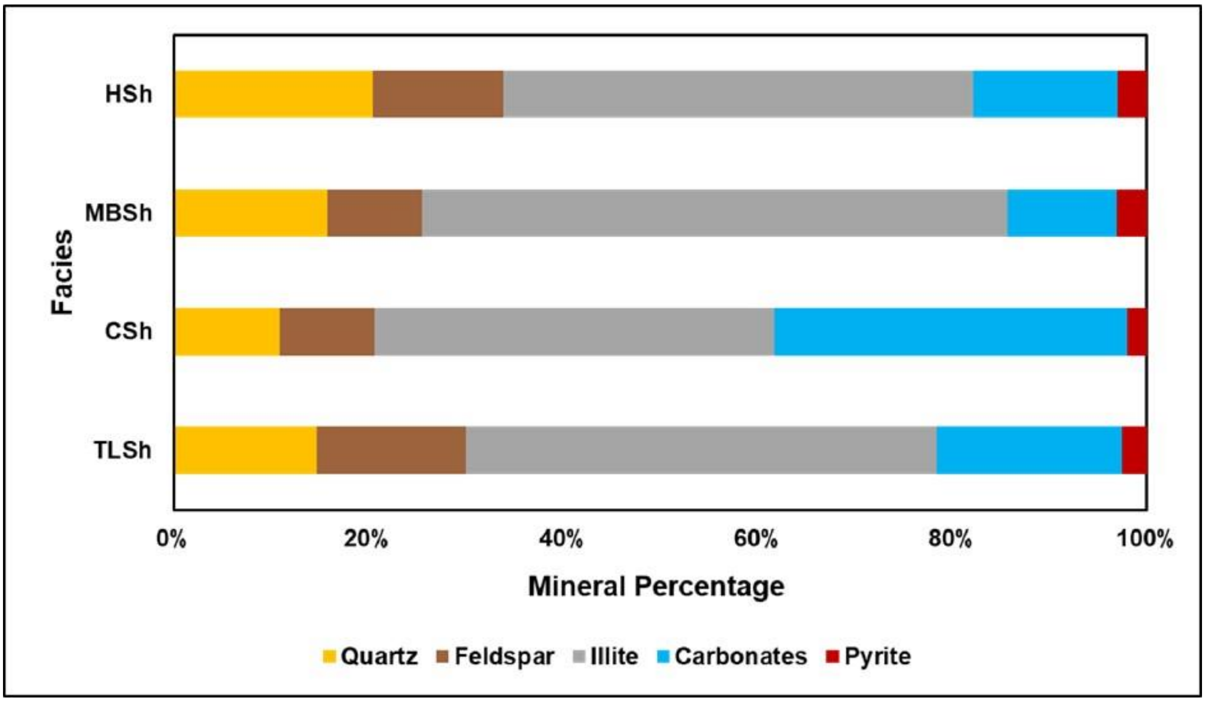

Figure 2.7: Averaged XRD based mineralogical quantification of Goldwyer-III shale sedimentary facies, dominant minerals are clay (illite), quartz, feldspar, carbonates and pyrite.

2.3.1.3 Massive black shale (MBSh)

Description: The massive black shale is observed as a pure black shale with no concretions or thin beds (Figure 2.2b&c and Figure 2.3e). However, visible pyrite is observed abundantly at different depths. No visible bioturbation and no significant sedimentary feature except shell fragments are found in this facies (Figure 2.5c). Overall, this facies has an intermediate thickness in Theia-1 well. The trilobites are frequently observed in MBSh facies (Figure 2.3d). The MBSh facies is very fine-grained, sub-angular shaped, and moderate to poorly sorted (Figure 2.6c). The massive black shale is mainly composed of clays (mostly illite) with an average content of almost 65%. The quartz is found to be about 16%, and the feldspar is present as an average amount of 8% (5% K-feldspar and 3% albite). Moreover, the carbonate content in this facies is averaged as 11%, whereas in a few samples contained no carbonates. The massive black shale has almost 3.5% pyrite (Figure 2.7 and Figure 2.8). In the same way, the total organic carbon in massive black shale is to be found as around 4wt% and Th/U ratio as an average of 3.8 with about 6 ppm uranium content. However, it is interesting to highlight that not all black shales are organic-rich as few samples from MBSh facies show less TOC values (<3 wt. %) (Figure 2.9 and Figure 2.10).

Interpretation: The high organic content is the most distinctive feature of MBSh facies that represents a deep subtidal environment situated below a fair-weather wave base (in the distal part) (Barnaby & Ward, 2007; Christ et al., 2012; Lee & Kim, 1992). The high TOC, fine-grained and organic matter presence indicate low energy (distal) depositional setting for this facies (Farouk et al., 2017; Ibach, 1982). Moreover, the presence of moderate bioturbation and benthic fauna (trilobites) indicate a deep subtidal environment defined by a quiet lagoon (Aghaei et al., 2013; Ferguson, 2016; Mohammed et al., 2020).

2.3.1.4 Heterolithic shale (HSh)

Description: As shown in Figure 2.2 to Figure 2.4, the heterolithic shale facies is light to dark grey with alternating high-angle laminations and thinly bedded carbonate along with silt layers. The lenticular beds of carbonates with moderate to high bioturbation are also observed. Highly bioturbated lenticular bedding (Figure 2.4c) (most probably Rosselia, Teichichnus, and Plaolites, as also reported by Finder Exploration in the reports), wave ripples, mud rip-up clasts, and cross laminations are also perceived in HSh facies (Figure 2.4b-d and Figure 2.5d). The HSh facies is fine to medium-grained, angular to sub-angular shaped, and moderate to poorly sorted (Figure 2.6d). The heterolithic shale consists of clays with an average amount of about 40%, and the quartz is approximately 22%. The feldspar content is almost 16% (11% K-feldspar and 5% albite), whereas this facies is comprised of carbonates with an average amount of 15% (Figure 2.7 and Figure 2.8). A small proportion of pyrite is also present in this facies as 3%. This facies also consists of the illite as an abundant clay mineral. The average value of TOC in heterolithic shale is around 2.5-3 wt%; however, there is heterogeneity in this value due to different lithology layers in heterolithic beds.

The Th/U ratio is approximately 1.2 and uranium content fluctuates between 0.5-5.2 ppm due to alternate organic rich and organic poor layers. Moreover, as the spectral gamma-ray can help us to identify organic matter and depositional setting (Klaja & Dudek, 2016). Based on SGR analysis, it is observed that the facies with higher U/K and lower Th/U ratios have more organic matter, and it is also validated with high TOC values in the respective depths.

Interpretation: The heterolithic beds with mixed lithologies are the main diagnostic features of heterolithic shale. The alternate thin laminations of silt, carbonate bands and clay layers indicated low energy with significant periods of moderate to high energy (outer-ramp to distal and proximal-mid ramp cycles) depositional setting (Ferguson, 2016). The variation in TOC values illustrates the fluctuation of oxic-dysoxic-anoxic cycles for this facies. In a few samples, the TOC is very low (<0.3wt %) due to higher sedimentation-to-dilution ratio (Ibach, 1982).

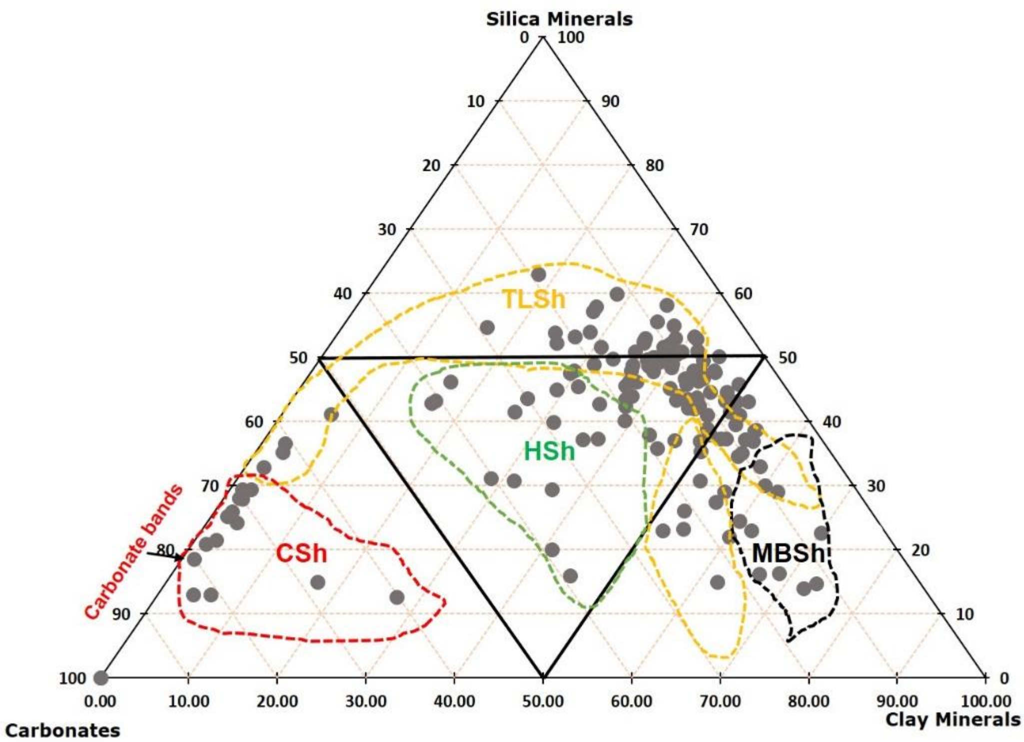

Figure 2.8: Ternary diagram of XRD and FTIR based mineralogy showing classes of different facies with a range of mineralogy. According to the content of clays-carbonates-silica minerals, the TLSh facies has a wide range of mineral compositions

and TOC. FTIR continuous data points for quantitative mineralogy adapted from Finder Exploration reports.

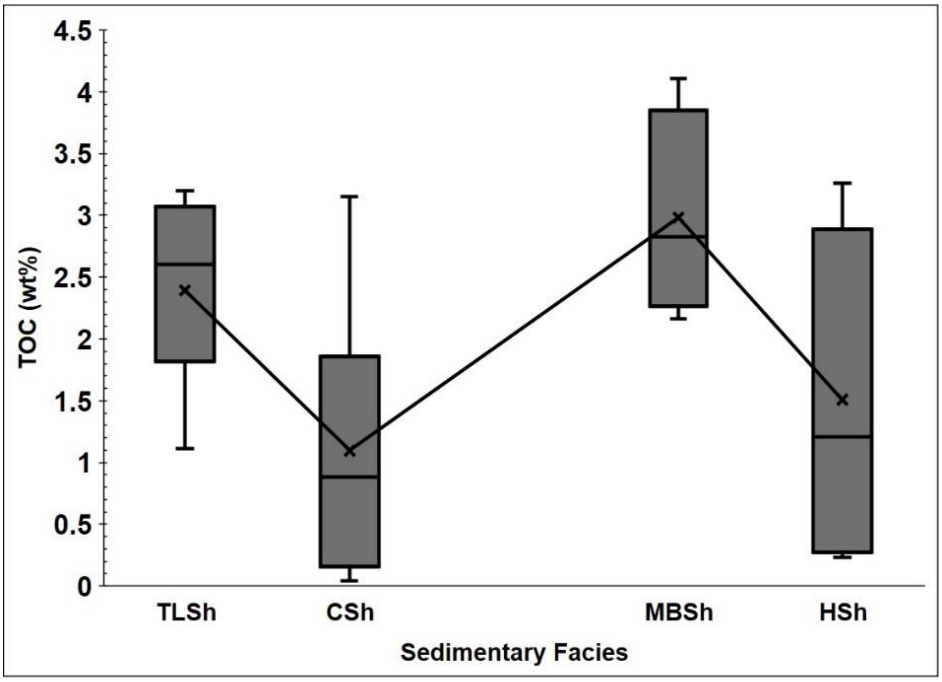

Figure 2.9: Average TOC (wt %) values of each sedimentary facies to illustrate the comparison.

2.3.2 Kerogen type and thermal maturity

Based on the geochemical analysis (rock eval pyrolysis), it is depicted that the Goldwyer-III shale mainly consists of type II-III and type III organic matter subject to the sedimentary facies. The depositional environment controls this variation in organic matter types, such as from distal to the proximal setting; the organic matter is type II-III and type III, respectively. The type III kerogen type may be due to the presence of graptolites in the sediments or to localised oxidation of some organic matter (L. Johnson et al., 2020; Johnson, 2019). It can also be related to the hydrocarbon generation potential of different facies such as the deep samples (showing kerogen type III) are in the dry gas window with the least hydrocarbon generation potential. Whereas the samples from shallow depths are in oil window with more hydrocarbon generation potential (Jin & Sonnenberg, 2013). Moreover, the Tmax vs HI plot shows that the shale facies (mainly with type III kerogen) are in the early mature window (Figure 2.11). The Tmax varies from 425°C (for Csh facies deposited at proximal environment) to 455°C (for TLSh and MBSh deposited in medial to distal setting) (Farouk et al., 2016). The organic petrography has also shown that most of the samples have graptolite and early generated bitumen (Figure 2.12a), whereas, only a few samples from Theia-1 well have algae such as Gloeocapsomorpha Prisca (G. Prisca). The previous studies on Goldwyer-III shale also reported presence of Telaginite derived from G. Prisca, lamalginite and liptodetrinite as shown in Figure 2.12b and c (Spaak et al., 2017).

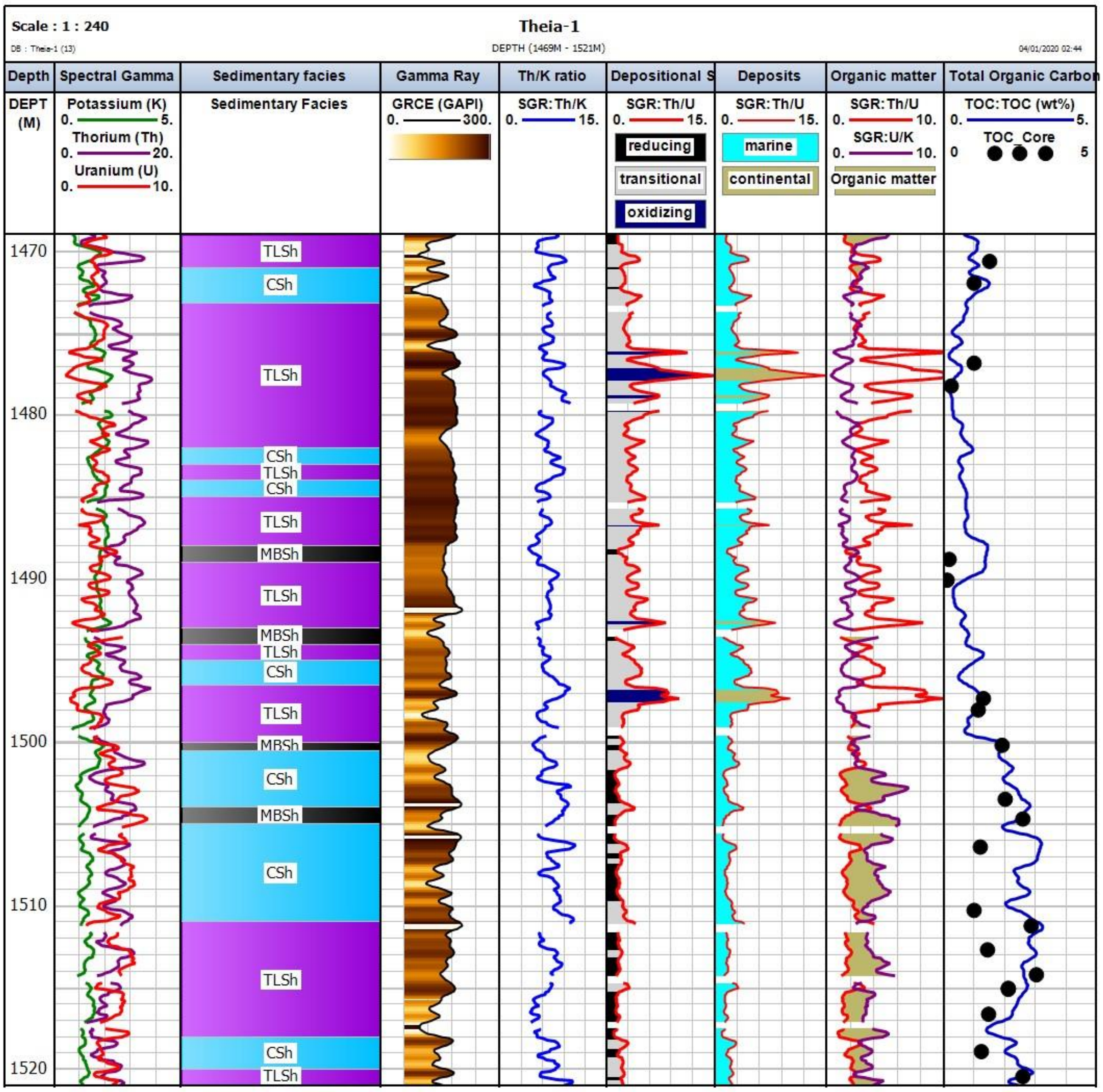

Figure 2.10: Spectral Gamma-ray analysis (Track-1: Depth; Track-2: Spectral gamma-ray logs responses; Track-3: Sedimentary facies; Track-4: Gamma-ray log response; Track-5: Th/K ratio; Track-6: Depositional setting; Track-7: Deposits type; Track-8: Organic matter presence; Track-9: TOC) helped to identify organic matter distribution in reducing environment and that is confirmed by TOC: at a depth interval of 1470-1520m in Theia-1 well, it can be observed that the reducing marine zones in which organic matter (green filled) is more, TOC is also higher and vice versa.

2.3.3 HyLogger3 summary and shale facies signatures

TIR and SWIR data were used to identify the different mineral assemblages in each facies. As this study is focused on the Goldwyer Formation that is comprised of three units (Goldwyer-I, II and III), it is also shown by TIR data and confirmed by well logs, as shown in Figure 2.13 that the Goldwyer-I and III are shale zones (with more clay especially illite) and Goldwyer-II is carbonates rich. The FTIR patterns in each facies confirm the presence of abundant minerals, and this is consistent with the HyLogger3. The wavelengths and reflectance responses are also recognised by HyLogger3 to differentiate the facies (Figure 2.14a-e). The abundance of few minerals in each facies with a distinct spectrum validated by modelled spectrum through TSG library is well illustrated such as montmorillonite in TLSh (Figure 2.14a), muscovite in MBSh (Figure 2.14b), calcite in CSh (Figure 2.14c), palygorskite in HSh (Figure 2.14d) and carbonates in Csh (Figure 2.14e).

TIR data suggests that different facies has a unique prominent mineral. As shown in Figure 2.15 and Figure 2.16 that the TLSh is rich in silica minerals (quartz and feldspar) and clays, whereas the CSh is enriched in carbonate minerals. In TIR wavelength range, illite (confirmed by XRD having a peak on 10 A^{o}) is identified as the main clay mineral as shown at depth: 1499.05m in Figure 2.19. The calcareous shale has carbonates as a major mineral, and its proportion changes with vertical variation in facies. The SWIR spectra suggest that the clays are the dominant hydrous mineral group over most of the cored intervals. The carbonates are observed in the TIR data. It is clearly shown that the concentration of minerals is changing with different facies.

However, some aspectral minerals (named as invalid and patterns are shown in Figure 2.15 and Figure 2.16) are also found in TIR and SWIR data due to the absence of library of such specific minerals. However, it can be observed that the abundance of these minerals is increasing in black shale zones with high TOC values. Therefore, these spectrums are expected to be due to organic matter.

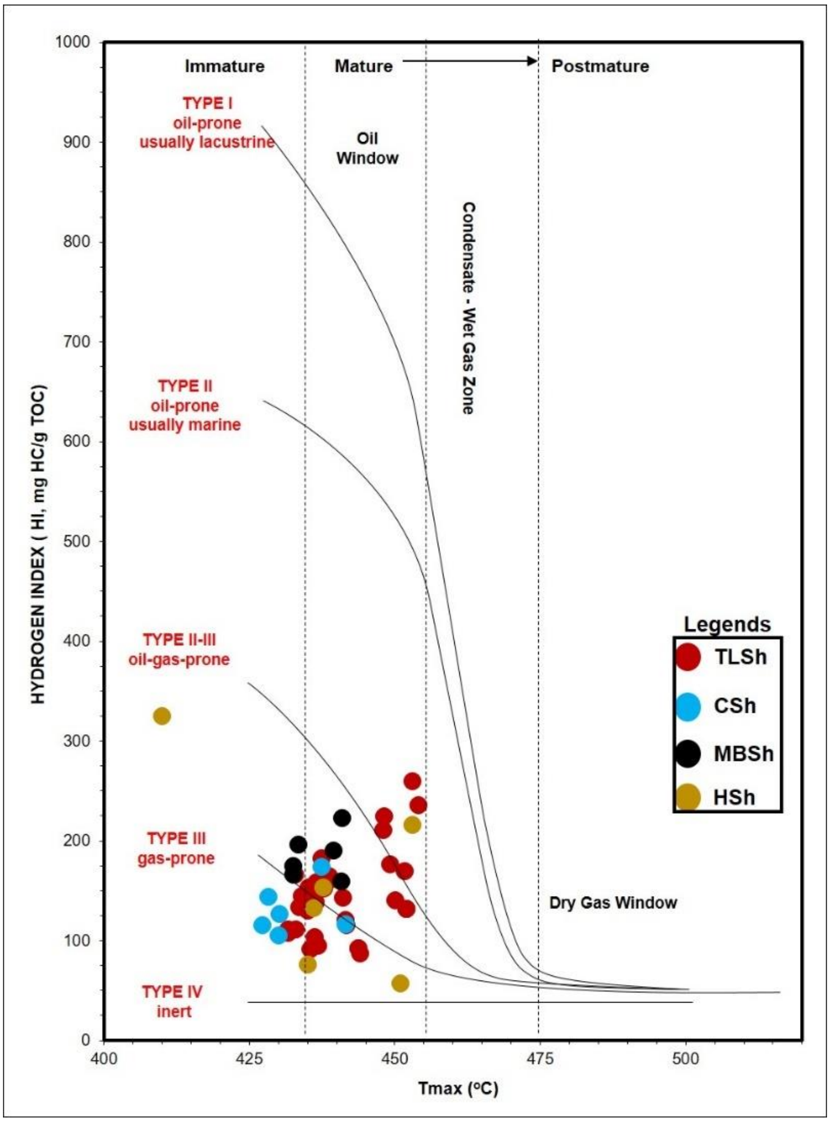

Figure 2.11: Van Krevelen diagram to show the kerogen type and maturity based on Tmax and Hydrogen Index measured by rock eval pyrolysis (few data points taken from Finder exploration reports).

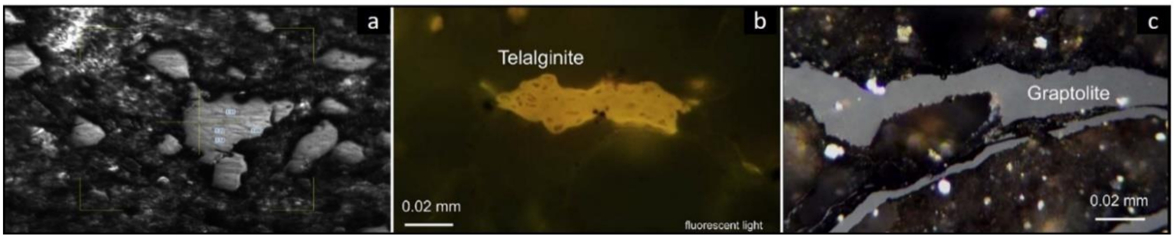

Figure 2.12: Photomicrographs from Goldwyer-III shale samples showing a) organic matter fragments (might be early generated bitumen or graptolite); b) Telalginite derived from G. Prisca identified by (Spaak et al., 2017); c) Graptolite identified by (Spaak et al., 2017).

2.3.4 Integration of high-resolution HyLogger3 and petrography data

The high-resolution HyLogger3 and XRD data suggest that clay minerals are illite rich with a minor amount of smectite over most of the shale facies intervals. The integration of HyLogger3 data with petrographic information provides a clear understanding and validation of our results (Figure 2.17a-e). However, few zones occur where HyLogger3 data does not show any mineral (with the name invalid) or 100% mica. In these zones, no clearly defined clay mineral profiles are recognised on high-resolution spectral logs. Therefore, the examination of the petrographic data confirmed these minerals (Figure 2.17a and b). For instance, at 1499.05m, the HyLogger3 spectra showed the presence of carbonates, mica, and feldspar, and this was observed by petrography. However, the SEM image in the corresponding depth reveals that illite is present in these facies (Figure 2.17c). In most facies, the illite is found as a major clay mineral (due to its peak at 10A^{o}) with subordinate smectite and kaolinite, and HyLogger3 does not observe the kaolinite.

However, SEM revealed the clay type morphology, as shown in Figure 2.17d. In HyLogger3 a general term "White Mica" is used that is a group of illite, muscovite, pyrophyllite and phengite. Similarly, at depth 1508.96m, pyrite was not recognised by HyLogger3 and FTIR; however, the SEM confirmed the presence of pyrite. In the case of aspectral or invalid minerals, the core images and petrographic data integrated with image logs confirmed that such spectrums are observed in organic-rich shales having higher total organic carbon.

The integration of high-resolution image logs and HyLogger3 data with petrography helped us to provide a continuous and well-defined facies distribution over the shale units of Goldwyer-III. As shown in Figure 2.17, the clay and silty layers observed in thin sections are also recognised in HyLogger3 data with the prominent minerals. Moreover, the calcite filled fractures observed in petrographic data and image logs have a higher concentration of carbonates minerals in TIR and SWIR data. Similarly, the FTIR data as shown in Figure 2.15e, also confirmed the presence of prominent minerals in the respective facies, for instance, the Csh has the highest peak of carbonate minerals and TLSh has higher peaks of clays and silicates in different samples due to thin laminations of quartz silt and clay.

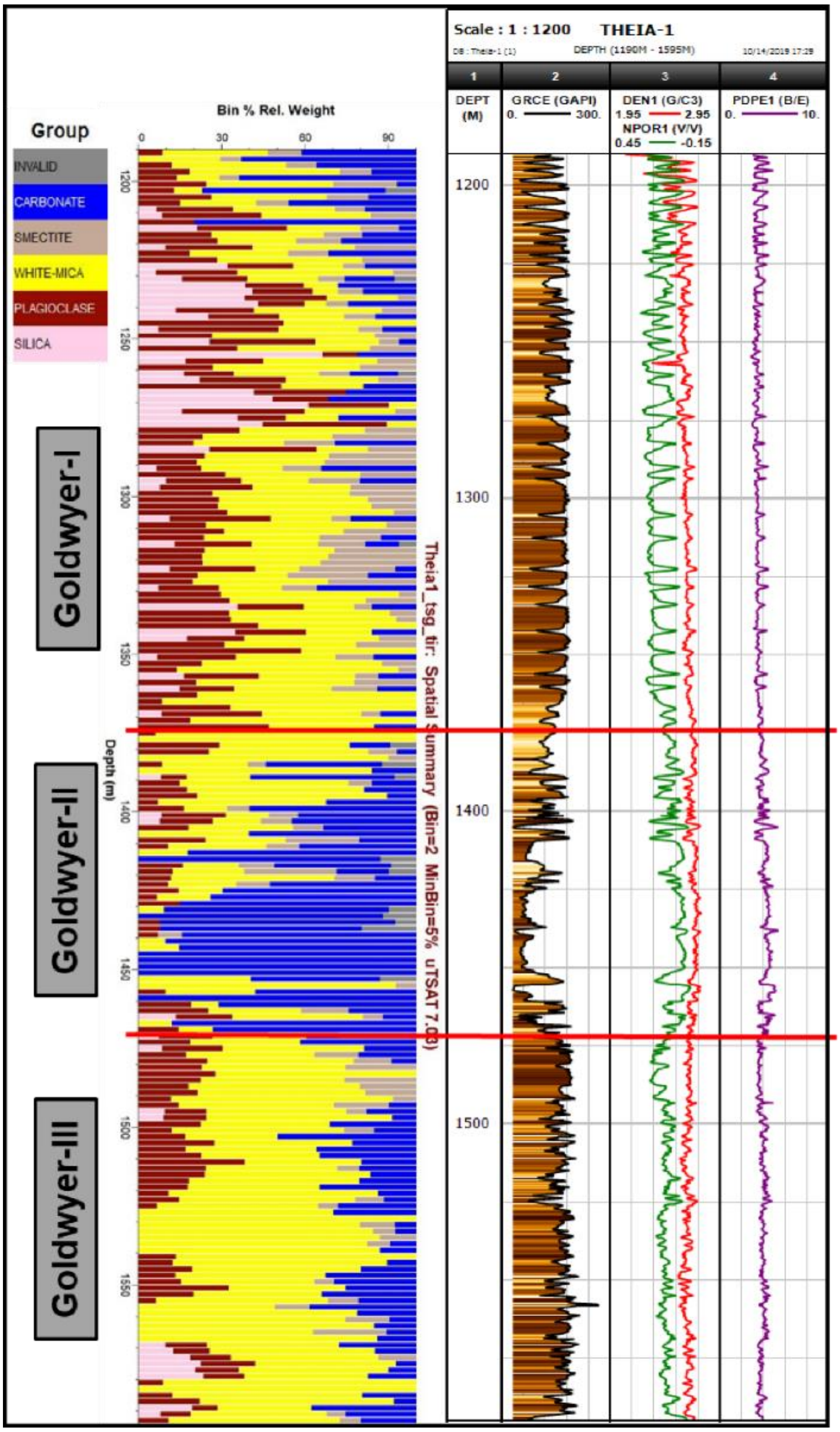

Figure 2.13: The TIR data showing the boundaries in the whole Goldwyer Formation, such as There are some striking differences between Goldwyer 1, II and II. For example, G1 has much more quartz (according to TSA) than the other two. Also, there seems to be much more cycling in G1 compared to the other two. G3 contains the highest amounts of white mica. The same division is also confirmed by the well logs (Gamma-ray, density, neutron porosity and photoelectric factor PEF).

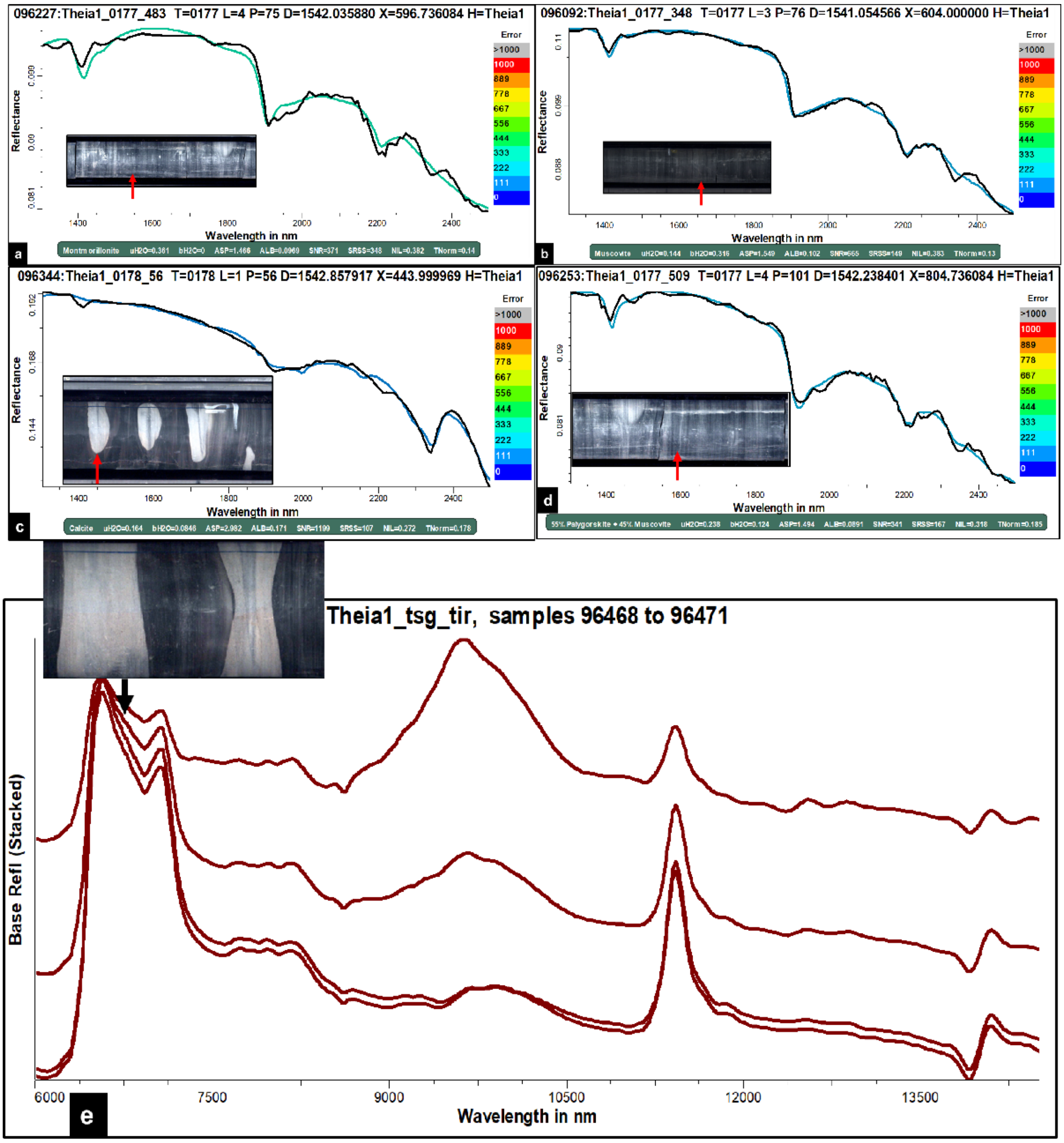

Figure 2.14: Minerals Spectra (green and blue) matching with modelled spectrum (black) in various sedimentary facies, such as a) montmorillonite spectrum in TLSh facies; b) muscovite spectrum in MBSh facies; c) calcite spectrum in CSh facies; d) palygorskite spectrum in HSh facies. An example of stacked spectra for calcite rich concretion in CSh facies with reflectance at around 6500 nm wavelength and siliceous rich layer in TLSh facies having reflectance at about 9500 nm wavelength.

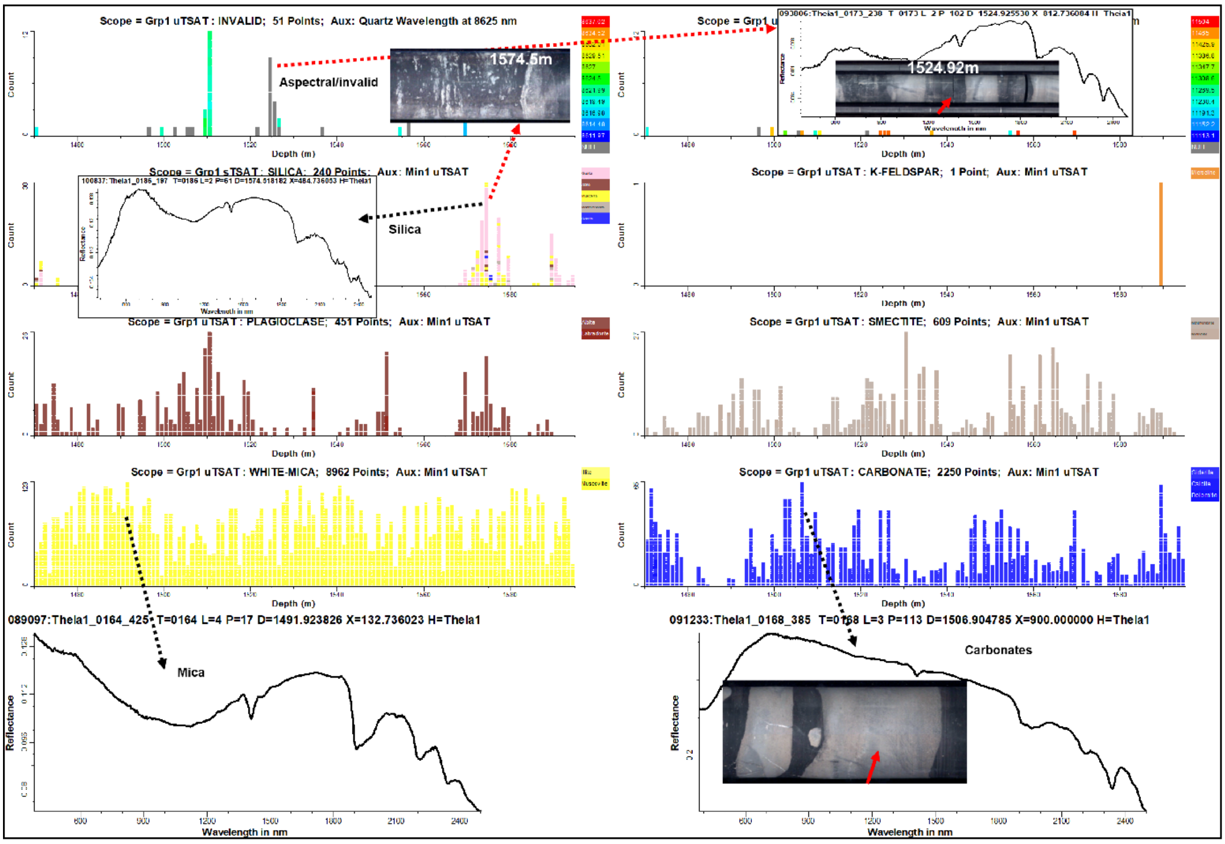

Figure 2.15: Validation of HyLogger3 spectra for different minerals with core linescan, such as abundant aspectral/invalid spectra found in MBSh (Argillaceous and organic-rich facies) (shown in the first row); abundance of silica, mica and carbonate spectra also shown with core line scans.

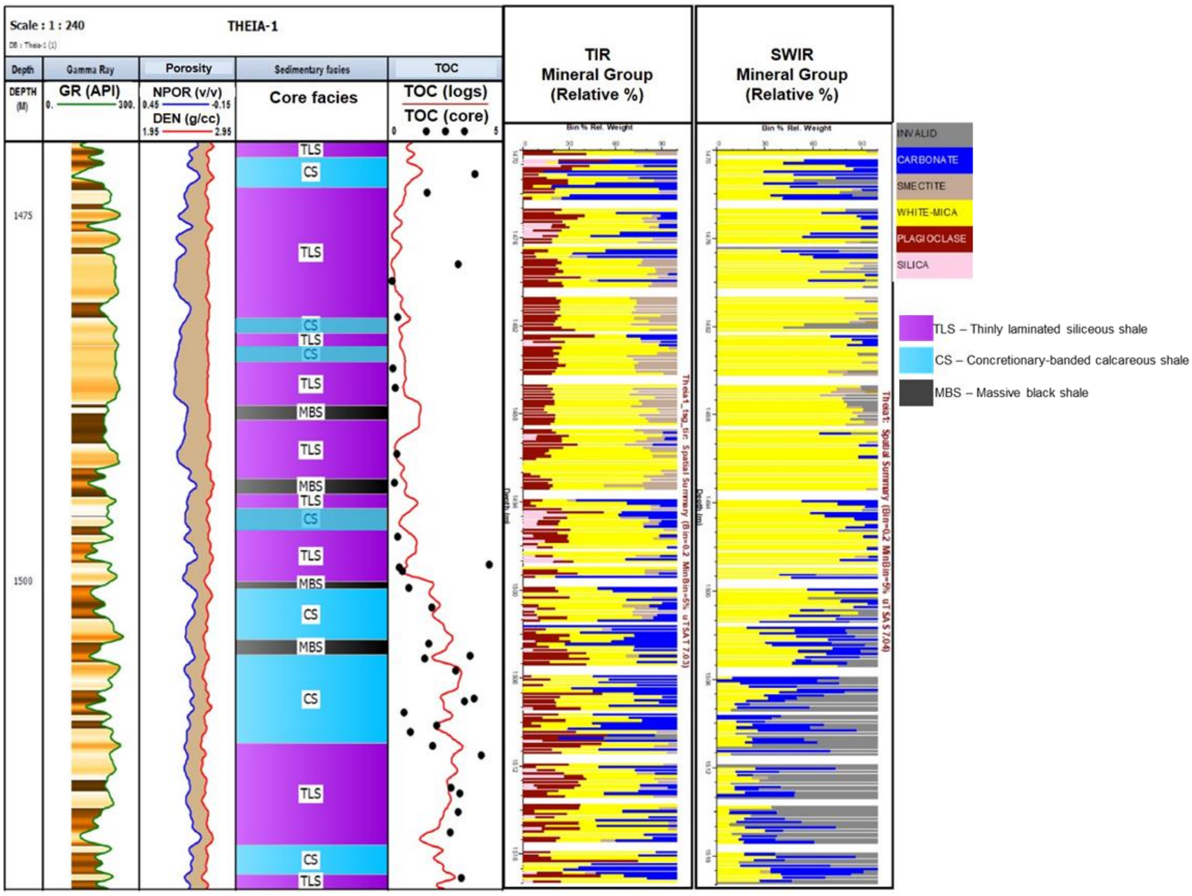

Figure 2.16: Summary well plot for Goldwyer-III shale (1470-1520m) showing continuous wireline log data (Track-2: Gamma-ray log; Track-3: Neutron porosity and density logs; Track-5: continuous TOC by Passey method and TOC on the core, core linescan (mosaiced core tray imagery output from TSG), TIR and SWIR based mineralogy. Note the invalid (aspectral) minerals are more abundant in the high TOC facies this may be due to an organic matter spectrum.

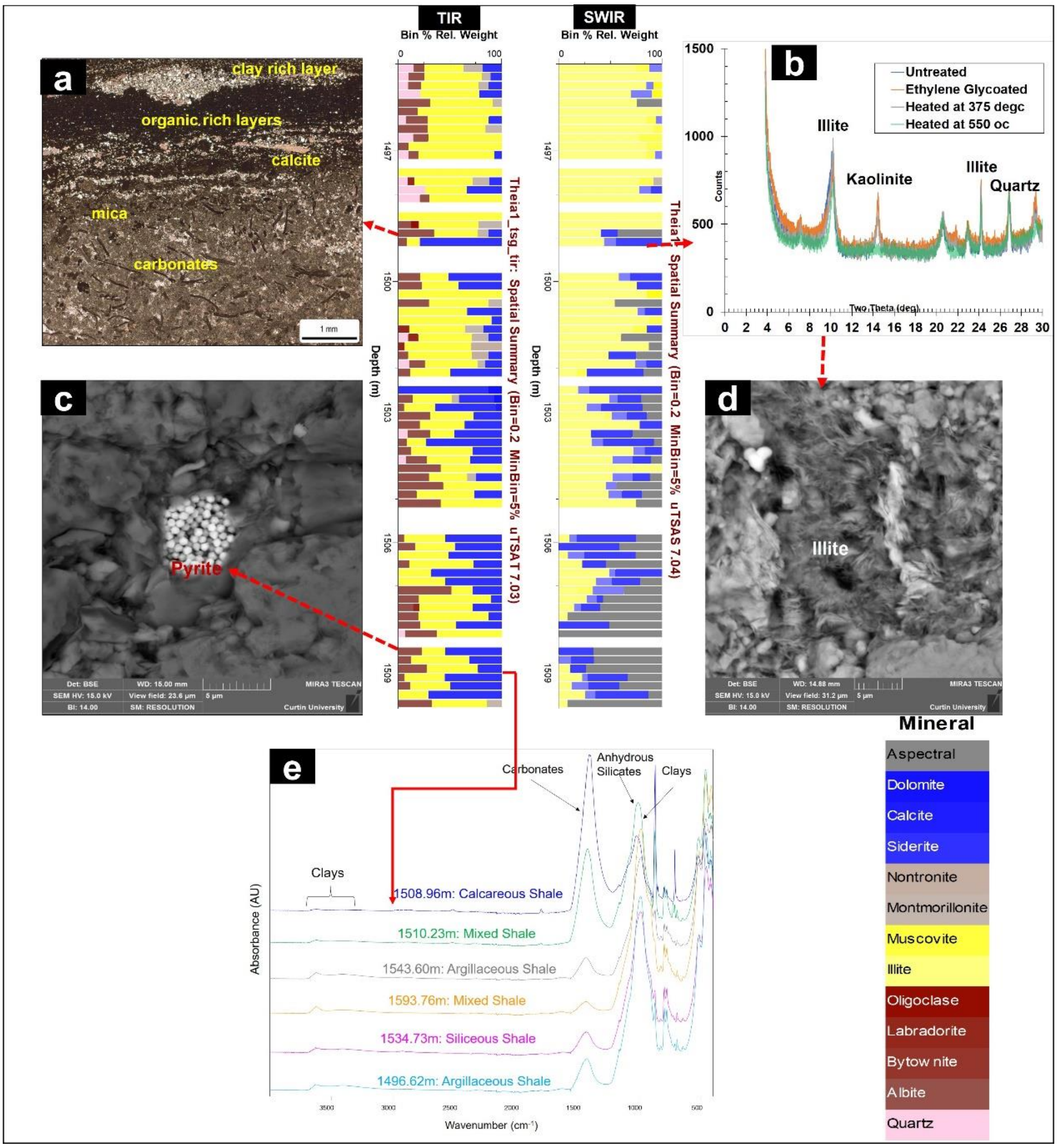

Figure 2.17: Integration of high-resolution HyLogger3 data with petrographic data for Theia-1 well, a) showing thin-section having calcite and mica layers corresponding to the TIR and SWIR data, b) confirmation of illite peak at 10Ao c), and d) SEM images showing pyrite and illite morphology those are not identified by HyLogger3, e) FTIR results validation with HyLogger3, for instance, calcareous shale is rich in carbonates based on FTIR as well as HyLogger3.

2.4 Discussion

2.4.1 Facies heterogeneity in Goldwyer-III shale

Based on various studies, it is a fact that every shale is unique and heterogeneous due to variations in mineral composition, fabrics, and petrophysical properties. It is very crucial to understand the heterogeneity in shales as it has a direct impact on gas shale evaluation, exploration, and development (Chen et al., 2015; P. N. K. De Silva et al., 2015; Jiang et al., 2016; Passey et al., 2010; Suarez-Rivera et al., 2006). The heterogeneity intensity depends on the depositional setting at a broader scale. The marine shales are relatively widely distributed and have less stratigraphic variations over time. The Marcellus shale is a typical example of marine shale in West Virginia (Bruner et al., 2015). This study is mainly focused on the shale unit in Goldwyer Formation (Goldwyer-III). According to (Haines, 2004), the Goldwyer Formation is mainly of open marine to intertidal origin, varies from mudstone-dominated in basinal areas to limestone-dominated in some platform and terrace areas, and has locally undergone significant secondary dolomitisation.

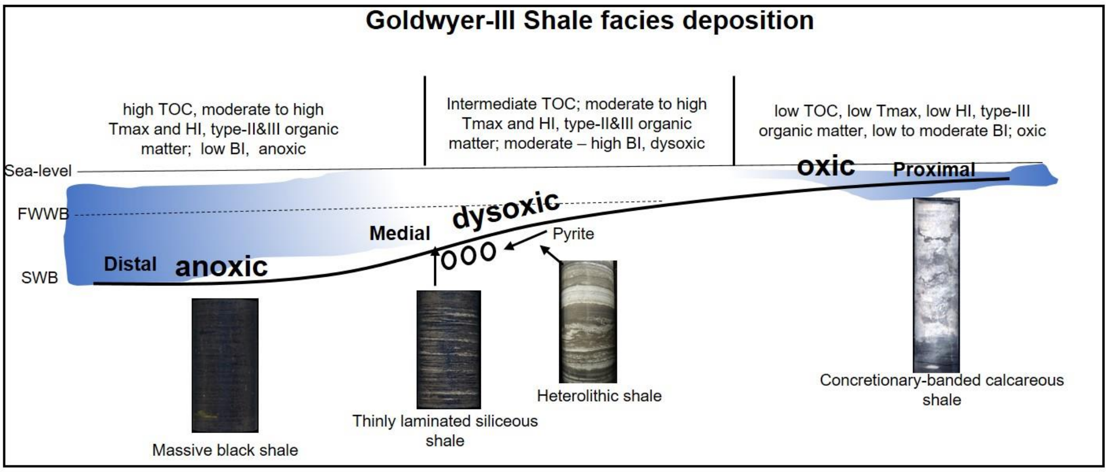

Figure 2.18: A simplified conceptual depositional model to understand the deposition of different facies in Goldwyer-III shale, TOC = total organic carbon; HI = hydrogen index; BI = brittleness index.

The heterogeneity of marine shales can understand by variations in sedimentary features, lithology, TOC, rock fabric and mineralogy in the Goldwyer Formation (Goldwyer-III) (Figure 2.2 to Figure 2.10). Such vertical heterogeneity can be expected due to sea-level fluctuations and some diagenetic alterations (Bruner et al., 2015; Ferguson, 2016; Haines, 2004; Jiang et al., 2016; Liang et al., 2012). The organic richness, such as total organic carbon and organic matter in marine shale is also mainly dependent on depositional processes (Ibach, 1982; Stow et al., 2001). Such as most of the organic matter that enters the marine realm (from terrigenous input or primary marine productivity) is primarily affected by oxidation and bacterial degradation. The productivity of organic matter depends on many factors; however, one of the important ones is anoxicity that tells about the oxygen level. From the distal to the proximal marine setting, TOC gradually decreases due to the oxic regime (Bruner et al., 2015; McCollum, 1988; Murphy et al., 2000; Schieber, 1999). The same phenomenon was also recognised in Goldwyer-III shale facies. Referred to Figure 2.18, the facies with different TOC and brittle minerals (e.g. silica minerals) are deposited in different depositional settings. Such as the CSh facies with low TOC and low to moderate amounts of brittle minerals were deposited in high energy, proximal parasequence with oxic conditions. Whereas the TLSh and HSh facies with moderate TOC and moderate to high brittle minerals were deposited in medial conditions with oxic-dysoxic fluctuations. In comparison, the MBSh facies with the highest TOC and low brittle minerals deposited in the low energy, distal setting with anoxic conditions.

2.4.2 Validation and limitation of HyLogger3 data for shale

HyLogger3 spectra (TIR and SWIR mainly) have been examined and integrated with petrographic data (e.g. XRD, SEM, thin sections), well logs, and TOC data (Figure 2.16 and Figure 2.17). The clays are dominant minerals in Goldwyer-III shale with a variable amount of carbonates and silica minerals (quartz and feldspar). The SWIR spectrum helped to identify the clay minerals and then validated them with SEM and XRD data. Whereas the quartz and carbonates are recognised by TIR data; however, the carbonates reflectance is also observed in the SWIR spectrum. The calibration and confirmation of different mineral groups identified by XRD and HyLogger3 spectra are shown in Figure 2.17. It can be observed that some aspectral/invalid proportions are found in different facies (Figure 2.16). One aspect that can be considered is that the library spectra employed do not always cover all of the natural heterogeneity in particular facies, so it does not address volume scattering issues (Ayling et al., 2016; Hill & Mauger, 2016).

However, there are some limitations in HyLogger3 data such as the absolute values are not measured, and the technique is unable to detect small quantities of certain minerals (Higgs et al., 2015). For instance, SEM observed pyrite and confirmed by XRD, but the VNIR spectrum did not contain any significant peak attributed to pyrite (Figure 2.17). The sample preparation is another factor that contributes to a lower correlation between XRD and the Hylogger. For instance, Hylogger measurements are made directly on a heterogeneous sample, whereas the XRD measures a sample that has been pulverised and homogenised. Moreover, the SWIR data has shown the spectrums of mica, whereas the XRD data confirmed that illite and mica both are present in Goldwyer-III shale. Another critical issue is observed in HyLogger3 data that is very crucial for organic-rich shales. In SWIR and even TIR data, invalid or aspectral mineral groups are shown. However, based on TOC data, spectral gamma-ray log, and petrographic data, it is confirmed that such regions (with invalid or aspectral groups) are organic-rich shales with high TOC and uranium contents (Figure 2.16). Others have also observed the same issues (Ayling et al., 2016; Higgs et al., 2015). Further work is recommended to address some of these issues.

2.4.3 "Suitable zones" identification and distribution through high-resolution data integration

It is crucial to have continuous mineralogical and petrophysical details to understand shale heterogeneity. However, collecting the samples at a minimal interval (about 0.2m) for high-resolution heterogeneity assessment is also challenging. A favourable zone must be much thicker than 0.2m to be considered for gas production. As shown in Figure 2.2 to Figure 2.4, the sedimentary features and lithology changed at a millimetre scale and the available samples do not cover the whole spectrum of understanding about Goldwyer-III shale. Subsequently, the HyLogger data (SWIR and TIR spectra) was used to understand the heterogeneities based on different minerals abundance. This information can be utilised for a quick decision about the development of gas shale reservoirs. The "suitable zones" are identified based on mineral composition and brittleness index through XRD and FTIR-based mineralogy, as well as image logs, features as shown in Figure 2.19. Many methods exist for the determination of the brittleness index (BI); however, in this study, the brittleness index is determined by mineral contents as we have continuous mineralogy details through HyLogger3 and FTIR information. Many equations are proposed and applied by (Feng et al., 2019; Iqbal et al., 2018; Jarvie et al., 2007; Jin et al., 2014; Rybacki et al., 2016; Wang & Gale,

2009) for brittleness index determination through mineralogy and mechanical testing, and we applied the following equation (Eq. 2.3):

$$BI = \frac{Q}{Q+Car+Clay}100 \quad \text{(Eq. 2.3)}$$

The quartz (Q), carbonates (Car) and clay abundances were determined by XRD and FTIR. Therefore, two different brittleness indices are shown in Figure 2.19, such as based on FTIR and XRD mineralogy, and a good match is observed among those. The "suitable zones" are recognised based on the brittle mineral presence and TOC content as both factors are crucial for shale reservoir development. As suggested by (Guo et al., 2015) that the rock with BI>0.4 (40%) can be considered as brittle and suitable for fracturing. Therefore, based on this cut-off value for BI and TOC>2.5wt%, an example of favourable sweet spots is indicated by green rectangles, and SCMI image logs confirm those due to the presence of some fractures and brittle minerals layers. So, a continuous curve for BI and mineralogy is determined by FTIR, petrography, and HyLogger3 integration that helped us to propose suitable spots in the Goldwyer-III shale. Based on these details, most of the favourable zones are recognised in thinly laminated siliceous shale and heterolithic (mixed) shale. Moreover, it is also a fact that the substantial dissolution of the carbonate minerals can increase the effective fracture volume (Paukert Vankeuren et al., 2017).

The distribution of Goldwyer-III shale facies is depicted through a vertical profile by applying the proposed workflow for three wells (Theia-1, Pictor East-1, and Canopus-1). As shown in Table 2.2, this study validated the core results with well logs and defined the cut-off values for different wireline logs (gamma ray GR, density DEN, deep resistivity LLD, sonic DTC, and photoelectric factor PEF) ranges, TOC and mineral composition for each facies. The proposed classification scheme and cut-off values of different well logs were integrated to understand and correlate the vertical and lateral heterogeneities of Goldwyer-III shale facies in three wells (Figure 2.20). Such a correlation shows that the thickness of promising and favourable facies (TLSh and HSh) is decreasing from SW to NE of the Broome Platform. Therefore, the SW of the Broome Platform can be a suitable spot for drilling future wells for the successful exploration and development of Goldwyer-III shale.

2.4.4 Comparison of Goldwyer-III shale with Global marine shales

All commercially operating US shale plays are of marine type (Boyer et al., 2011). The marine shales consist of mudrocks, usually deposited on muddy coastlines, near shore, basinal slopes and basinal floors (Pashin et al., 2011). These shales can consist of brittle minerals (e.g. quartz) that increase the brittleness index of the shale. In this study, some of the major shale formations, such as Marcellus shale, Bakken shale, Barnett shale, and Eagle Ford shale from the US as well as Longmaxi shale from China are discussed and compared with Goldwyer-III shale. The Marcellus shale is an organic-rich black shale with limestone, carbonates and pyrite (P. N. K. De Silva et al., 2015). Whereas, the Barnett shale consists of several facies such as laminated argillaceous mudstones, carbonate concretions and skeletal argillaceous lime packstones (Day-Stirrat et al., 2008). However, the Barnett shale is not black; it is still an organic-rich shale (Schulz & Horsfield, 2010).

In the same way, the Eagle Ford shale is a dark, laminated shale with thinly inter-stratified and consists of limestone and carbonaceous quartzose siltstones (Dawson, 2000). Moreover, the Bakken shale is also considered as organic-rich shale with some carbonates. Whereas, the Longmaxi shale from China is also organic-rich having several facies due to variations in mineralogy proportions (Wu et al., 2018).

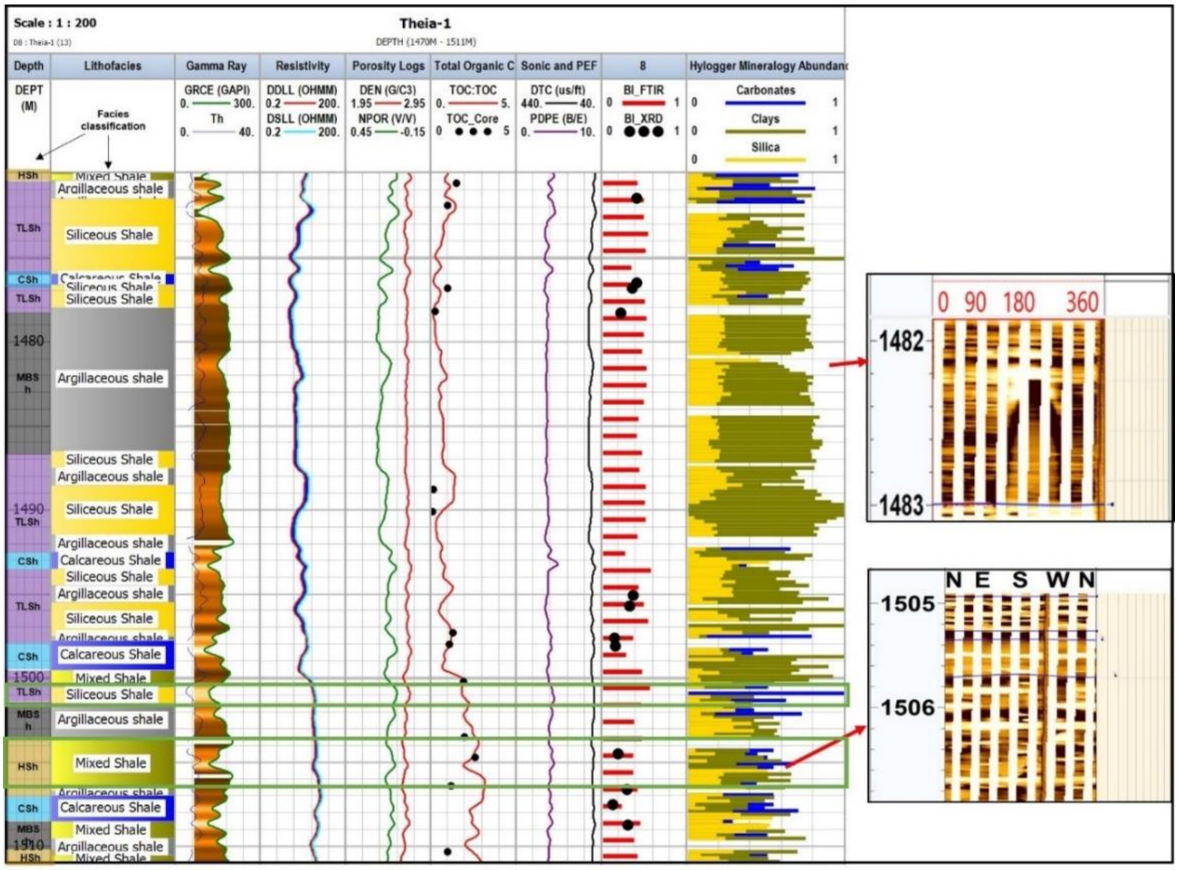

Figure 2.19: An example of "High-quality zones" identified through integrated brittleness index (XRD and FTIR) and mineral abundance, image logs and core description approaches. Track-8 shows brittleness index (BI). Green rectangles show suitable brittle zones based on 0.4 brittleness index cut-off and TOC=2.5 wt% cut-off. The image logs show the fractures and brittle minerals (light coloured) against suitable zones.

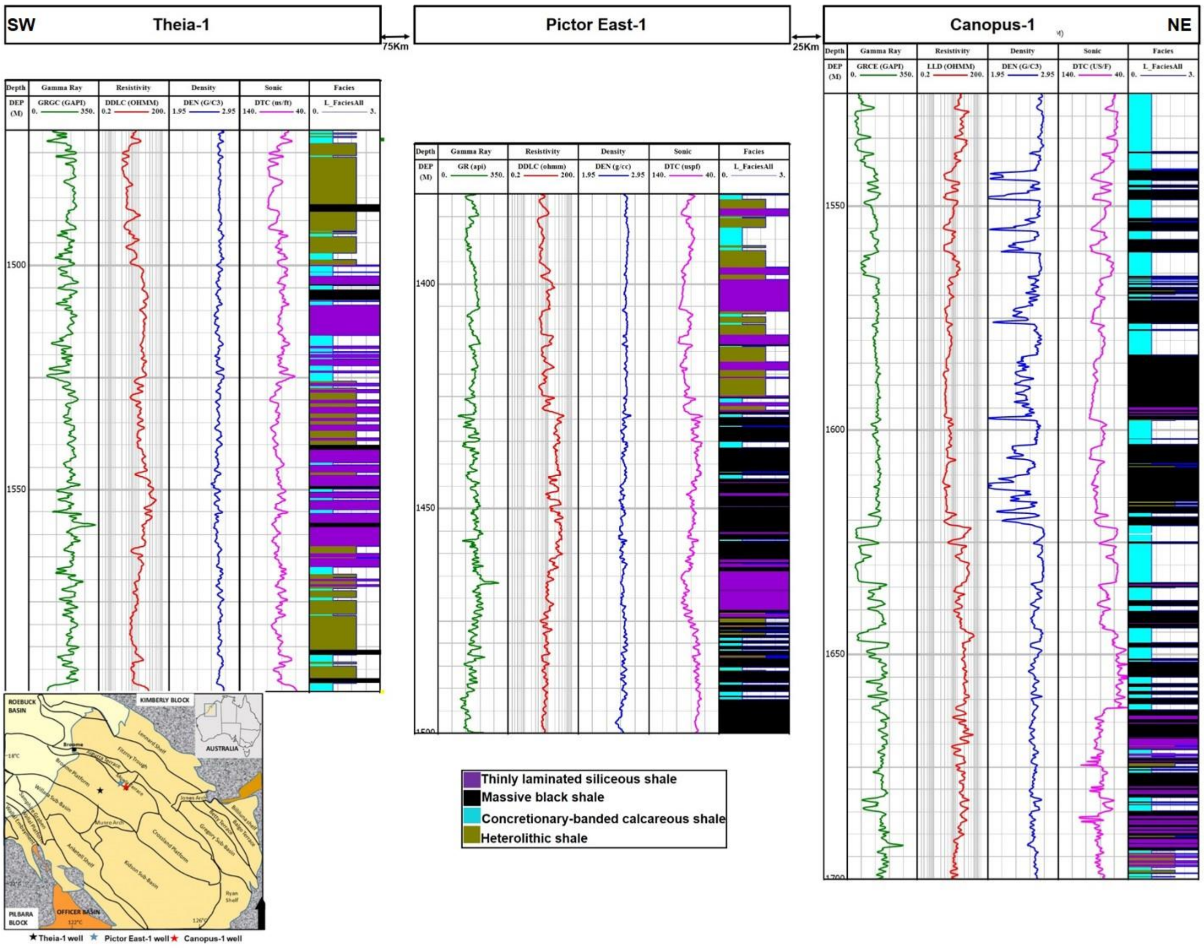

Figure 2.20: The correlation of three wells (Theia-1, Pictor East-1 and Canopus-1) from the Broome Platform illustrating the vertical and lateral heterogeneity of Goldwyer-III shale facies.

Table 2.2: Defined cut-off values of different well logs (e.g. GR, DEN, LLD, DTC and PEF), TOC and mineral components for identified facies in Goldwyer-III shale.

Facies	GR	DEN	LLD	DTC	PEF	TOC	Silica mineral	Carbon ates	Total Clays
TLSh	140-250	2.62-2.67	3.1-12	85-100	3.5-4.2	2.5	≤35	<15	>50
CSh	70-150	2.67-2.72	11.5-60	75-85	4-4.5	1.7	<25	>35	≤45
MBSh	210-260	2.58-2.63	5.5-35	80-85	3.8-4	>3.5	<20	<15	>50
HSh	150-220	2.65-2.7	4.1-25	75-90	3.8-4.1	≤3	≤35	≥25	≤40

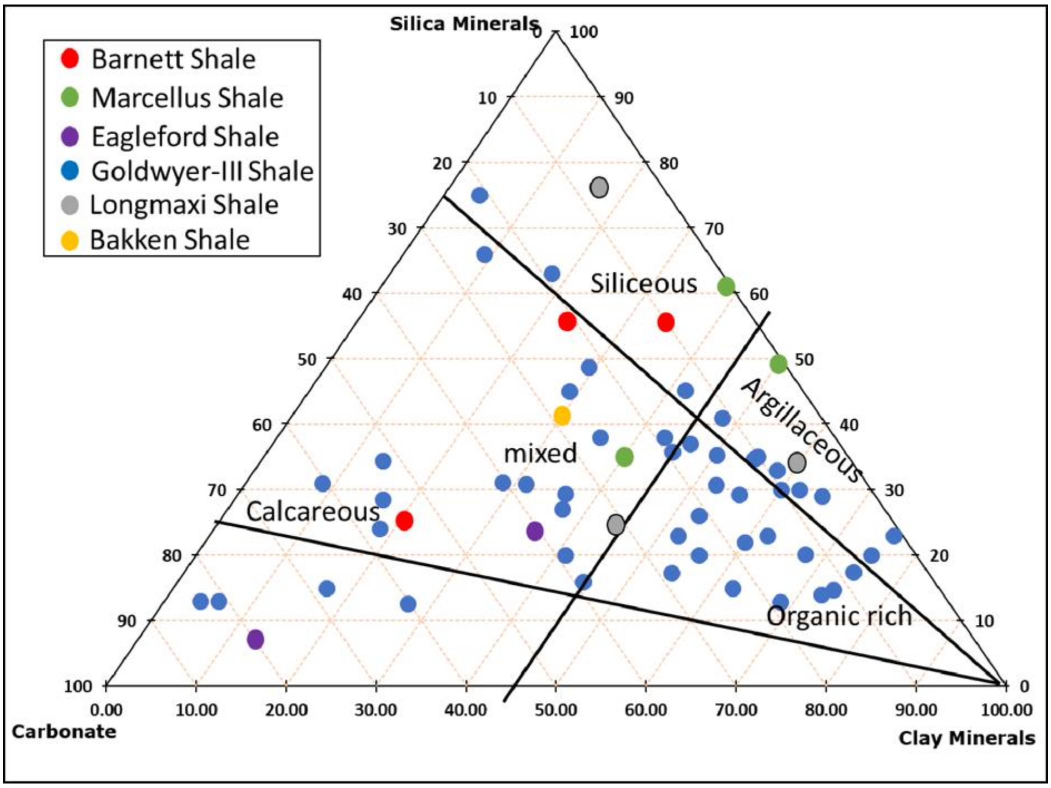

Figure 2.21: A comparison of Goldwyer-III shale with US and China shales to understand the facies and mineralogy proportions.

In comparison, the Goldwyer-III shale from the Broome platform is also comprised of light to dark-coloured facies with low to high TOC and brittle minerals content. The typical characteristics of different marine shales are compared in Table 2.3 and Figure 2.21. Generally, the Goldwyer-III shale is considered more complex as it is clay-rich (mainly illite) with a higher content of clay minerals as compared to other marine shales. However, still, it is comprised of a few organic-rich siliceous and mixed lithology layers in TLSh and HSh facies with a higher brittleness index. Moreover, it is very easy to bypass the brittle zones in clay-rich shales (e.g. Goldwyer). However, through integration and correlation with the other three wells, it is depicted that the producible facies (TLSh and HSh) are decreasing from SW to NE of Broome Platform (Figure 2.20). Therefore, the SW part of Broome Platform provides better opportunities for Goldwyer-III shale reservoir development. This study has introduced a sophisticated workflow based on high resolution techniques that can be followed to identify the suitable layers in complex heterogeneous shales such as we identified in TLSh and HSh facies of Goldwyer-III shale.

Table 2.3: Typical organic richness and mineral compositions in different marine shales.

Formation	**Age**	**Depth (m)**	**Average Thickness (m)**	**TOC (wt %)**	**Mineral Composition**			**Depositional Setting**
					Silica minerals	Total Clay	Carbonates	
Goldwyer-III Shale	Ordovician	1470 - 1600	100-120	1-4.5	12.5-65	5.5-70	20-75	marine
Barnett Shale (Jia & Sheng, 2017)	Missisipian	2000 - 2500	60-240	5-8.5	35-50	10.5-50	0-30	marine
Marcellus Shale (Bruner et al., 2015; Jia & Sheng, 2017)	Devonian	2700	12-270	1.5-20	10.5-60	10.2-35	3.1-50	marine
Eagle Ford Shale (Patel et al., 2014; Stegent et al., 2010; Sun et al., 2015)	Cretaceous	2400 - 3600	45-105	2-6.5	15-26	5.5-45	0-61	marine
Longmaxi Shale (Wu et al., 2018)	Ordovician-Silurian	2300 - 2500	15-250	1.1-5	20-75	15-60	5.1-32	marine
Bakken Shale (Kurtoglu et al., 2013; van Hattum et al., 2019)	Late Devonian	2100 - 3300	6.5-45	2.1-18	27-54	12.5-54	13-59	marine

2.5 Conclusions

According to the integration of geochemical and petrographic data with high-resolution HyLogger3, image logs, and core scan, this chapter concludes that:

i. The Goldwyer-III shale (Goldwyer-III) is highly heterogeneous in terms of sedimentary features, lithology, mineralogy, total organic carbon, and rock fabric. The Goldwyer-III shale in our study area is divided into four facies based on colour, lithology and sedimentary features, such as thinly laminated siliceous shale (TLSh), concretionary-banded calcareous shale (CSh), massive black shale (MBSh) and heterolithic shale (HSh). The variation in sedimentary characteristics is linked with the depositional setting. The massive black shale is deposited in the distal setting with anoxic conditions and thinly laminated siliceous shale, as well as heterolithic shale, are deposited under distal to proximal setting with dysoxic-anoxic cycles. Whereas the concretionary-banded calcareous shale is deposited in the proximal setting with the oxic environment. Therefore, TLSh, MBSh and HSh have a higher TOC value (up to 4.5 wt%), Tmax (up to 450 °C) and hydrogen index (up to 250 mgHC/g) comparatively. Whereas, the CSh facies has least TOC, Tmax and hydrogen index.

ii. The integration and validation of HyLogger3 data and FTIR with core linescan, image logs and petrographic data provided us with new insight for understanding of facies heterogeneities in Goldwyer-III shale (marine) by continuous mineralogical information (at 0.1mm interval). It helped us in the identification of "suitable zones" for hydraulic fracturing.

iii. The results show that Goldwyer-III shale is comprised of some brittle zones with higher TOC values suitable for hydraulic fracturing. These high-quality brittle zones are recognised in TLSh and HSh facies based on mineralogy-derived brittleness index and TOC.

iv. Generally, Goldwyer-III shale is considered as clay-rich (mainly illite) shale; however, it consists of some organic-rich and siliceous layers with higher TOC and brittle minerals content. Without heterogeneity understanding, these suitable zones can be overlooked. Therefore, the continuous high-resolution hyperspectral core log data, combined with FTIR, petrography and conventional core logging applied in this study, provided a much better understanding of facies heterogeneity in shale. This approach can improve economic decisions when developing gas shale reservoirs.

v. The correlation and distribution profile of Goldwyer-III shale facies among three wells from Broome Platform, Canning Basin have shown the vertical and lateral heterogeneities. This heterogeneity understanding helped us to conclude that the SW part of Broome Platform can act as a promising location for drilling the future wells for successful exploration and development of Goldwyer-III shale.

Chapter 3 Shale Lithofacies Controls on Porosity and Pore Structure

Summary

The hydrocarbon storage and transport capacity of shale reservoirs depend on their complex pore systems. This study focuses on Ordovician Goldwyer Formation (Goldwyer-III shale) from Canning Basin, Western Australia. Multi-scale qualitative (X-ray diffraction, field emission scanning electron microscope, TESCAN integrated mineral analyser (TIMA) and thin-section analysis) and quantitative (Rock-Eval® pyrolysis, helium porosity on crushed samples, low-pressure gas adsorptions (N2 and CO2) and mercury injection capillary pressure (MICP)) approaches were applied on shale samples. The results indicate that the Goldwyer-III shale comprises five main lithofacies (namely organic-rich shale, argillaceous shale, siliceous shale, calcareous shale, and mixed shale) based on mineral composition and total organic carbon (TOC) content. The organic-rich and siliceous shales have the highest porosity (>10%) followed by mixed shale and other lithofacies. Three types of pores, namely organic pores, interparticle, and intraparticle pores, are identified in Goldwyer-III shale. Most of the pores are narrow slit-like or bottle-necked-shaped pores. The micropore and mesopore volumes and specific surface area (SSA) of all lithofacies are positively related to TOC except for the argillaceous shale. Conversely, the micro and mesopore parameters (SSA and pore volumes) exhibited inverse relations with total clay content for all lithofacies except argillaceous shale. This indicates that the total clay and TOC content is the main controlling factors for the pore structure of Goldwyer-III shale. The whole pore aperture exposed mesopores are more abundant in Goldwyer-III shale; however, a few micro and macropores are also found in different lithofacies. The organic-rich, siliceous and mixed shales could be deemed as the essential lithofacies types for fluid flow via pore systems due to high porosity and feasible pore structures.

3.1 Introduction

The successful gas exploration from North American shales has encouraged worldwide shale reservoir development (Curtis, 2002; Loucks et al., 2009; Rezaee, 2015). However, the commercial success of shale reservoirs has overtaken the scientific consideration of shale characterisation, especially microstructural, lithofacies classification and pore structure understanding remains insufficient. The total porosity and pore structure are crucial parameters for the evaluation of shale reservoirs. Detailed knowledge of these parameters can help better recognise gas storage capacity and transport mechanisms. However, the total porosity and pore systems characterisation of unconventional shale reservoirs is challenging due to their micro to nano-sized pores and ultra-low permeability (Clarkson et al., 2013; Yang et al., 2015). The pore size range of shale is defined in nanometers (nm) by the International Union of Pure and Applied Chemistry (IUPAC) such as the micro and mesopores are <2 nm and 2-50 nm, respectively (Rouquerol et al., 1994). Moreover, the free and adsorbed gas contents are also mainly controlled by pore structure parameters, such as specific surface area, pore volume, pore types, and pore size distribution (Yang et al., 2019; Yuan et al., 2019). Therefore, advanced techniques are usually applied for the characterisation of complex pore systems in shale. For example, the pore geometry and pore size are well described by direct imaging methods such as computed tomography scanning (CT), field emission scanning electron microscopy (FE-SEM), and atomic force microscopy (AFM) (Loucks et al., 2009; Passey et al., 2010). Whereas, the indirect methods for quantitative assessment of pore structure parameters include low-pressure nitrogen (LPN2) and carbon dioxide (LPCO2) gas adsorptions, mercury injection capillary pressure (MICP), and helium pycnometer (Ross & Marc Bustin, 2009; Yang et al., 2019).

The pore structure of shale is highly affected by mineral composition, organic richness, thermal maturity, sedimentary features and diagenesis (Katsube & Williamson, 1994; Luo & Zhong, 2020; Ross & Marc Bustin, 2009; Schieber, 2013; Yang et al., 2018; Yang et al., 2015; Yuan et al., 2019; Zhang et al., 2018). Due to several sedimentary environments and mineralogical variations, the shale lithofacies develop different pore types (Arthur &

Sageman, 1994; Gao et al., 2018; Liu et al., 2019; Macquaker & Gawthorpe, 1993; Slatt & O'Brien, 2011; Yang et al., 2015). Moreover, some primary pores transform into secondary pores due to diagenetic processes such as compaction, dissolution, and cementation (Bjørlykke & Høeg, 1997; Guo et al., 2017; Mazzullo & Harris, 1992; Walderhaug, 2000; Zhang et al., 2018). There exist discrepancies in the pore system due to a high degree of heterogeneity in shale caused by variations in organic matter and inorganic minerals. It is crucial to recognise the specific controlling factors for porosity and pore structure evaluation for each lithofacies.

This study provides an opportunity to describe the lithofacies controls on porosity and pore structure for Ordovician Goldwyer Formation. Several studies have used different qualitative and quantitative techniques for the geological and pore structure characterisation of this Formation (Delle Piane et al., 2015; Josh et al., 2019; Labani et al., 2013; Yuan et al., 2019; Yuan et al., 2018). However, these approaches were applied without considering lithofacies classification and their controls on the pore systems. The Goldwyer Formation consists of three units such as Goldwyer-I (mainly shale), Goldwyer-II (mainly carbonates), and Goldwyer-III (shale unit). However, based on previous studies, the Goldwyer-III is considered a potential shale reservoir unit due to higher TOC content (van Hattum et al., 2019); therefore, this chapter focuses on the Goldwyer-III shale.

The objectives of this work are achieved by applying both qualitative (x-ray diffraction (XRD), TESCAN integrated mineral analyser (TIMA), thin-sections, FE-SEM and rock eval pyrolysis) and quantitative (helium porosity, LPN2, LPCO2, and MICP) methods. A workflow for shale lithofacies classification is introduced, and then porosity and pore structure are critically discussed for individual facies. This knowledge will help provide a detailed understanding of pore structure variation concerning different lithofacies. Moreover, this research will also help identify the good quality lithofacies types for fluid flow via pore systems for the fracturing job. Through this research, we suggest how a straightforward and integrated approach can act as a fundamental and efficient step for determining suitable beds with good reservoir potential in marine shales.

3.2 Materials and methods

3.2.1 Shale Characterisation

45 core samples and cuttings of Goldwyer-III shale drilled in the Theia-1 borehole were collected from the WA Geological Core Store, Department of Mines, Industry Regulation and Safety (DMIRS). Previous geochemical studies have shown that the Goldwyer-III shale is comprised of kerogen types II and III, and the Tmax is up to 460 °C indicating the presence of thermally mature organic matter zones in this shale (Johnson, 2019; Johnson et al., 2018). The samples were selected from the bottom to top section to cover each lithofacies with different mineralogy and TOC content. The samples were dried overnight in a vacuum oven at 65°C to use for the required analyses. The mineral composition was determined by X-ray diffraction (XRD) analysis on bulk shale core chip samples. The scanning electron microscopy (SEM) analysis was undertaken on representative core chip samples for pore imaging by using a Mira-3 Variable Pressure Field Emission Electron Microscopy (VP-FESEM). Total organic carbon was measured on bulk powdered samples using Rock-Eval® Pyrolysis. A detailed description of these analyses (XRD, VP-FESEM, and Rock-Eval® Pyrolysis) is provided in chapter 2.

3.2.2 TESCAN integrated mineral analyser

The automated mineralogy distribution mapping and grain size analysis of representative shale mounted blocks were carried out by the TESCAN Integrated Mineral Analyser (TIMA3 FE GMU) located at John De Laeter Centre, Curtin University. Twenty-five impregnated, thin stained sections were gathered from DMIRS and analysed at millimeter to micrometer using transmitted light microscopy.

3.2.3 Crushed rock porosity

The total porosity was measured on crushed shale samples; this process was introduced by Luffel et al., 1992. It was suggested that the pores are connected in shale; however, the connection is so small that even helium needed a substantial amount of time to equilibrate and reach all the pore spaces due to the low permeability of shale. The available oven-dried shale samples for this study included cuttings (rock pieces) and cylindrical core plugs. The grain density of all the samples was measured by AccuPyc II 1340. The bulk volume of the rock pieces was found by using a liquid pyknometer (liquid immersion). The samples were crushed using a special mortar to avoid the loss of the sample. The porosity was calculated by using the following equation (Ahmad, 2014; Luffel et al., 1992):

$$\emptyset = \frac{V_b - V_g}{V_b} * 100 \quad \text{(Eq. 3.1)}$$

V_b: Bulk volume of the sample (cm3)
V_g: Grain Volume of the crushed sample (cm3)
Ø = Total porosity of the sample in percentage (%)

The crushed rock porosity method helps to calculate the total porosity accurately that considers all types of pores, such as micro, meso, and macropores. That's why it is usually higher than the porosity measurement on core plugs of shale. Introducing this method is helpful for microporous rocks as the porosity measurement on crushed samples avoids the errors related to insufficient drying of samples (e.g., overestimating the core plug mass) (Klaja et al., 2015). Moreover, due to the low flow rate through shale samples, it is not practical to use core plugs under confined conditions to simulate reservoir stress. Therefore, crushed samples are more useful for shale porosity measurement (Bustin et al., 2008; Dong et al., 2015; Luffel et al., 1992).

3.2.4 Low-pressure gas adsorption tests

The pore structure consisting of pore size distribution, pore volume and specific surface area of shale was examined by low-pressure gas adsorption (LPGA) (<18.4 psi). Before the analysis, the required powdered samples (100-60 mesh/150-250 μm) were degassed for 8 hours to clean the pore surface. The low-pressure adsorption experiments were carried out using the Micromeritics Tristar 3020 instrument located at the Chemical Engineering Department, Curtin University. The LP-N2-GA tests were conducted at 77K temperature to characterise pores ranging from 2nm to about 200nm, while the LP-CO2-GA was achieved at 273.15K temperature to illustrate micropores ranging from 0.35nm to 2nm. The Brunauer-Emmett-Teller (BET) model theoretically described the experimental isotherms, and this was combined with the density functional theory (DFT) available in equipment's built-in software to invert the data for the pore size distribution (Lastoskie et al., 1993; Seaton & Walton, 1989). The isotherms were interpreted based on pre-defined patterns, as shown in Figure 3.1.

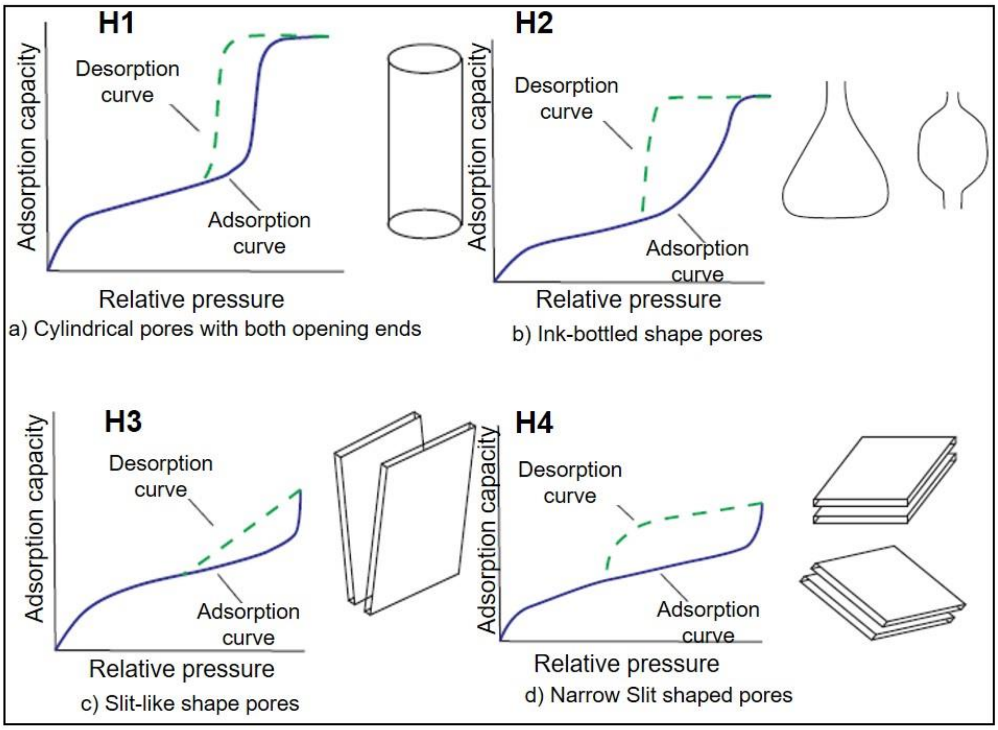

FIGURE 3.1: Pore types classification based on adsorption-desorption hysteresis loops (H) (Xue et al., 2016; Yan et al., 1979).

3.2.5 Mercury injection capillary pressure analysis

To cover the full spectrum of pore size range for the shale (for macropores), the MICP analysis was carried out using Micromeritics Autopore IV 9500 V1.09 porosimeter. The shale rock piece (10 g) was evacuated under the required conditions. The non-wetting fluid such as mercury act as the active probe to access the pore by following these parameters: the contact angle of 130°; Hg density of 13.53 g/mL; mercury surface tension as 485 dynes/cm. Hg filling pressure as 0.51 psi was applied, followed by injecting high pressure (0.1 MPa to 413.7 MPa equals to 60,000 psi) related to the pore throat size (3.6 nm to 1100 µm). The Washburn equation was applied to analyse the pore throat size distribution by assuming the cylindrical pores equation (Eq. 3.2):

$$r_i = \frac{-2\sigma cos\theta}{Pc} \quad \text{(Eq. 3.2)}$$

Where ri is considered as the pore throat radius measured in µm; θ is the mercury contact angle (130°); whereas, σ is the mercury surface tension (485 dynes/cm) and Pc is the mercury injection pressure (ranged from 14.5 to 60,000 psi).

3.3 Results

A classification of Goldwyer-III shale's facies based on sedimentary features is already explained in Chapter 2. However, the classification in Chapter 2 is based on core logging. As the shale is heterogeneous at a finer scale, so an analytical approach supported by high-resolution techniques is applied in this Chapter to evaluate the lithofacies. The results of the comprehensive analytical studies are discussed separately for each lithofacies. The detailed results from the compositional analyses are given in Appendices A1, A2, and A3.

3.3.1 Shale Lithofacies classification

Several classification schemes have been proposed for fine-grained mudrocks or shales though there is no universally accepted standard classification scheme for shale lithofacies (Folk, 1980; Lazar et al., 2015; Milliken, 2014). The classification schemes usually categorise different lithofacies in shales based on lithology, mineral composition, grain size and organic content integrated with the sedimentary characteristics. Similarly, the Goldwyer-III shale lithofacies are characterised here based on three distinctive features, macroscopic sedimentary characteristics, mineral compositions, and TOC content (Table 3.1 and Appendix-A1). A general scheme is proposed for Goldwyer-III shale facies classification based on data patterns and by applying three cut off values. These cut off values include TOC (>3%), clay content (>45%) and quartz to carbonate ratio (3:1) (Figure 3.2). According to the clay-silica and carbonate cut-off values, the Goldwyer-III shale can be divided into five lithofacies: argillaceous shale (total clay content > 45%), organic-rich shale (total clay content > 45%), siliceous shale (Q/C ratio > 3:1), calcareous shale (Q/C ratio < 3:1), and mixed shale (equal proportions of all minerals). The organic-rich shale is defined by having TOC>3wt%. The observed sedimentary features in the Goldwyer-III shale are illustrated in Figure 3.3.

Table 3.1: Averaged values of mineral composition, geochemical parameters, densities, porosity and pore structure elements of different Goldwyer-III shale lithofacies (n=45).

Lithofacies	Mineral composition (wt%)			TOC (wt%)	Tmax (°C)	HI	OI	Bulk density (g/cc)	Grain density (g/cc)	Total Porosity_ He (Fraction)	BET surface area (m^2/g) LPNA	BET surface area (m^2/g) LPCO2	Micropore volume (cm^3/g)	Mesopore volume (cm^3/g)	Macropore volume (cm^3/g)
	Silica (Qtz+Fspar)	Total clay	Carbonates												
Argillaceous Shale	27.0	58.9	11.0	1.8	444.7	143.2	43.6	2.51	2.71	0.09	12.485	1.690	0.00220	0.044	0.00072
Organic rich Shale	36.5	51.5	10.8	3.7	436.5	161.6	9.4	2.44	2.65	11.6	13.650	1.824	0.00320	0.052	0.0022
Siliceous Shale	46.0	45.1	11.1	2.5	457.7	150.6	30.6	2.48	2.76	0.10	19.141	1.884	0.00244	0.038	0.0017
Calcareous Shale	13.9	24.1	59.8	0.7	423.7	83.5	69.5	2.56	2.71	0.06	5.020	0.727	0.00213	0.022	0.0015
Mixed Shale	31.8	39.1	26.4	1.4	439.7	123.4	145.2	2.51	2.71	0.10	7.062	0.443	0.00116	0.023	0.001

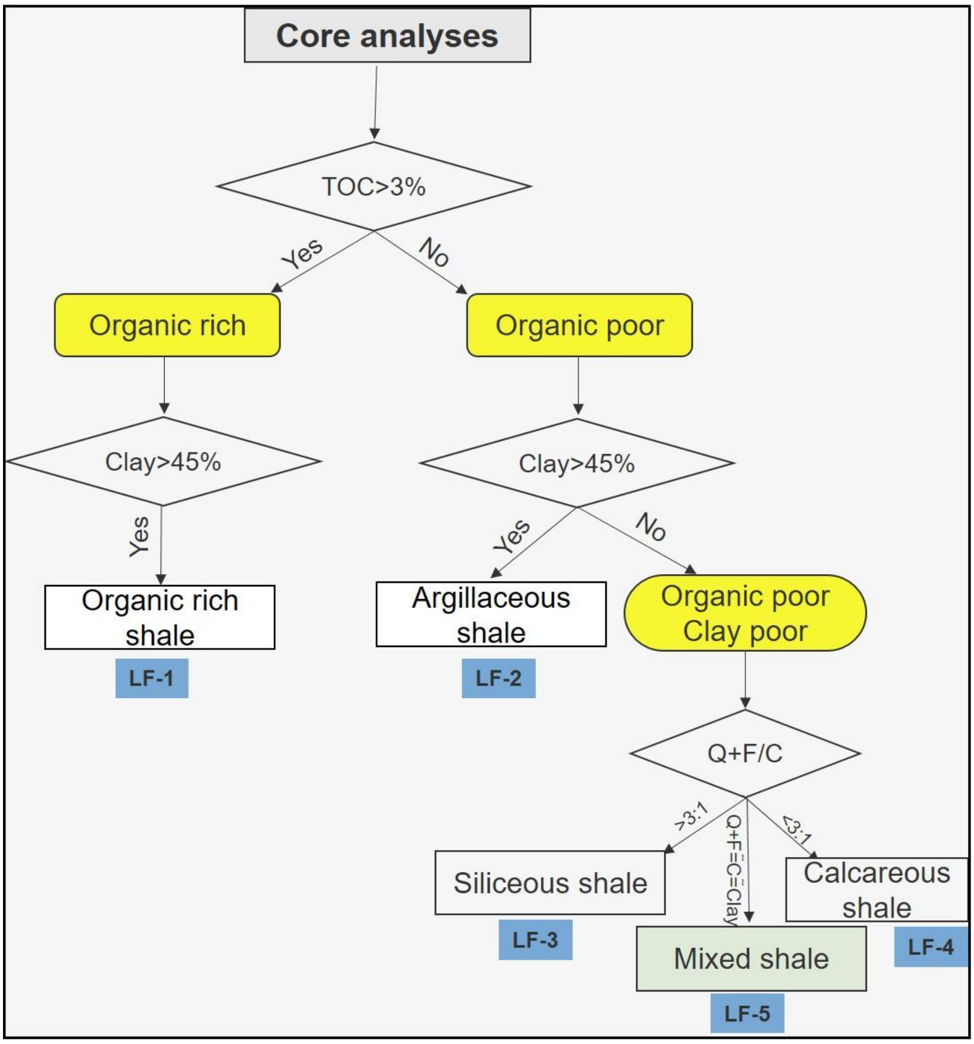

Figure 3.2: Schematic workflow used to classify Goldwyer-III shale lithofacies (LF) based on mineral composition via XRD and TOC data.

The XRD mineralogy was plotted in a ternary diagram to understand shale lithofacies' heterogeneity (Figure 3.4). The averaged mineral composition values, geochemical parameters and petrophysical properties for each lithofacies are given in Table 3.1. In contrast, the properties of each sample are provided in Appendix-A (Appendix-A1 to A3).

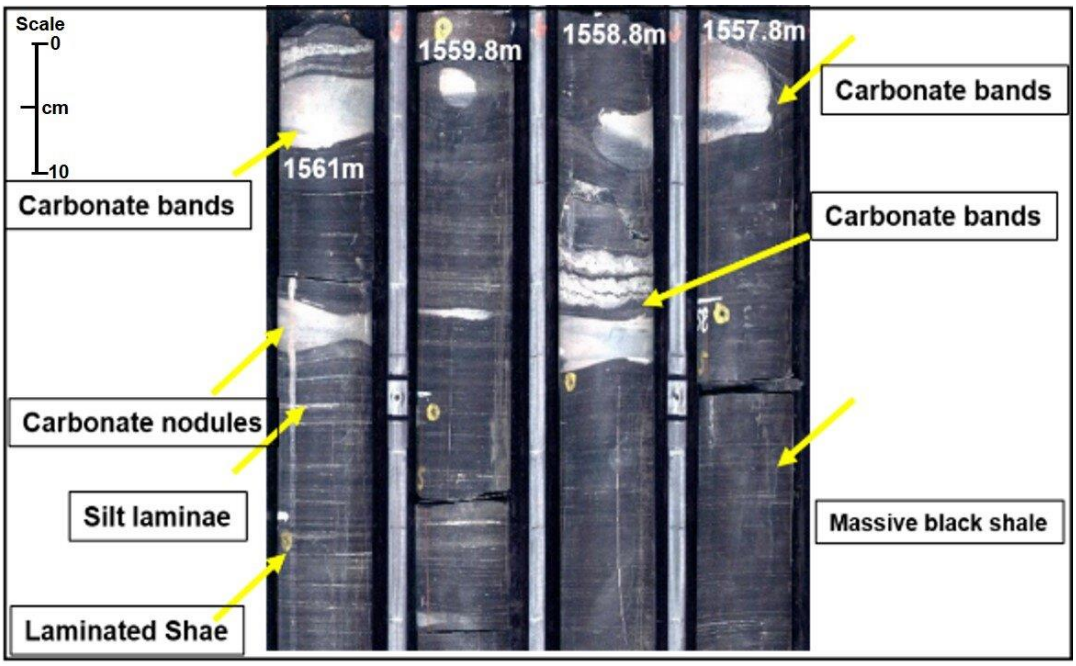

Figure 3.3: Sedimentary features observed in Goldwyer-III shale through Theia-1 core.

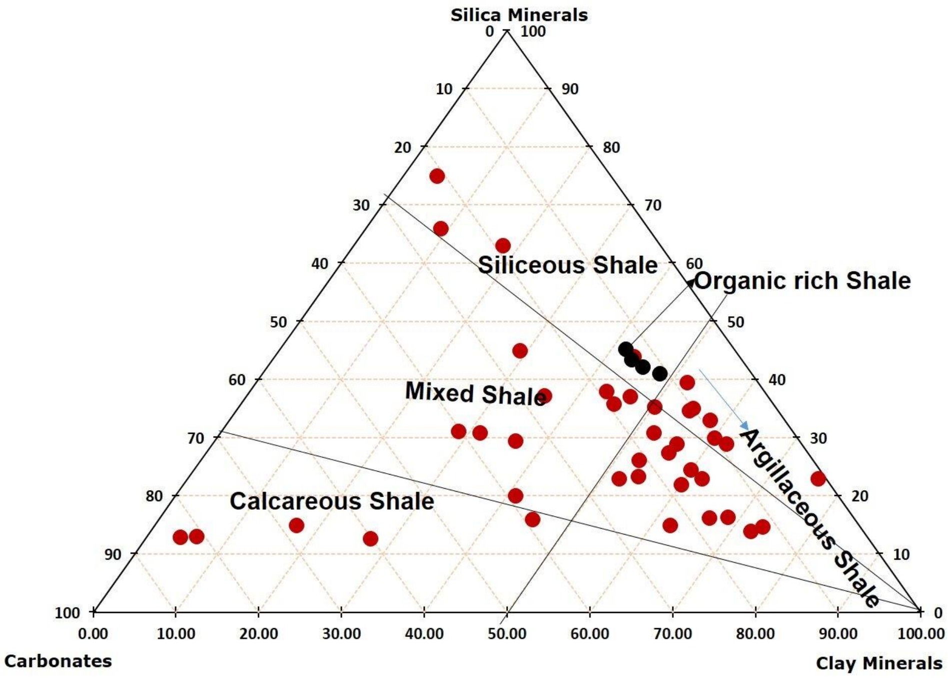

Figure 3.4: Ternary diagram showing lithofacies classification based on XRD mineralogy (in percentages) from two wells (Theia-1 and Pictor East-1).

3.3.2 Argillaceous Shale

The argillaceous shale is the predominant lithofacies in Goldwyer Formation intervals (Table 3.1 and Appendix-A1). This lithofacies is characterised by light to dark grey colour, laminated clay and silt at the core scale (Figure 3.5a). According to mineral distribution mapping and quantification, this lithofacies has the highest clay content ranging from 45% to 75% (averages 59%) (Figure 3.6a), the dominant clay mineral being illite. The silica minerals vary from 10% to 35% (average 25%) and the carbonates range from 5% to 20% with an average of 11%. The TOC content of argillaceous shale ranges from 0.34 wt% to 3.2 wt% (average 2 wt.%).

3.3.3 Organic rich shale

The organic-rich shale is a massive black at the core level, as shown in (Figure 3.5b). The samples of organic-rich shale are found to be silica and clay-rich. This lithofacies has clay content ranging from 45% to 50%. Illite is the dominant clay type, with a minor amount of kaolinite and smectite. The average silica minerals are about 37%, and carbonates are around 11%. This lithofacies is the most organic-rich in Goldwyer Formation, having an average TOC of 3.7 wt.% (Table 3.1, Appendix-A1 and A2).

3.3.4 Siliceous Shale

The siliceous shale is light grey in colour, comprising thin laminations of quartz silt and clay in places (Figure 3.5c). This lithofacies is comparatively rich in silica minerals with a range from 35% to 63% (averages 46%), as confirmed by mineral distribution mapping through TIMA analysis as well (Figure 3.6b). Due to some interbedded carbonate laminations, it has an average carbonate content of 11%. The quartz to carbonate ratio in this facies is higher than 3:1. The total clay content (mostly illite) ranges from 40% to 45% (averages 45%) and the TOC content of this lithofacies ranges from 1.21 to 3.2 wt% (averaged as 2.5 wt%) (Table 3.1, Appendix-A1 and A2).

3.3.5 Calcareous Shale

The calcareous shale comprises dark grey calcareous mudstone bands interbedded with mudstone bands containing calcareous concretions (Figure 3.5d). The mudstone bands comprise thin calcareous clay and silt laminations intercalated with and deformed around the early diagenetic and subsequently differentially compacted concretions. This lithofacies is commonly fossiliferous and bioturbated. This lithofacies has high carbonate contents ranging from 40% to 82% with an average of 60% (Figure 3.6c). The silica minerals vary from 12% to 16% (average 14%). The total clay content of calcareous shale ranges from 17%

to 45%, 24%. This lithofacies is comprised of the lowest TOC content, with an average of 0.7 wt%. (Table 3.1, Appendix-A1 and A2).

3.3.6 Mixed Shale

The mixed shale is a heterolithic lithofacies occurring as a medium to dark grey shale with alternating thin laminations of mudstone, silt, and carbonate. Some beds have moderate to high amounts of bioturbation (Figure 3.5e). This lithofacies is comprised of the inter-mixing of different minerals with almost the same proportions. For this lithofacies, the total clay content (mostly illite) ranges from 28% to 55% (average 39%) (Figure 3.6d), silica minerals range from 20% to 45% (averaged 32%) and the carbonates content ranges from 13% to 40% (averages 26.4%). Like the mineral contents, this lithofacies' TOC content also ranges from 0.04 wt.% to 3.15 wt.% (Table 3.1, Appendix-A1 and A2).

3.3.7 Porosity and grain density

As shown in Table 3.1 and Appendix-A3 and Figure 3.7, the selected shale samples' helium grain or skeletal density ranges from 2.62 g/cc to 2.77 g/cc, and their equivalent bulk densities are in the range of 2.40 g/cc to 2.70 g/cc. These densities yield porosity ranges from 2.4% to 12.8%. Regarding respective lithofacies, the argillaceous shale has an average value of grain and bulk densities of 2.71 g/cc and 2.51 g/cc, respectively. The average porosity of argillaceous shale is determined as 9%. The organic-rich shale has respective average values of grain and bulk densities as 2.65 g/cc and 2.44 g/cc. The average porosity of organic-rich shale is 11.6%. Furthermore, the average grain and bulk densities of siliceous shale are 2.76 g/cc and 2.48 g/cc, respectively. The average porosity of siliceous shale is 10%. Similarly, the calcareous shale has average grain and bulk density values of 2.71 g/cc and 2.56 g/cc, respectively. The average porosity of this lithofacies is 6%. Moreover, the average grain and bulk densities of mixed shale are 2.71 g/cc and 2.51 g/cc, respectively. The average porosity for this lithofacies is 10%.

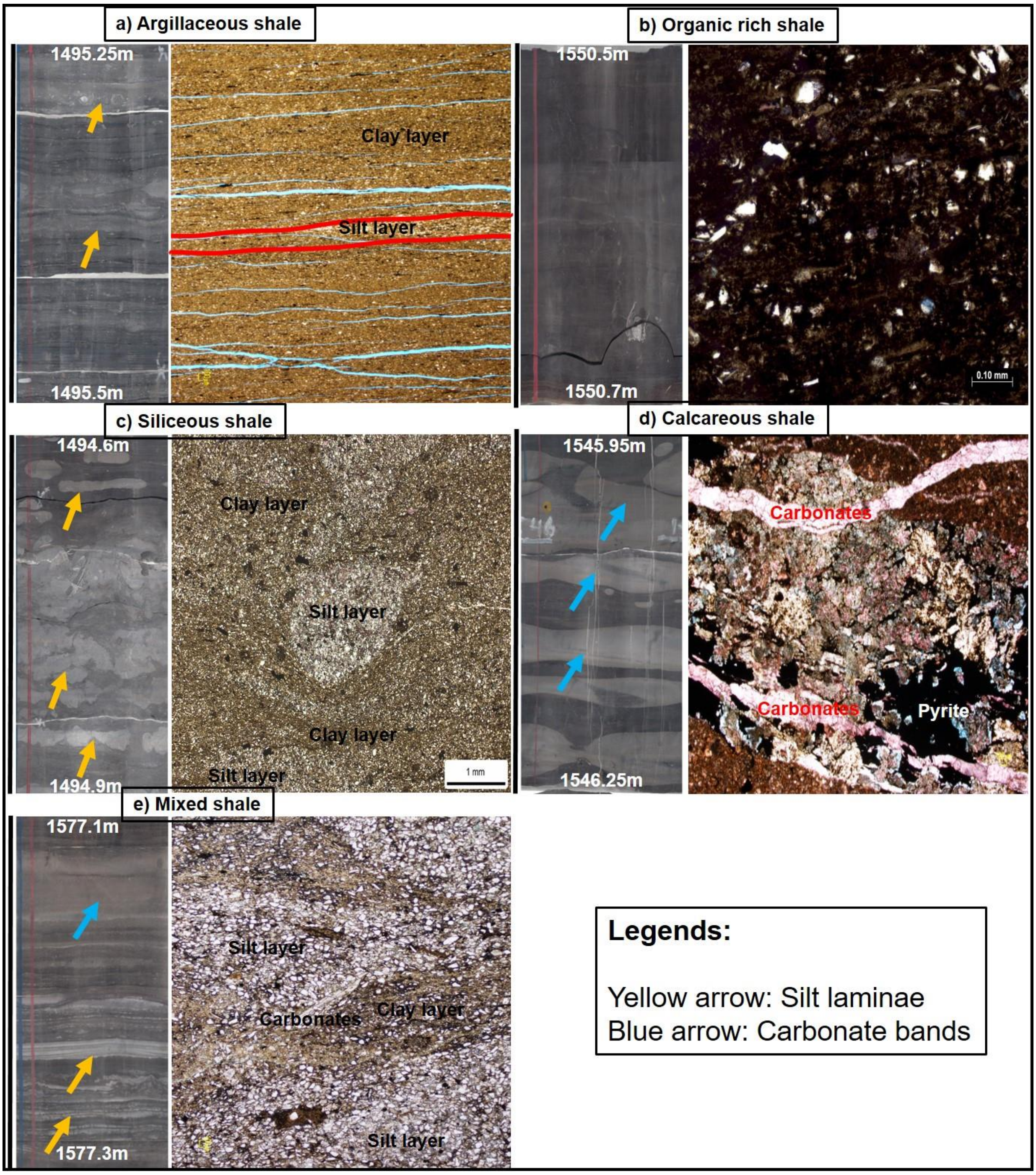

Figure 3.5: The identification of sedimentary features and lithology by core images and thin sections in different Goldwyer-III shale lithofacies.

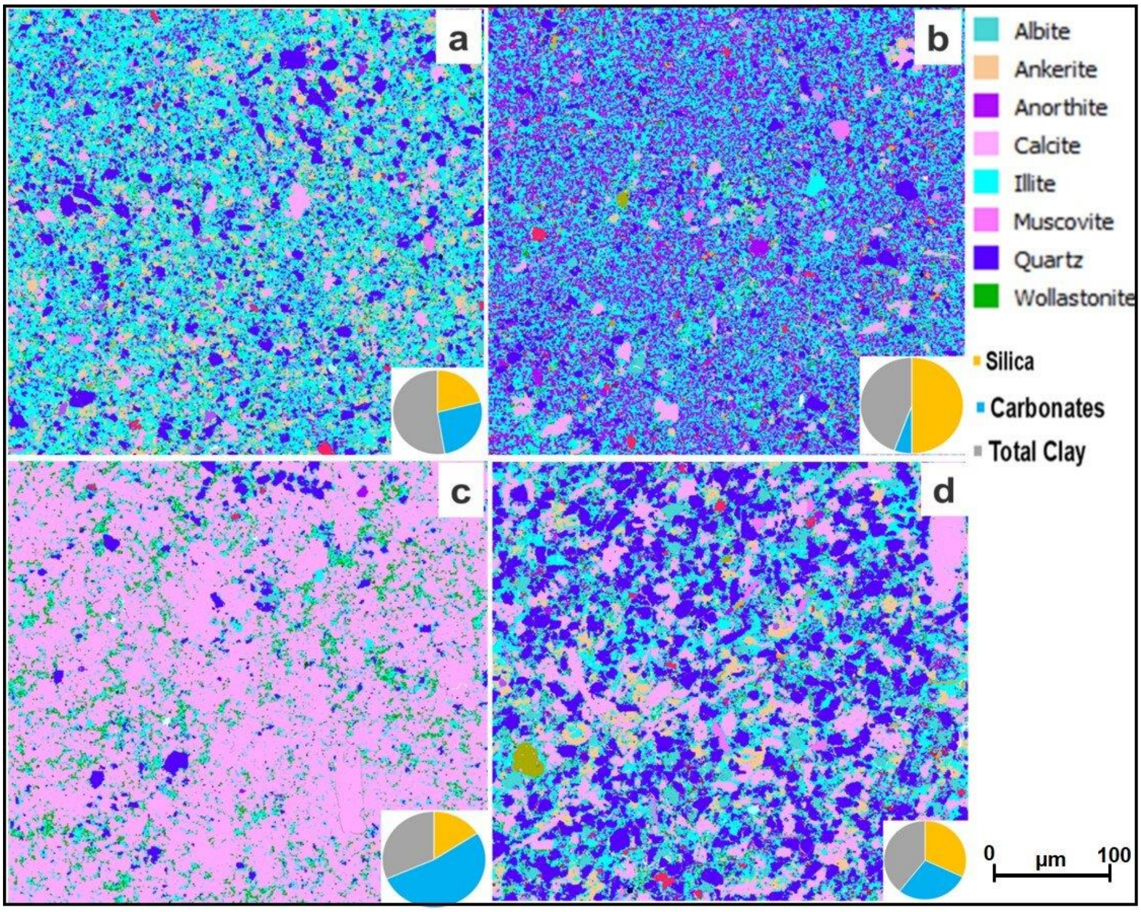

Figure 3.6: Mineral distribution mapping illustrating the mineralogy of different lithofacies such as a) Argillaceous shale (illite rich); b) Siliceous shale (silica minerals e.g. Quartz, Anorthite and Albite rich); c) Calcareous shale (Calcite rich); d) Mixed shale (intermixing of minerals).

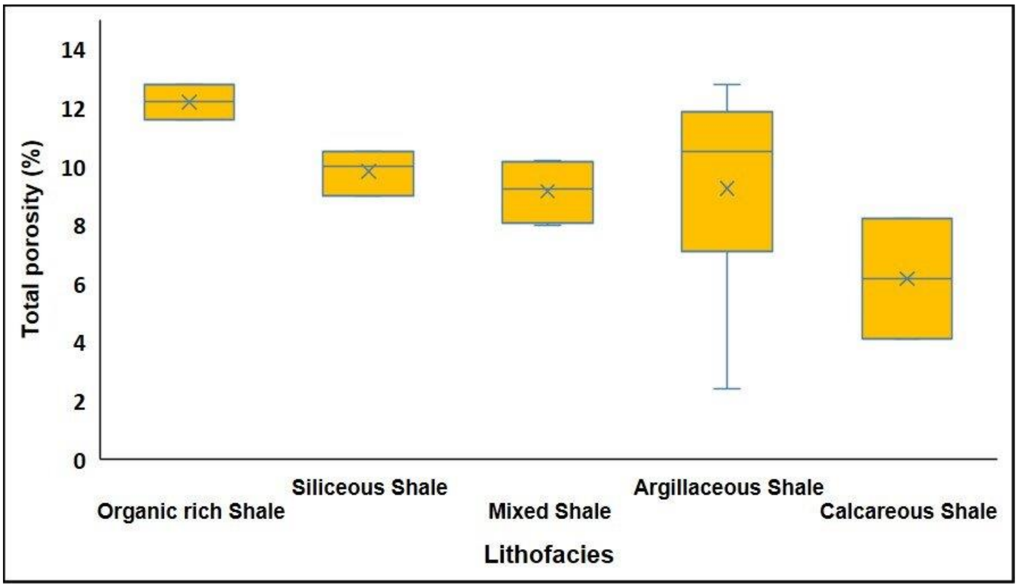

Figure 3.7: Total porosity range of different lithofacies in Goldwyer-III shale.

3.3.8 Pore types and morphology

FE-SEM results show that Goldwyer-III shale consists of three types of pores: interparticle, intraparticle, and organic matter pores (Figure 3.8 to Figure 3.10). However, the pore structure differs between shale lithofacies. The organic-rich shale consists mainly of organic pores in various forms, such as isolated, irregular or harbour like organic dissolution pores (Figure 3.8a and b); nano-scaled pores in the organic matter mixed with pyrite framboids (Figure 3.8c); pits-like organic pores associated with clay (Figure 3.8d); isolated pores, shaped as irregular, bubbles and slit-shaped in organic matter (Figure 3.8e and f). It can also be observed that these organic pores are nano-scaled and most of them seem isolated in 2-D images.

The interparticle pores are associated with inorganic minerals (Figure 3.9). The argillaceous and siliceous shales mainly consist of interparticle pores between the calcite and quartz, illite and pyrite framboids (Figure 3.9a-f). The interparticle pores in pyrite framboids are incompletely filled. However, a few slit-like intraparticle pores have also been observed within clay in argillaceous shale (Figure 3.9a-c). The intraparticle pores are found within the particles such as clay minerals, quartz, calcite, or pyrite. The calcareous and mixed shales consist of intraparticle pores within calcite, quartz, and pyrite (Figure 3.10a-b). These pores linked to calcite and pyrite have triangular or polygonal shapes. The interparticle pores between inorganic minerals are also observed in calcareous and mixed shale lithofacies (Figure 3.10a-d).

3.3.9 Pore structure characterisation

The quantitative pore characterisation of Goldwyer-III shale was carried out based on low-pressure nitrogen (N2) and carbon dioxide (CO2) gas adsorptions. The low-pressure N2 adsorption method provides a good understanding of mesopores characterisation, and CO2 adsorption applies better for micropores quantification.

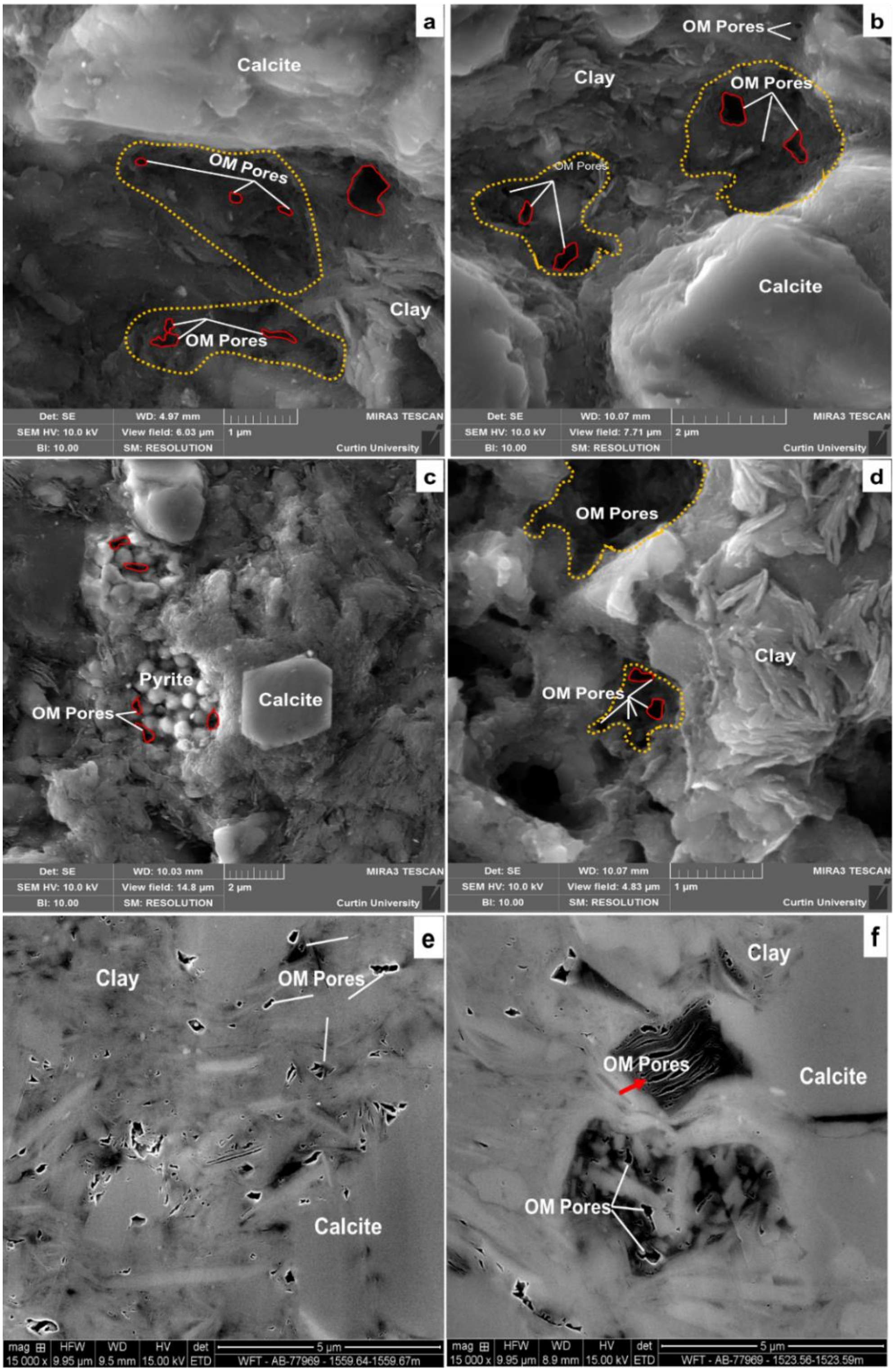

Figure 3.8: FE-SEM images illustrating nano-pores associated with organic matter (OM pores) observed in organic-rich lithofacies.

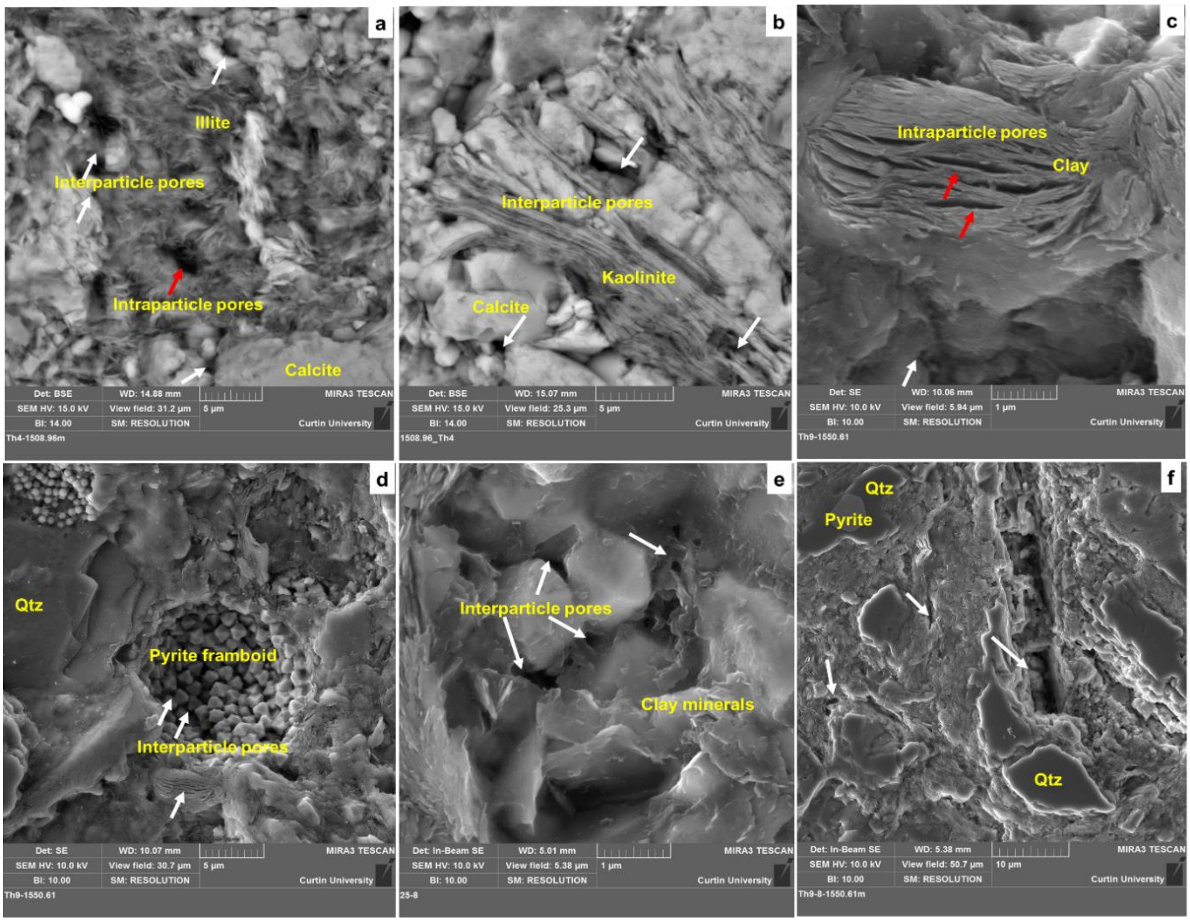

Figure 3.9: Inter and intra-particle pores (white arrows) identification through FE-SEM imaging in a-b) Argillaceous Shale; c-e) Siliceous Shale.

3.3.10 Low-pressure nitrogen adsorption (LPN2)

The LPN2 adsorption-desorption isotherms of the Goldwyer-III shale lithofacies are illustrated in Figure 3.11. According to the IUPAC classification, the isotherm types for the studied Goldwyer-III shale are type IV, specific for mesoporous materials. Hysteresis loops (H) are interpreted based on the IUPAC classification scheme (referred to Figure 3.1), which vary in different lithofacies. For example, the organic-rich shale is principally H3, indicating slit-like pores. However, the other Goldwyer-III shale lithofacies show a combination of types H3 and H2, which depict the complex pore shape as bottle-necked and slit-like.

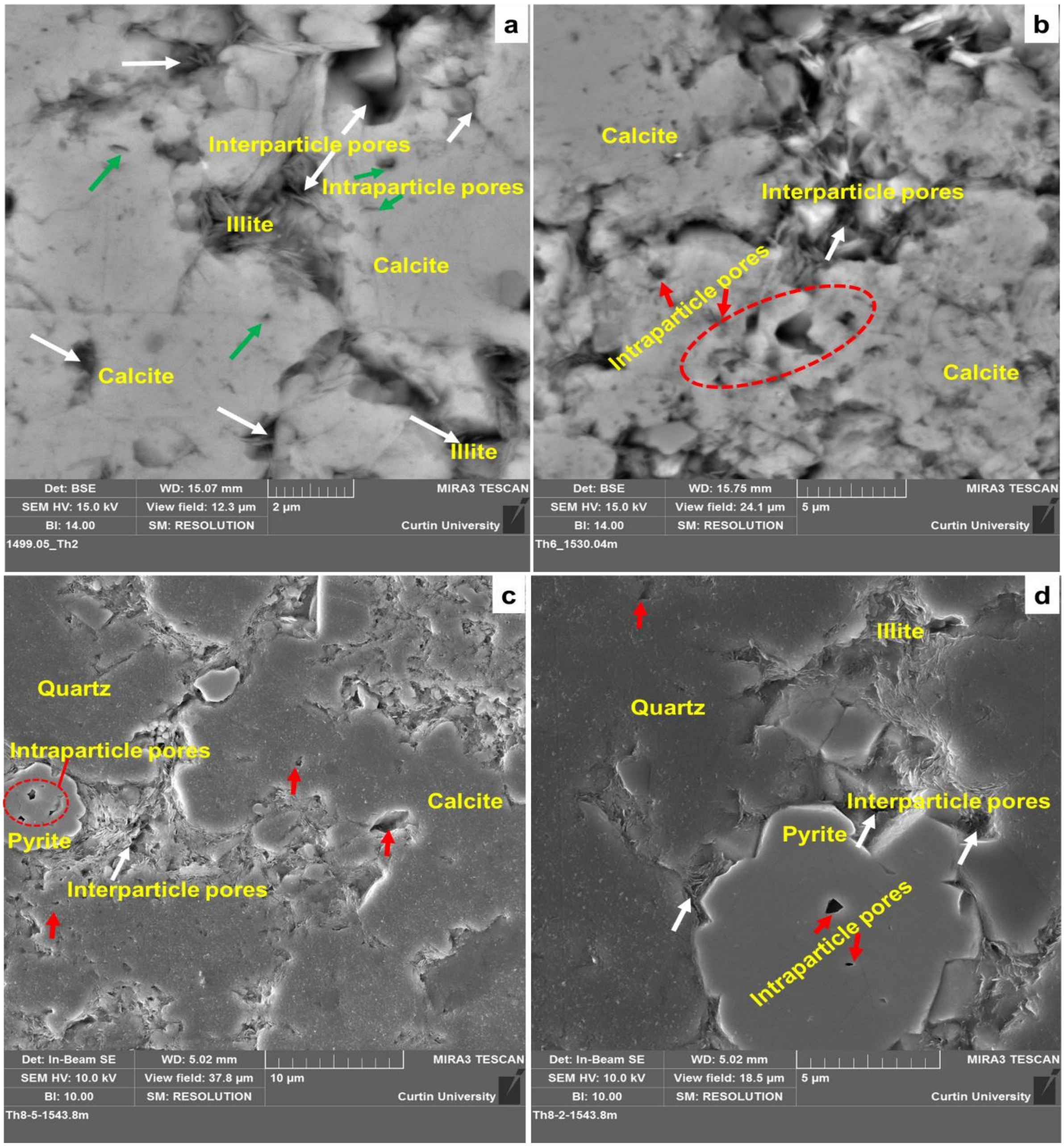

Figure 3.10: a-b) Inter and intra-particle pores (green and red arrows) in Calcareous shale; c-d) inter and intra-particle pores in mixed shale of Goldwyer-III shale, green and red arrows showing intra-particle pores and white arrows indicate interparticle pores.

In comparison, the calcareous shale illustrates type H4 indicating wedge or narrow slit-shaped pores. The gas adsorption capacity of each lithofacies varies due to TOC and total clay content differences. The organic-rich and argillaceous shales with high TOC and clay have higher adsorption capacity - 38 cm^3/g and 34 cm^3/g, respectively. In comparison, the siliceous, calcareous and mixed shales have average adsorption capacities of 23 cm3/g, 4.5 cm^3/g and 20 cm^3/g, respectively. The low adsorption capacities of these three lithofacies are due to low TOC and clay contents. The hysteresis loops in argillaceous and siliceous shales are larger than in other lithofacies, indicating the pore system in siliceous and argillaceous shales is more complex than in other lithofacies. Referred to Table 3.1 and Appendix-A3, Brunauer-Emmett-Teller (BET) specific surface areas of the Goldwyer-III shale samples range between 1.2 m2/g and 22 m2/g with an average of 12.5 m2/g. This range varies for each lithofacies. For example, the BET-specific surface areas of organic-rich and argillaceous shales are higher than siliceous, calcareous, and mixed shales. The average BET, specific surface areas of organic-rich and argillaceous shale, are 13.6 and 12.5 m^2/g, respectively, while those of siliceous, calcareous, and mixed shales are 19.14, 5.02, and 7.06 m^2/g, respectively.

The pore size distributions (PSD) determined by the BJH method for different lithofacies are shown in Figure 3.12. This analysis suggests that almost every sample shows pore distribution in the mesopores region (diameter > 2nm). However, the high TOC samples (>3 wt%) illustrate bimodal distribution that shows the micropores region. It can also be observed that the samples with high clay content within the same lithofacies show higher mesopore volumes than clay-poor samples. The mesopores volumes of Goldwyer-III shale vary between 0.00389 cm3/g and 0.054 cm3/g. The argillaceous and organic-rich shales have higher average mesopores volumes, such as 0.052 and 0.048 cm^3/g, respectively. In comparison, the siliceous, calcareous, and mixed shales have comparatively low mesopores volumes, such as 0.028, 0.005, and 0.03 cm^3/g, respectively.

3.3.11 Low-pressure CO2 adsorption

CO2 adsorption was applied to characterise the micropores (0.3 to 2 nm) in Goldwyer-III shale lithofacies. The adsorption isotherms indicate that all lithofacies show a typical type I curve that specifies larger inner surface areas (Sing, 1985). As shown in Appendix-A3, organic-rich shale's adsorption capacity averages around 1 cm3/g, whereas, for argillaceous shale, it ranges from 1 to 1.6 cm3/g. Conversely, siliceous and mixed shales' adsorption capacity is between 0.98-1.7 and 0.85-1.2 cm3/g, respectively. It is observed that these lithofacies have concentrated ranges of adsorption capacity. In comparison, the calcareous shale has an extensive range of adsorption capacity that varies between 0.5 to 2 cm^3/g.

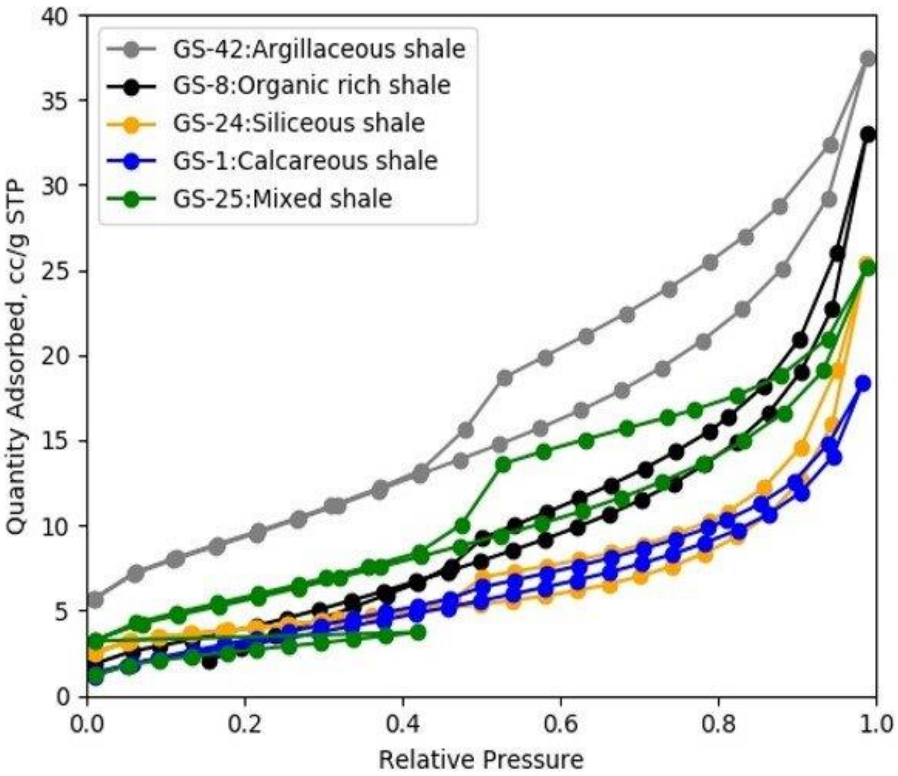

Figure 3.11: Low-pressure nitrogen adsorption (LPNA) isotherms of different lithofacies of Goldwyer-III shale.

As shown in Figure 3.14, the micropore size distribution suggests that all lithofacies show bi- to tri-modal distributions having pore diameters at 0.6-0.8nm, 1.2-1.4nm and 1.4-1.6nm, respectively. The micropores volumes of Goldwyer-III shale range between 0.0008 cm3/g and 0.00273 cm3/g. The average micropore volumes in organic-rich and argillaceous shales are 0.0024 and 0.0025 cm3/g, respectively whereas siliceous and mixed shales have average micropores volumes of 0.0021 and 0.00178 cm3/g, respectively. In comparison, the calcareous shale has the lowest micropores volume of about 0.00084 cm^3/g.

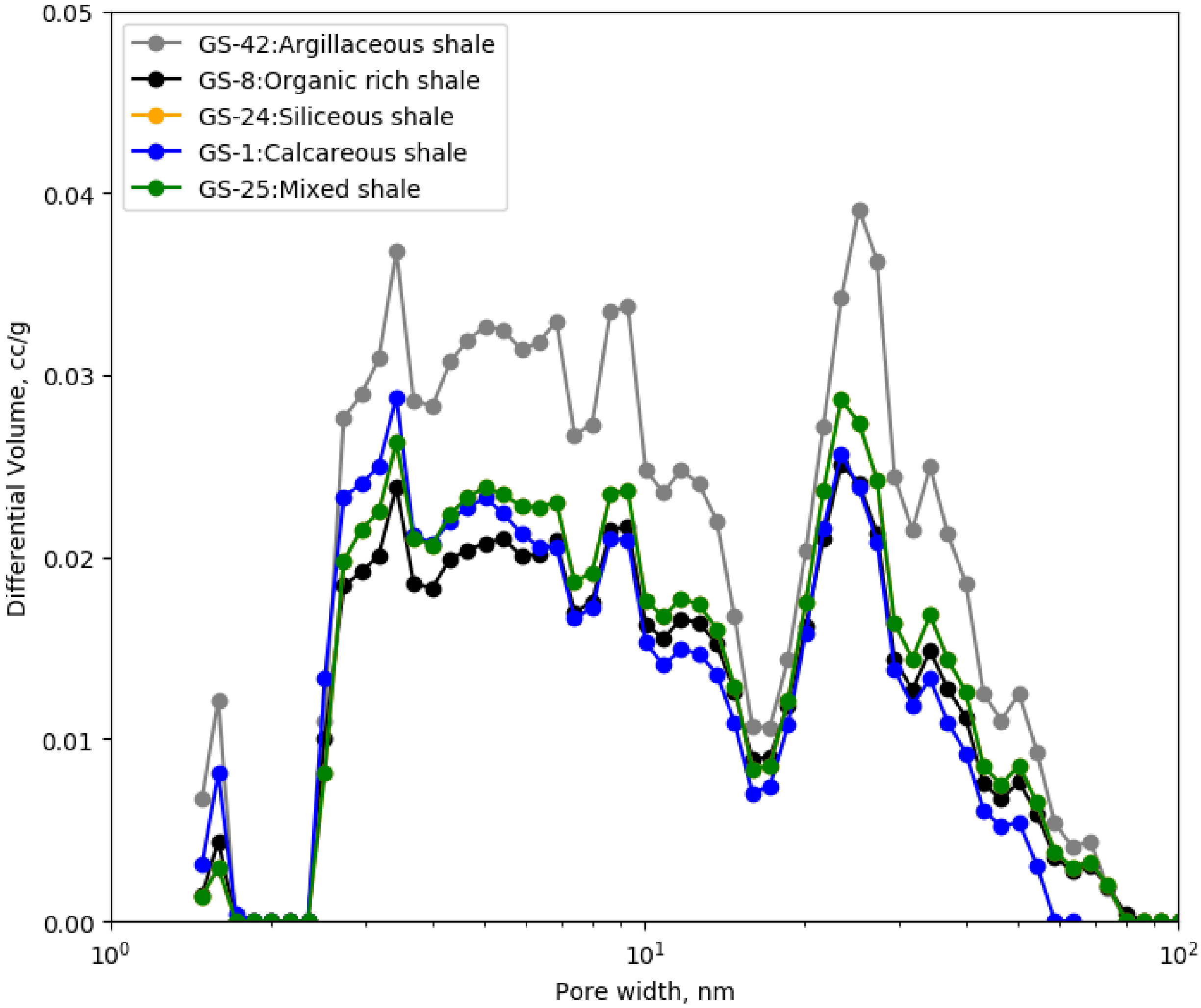

Figure 3.12: Mesopores size distribution based on LPNA test of representative samples of Goldwyer-III shale lithofacies.

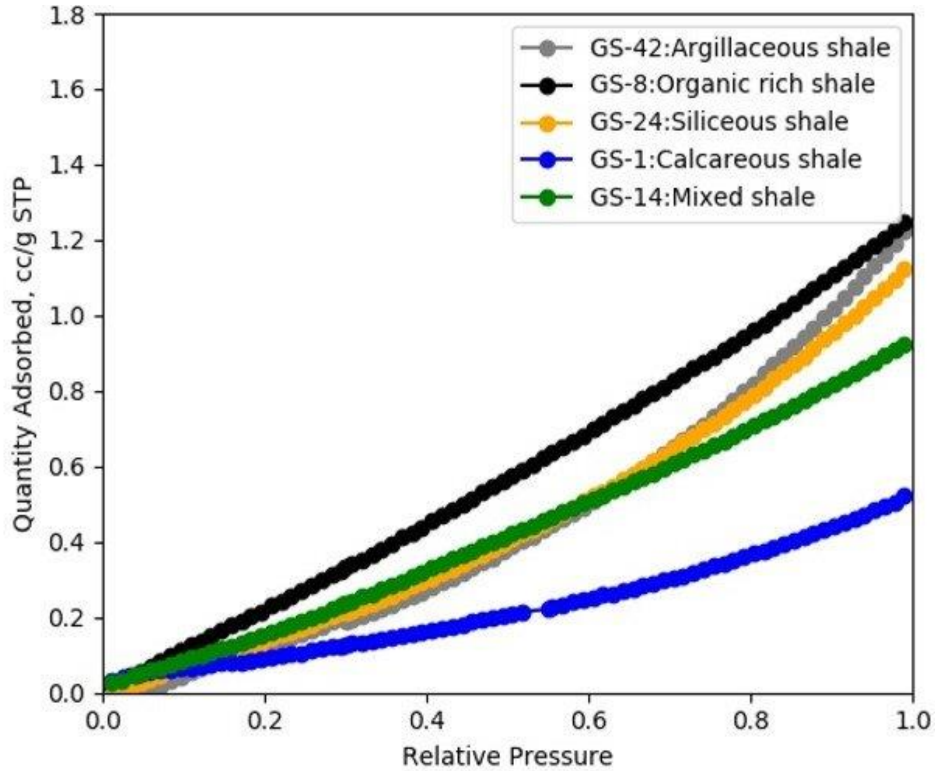

Figure 3.13: Low-pressure CO_2 adsorbed isotherms for representative shale samples.

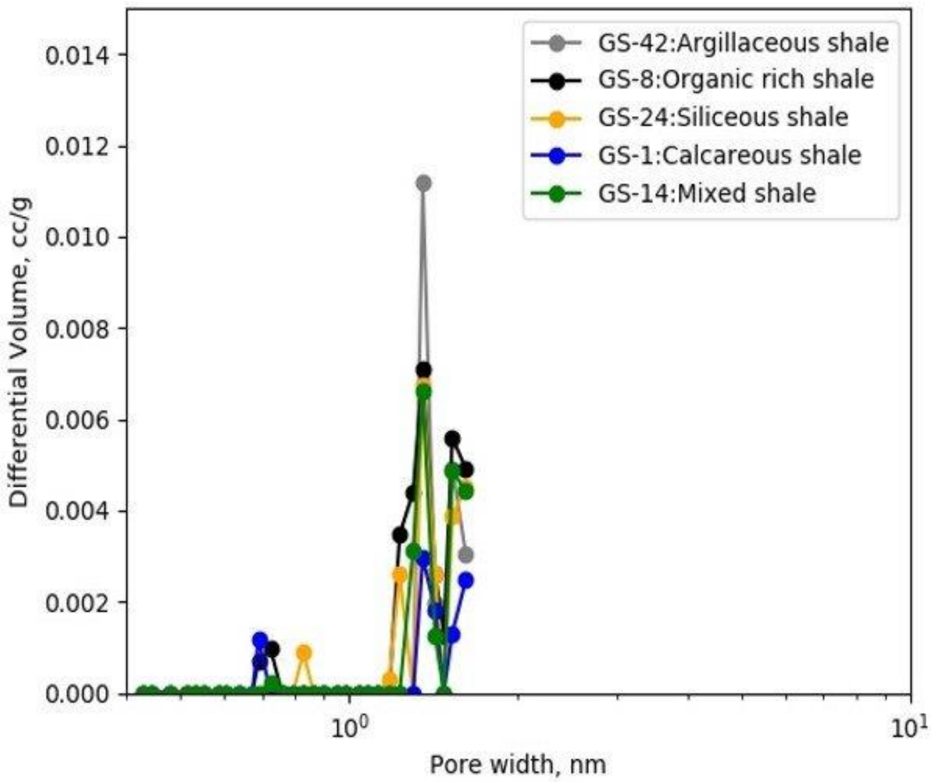

Figure 3.14: Micropore size distribution based on CO_2 adsorption of representative Goldwyer-III shale lithofacies samples.

3.4 Discussion

3.4.1 Effect of lithofacies on pore types

The pore types in the examined Goldwyer-III shale samples depend on the inorganic minerals, framework grains, and organic matter distribution, all of which vary among different lithofacies (Gou et al., 2020; Wang et al., 2020). The identified pores include inter-particle pores defined by clay flakes, quartz, pyrite, and carbonates particles, and intra-particle pores, mainly associated with illite, pyrite, and organic matter pores. As shown in Figure 3.8 to Figure 3.10, these pores are not evenly distributed in the Goldwyer-III shale. The organic matter pores in shale look isolated in 2-D SEM images; however, these pores are connected in 3-D image stacks (Schieber, 2013).

The SEM analysis of Argon ion-milled samples revealed that the organic-rich shale lithofacies mainly consist of organic matter pores (Figure 3.8). Some pores are also developed within pyrite framboids. The organic matter (OM) pores are intra-particle pores that form within the organic matter. According to (Loucks et al., 2009), the OM pores are only observed in the mature shales (if thermal maturity is more than 0.6%). As the thermal maturity of Goldwyer-III shale is more than 0.6% (0.6-1.3%) (Foster et al., 1986; Johnson, 2019; Torghabeh et al., 2019), therefore, this fact also justified the presence of OM pores in mature organic-rich shale with type-II and III kerogens. The organic matter is also confirmed by (Spaak et al., 2017) based on organic petrological analyses of different samples from other wells in the Canning Basin, as shown in Figure 3.15. It is shown that the telalginite organic matter is commonly derived from Gloeocapsomorpha Prisca (G. Prisca) in Goldwyer-III shale. Moreover, OM pores' development in these facies can also be due to the dehydrogenation and hydrocarbon generation reaction of OM with the maturity level during shale diagenetic processes. These processes increased the OM pores size and numbers (Guo et al., 2014; Ma et al., 2015; Schieber, 2013; Wang et al., 2017).

The argillaceous and siliceous shales are mainly enriched in interparticle pores existing between the grains (Figure 3.9). These pores are primarily developed between calcite or quartz and clay minerals. Such pore types developed due to anti-compaction behaviour of calcareous and siliceous minerals resulting from the accumulation and directional alignment of these minerals around clay minerals (Figure 3.9a and b) (Klaver et al., 2015; Loucks et al., 2012; Loucks et al., 2009). The calcareous and mixed shales mainly consist of intra-particle pores (Figure 3.10). These pores are observed as isolated within calcite, pyrite or illite minerals. The calcareous and mixed shale lithofacies are more abundant with increasing the depth in the Theia-1 well (around 1530m to 1590m). Therefore, due to compaction and cementation, the interparticle pores were reduced and as a result, intra-particle pores developed in Goldwyer-III shale.

3.4.2 Influence of lithofacies on pore structure

BET-specific surface area (SSA) and pore volumes are the critical parameters affected by Goldwyer-III shale's lithofacies. Based on the statistical approach and previously published data, the mesopores control the total SSA and total pore volumes of Goldwyer-III shale (Labani et al., 2013, Yuan et al., 2019). However, micropores are also observed, and their contribution is subject to specific lithofacies. Figure 3.14 shows that the organic-rich shale contributes more micropores volume followed by calcareous shale, than other lithofacies. It can be related to higher TOC, and OM pores development in organic-rich shale (Zhang et al., 2016). Overall, the TOC values and total clay (mainly illite) are the main controlling factors of pore systems in Goldwyer-III shale.

3.4.3 Effect of TOC

The pore structure parameters (SSA and pore volumes) show a linearly increasing relationship with TOC, which signifies an interaction between pore structure parameters and the organic matter of Goldwyer-III shale (Figure 3.16). However, it is noteworthy that the relationship of TOC with micropore volume for siliceous, calcareous, and mixed shales is comparatively stronger compared to mesopore volumes due to the presence of organic-rich laminae in these facies (Figure 3.16a and c). Moreover, it is also found that the micropore and mesopore volumes showed a strong linear relation with TOC for organic-rich shale, but a very weak relationship was observed for argillaceous shale (Figure 3.16b and d). The results indicate that the lithofacies with higher TOC (>3 wt%) often develop the interparticle as well as organic matter pores in organic-rich shale (Figure 3.8). The positive and comparatively strong relationship between TOC and BET SSA for micropores in organic-rich and argillaceous shales justifies the micropores development in these facies (Figure 3.16e). In terms of mesopores, the positive linear relationship also indicates that the organic matter influenced the BET SSA in all facies (Figure 3.16f). The micropores development in organic-rich shale can also affect its adsorption capacity (Song et al., 2020). It can also be related to the thermal evolution of shales as OM pores usually develop under moderate thermal evolution (Ro ≤ 2%) (Curtis et al., 2012; Luo & Zhong, 2020; Milliken et al., 2013; Zhang et al., 2016) and Goldwyer-III shale falls under this range as well (Johnson, 2019; Johnson et al., 2018). Moreover, the secondary cracking at a high maturity level also causes nano-pores' development in the shale (Wang et al., 2020). The organic-rich laminae in organic-rich, siliceous, and argillaceous shales also played a vital role in micropores' development due to higher TOC values. Therefore, the organic-rich lithofacies consists of both meso and micropores that increase the total pore volumes.

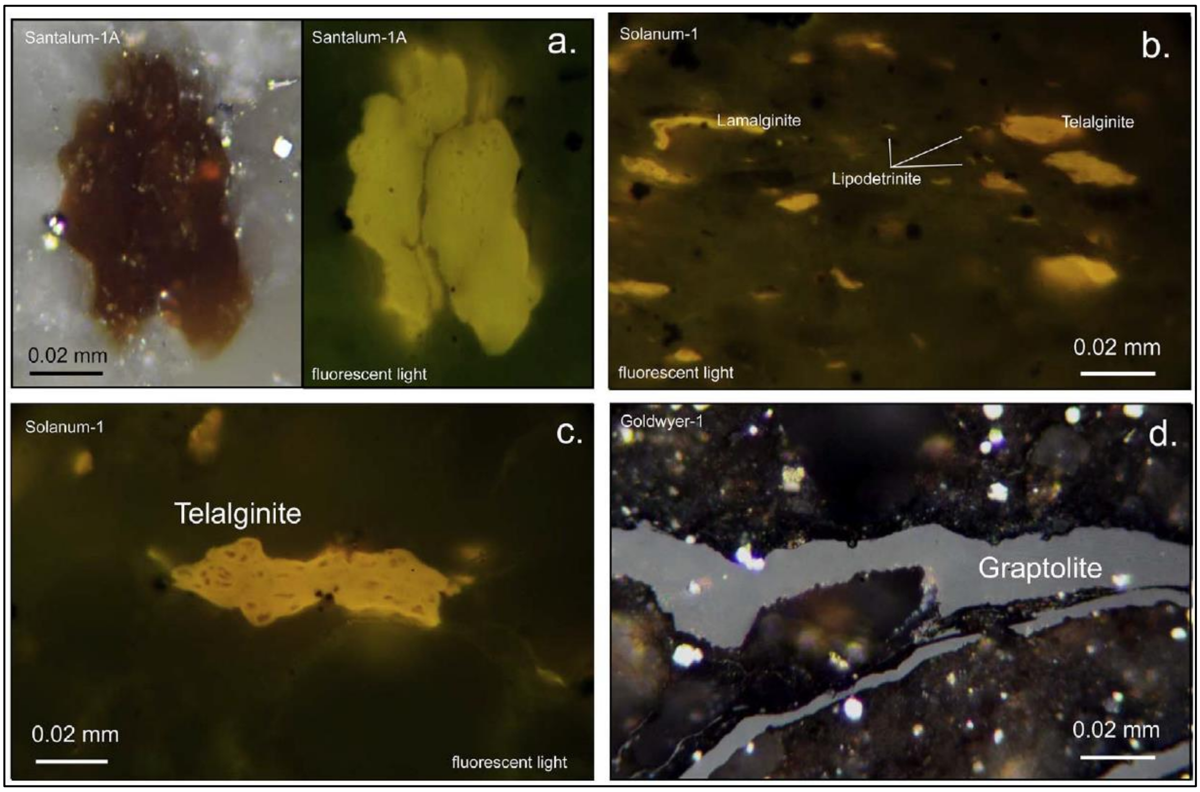

Figure 3.15: Photomicrographs adapted from (Spaak et al., 2017) for Goldwyer Formation samples from different wells: a) Telalginite derived from G. Prisca; b) Telalginite derived from G. Prisca, lamalginite and liptodetrinite; c) Telalginite derived from G. Prisca; d) Periderm layering in a graptolite.

3.4.4 Effect of clay minerals

Generally, the clays are very important for developing micro-nano scale pores in shale (Wu et al., 2018). The Goldwyer-III shale is enriched in clay minerals, and their proportion varies in different lithofacies. Previous studies revealed that the clay minerals have huge SSA and the pore volumes in the shales (Ross & Marc Bustin, 2009). However, the SSA varies with different clay minerals in the following order: smectite > mixed illite-smectite > illite > chlorite > kaolinite (H. Fu et al., 2015). In terms of micropore volume and SSA, all Goldwyer-III shale lithofacies exhibits a weak correlation with total clay content except argillaceous shale (Figure 3.17a, b,e). This is because the smectite-to-illite conversion process usually decreases the required initiation energy of pyrolysis (Jarvie et al., 2007). This process may increase the organic matter pores in the clay-organic matter complex. However, some lacustrine shales deposited in China show a relatively good relationship of micropores structure parameters with the clay minerals, which may be due to difference in clay mineral type and depositional setting (Liu et al., 2019).

Nevertheless, the SSA and pore volume of mesopores in argillaceous shale show a positive linear correlation with total clay content ($R2>0.7$) (Figure 3.17c). This may be because the clay minerals in Goldwyer-III shale are mostly illite, which has a higher primary SSA. Moreover, the clays are not stiff and can be deformed easily. The larger pores in the clay minerals, such as illite, can be affected by diagenetic processes such as compaction, cementation, and dissolution (H. Fu et al., 2015; Gao et al., 2018; Liu et al., 2019). Conversely, the mesopore volumes of siliceous, calcareous, and mixed shales exhibited an inverse relationship with total clay content (Figure 3.17d) due to the higher range of silica and carbonates minerals. Compared to micropores' SSA, the BET SSA of mesopores showed a good correlation with clay content (Figure 3.17e,f) because the Goldwyer-III shale is illite rich. Almost the same relationship trend between mesopore volume and SSA with clay minerals was also observed (Yuan et al., 2019).

Moreover, the silica minerals (quartz and feldspar) showed a positive relationship with all lithofacies except organic-rich and argillaceous shales (Figure 3.17f). The reason is that the silica minerals such as quartz and feldspar have small specific areas (3.9 m2/g and 6.6 m2/g, respectively) (Ji et al., 2014; Kuila & Prasad, 2013). Therefore, the silica content can effectively help to expand the microspore SSA and PV. It can also be inferred that the siliceous shale in Goldwyer-III shale relatively has higher micropore SSA and pore volume (Appendix-A3).

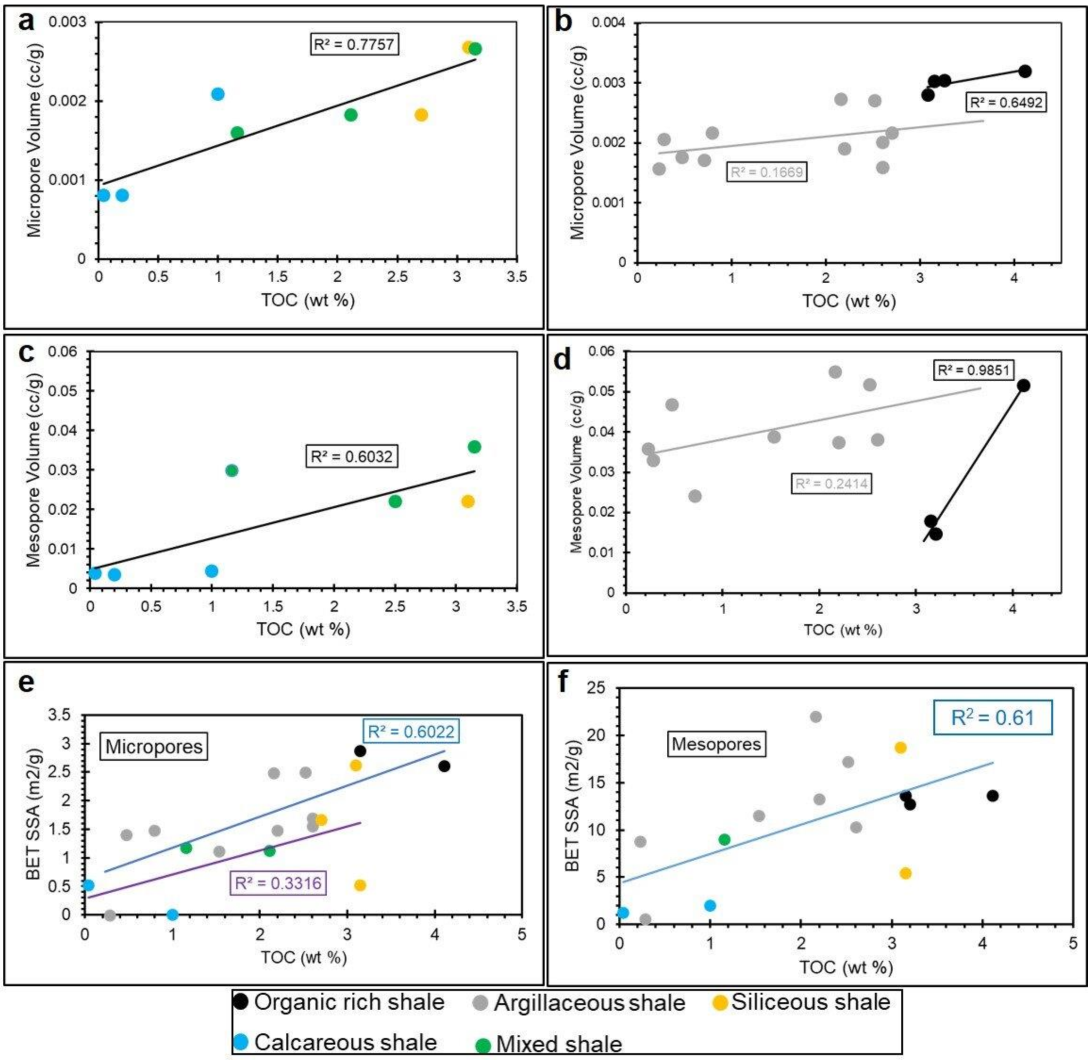

Figure 3.16: Relationship of TOC with pore structure elements (e.g. micro and mesopore volumes, BET specific surface area).

3.4.5 Controlling factors on porosity

It is very critical to understand the geological controls on the porosity of shale. TOC content's positive relations with specific surface area and pore volume show that organic matter mainly controls the pore system of Goldwyer-III shale. The porosity of different lithofacies in Goldwyer-III shale is positively correlated with the TOC with an inorganic-minerals-related porosity (at interception) of 3.5%

(Figure 3.18a). Goldwyer-III shale lithofacies' average porosity is in the following order: organic-rich shale > siliceous shale > mixed shale > argillaceous shale > calcareous shale. The porosity of organic-rich shale samples (averaging 11.6%) is comparatively higher than other lithofacies due to high TOC content. Similarly, the porosity of siliceous shale (averaging 10%) is more significant than other lithofacies due to the higher range of TOC values in some samples. As shown in Figure 3.18a, a strong positive relationship (R2 = 0.8) between TOC content and porosity was observed for organic-rich and argillaceous shales, whereas this relationship was comparatively weaker for other lithofacies weaker (R2=0.3). Moreover, the influence of inorganic minerals on porosity cannot be neglected in siliceous, mixed, and calcareous shales. The total clay content shows a positive trend with porosity for these lithofacies (if clay content is less than 45%).

However, no relationship was found between organic-rich and argillaceous shales (if clay content is >45%) (Figure 3.18b). This may be due to interparticle pores between clay and quartz or calcite in siliceous, mixed, and calcareous shales. In the case of argillaceous shales, the interparticle pores are filled with illite, reducing the porosity (Iqbal & Rezaee, 2020; Yuan et al., 2019). Two different relationships between brittle minerals (quartz, feldspar, and carbonates) and porosity are observed for Goldwyer-III shale so that the organic-rich and argillaceous shales with brittle minerals<45% show a direct relationship. Whereas, in siliceous, mixed and calcareous shales (if brittle minerals>45%), an inverse relationship is found (Figure 3.18c). This may be due to isolated intraparticle pores in siliceous, mixed, and calcareous shales, and interparticle pores between clay and the brittle minerals in organic-rich and argillaceous shales.

Furthermore, a positive correlation is shown between porosity and pore volumes (Figure 3.18d and e). However, the correlations of porosity with micropore and mesopore volumes for organic-rich and argillaceous shale (R2>0.7) are strong as compared to other lithofacies (R2 <0.2). This can be due to micropores associated with organic matter and clay minerals that increase porosity.

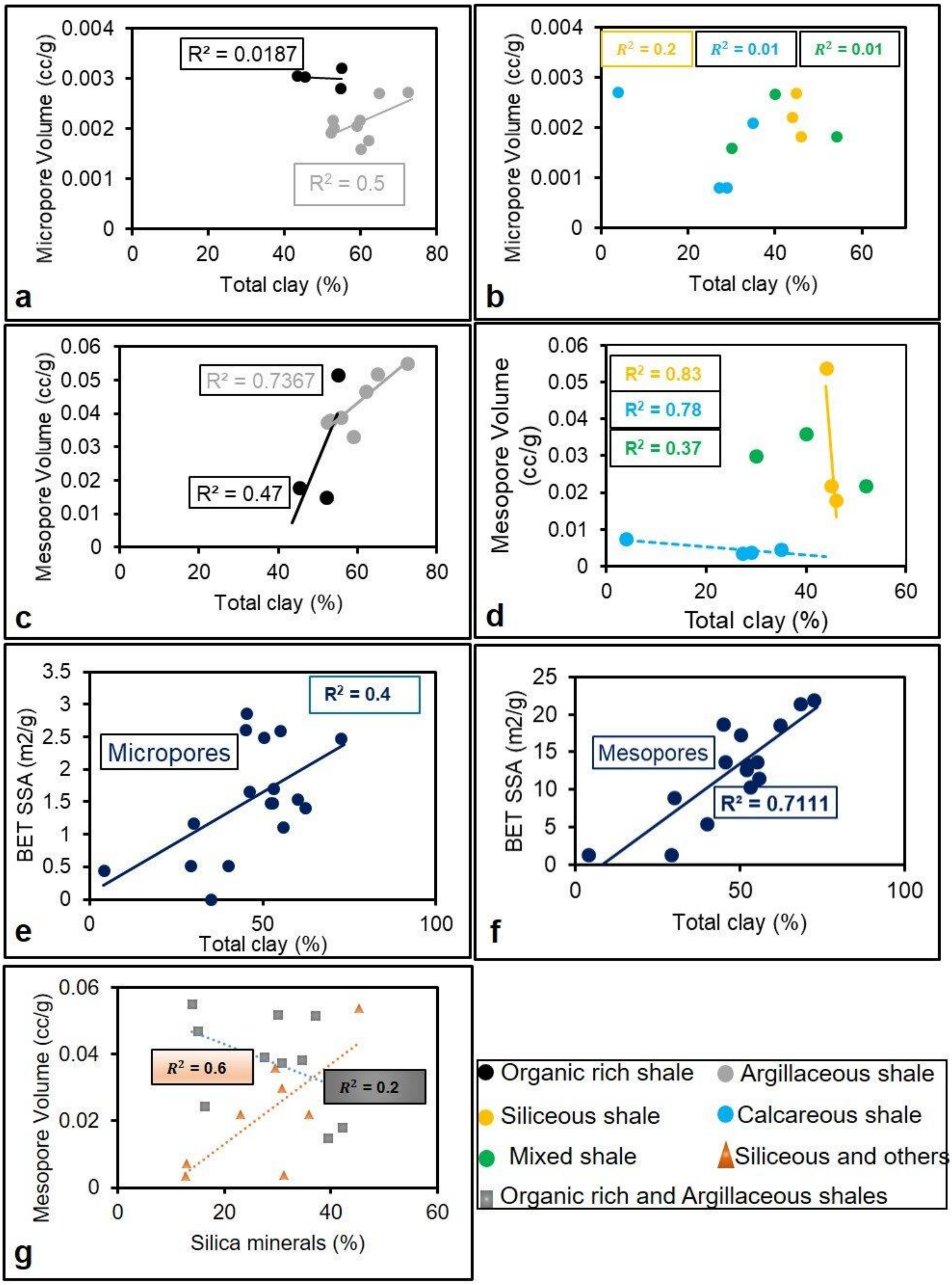

Figure 3.17: Relationships of total clay content with pore structure elements with respect to different lithofacies in Goldwyer-III shale.

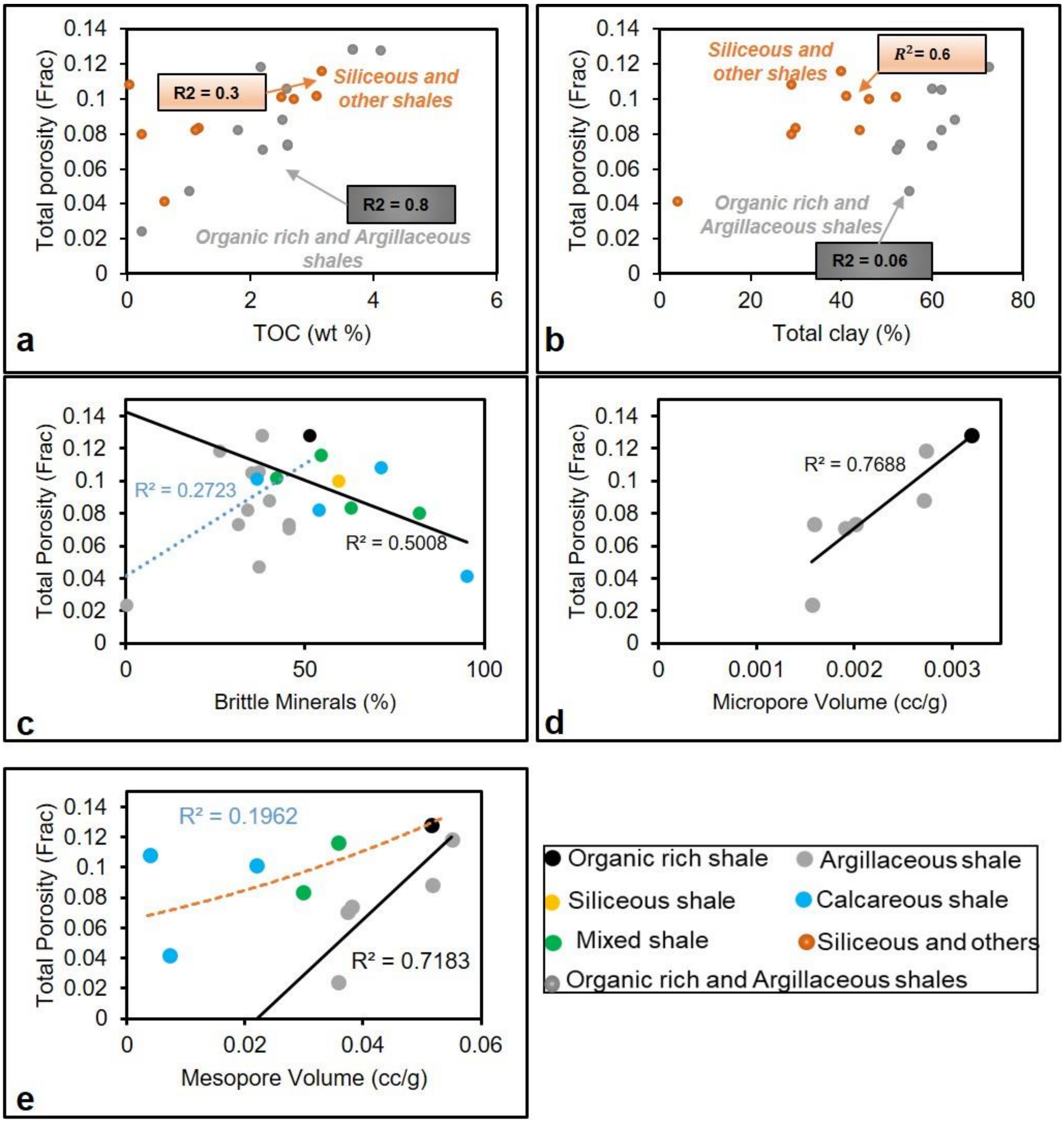

Figure 3.18: Relationship of total porosity with influencing factors with respect to different lithofacies in Goldwyer-III shale.

3.4.6 Implications for storage capacity of shale reservoir

The lower Goldwyer-III shale is divided into five lithofacies based on mineral composition and TOC (ranging from 0.05 to 4.11 wt %). Among all the lithofacies, the organic-rich, siliceous, and mixed shales have comparatively higher total porosity and micro and mesopore volumes (Figure 3.7 and Figure 3.19). Therefore, the free gas storage capacity of these lithofacies is probably higher than argillaceous and calcareous shales. Moreover, positive correlations have been reported between clay content, TOC content, and gas adsorption capacity of the marine shales (Chen et al., 2016; Yang et al., 2019; Zou & Rezaee, 2019). The organic-rich and few samples of siliceous and mixed shale lithofacies have higher TOC values (>3 wt %). Therefore, it can be suggested that these lithofacies are the most favourable in Goldwyer-III shale as higher pore volume is essential for fluid flow via the pore system when hydro-fractured.

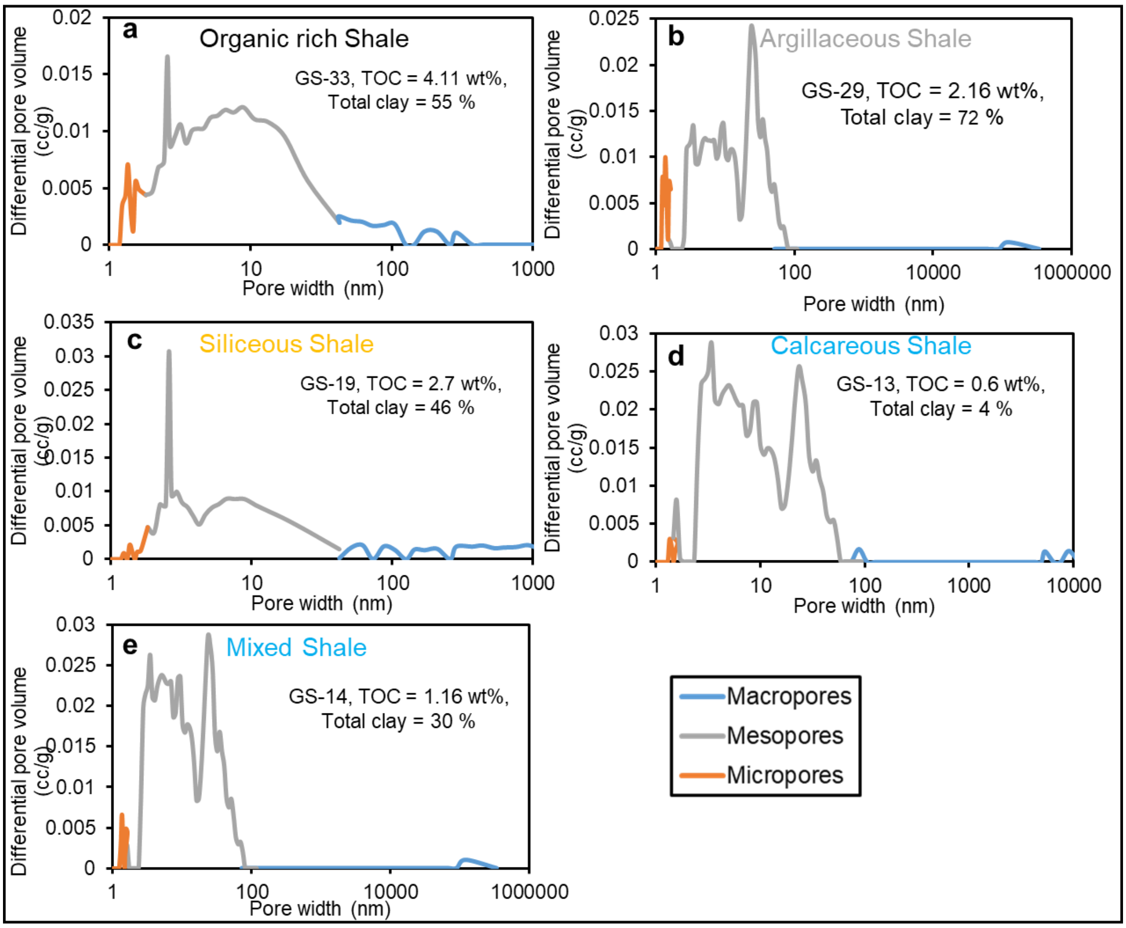

Figure 3.19: Pore aperture (micro, meso and macropores distributions) in different lithofacies of Goldwyer-III shale.

3.5 Conclusions

Based on the results of the multi-scale qualitative and quantitative characterisation of Ordovician Goldwyer-III shale deposited in a marine setting, the following conclusions are drawn:

i. The Goldwyer-III shale is divided into five different lithofacies, namely organic-rich shale, argillaceous shale, siliceous shale, calcareous shale and mixed shale, based on TOC content and mineral composition.

ii. The total porosity is controlled by lithofacies distribution so that organic-rich shale>siliceous shale>mixed shale>argillaceous shale>calcareous shale.
iii. The organic-rich shale mainly contains slit-shaped organic pores, whereas the argillaceous and siliceous shales are comprised of bottle-necked slit-shaped interparticle pores. The calcareous and mixed shales contain predominantly wedge-shaped or narrow slit-like intraparticle pores.
iv. Organic matter and interparticle pores are the main controlling factor for organic-rich and argillaceous shales' porosity. In contrast, the clay content (mostly illite) affected the porosity of other lithofacies.
v. The whole pore aperture description revealed that mesopores are the most abundant pores in the Goldwyer-III shale. The presence of micro and macro pores in the Goldwyer-III shale is subjected to the lithofacies type.
vi. The organic-rich, siliceous, and mixed shale lithofacies in Goldwyer-III shale are suggested to be more critical for fluid flow via pore systems.

Chapter 4 Porosity and Water Saturation Estimation for Shale Reservoirs

Summary

Porosity and water saturation are the most critical and fundamental parameters for the accurate estimation of gas content in shale reservoirs. However, their determination is challenging due to the direct influence of kerogen and clay content on the logging tools. The porosity and water saturation over or underestimate the reserves if the corrections for kerogen and clay content are not applied. Moreover, it is very difficult to determine the formation water resistivity (Rw) and Archie parameters for shale reservoirs. In this study, the current equations for porosity and water saturation are modified based on kerogen and clay content calibrations. The porosity in shale is composed of kerogen and matrix porosities. The kerogen response for the density porosity log is calibrated based on core-based derived kerogen volume. The kerogen porosity is computed by a mass-balance relation between the original total organic carbon (TOCo) and kerogen maturity derived by the percentage of convertible organic carbon (Cc) and the transformation ratio (TR). In contrast, the water saturation is determined by applying kerogen and shale volume corrections on the Rt. The modified Archie equation is derived to compute the water saturation of the shale reservoir. This equation is independent of Rw and Archie parameters. The introduced porosity and water saturation equations are successfully applied for the Ordovician Goldwyer formation shale from Canning Basin, Western Australia. The results indicate that based on the proposed equations, the total porosity ranges from 5 to 10%, and the water saturation ranges from 35 to 80%. Whereas the porosity and water saturation were overestimated by the conventional equations. The results were well-correlated with the core-based porosity and water saturation. Moreover, it is also revealed that the porosity and water saturation of Goldwyer Formation shale are subject to the specific rock type. Therefore, the introduced porosity and water saturation can be helpful for accurate reserve estimations for shale reservoirs.

4.1 Introduction

The organic-rich shale reservoirs have gained more attention in the last decades due to the depletion of conventional reservoirs (Jenner & Lamadrid, 2013; Rezaee, 2015). For reliable volumetric calculation of the reserve, the porosity and water saturation are the most critical parameters to estimate (Kadkhodaie & Rezaee, 2016; Ross & Marc Bustin, 2009; Walls & Sinclair, 2011; Yu et al., 2018). The shale reservoirs contain free and adsorbed gases. The free gas associates within the pore spaces, whereas the adsorbed gas is usually linked with the clay minerals and organic matter (Ambrose et al., 2012; Kadkhodaie & Rezaee, 2016; Kale et al., 2010; Rezaee, 2015; Sondergeld et al., 2010; Yu et al., 2017). However, the complex pore system and organic matter, together with inorganic mineral constituents, affect the well-logging tool responses needing to be considered during petrophysical evaluation. Previous studies demonstrate that the porosity can be overestimated by using empirical equations without applying kerogen corrections. Therefore, the conventional approaches for porosity estimation are not feasible for organic-rich shale reservoirs. Many authors selected petrophysical models based on wireline logs to generate a set of simultaneous equations to estimate the kerogen content, mineral volume, and pore volume (Arredondo-Ramírez et al., 2016; Q. Fu et al., 2015; Jacobi et al., 2009; Sondergeld et al., 2010). The introduced methods are most suitable for composition computation; however, it is hard to accurately determine all the required coefficients. Similarly, few authors standardised the well logs by multiplying the log data with defined coefficients to match the results with the core-derived porosity (Q. Fu et al., 2015). However, such equations were limited to a specific area and dataset due to the heterogeneity of shale in terms of thermal maturity, mineral composition, and organic matter content. Moreover, the organic-rich shales consist of organic as well as matrix porosities (Labani et al., 2013; Yu et al., 2017; Yu et al., 2018; Yuan et al., 2019; Yuan et al., 2018). In this study, the porosity for the shale reservoir is estimated by using a kerogen-corrected density log, and the kerogen porosity is calculated by using a mass balance method based on original total organic carbon (TOCo) and kerogen maturity. The core-based total organic carbon (TOC) and porosity were used to validate the results.

Similarly, the accurate estimation of water saturation also plays a key role in economic evaluations of shale reservoirs. However, the investigations of the water saturation determination methods did not get much attention in the literature. Already available water saturation equations, e.g., Archie and Simandoux work better for conventional reservoirs (e.g., sandstone and shaly sands) (Archie, 1942; Simandoux, 1963). However, the accurate determination of the unknown parameters, such as formation water resistivity (Rw), cementation exponent (m), and saturation exponent (n), is very challenging for shale reservoirs (Akbar et al., 2018; Bust et al., 2013; Kadkhodaie & Rezaee, 2016; Rezaee, 2015; Wang & Gale, 2009). The shale reservoir is a mixture of inorganic material (e.g., clays and detrital grains), kerogen, clay-bound water, free and capillary-held water, free and adsorbed gas (Kadkhodaie & Rezaee, 2016; Rezaee, 2015). However, the resistivity tool measures a reflection of constituent minerals and fluids of shales. Therefore, it is very critical to correct the resistivity log for shale and kerogen effects. In this research, a water saturation equation independent of water resistivity and Archie's parameters is introduced. Based on core-derived water saturation validation, this equation worked very well compared to other equations. However, it is always hard to take and interpret pressurised core samples from shale reservoirs. Therefore, sometimes it is impractical to measure water saturation through core samples in shale.

A case study from the organic-rich Ordivician Goldwyer Formation (Goldwyer-III shale unit), Canning Basin, Western Australia, is presented to verify both techniques for porosity and water saturation estimations. The Goldwyer Formation of Lower to Middle Ordovician age has an average thickness of almost 400 m, whereas it's thickest encounter (740 m) is recorded in Blackstone 1, a Lennard Shelf Sub-basin well. The Goldwyer-III shale is deposited in an open marine setting having thin laminations of quartz silt and carbonates bands with alternating black shale layers. The mineral composition of Goldwyer-III shale includes quartz, carbonates, clay minerals, and pyrite (Yuan et al., 2019). The illite is a more abundant clay mineral in this shale. The Goldwyer-III shale is thermally mature having kerogen types-II and III, and the total organic carbon content (TOC) varies from 0.35 to 4.5wt% (Johnson, 2019; Johnson et al., 2018). The results indicate a good match between core-based and corrected well logs-based estimations. Archie equation overestimated the water saturation; however, the proposed modified equation provided us with better results.

4.2 Methods and Techniques

As illustrated in the simple shale reservoirs petrophysical model (Figure 4.1), the organic-rich shales are composed of kerogen and non-kerogen parts. A systematic workflow is developed to estimate the porosity and water saturations by considering the organic matter and matrix of the shale.

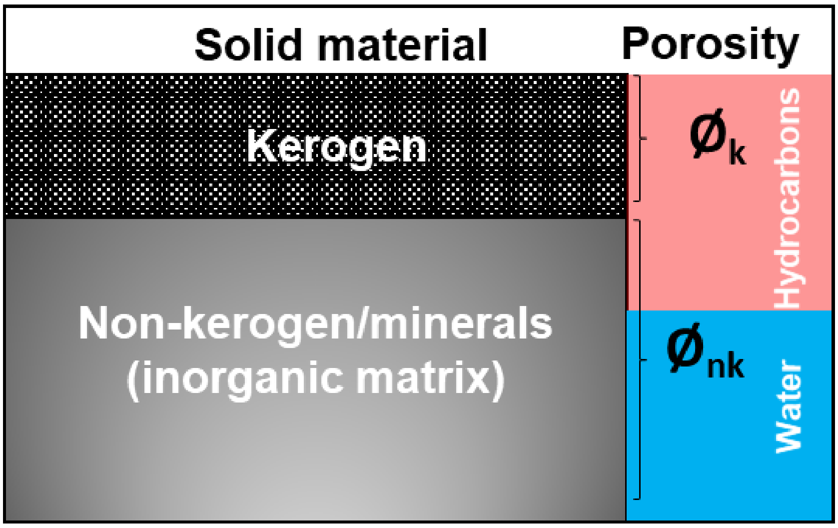

Figure 4.1: A typical conceptual petrophysical model for shale reservoirs showing kerogen porosity $Ø_k$ and non-kerogen $Ø_{nk}$ (inorganic matrix) porosity, modified from (Yu et al., 2018).

4.3 Porosity estimation

The conventional density-based porosity equation is described in Eq. 4.1:

$$ØD = \frac{\rho_{ma} - \rho_b}{\rho_{ma} - \rho_f} \qquad \text{(Eq. 4.1)}$$

Where $ØD$ = density porosity (%), ρ_{ma} = matrix density (g/cc), ρ_b = bulk density (g/cc), ρ_f = fluid density (g/cc). Unlike in conventional reservoirs (sandstone or limestone), the bulk density acquired through density log in organic-rich shale usually overestimates the porosity. Therefore, the kerogen correction is applied to avoid porosity overestimation. The kerogen volume is determined by using Eq. 4.2 (Tissot & Welte, 1984):

$$V_k = \frac{\gamma * TOC * \rho_b}{100 * \rho_k} \quad \text{(Eq. 4.2)}$$

where, V_k is the kerogen volume in fractions; TOC is total organic carbon content (wt%); ρ_b is the bulk density from the density log (g/cc); $^{\gamma}$ is the kerogen conversion factor; and ρ_k is the kerogen density (g/cc). TOC is determined by the rock eval pyrolysis method on powdered shale samples, and the continuous TOC for the whole interval is estimated by the Passey method (Passey et al., 1990); $^{\gamma}$ is proposed by (Tissot & Welte, 1984), and the selected values are shown in Table 4.1.

Table 4.1: Conversion factors for TOC to kerogen, adapted from Tissot and Welt (Tissot & Welte, 1984).

Stage	Type of Kerogen		
	I	II	III
Diagenesis	1.25	1.34	1.48
End of Catagenesis	1.20	1.19	1.18

Based on rock eval pyrolysis results for this study, the kerogen types are 30% type-II and 70% type-III. Therefore, the kerogen conversion factor for the studied formation is calculated as 1.18; and ρ_k is determined by the relationship of lab-based TOC and the reciprocal of lab-based derived grain density on shale samples by (Eq. 4.3). A good relationship between TOC and the reciprocal of grain density (ρ_g read as RHOG) is observed in Figure 2. Eq. 4.3 is derived based on the relationship between TOC and the reciprocal of grain density (Figure 4.2).

$$\frac{1}{\rho_g} = A \times TOC + B \quad \text{(Eq. 4.3)}$$

ρ_g is the matrix density if TOC is zero and ρg_k is kerogen density if TOC is 100%. A and B are based on the linear relationship seen in Figure 4.2. From the relation found in Figure 4.2, the matrix density for the samples of this study is 2.79 g/cc, and kerogen density is 1.24 g/cc. The well logs are calibrated by eliminating the kerogen effect, and the following equations Eq. 4.4 and 4.5 are applied for matrix porosity estimation through density log:

$$\rho_{bk_c} = \frac{\rho_b - \rho_{k \times V_k}}{1 - V_k} \quad \text{(Eq. 4.4)}$$

$$Økc = \frac{\rho_{ma} - \rho_{bk}}{\rho_{ma} - \rho_f} \quad \text{(Eq. 4.5)}$$

Where, ρ_{bk_c} is kerogen-corrected bulk density (g/cc); ρ_k is kerogen density (g/cc); V_k is kerogen volume (fractions), and $Økc$ is kerogen-corrected density porosity (%). As the porosity in organic-rich shale is associated with organic matter and inorganic minerals, it is crucial to estimate the porosity within organic matter (kerogen). An equation for kerogen porosity was proposed by (Peters et al., 2005) using the mass-balance relation Eq. 4.6.

$$Ø_k = ([TOC_o * C_c] * ^{\gamma})TR\frac{\rho_b}{\rho_{\ k}} \quad \text{(Eq. 4.6)}$$

where, $Øk$ = kerogen porosity (%), TOCo = original total organic carbon, Cc = convertible carbon fraction and TR = transformation ratio.

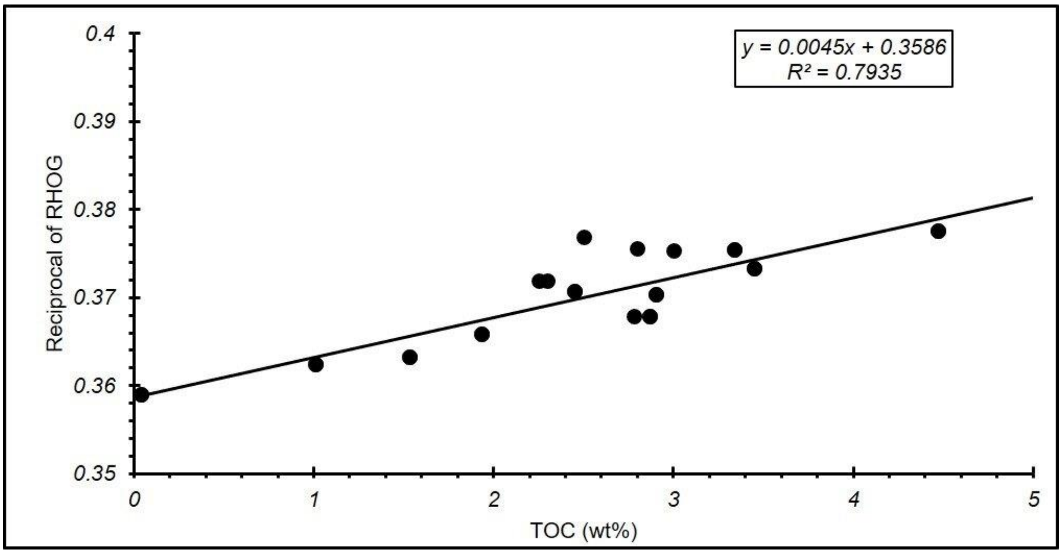

Figure 4.2: The direct relationship between core-based derived total organic carbon and reciprocal of grain density provides helpful information for the estimation of kerogen and matrix densities.

$$TOC_o = \frac{TOC}{1 - TR \times C_c} \quad \text{(Eq. 4.7)}$$

$$TR = 1 - \frac{HI_p[1200 - HI_o(1 - PI_o)]}{HI_o[1200 - HI_p(1 - PI_p)]} \quad \text{(Eq. 4.8)}$$

Where: HIp = present hydrogen index (mg/g), HIo = original hydrogen index (mg/g), PIp = present production index and PIo = original production index. The following equations

(Eq. 4.9) were used to estimate the original hydrogen index and present hydrogen index proposed by Peters et al., 2005:

$$HI_o = \frac{TypeII}{100} \times 450 + \frac{TypeIII}{100} \times 125 \qquad \text{(Eq. 4.9)}$$

For this study:

$$HI_o = 225mg/g$$

$$HI_p = 170mg/g$$

$$S1/S1+S2 \quad = PI_p = 0.35$$

The convertible carbon fraction is determined by using the relationship proposed by Kilgore et al., 1972 such as $C_c = 0.085 \times HI_o$=18.91%. Although, the transformation ratio (TR) can be determined by Claypool equation, as explained in Eq. 4.8 (Peters et al., 2005). However, for this study, the TR value is taken as 88% which is adapted from (Johnson, 2019; L. M. Johnson et al., 2020) based on organic geochemistry and basin modelling of Goldwyer-III shale. So, the equation for kerogen porosity will be as Eq. 4.10. By eliminating the kerogen effect and adding the kerogen porosity Eq. 4.11, the final Eq. 4.12 is applied to compute total density porosity for shale reservoirs.

$$\O_k = 0.2 \times TOC * \rho_b \qquad \text{(Eq. 4.10)}$$

$$\O D_{Total} = \left[\left(\frac{\rho_{ma} - \rho_{bk_c}}{\rho_{ma} - \rho_f}\right) + \O_k\right] \qquad \text{(Eq. 4.11)}$$

$$\O D_{Total} = \left[\left(\frac{\rho_{ma} - (\frac{\rho_b - \rho_{k \times V_k}}{1 - V_k})}{\rho_{ma} - \rho_f}\right) + (0.2 \times TOC * \rho_b)\right] \qquad \text{(Eq. 4.12)}$$

4.3.1 Calculation of water saturation

The water saturation estimation in shale is mainly dependent on its organic (kerogen) and inorganic components (minerals). Archie equation (Archie, 1942) is mainly famous for water saturation calculation in clean reservoirs. The equation was developed based on a function between formation conductivity and the conductivity of fluids in the pore spaces of a reservoir, such as Eq. 4.13:

$$C_t = \frac{S_w^n \times C_w}{F} \qquad \text{(Eq. 4.13)}$$

Where C_t = total conductivity (ohm-1-m-1), C_w = formation water conductivity (ohm-1-m-1), n = saturation exponent usually equals to 2, S_w = water saturation %). The equation can be written in terms of resistivity as follows in Eq. 4.14:

$$\frac{1}{R_t} = \frac{\text{Ø}^m . S_w^n}{a. R_w} \qquad \text{(Eq. 4.14)}$$

Where R_t = true resistivity measured by logging tool (ohm-m), Ø = porosity (%), m = cementation exponent, n = saturation exponent usually equals to 2, a = tortuosity factor usually considered as 1 and R_w = formation water resistivity (ohm-m). Eq. 4.14 is known as the Archie equation for clean formations. Later, this equation did not provide acceptable and accurate results for the shaly formations. Therefore, other approaches, such as Simandoux considered the shale effect on water saturation and developed an equation Eq. 4.15 by considering the volume of shale in the equation that was further modified by Schlumberger, 1972 and the modified Simandoux equation (Eq. 4.15) is (Simandoux, 1963):

$$\frac{1}{R_t} = \frac{\text{Ø}^m . S_w^n}{a. R_w . (1 - V_{sh})} + \frac{V_{sh} . S_w}{R_{sh}} \qquad \text{(Eq. 4.15)}$$

Where R_{sh} is the resistivity of shale (ohm-m) and V_{sh} is the volume of shale (fraction).

The conventional water saturation models, e.g. Simandoux equation, modified Simandoux, total shale, and modified total shale equations, provided better results for shaly formations as these equations are derived based on the conductivities of clays and non-clay matrix. However, these models overestimate the water saturation for organic-rich shales. Therefore, a modified water saturation equation is applied in this study. An equation was proposed by (Kadkhodaie & Rezaee, 2016; Rezaee, 2015) for water saturation calculation for shale reservoirs. The derivation details of the equation are explained by (Archie, 1942) simplified equation for water saturation (Eq. 4.16):

$$S_w = \sqrt{\frac{R_o}{R_t}} \qquad \text{(Eq. 4.16)}$$

where, R_o is the rock resistivity in lean shale interval where water saturation is deemed 100% (ohm-m) and R_t is the rock resistivity in the organic-rich shale reservoir with some degree of oil/gas saturation. Therefore, Ro and Rt are the key parameters for water saturation calculations.

As the organic-rich shale reservoirs have a higher content of total clay and organic matter, it is necessary to conduct corrections (total organic carbon and total clay) for the true formation resistivity (Rt). The clay minerals decrease the formation resistivity, and the kerogen increases the resistivity. So, the TOC and shale corrections are used for Rt. First, the correlation is developed between the true resistivity log and TOC measurements (on powdered shale samples through rock eval pyrolysis) Eq. 4.17, Figure 4.3).

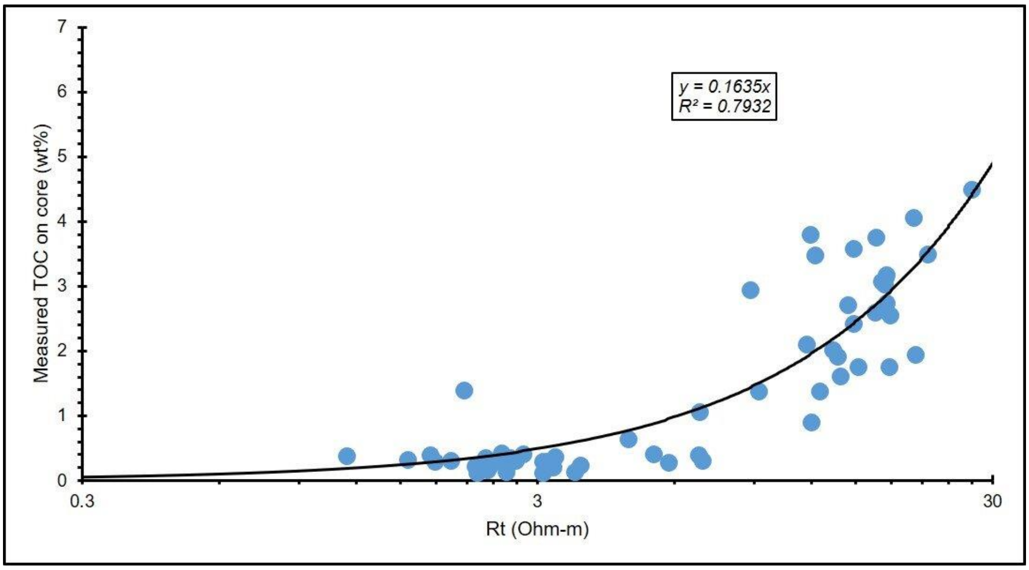

Figure 4.3: Direct relationship between true resistivity and measured total organic carbon showing the influence of organic matter on resistivity tool.

A negative correlation Eq. 4.18 is found between laboratory-based water saturation measured on shale samples and rock eval pyrolysis-based TOC. This relationship shows that with the increase in TOC, the water saturation reduces, indicating hydrocarbon saturation in the shale interval (Figure 4.4).

$$TOC = 0.1635 \times R_t \qquad \text{(Eq. 4.17)}$$

$$Sw_{core} = -0.0981 * TOC_{core} + 0.825 \qquad \text{(Eq. 4.18)}$$

The true resistivity is corrected in terms of subtracting a factor A (Eq. 4.19) due to TOC that can be evaluated by deciding, such as:

$$A = V_k^2 * R_k \qquad \text{(Eq. 4.19)}$$

If TOC is 100% then Rt will be considered as kerogen resistivity Rk (based on Eq. 4.17) so for this study based on Figure 4.3 R_k = 613 ohm-m and Figure 4.5 Rsh = 1.97 ohm-m are used.

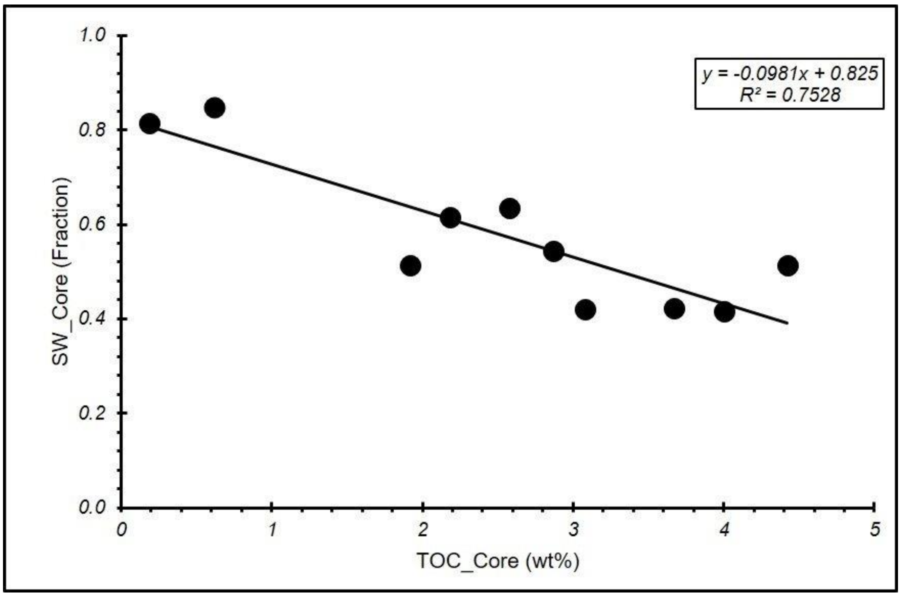

Figure 4.4: An inverse relationship between core-based total organic carbon and water saturation showing the fact that the organic matter increases gas saturation.

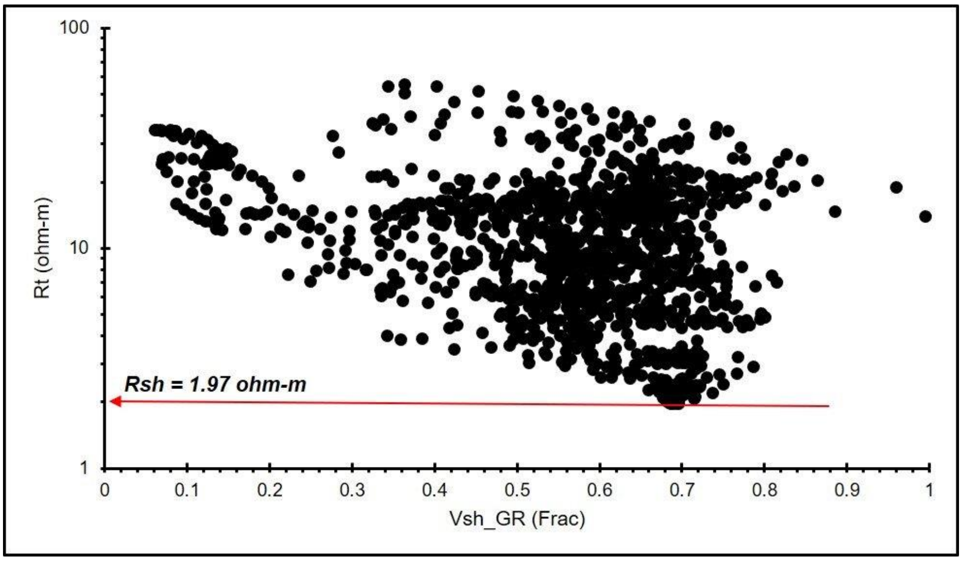

Figure 4.5: The shale resistivity estimation based on shale volume and true resistivity relationship.

Based on the correlation, the TOC_{max} is found as 4.91 wt%. Another factor B (Eq. 4.20) because of clay minerals effect on resistivity is defined by many authors (Clavier et al., 1984; Leveaux & Poupon, 1971; Simandoux, 1963), such as:

$$B = V_{sh}^{2}.R_o \quad \text{(Eq. 4.20)}$$

The squared form of the shale volume will be more convincing in the calculation of reduced resistivity because of the shale volume. It can be due to the nonlinear relationship between Ro and Rw in shales (Leveaux & Poupon, 1971; Simandoux, 1963). For this study, the Ro is taken as 1.97 ohm-m (Figure 4.5). By compensating the shale and organic matter effects on the true resistivity, the modified equation is introduced as (Eq. 4.21):

$$S_w = \sqrt{\frac{R_o}{R_t - (V_{kr}^2 * R_k) + (V_{sh}^2 * R_{sh})}} \quad \text{(Eq. 4.21)}$$

4.4 Results and Discussion

In this section, the applications of proposed porosity and water saturation equations are implemented for the Ordovician Goldwyer-III shale formation drilled in Theia-1, Pictor East-1, and Canopus-1 wells in Canning Basin, Western Australia. The kerogen-corrected total porosity (matrix porosity plus kerogen porosity) was estimated by using Eq. 4.12. The total porosity on crushed shale samples (core porosity) ranges from 2 to 13%, measured through the difference between the bulk volume of shale samples and the grain volume of the crushed, cleaned, and dried samples. The Goldwyer-III shale porosity shows the same range of porosity as most of the organic-rich shales (Chalmers et al., 2012; Mastalerz et al., 2013; Sondergeld et al., 2010; Wei et al., 2016; Wu et al., 2017; Yu et al., 2018; Yuan et al., 2019). The Goldwyer-III shale consists of three types of pores such as organic pores, interparticle and intraparticle pores as shown in Figure 4.6. The results show that the conventional porosity estimation through density log overestimates the porosity which may affect the accurate reserve estimation in shale. Such as the porosity based on Eq. 4.1 provided the porosity range from 8 to 15% for Goldwyer-III shale (Figure 4.7). However, after applying the kerogen corrections, the corrected porosity ranging from 5 to 10% gives more accurate results that can be well-compared with core porosity (Table 2.2 and Figure 4.7). Moreover, the clay minerals also affect shale's pore structure, directly affecting the water saturation. The Goldwyer-III shale also consists of interparticle pores influenced by illite that may change the water saturation (Figure 4.6). The core-derived TOC varies from 0.35 to 4.5wt% in this study. The log-derived TOC matches well with core-based TOC, and the equivalent kerogen volume also validates the results (Figure 4.7). It can also be observed in Table 4.2 and Figure 4.7 that the clusters (e.g., siliceous and argillaceous shales) with higher TOC value have higher porosity (about 8-10%) due to the addition of organic pores (kerogen porosity) in the matrix porosity.

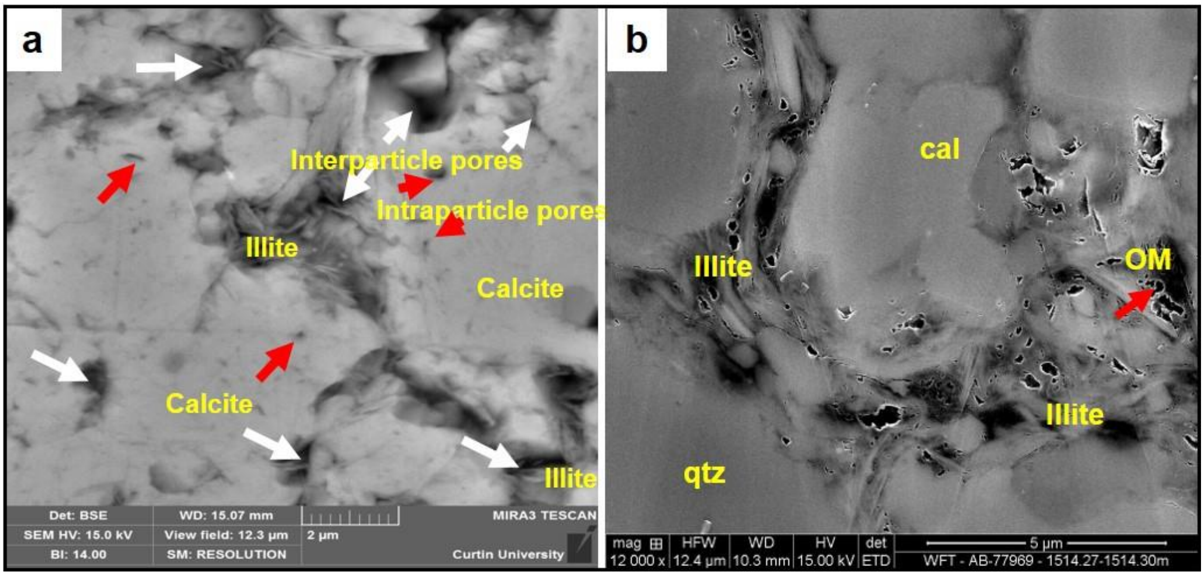

Figure 4.6: Different pore types observed in Goldwyer-III shale based on scanning electron microscope images, such as a) interparticle pores indicated by white arrows and intraparticle pores indicated by red arrows; b) organic matter pores (OM), mineral components include calcite (cal), quartz (qtz) and illite.

The water saturation was estimated by Eq. 4.21 by considering the kerogen and shale effects on the resistivity. The required kerogen volume and kerogen resistivity were computed by using the dataset (well logs) and core information from three wells (Theia-1, Pictor East-1, and Canopus-1) drilled in Canning Basin. The results for Theia-1 well are illustrated in Figure 4.7. Similarly, the shale resistivity was taken based on the dataset for these three wells. It can be observed in Figure 4.7 that with the increase in shale volume (e.g., at depth 1546.5 m), the deep resistivity is decreased that enhancing the water saturation. In conventional reservoirs, shale resistivity is usually determined from the averaged deep resistivity log reading against shale interval having higher gamma-ray log reading. However, in shale reservoirs, the shale resistivity is obtained from the average reading of the deep resistivity log against an organic lean interval. In this study, the shale resistivity in the organic lean interval is determined as 1.97 ohm-m based on the relationship between shale volume and true resistivity developed by this study (Figure 4.5). It is impractical to determine the fluid-water contact in heterogeneous shale reservoirs; therefore, an organic lean shale is treated to be fully brine saturated rock, Sw = 1 (Kadkhodaie & Rezaee, 2016).

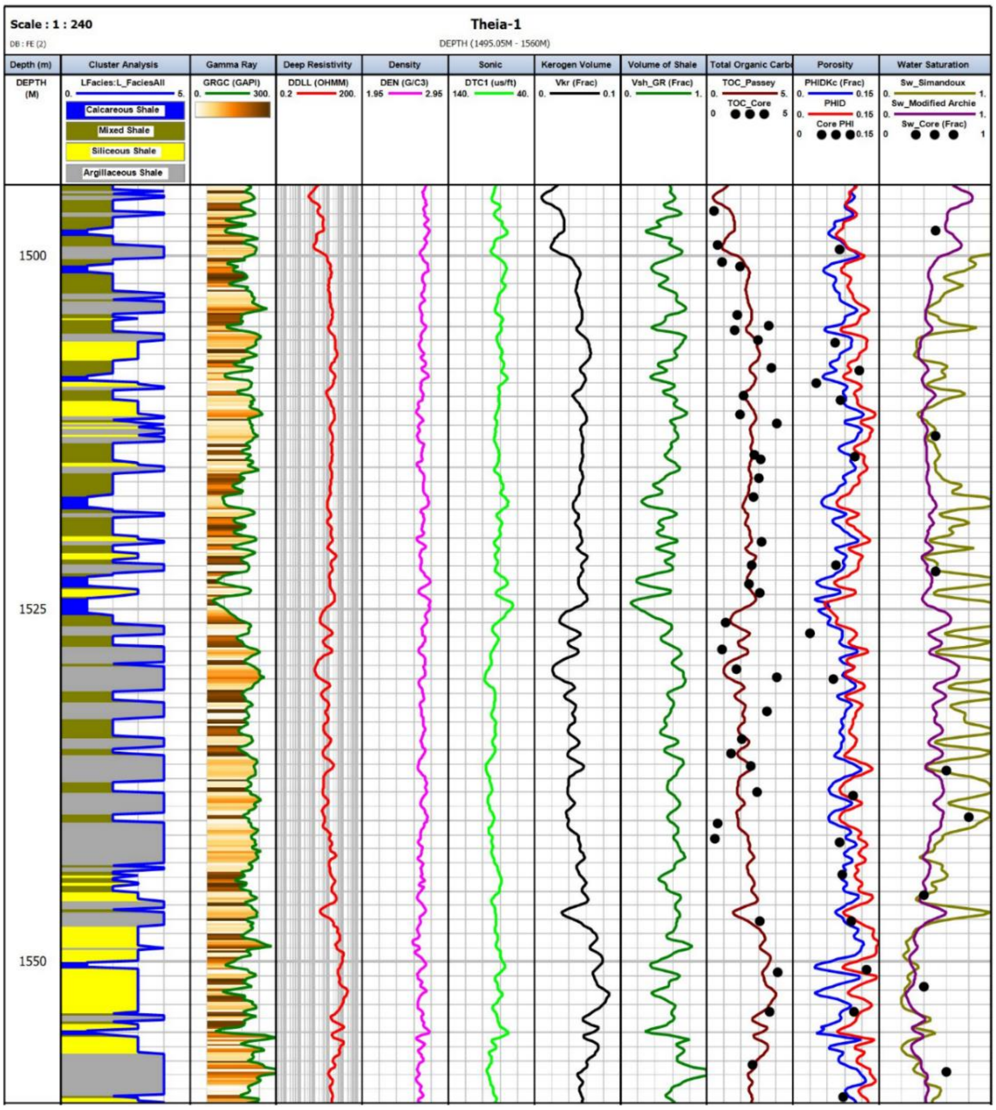

Figure 4.7: Petrophysical evaluation of Goldwyer-III shale providing an accurate estimation of porosity and water saturation through proposed equations as validated by core-based measurements. Track-1: Depth in meters; Track-2: Cluster analysis to identify cluster based facies; Track-3: Gamma ray log; Track-4: Deep resistivity log; Track-5: Density log; Track-4: Sonic (DT) log; Track-4: Kerogen volume; Track-4: Shale volume based on Gamma ray log; Track-4: TOC based on Passey's method and core measurements; Track-4: Kerogen corrected total density porosity (PHIDKc) based on the proposed equation in this study, density based porosity (PHID) & Total porosity based on core samples; Track-4: Water saturation (Sw) based on Simandoux equation (overestimated) and modified Archie's equation (by this study) and core derived Sw.

In the same way, the zones with higher TOC value and kerogen volume (such as organic-rich siliceous shale – cluster 3 (siliceous shale) at depth 1550 m) have the lowest water saturation. The inverse relationship between core-based TOC and Sw is also confirmed in this study (Figure 4.4). So, the kerogen resistivity (R_{kr} = 613 ohm-m) is determined by Eq. 4.17 by putting the TOC value as 100%. Therefore, the modified Archie equation applied in this study provides much better results (well correlated with core-derived S_w) than the Simandoux equation (Table 4.2 and Figure 4.7). It can be observed that the Simandoux method overestimated water saturation as it is impossible to have more than 100% Sw. Another key factor of this overestimation is the inaccurate determination of water resistivity and cementation exponent (m) values. Therefore, the modified Archie equation applied in this study is simple and accurate, subject to the resistivity corrections for shale and kerogen.

Table 4.2: Comparison of averaged total porosity and water saturation determined by conventional equations (PHID and Sw_Simandoux) and introduced by this study (PHIDKc and Sw_modified Archie). The conventional equations overestimated the porosity and water saturation in shale.

Cluster	Lithofacies	TOC (wt. %)	PHIDKc %	Sw_Modified Archie %	PHID %	Sw_Simandoux %
Cluster-1 (Blue)	Calcareous shale	0.7	5	55	6	90
Cluster-2 (Olive)	Mixed shale	1.4	8.5	45	10	80
Cluster-3 (Yellow)	Siliceous shale	2.5	8	35	12	45
Cluster-4 (Grey)	Argillaceous shale	3.5	9	80	13	>100

4.5 Conclusions

In this research, effective equations for two critical petrophysical parameters of shale reservoirs (total porosity and water saturation) have been introduced. These equations are compensated based on kerogen effects for density logs to estimate more accurate total porosity. Similarly, the resistivity log was corrected based on kerogen and shale effects to compute the accurate water saturation for shale reservoirs. This study shows that the density log overestimates the total porosity (8-15%). Whereas the total porosity based on kerogen-corrected density log and kerogen porosity matches perfectly with the core-based porosity having porosity ranging from 5 to 10%. In the same way, the Simandoux equation overestimated the water saturation with more than 100% Sw in most of the intervals. However, the proposed water saturation equation (modified Archie's equation) provided better results, and the correlation with core-based water saturation ranged from 35 to 80%. Moreover, the introduced modified Archie equation is independent of water resistivity, and Archie parameters as these inputs are very difficult to obtain for shale reservoirs. Finally, this study revealed that cluster-2 (mixed shale lithofacies) and cluster-3 (siliceous shale lithofacies) have more gas shale potential in Goldwyer-III shale. This study has proposed a step-to-step workflow for accurate estimation of porosity and water saturation based on well logs for organic-rich shale. This workflow will be helpful for accurate reserve estimations in the shale reservoirs.

Chapter 5 3-D Petrophysical and Geomechanical Modelling for Prospectivity Evaluation of Shale

Summary

The identification and evaluation of suitable beds for gas shale reservoirs are essential at a local and regional scale to make the right decisions for its development. This chapter presents a systematic workflow for petrophysical and geomechanical modelling of Goldwyer-III shale. Supervised machine learning was applied for the prediction of unavailable petrophysical logs, which helped to compute the continuous profile of petrophysical and geomechanical properties. Unsupervised machine learning was applied to classify the clusters equivalent to lithofacies which were used for 3-D facies modelling. After computing the petrophysical and geomechanical properties, the 3-D model was generated based on the available dataset for the study area. The mechanical stratigraphy helped to identify the producible and brittle layers in Goldwyer-III shale. This integrated approach provided insights into the potential and successful development of Goldwyer-III shale as a gas shale reservoir.

5.1 Introduction

The identification of suitable beds for shale reservoir development and their integration with the reservoir properties of shales is important because only specific beds are producible and suitable for hydraulic fracturing (Kale et al., 2010). Moreover, the understanding of such beds is important for gas shale reservoirs development at local to regional scale. Previous studies have highlighted different approaches and challenges for developing the workflow for rock typing of gas shale reservoirs (Bust et al., 2013; Gupta, 2017; Gupta et al., 2017; Kale et al., 2010; Passey et al., 2010). However, minimal research has been conducted for their evaluation by integrating lithofacies with petrophysical and geomechanical properties at the core to regional scale. It is especially important to link the production potential of shale reservoirs with geomechanics to design a successful hydraulic fracturing scheme.

Mechanical stratigraphy can be defined by measuring the geomechanical properties (e.g. Young's modulus, Poisson's ratio, compressive strength, brittleness index and internal friction coefficient) (Charsky et al., 2017; M. Iqbal et al., 2021). There are significant benefits when it is possible to link lithofacies with mechanical stratigraphy in gas shale reservoirs in order to delineate the best hydraulic fracture zones in the vertical and horizontal directions and to optimise the landing zones. This approach can be compared to identifying the best flow zones in conventional reservoirs. The results given here also provide the opportunity to evaluate the gas shale reservoir potential for the Goldwyer Formation by integrating the geological, petrophysical, and geomechanical properties.

This chapter is focused on Goldwyer-III shale, which has the best potential as a gas shale reservoir in the Theia-1 area (van Hattum et al., 2019). The TOC of Goldwyer-III shale ranges from 0.15 to 4.5 wt%, and illite is the dominant clay mineral (Delle Piane et al., 2015; M. Iqbal et al., 2021; Iqbal et al., 2022). The dataset for this part of the study included detailed core samples, logs, and laboratory analyses from Theia-1 well, augmented by petrophysical logs from 14 nearby wells. Supervised machine learning was applied to predict the missing logs and thereby generate synthetic logs. The unsupervised machine learning (K-means clustering) was applied for the classification of geomechanically suitable zones. The recognised mechanical stratigraphic layers were then combined with core-based lithofacies to analyse producible and brittle layers to improve the development planning of gas shale reservoirs. The petrophysical properties such as porosity, water saturation and adsorbed gas were estimated with calibration of laboratory-based core measurement and wireline logs according to the equations proposed by (Iqbal & Rezaee, 2020; Zou & Rezaee, 2019).

The current workflow is divided into two sections (i) deriving mechanical and reservoir properties by combining laboratory results with the well logs (ii) deriving mechanical stratigraphy by clustering, and a combination of petrophysics with rock mechanical data. The input dataset includes composite wireline logs, geochemical information, mineral composition, petrography, and triaxial deformation data. The four-fold classification of the lithofacies from the Goldwyer-III beds was covered in Chapter 2 and in (M. A. Iqbal et al., 2021). The geo-mechanical properties such as static Young's modulus (Esta), Poisson's ratio (νsta), compressive strength (σTCS), deformation (BIE) brittleness, static anisotropy of Young's modulus and internal friction coefficient (μi) were calculated based on equations for Goldwyer-III shale proposed by (Mandal, 2021; Mandal et al., 2020). The 3D regional models of facies, petrophysical and geomechanical properties were made in Petrel software. This multiscale approach helped to identify the suitable layers for gas shale reservoir development and their spatial distribution.

5.2 Methods

5.2.1 Sample selection and characterisation

A total of 45 shale samples were selected at a regular intervals from the Goldwyer-III shales drilled in Theia-1 for this study. The samples included sufficient core plugs and cuttings for the respective analytical experiments. Representative samples were taken to cover the different mineral compositions and total organic carbon (TOC) contents for analysis by scanning electron microscope. Detailed descriptions of the porosity and pore structure measurements by helium pycnometer, low-pressure gas adsorption (N_2 and CO_2) tests, mineral compositions, and morphology are explained in Chapters 2 and 3. The results of these analyses will be used here.

5.2.2 Petrophysical properties

The important petrophysical properties that need to be estimated and modelled here for the gas shale reservoirs are TOC, total porosity, water saturation, and adsorbed gas contents. These properties were obtained from laboratory experiments on representative samples using core plugs. The TOC was estimated from the Rock-Eval pyrolysis. The total porosity was estimated from grain and bulk densities. The adsorbed gas was estimated from the methane adsorption isotherms, which were measured at three different temperatures using the method (Ekundayo et al., 2021). The experimental results on representative samples were used to produce empirical relationships with the logs and obtain continuous petrophysical property profiles for the modelling.

The continuous profile of TOC was obtained by using Passey's method (Passey et al., 1990) through well logs which was calibrated with laboratory-based TOC. The total porosity was estimated by applying the kerogen and clay content corrected modified equation (Eq. 4.12) based on the density log proposed by (Iqbal & Rezaee, 2020). The detailed workflow for deriving these equations is explained in Chapter 4. The adsorbed gas was computed for the well logs based on the empirical equations calibrated to the core (Eq. 5.1 and Eq. 5.2) for Langmuir volume (V_L) and Langmuir pressure (P_L) the Goldwyer-III shale proposed by (Zou & Rezaee, 2019) and (Ekundayo et al., 2021). Then the adsorbed gas volume (V_{ads}) was estimated by using the equation (Eq 5.3) proposed by (Chalmers & Bustin, 2007).

$$V_L(T)=(13.87*\text{TOC}+0.79V_{sh}-4)-(\text{T}-T_o)(0.35*\text{TOC}-0.05) \quad \text{(Eq. 5.1)}$$

$$P_L=0.8237*V_L(T)+2.22 \quad \text{(Eq. 5.2)}$$

Then the adsorbed gas volume (Vads) was estimated by using the equation (Eq 5.3) proposed by (Chalmers & Bustin, 2007).

$$V_{ads}=\frac{V_L P}{P+P_L} \quad \text{(Eq. 5.3)}$$

5.2.3 Geomechanical properties

Geomechanical properties are used to help design hydraulic fracture simulations for unconventional reservoirs, including compressive strength, Young's modulus, Poisson's ration and brittleness index. The laboratory-based geomechanical and elastic datasets for these parameters were used to calibrate the well logs. The static-dynamic conversion equations given by (Mandal, 2021; Mandal et al., 2020) for Goldwyer-III shale were used in this study to get the continuous profiles of static Young's modulus and Poisson's ratio from their dynamic counterparts. Empirical equations developed from the comprehensive geomechanical characterisation of Goldwyer-III shale (Mandal, 2021) were as follows.

.

$$\sigma_{TCS} = 4.13 \ x \ E_v + 82.07 \quad \text{(Eq. 5.4)}$$

$$\mu_i = 1.62 \ x \ \rho_b - 3.58 \quad \text{(Eq. 5.5)}$$

$$BI_E = 0.29 \ x \ {E_{sta}}^{0.30} \quad \text{(Eq. 5.6)}$$

$\frac{E_h}{E_v} = 8.226 \ x \ E_v{}^{-0.508}$ (Eq. 5.7)

where ρ_b, is bulk density (ranges from 2.3 to 3 g/cc);

BI_E is the brittle index and ranges from 0 (ductile) to 1 (brittle);

E_h, E_v are static horizontal and vertical Young's modulus (GPa) respectively.

These empirical formulas achieved R^2 values of 92%, 64%, 79% and 56% respectively (Mandal, 2021).

5.2.4 Supervised Machine Learning

Supervised Machine Learning uses labelled data to predict the accuracy of a model. This method was used here as part of a systematic workflow to predict and generate the synthetic logs in wells where they were absent, so those wells could be used for subsequent petrophysical analysis and clustering. The workflow consists of three main steps: data preparation, model selection, and prediction of missing logs, including the neutron porosity NPHI and density RHOB as shown in Figure 5.1 and described in detail in the following sections.

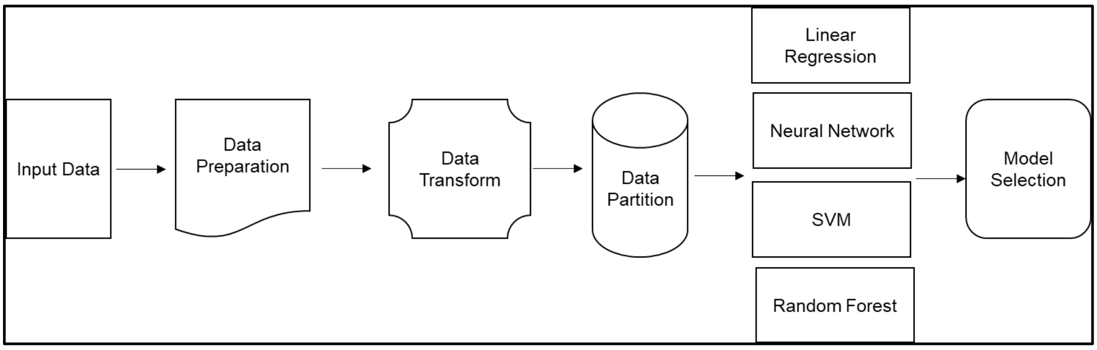

Figure 5.1: Systematic workflow designed for synthetic log generation.

5.2.4.1 Data availability

The Goldwyer-III shale has been drilled in a limited number of wells in the Canning Basin. The location of wells for which logs are available are shown in Figure 1.1, most occurring on the Broome Platform with one well on the Crossland Platform. Fourteen wells were selected for this study, providing a good spatial distribution (Table 5.1). The sonic log was missing from one well and so was predicted using the well-established Gardner's equation (Gardner et al., 1974):

$V_p = 108\rho^4$ (Eq. 5.8)

$DT = \frac{V_p}{304800}$ (Eq. 5.9)

where, Vp is primary wave velocity in m/s and DT is sonic log in μs/ft.

The density and neutron porosity logs were missing from three wells, so a supervised machine learning regression workflow was followed to generate the missing logs in those wells (Mclarty-1, Edgar Range-1, and Matches Spring-1). The input dataset contained the Gamma-ray (GR), deep resistivity (LLD), and sonic (DT) logs, and the workflow is given in Figure 5.2.

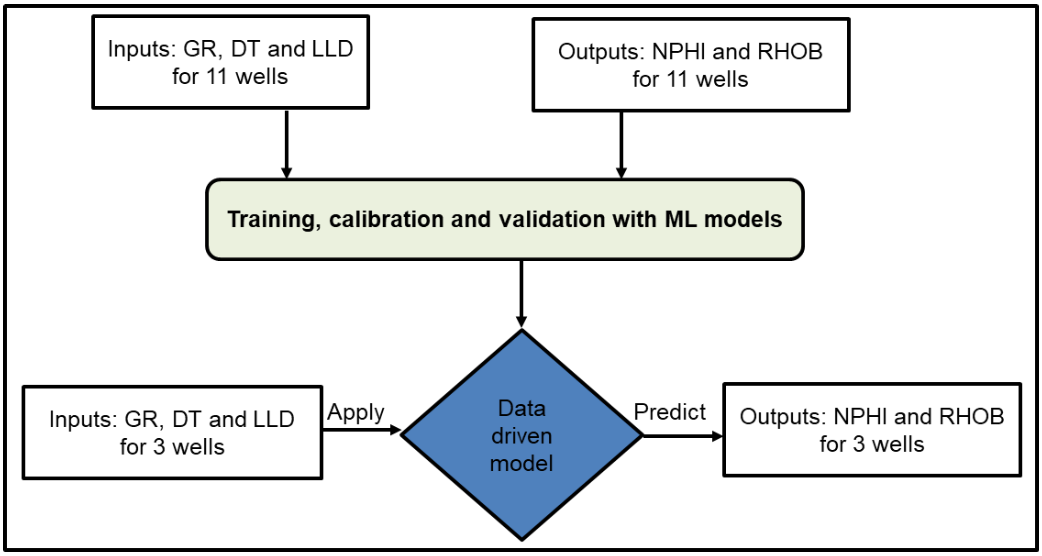

Figure 5.2: Workflow for missing log prediction with the ensemble learning approach.

Table 5.1: Data availability from the wells drilled in the Canning Basin.

Well Name	Location	GR	DEN	NPHI	DT	LLD
Theia-1	Broome Platform	Y	Y	Y	Y	Y
Cyrene-1	Broome Platform	Y	Y	Y	N	Y
Pictor East-1	Broome Platform	Y	Y	Y	Y	Y
Mclarty-1	Broome Platform	Y	N	N	Y	Y
Looma -1	Broome Platform	Y	Y	Y	Y	Y
Sharon Ann-1	Broome Platform	Y	Y	Y	Y	Y
Aquila-1	Broome Platform	Y	Y	Y	Y	Y
Edgar Range-1	Broome Platform	Y	N	N	Y	Y
Hilltop-1	Broome Platform	Y	Y	Y	Y	Y
Hedonia-1	Broome Platform	Y	Y	Y	Y	Y
Missing-1	Crossland Platform	Y	Y	Y	Y	Y
Canopus-1	Broome Platform	Y	Y	Y	Y	Y
Crystal Creek-1	Broome Platform	Y	Y	Y	Y	Y
Matches Spring-1	Broome Platform	Y	N	N	Y	Y

5.2.4.2 Data preparation, transformation, and partition

Several studies have applied different machine learning algorithms to generate synthetic curves (Akinnikawe et al., 2018; Bhatt, 2002; Eshkalak et al., 2014). The number, quality, and statistical behaviour of the input dataset is important for any machine learning project. Similarly, data gaps are a significant problem for data analytics which can mislead the outcome of any model. Hence, it is best to have a good input dataset for machine learning to use to predict the density and neutron logs for the three wells that do not contain those logs.

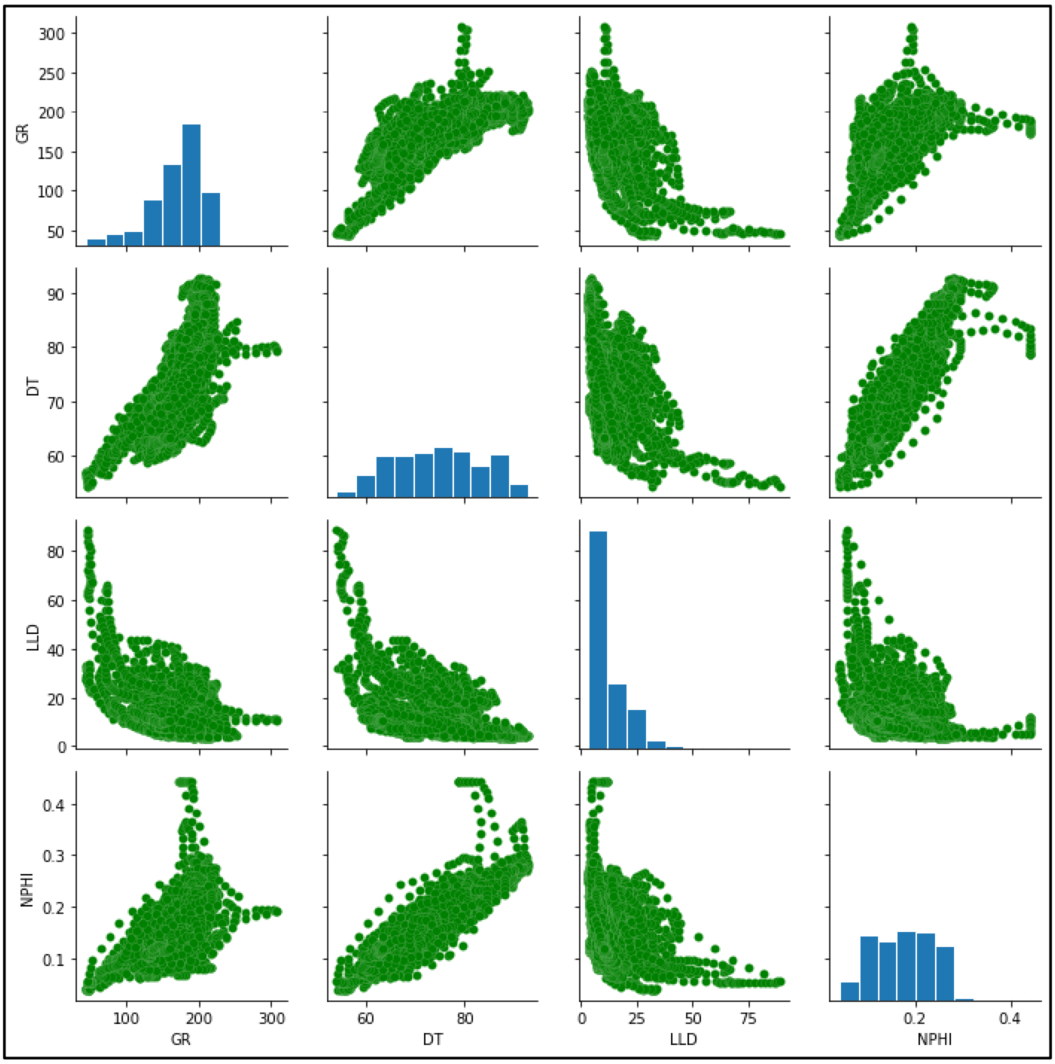

Figure 5.3: Data preparation after removing outliers from the dataset.

The transformed data needs to be partitioned based on the model requirements to get accurate synthetic logs before proceeding with the workflow described in Figure 5.2. The input dataset consists of GR, LLD, and DT logs with variable scales. It is important to have a uniform scale for all inputs, as some of the algorithms require data to have a Gaussian distribution. Therefore, the data were normalised about the mean to confine the ranges between -1 and +1 before training and validation. The outliers were removed, and the data was prepared, as shown in Figure 5.3 for use in this study.

In supervised machine learning the data is usually separated randomly into three sets for training, validation and testing commonly using 60%, 20% and 20% of the dataset respectively (Chen et al., 2014; Mandal et al., 2021). However, the data partitioning can be modified based on the objectives and data availability of any project. The training set is used first to train the model based on the model parameters, while the validation set is used for validating the model parameters to enhance the accuracy. After evaluation, the testing is performed on unknown datasets. This study split the dataset into 70:30 ratio subsets to perform training and validate the generated logs. The model was tested using Crystal Creek-1 as the blind well.

5.2.4.3 Model Selection

Three different models were tried for the generation of the synthetic logs: an artificial neural network (ANN); a support vector machine (SVM); and random forest (RF). Out of these methods, the best one was selected based on more reliable results. The details of these models are described below:

a. ARTIFICIAL NEURAL NETWORK

An artificial neural network (ANN) is an algorithm that attempts to mimic the human brain (Alfarraj & AlRegib, 2019; Emelyanova et al., 2016; Nasira et al., 2008). It contains three or more layers such as an input layer, one or more hidden layers, and an output layer. As shown in Figure 5.4, A neuron can pick an input vector x and then it calculates its scalar with a variable weight vector W and produces an output vector y by employing the non-linear activation function. The activation function, for example, sigmoid, always limits output between 0 and 1. Other activation functions, such as exponential linear unit (ELU), rectified linear unit (RELU), and hyperbolic tangent (tanh) can also be used (Mandal et al., 2021). The ANN algorithm runs through a forward transmission by getting output target values from known inputs, and randomly chosen weights and then calculating the error between estimated and actual target values. This error is back propagated through the network to refine the weights of each neuron. Before running any experiment, the hyper-parameters are fine-tuned (e.g., number of iterations, number of neurons, damping factor, etc.) by performing sensitivity analysis on training and validation datasets. In this study, the tuned hyperparameters used in the present application are in Table 5.2.

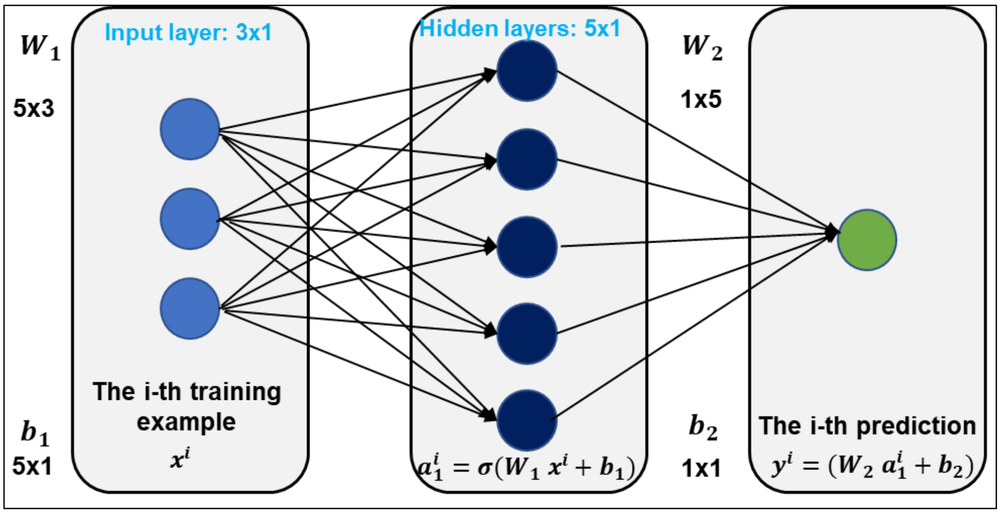

Figure 5.4: Schematic diagram of Neural Network is illustrating input layer, hidden layer and output layer to perform the model for best results.

b. Support Vector Machine

The Support Vector Machine method can be used for both classification and regression problems (Gunn, 1998; Kecman, 2005; Shmilovici, 2009). The Main purpose of SVM here is to solve the classification problem. The accuracy of SVM is high even with a limited amount of data to analyse for prediction. The objective of SVM is to find an optimum hyperplane that separates the data points into two classes. The Hyper plane in a SVM is built in multi-dimensional space or infinite dimensional space (Figure 5.5). Figure 5.5 illustrates the concept whereby there are two classes comprising the blue triangles and orange squares. The task of SVM is to differentiate between two classes by finding the best hyperplane. The black and red lines show two possible solutions and the associated uncertainty for each.

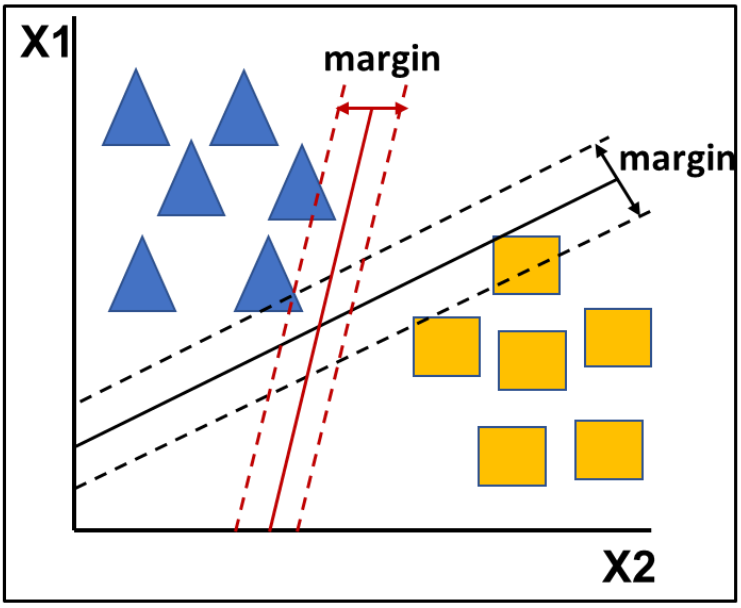

Figure 5.5: SVM schematic diagram illustrating selection of the maximal hyperplanes design to predict the best hyperplane for regression.

c. Random Forest

The random forest algorithm also can be used for both classification and regression (Liaw & Wiener, 2002; Svetnik et al., 2003). Random forest (or random decision forest) is an ensemble method that works by constructing decision trees to train the data (Figure 5.6). RF automatically adjusts the hyper-parameter and predicts better results, so there is no need to tune the hyper-parameter. The model creates sub-models independent classifiers or regressors and then calculates the average of the sub-models for better prediction. The algorithm effectively creates bundles of trees in a forest. A higher number of trees will give a more robust and accurate classification and will not overfit the model (Figure 5.6). The method helps to reduce underfitting and variance and is one of the most efficient Machine Learning methods for making predictions.

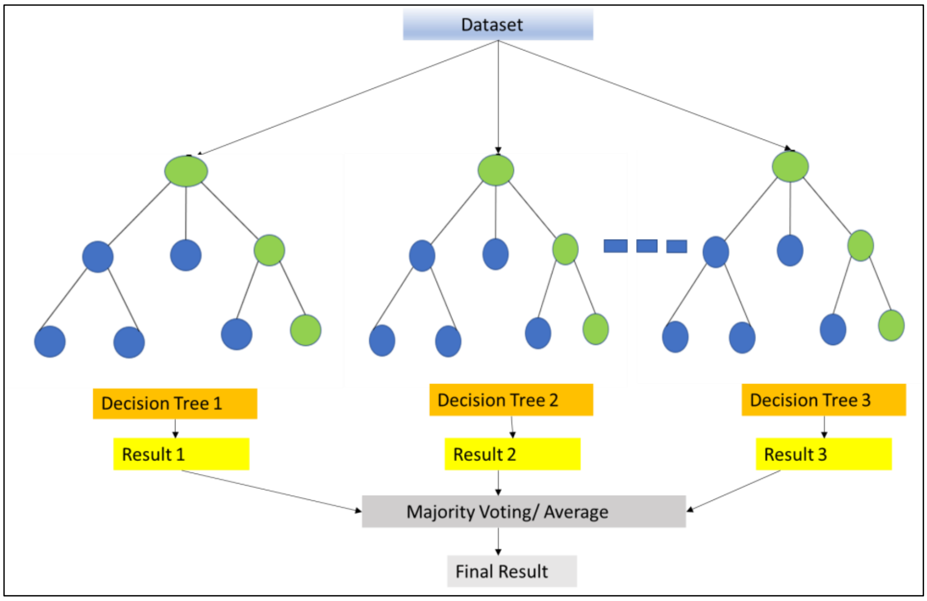

Figure 5.6: A schematic diagram depicting a Random Forest model showing different decision trees that determine the outcome of the model.

5.2.4.4 Model parameter optimisation

The most accurate predictor was selected based on model parameters optimisation. The grid search cross-validation (scikit-learn platform) approach was used to find the optimum values of parameters (Perry et al., 2021). The parameter selection was finalised before model validation. The achieved optimised parameters for each model are shown in Table 5.2.

Table 5.2: Model parameters obtained during this study for each model to get the best performance.

Model	Parameters	Value
Neural Netrwork	Alpha	1e-02,1e-01,1e-00
	Maximum iterations	15000,20000,25000
Support Vector Machine	C	100,150,200
	gamma	0.001,0.01,0.1
Random Forest	n_estimators	650
	max_depth	95
	max_leaf_nodes	1050

5.2.4.5 Model validation

Cross-validation is utilised to test the validity of the training dataset model and select the best model. Once the best model had been selected from the training dataset, it was then used on the entire dataset to predict the synthetic logs. The mean squared error (MSE) and R^2 regression metrics were computed for the selected models in the runs using the validation datasets to provide relative confidence levels for the selected models. These metrics were computed using the following equations:

$$MSE = \frac{1}{n}\Sigma_{i=1}^{n}(y - y_p)^2 \qquad \text{(Eq. 5.10)}$$

$$R^2 = 1 - \frac{\text{Sum of squared distances between the original and predicted value}}{\text{Sum of squared distances between the original and their mean value}} \qquad \text{(Eq. 5.11)}$$

These values indicate the best fit of the predicted model to the data in which the best fit should have the lowest MSE and R^2 should be the highest. Based on that, random forest (RF) algorithm worked well as compared to others.

5.2.5 Unsupervised Machine Learning

Unsupervised Machine Learning uses unlabelled or unclassified data to predict the accuracy of a model, in contrast to supervised learning uses labelled data described in the previous section. The outcomes in supervised learning are labelled and models learn from the training dataset by using labelled target outcomes. Unlike supervised learning, unsupervised learning cannot be used for regression and classification algorithms because the outcome values are unknown, and it might be impossible to train the algorithms. Unsupervised learning aims to recognise and classify hidden patterns by learning from a training dataset. An example could be classifying two different unlabelled bottles, one containing water and the other milk in which you want to predict which one is the milk bottle and which one is a water bottle. Once you taste both bottles you will be able to differentiate between milk and water bottle by tasting them, and this is effectively labelling the two bottles.

5.2.5.1 K-means clustering

K-means clustering is an unsupervised machine learning technique that learns a grouping from the data itself and doesn't require training data. The groups consist of samples with similar characteristics, which can be considered as distinct electro facies. The purpose of K-means clustering is to group similar datapoints and thereby discover hidden patterns with the help of the defined clusters in a dataset. K-means clustering tries to achieve this objective by partitioning a dataset of n observations into fixed number of k clusters where the data points are allocated to the cluster with the nearest mean. In general terms a cluster is defined as a collection of datapoints that can be grouped based on some measured similarities in the dataset (Reference). The fixed number k is defined as a target number which depicts the number of centroids in each dataset where the centroid is a real or imaginary location which depicts a centre of a cluster. K-Means algorithm requires the number of clusters to define before running the algorithm. There are various approaches for finding the optimal number of clusters, however, for this study, the 'elbow method' is used to decide the number of clusters. The elbow method is more rigorous techniques involving the Bayesian information criterion and optimizing the Gaussian nature of each cluster (Hamerly & Elkan, 2003). The sum of the squared distance of each point to the nearest cluster centroid. (Called inertia in scikit-learn) is plotted for an increasing number of clusters. As the number of clusters is increased and better fit the data, error is decreased. The elbow of the curve represents the point of diminishing returns where increasing the number of clusters does not reduce the error appreciably. Figure 5.7 schematically represents the method of K-means clustering.

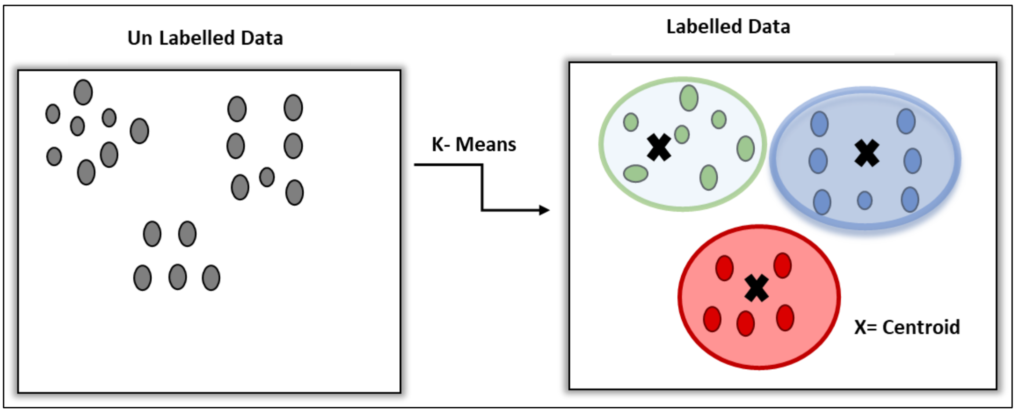

Figure 5.7: K-means clustering to separate and provide a better understanding of the data.

5.2.6 Goldwyer Formation 3-D Modelling

The regional distribution of the petrophysical properties for the classified rock types was analysed by 3-D modelling in Petrel (Schlumberger software). The 3-D model was used to map the shale gas distribution and assess the resource potential of the Goldwyer-III shale in the study area. The geocellular 3-D grid (modelling) involved two steps as described below:

5.2.6.1 Facies Modelling

The lithofacies clusters identified through the K-means clustering were entered into the Petrel as discrete logs for each well. These were then upscaled into the Goldwyer-III shale (the zones and layers). The lithofacies discrete logs were then interpolated through the 3D model of the Goldwyer-III shale constrained by the well tops. An example of Theia-1 well location and well tops are shown in Figure 5.8.

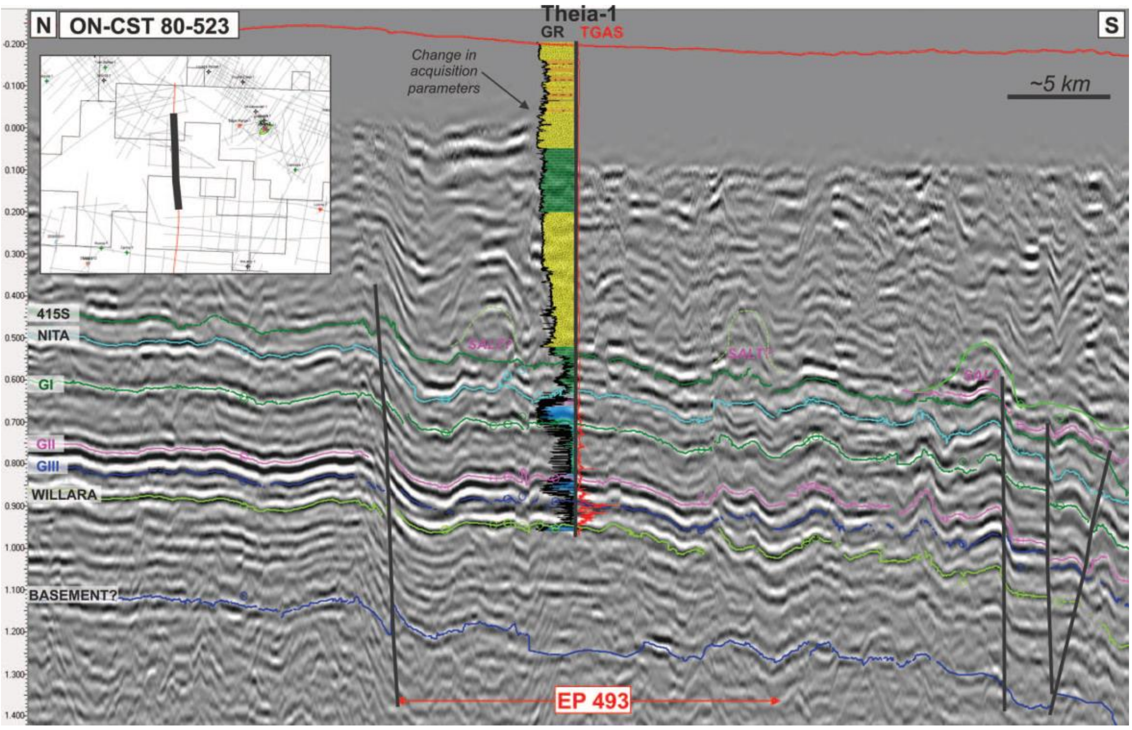

Figure 5.8: Seismic line showing location of Theia-1 well (Adapted from Van Hattum et al., 2019).

Interpolation of the lithofacies throughout the 3D model can be done using various methods in Petrel. In this study, the sequential indicator simulation algorithm is used with the variogram parameters derived from analysis of the upscaled lithofacies log data to get the best results (Table 5.3). The variograms were adjusted based on the data analysis and exponential variogram was used during the simulation process. Sequential indicator simulation is a stochastic, pixel-based method that allows generation of numerous and equiprobable realisations (Zhang, 2008). Forty realisations were generated, and the resulting facies model was used to calculate averaged thickness maps for each of the lithofacies.

Table 5.3: The variogram parameters used for 3-D modelling in Petrel.

Method	Property	Facies type	No. of realisations	Variogram type	Anisotropy range			Kriging type
					Majore dir	Minor dir	Vertical	
Sequential indicator simulation	Facies	Argillaceous Shale	40	Exponential	100000	100000	38	Ordinary
	Facies	Calcareous Shale		Exponential	100000	100000	35	Ordinary
	Facies	Siliceous Shale		Exponential	100000	100000	31	Ordinary
	Facies	Mixed Shale		Exponential	100000	100000	33	Ordinary

Method	Property	Facies type	No. of realisations	Variogram type	Anisotropy range			Total sill	Nugget	Kriging type
					Majore dir	Minor dir	Vertical		0.0001	
Sequential Gaussian simulation	All	Argillaceous Shale	40	Exponential	500	500	60	1.16	0.0001	Ordinary
	All	Calcareous Shale		Exponential	500	500	100	1.25	0.0001	Ordinary
	All	Siliceous Shale		Exponential	500	500	80	0.85	0.0001	Ordinary
	All	Mixed Shale		Exponential	500	500	74.6	1.7	0.0001	Ordinary

5.2.6.2 Petrophysical and Geomechanical Modelling

The continuous downhole values of all the petrophysical properties (TOC, porosity, water saturation and adsorbed gas content) and of the geomechanical properties were imported into Petrel for each of the wells. The logs were statistically evaluated in the Petrel data analysis module for input to the property modelling. This included variogram analysis for the subsequent simulations as per the parameters described in Table 5.3. The lithofacies clusters identified through the K-means clustering were entered into the Petrel as discrete logs for each well. These were then upscaled into the Goldwyer-III shale (the zones and layers). The lithofacies discrete logs were then interpolated through the 3D model of the Goldwyer-III shale constrained by the well tops. An example of Theia-1 well location and well tops are shown in Figure 5.8.

Interpolation of the lithofacies throughout the 3D model can be done using various methods in Petrel. In this study, the sequential indicator simulation algorithm is used with the variogram parameters derived from analysis of the upscaled lithofacies log data to get the best results (Table 5.3). The variograms were adjusted based on the data analysis and exponential variogram was used during the simulation process. Sequential indicator simulation is a stochastic, pixel-based method that allows generation of numerous and equiprobable realisations (Zhang, 2008). Forty realisations were generated, and the resulting facies model was used to calculate averaged thickness maps for each of the lithofacies.

The logs were then upscaled into the model layers to provide satisfactory vertical resolution using the arithmetic average method per layer. There are several simulation models which can be applied for petrophysical modelling, however, Sequential Gaussian Simulation (SGS) was used and it provided good results given the large inter-well distances (L. Johnson et al., 2020; Johnson, 2019). This provided a 3-D petrophysical model for each property throughout the Broome Platform and the western part of the Crossland Platform. The SGS method is commonly used for petrophysical modelling and this method is simple and robust for modelling of gas shales.

5.3 Results

5.3.1 Mineral composition and lithofacies

The mineralogy, organic composition, physical and gas properties for the lithofacies in the Goldwyer-III shales have been characterised by comprehensive analyses as discussed in Chapter 3.3 above, including XRD, TIMA, SEM, porosity, gas adsorption and MICP analyses. The results showed that four main lithofacies can be identified in the Goldwyer-III shales with the argillaceous shales being further divided into an organic rich and organic poor lithofacies based on laboratory analysis (defined in Chapter 2 and Iqbal et al., 2021a,b). The rock-type description and mineralogy of the four main lithofacies are summarised immediately below and will be discussed further in the following subsections. The results from the compositional analyses are given in Appendices A1, A2 and A3. The detailed description of the Goldwyer-III shale lithofacies is presented in Chapter 3.3.1 and a summary of each lithofacies' description integrated with petrophysical logs response is described below.

The argillaceous shale is dark grey to black either poorly bedded or with thin laminations of silt and clay (Figure 5.9a and b). The gamma ray response is typically high and flat or serrated and the sonic is slow (Figure 5.9a and Table 2.2). The density is mostly high suggesting that the shales are mostly low in TOC. The calcareous shale comprises dark grey calcareous mudstone bands interbedded with mudstone bands containing calcareous concretions (Figure 5.9c). The facies has a moderate, funnel shaped, spiky to serrated gamma ray curve response resulting from rapid changes between the mudstone to the carbonate bands. This facies has low sonic, high density and low TOC values (Figure 5.9c and Table 2.2).

The siliceous shale is light grey in colour comprising thin laminations of quartz silt and clay in places. Low to moderate, funnel shaped gamma ray log response is observed for this lithofacies. Moreover, this facies has moderate sonic, density and TOC values. (Figure 5.9d and Table 2.2). The mixed shale is a heterolithic lithofacies occurring as medium to dark grey shale with alternating thin laminations of mudstone, silt and carbonate. The moderate to high gamma ray and moderate sonic and density as well as high TOC response have been recognised in this facies (Figure 5.9e and Table 2.2).

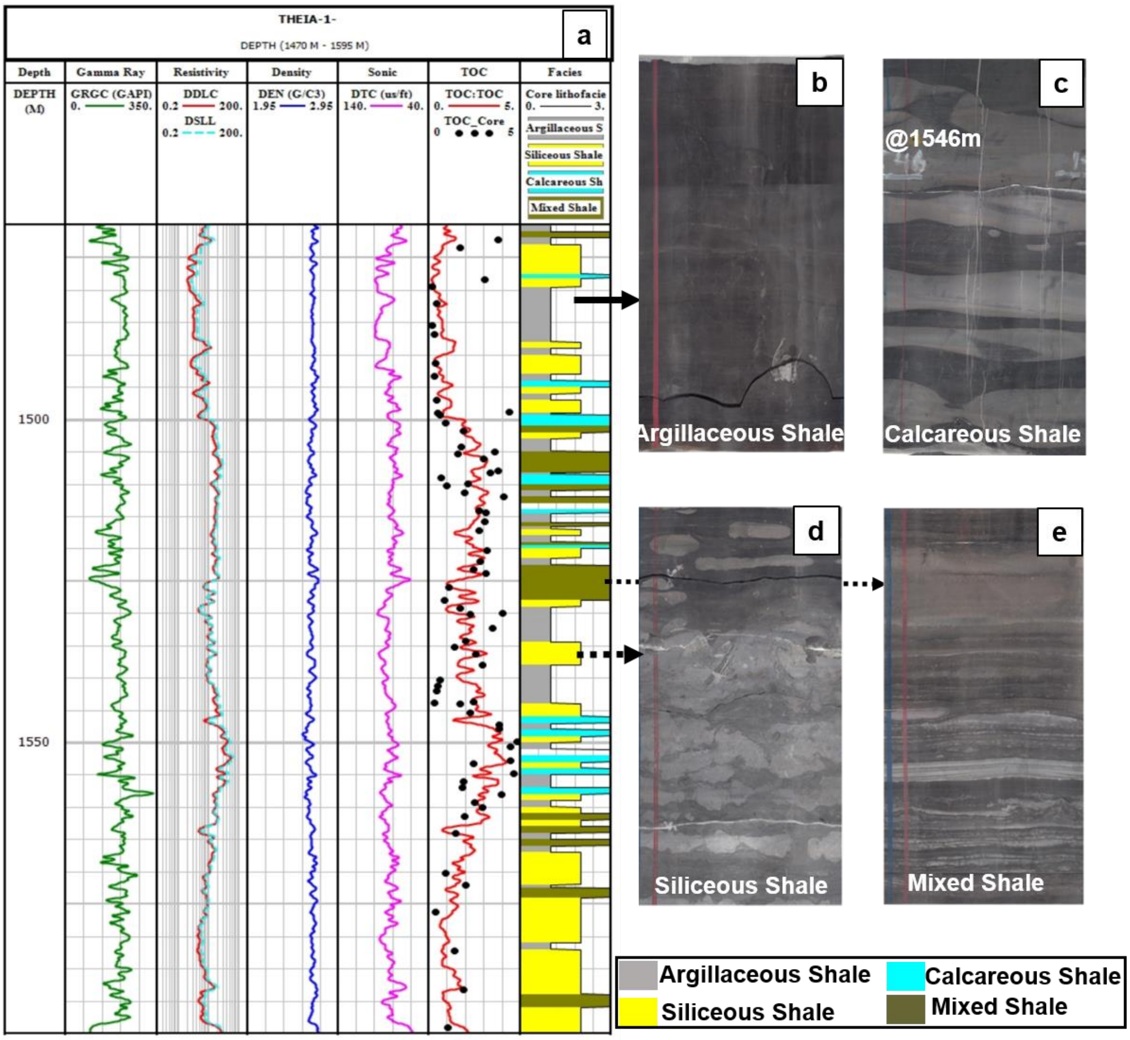

Figure 5.9: Vertical distribution of Goldwyer-III shale lithofacies in Theia-1 well and core images for each lithofacies as shown in b-e. The siliceous shale is highly bioturbated as shown in d.

5.3.2 Geochemical and petrophysical characteristics

The TOC content for the selected samples of Goldwyer-III shale from Theia 1 well range from 0.5 to 4.5wt% and the porosity ranges from 6-12% (Table 5.4 and Table 5.5). The organic rich layers in argillaceous shale and siliceous shale have highest TOC and porosity values compared to the other lithofacies. The siliceous shale has the best organic contents, with comparatively high TOC (averaged 2.53 wt%, high hydrogen index (HI) (150.64) and moderate oxygen index (OI) (30.61), but low S1 (1.03 mg/g), S2 (2.63 mg/g) and S3 (0.48 mg/g) (Table 5.4).

The argillaceous shale has moderate TOC (averaged 1.88 wt%, but ranging from 1 to 4 wt%) with the higher values from some organic rich layers. This lithofacies has moderate HI (143.21) and OI (43.57) and moderate S1 (1.73 mg/g), S2 (3.17 mg/g) and higher S3 (0.55 mg/g) (Table 5.4). The mixed shale also has moderate TOC (averaged 2 wt%), but lower HI (121.12) and OI (40.62). Similarly, the mixed shale has low to moderate S1 (1.69 mg/g), S2 (2.37 mg/g) and S3 (0.43 mg/g) (Table 5.4).

In contrast, the calcareous shales have low TOC (averaged 0.5 wt%), the lowest HI (83.48) and the highest OI (69.52). As expected, this lithofacies has low S1 (0.76 mg/g), S2 (0.89 mg/g) and S3 (0.40 mg/g) (Table 5.4). The Goldwyer-III shales contain type-I/II algal macerals and type III graptolitic organic matter, however, the samples from calcareous and mixed shales consist almost entirely of type-III graptolite organic matter and are probably oxidised (Johnson 2019; Johnson 2020).

Table 5.4: Averaged Geochemical properties of Goldwyer-III shale lithofacies.

Lithofacies	TOC (wt%)	S1 - (mg/g)	S2 - (mg/g)	S3 - (mg/g)	PI	Tmax(°C)	HI	OI	Kerogen Type
Argillaceous Shale	1.88	1.73	3.17	0.55	0.38	444.66	143.21	43.57	II&III
Calcareous Shale	0.72	0.76	0.89	0.40	0.60	423.68	83.48	69.52	III
Siliceous Shale	2.53	1.03	2.63	0.48	0.33	457.66	150.64	30.61	II&III
Mixed Shale	2.02	1.69	2.37	0.43	0.40	441.80	121.12	40.62	III

5.3.3 Porosity and water saturation

A detailed description of pore types, pore morphology, pore volume and porosity for Goldwyer-III shale lithofacies are given in Chapters 3 and 4. In summary, the organic rich layers in siliceous and argillaceous shales have highest porosity 11 and 12%, respectively. In comparison, the calcareous and mixed shales have low porosity of about 6 and 10% respectively. The bulk and grain densities for Goldwyer-III shale lithofacies range from 2.43-2.55 g/cc and 2.65-2.76 g/cc, respectively (Table 5.5). The typical water saturation is computed by using Eq. 5.2 estimated that the argillaceous shale has the highest water saturation (80%) and the siliceous shale has the lowest Sw value (35%). Whereas, the calcareous and mixed shales have 55% and 45% water saturation, respectively (Table 5.5 and Figure 5.10).

Table 5.5: Averaged petrophysical properties of Goldwyer-III shale lithofacies.

Lithofacies	Bulk density (g/cc)	Grain density (g/cc)	Water Saturation (%)	VL, cc/g	PL, Mpa
Argillaceous Shale	2.5138	2.71	0.80	5.6	6.65
Calcareous Shale	2.5591	2.71	0.55	3.014	4.71
Siliceous Shale	2.4830	2.76	0.35	4.17	5.37
Mixed Shale	2.5098	2.71	0.45	3.15	4.332

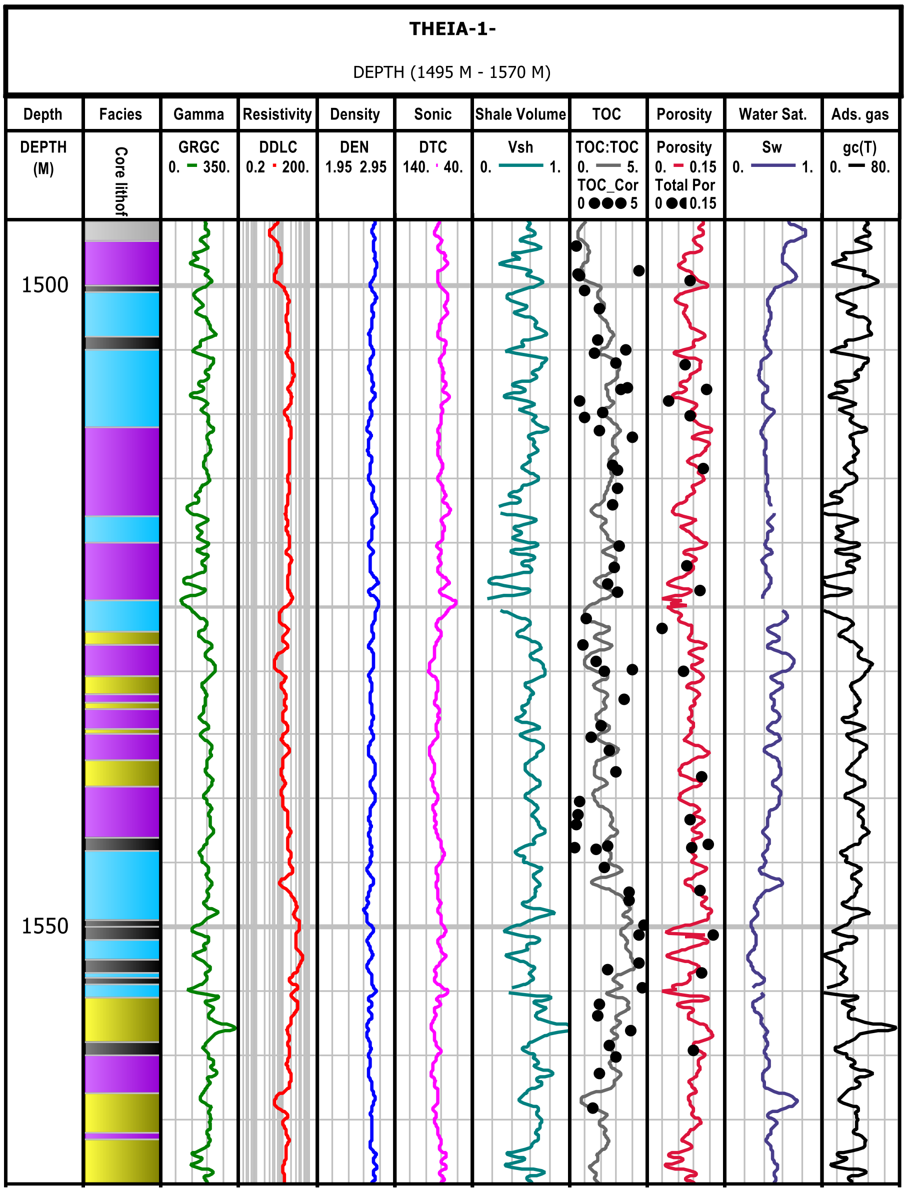

Figure 5.10: Petrophysical characterisation of Goldwyer-III shale estimated in Theia-1 well, colour codes represent argillaceous shale (dark pink and grey), organic rich shale (black), calcareous shale (blue) and mixed shale (green).

5.3.4 Methane Adsorption Isotherms of Goldwyer-III Shale Lithofacies

The results of the methane adsorption analyses, estimated for isotherms at 25°C temperature for a range of different lithofacies, on the Goldwyer-III shales is given in Figure 5.11. The calculated absolute adsorption isotherms (dotted points) and the corresponding Langmuir model fits (solid lines) are shown to have good fits with R^2 of about 99%. The argillaceous shale has the highest Langmuir volume and Langmuir pressure so it has the highest estimated adsorbed gas (70 scf/ton (Figure 5.11a and Table 5.5).

The siliceous and mixed shales have medium Langmuir volume and Langmuir pressure so they have medium estimated adsorbed gas (55 scf/tonn) (Figure 5.11b and Table 5.5). In contrast, the calcareous shale has the lowest Langmuir volume and Langmuir pressure so it has lowest estimated adsorbed gas (40 scf/tonn) (Figure 5.11b and Table 5.5).The absolute adsorption isotherms show the expected positive relationship with TOC and clay content.

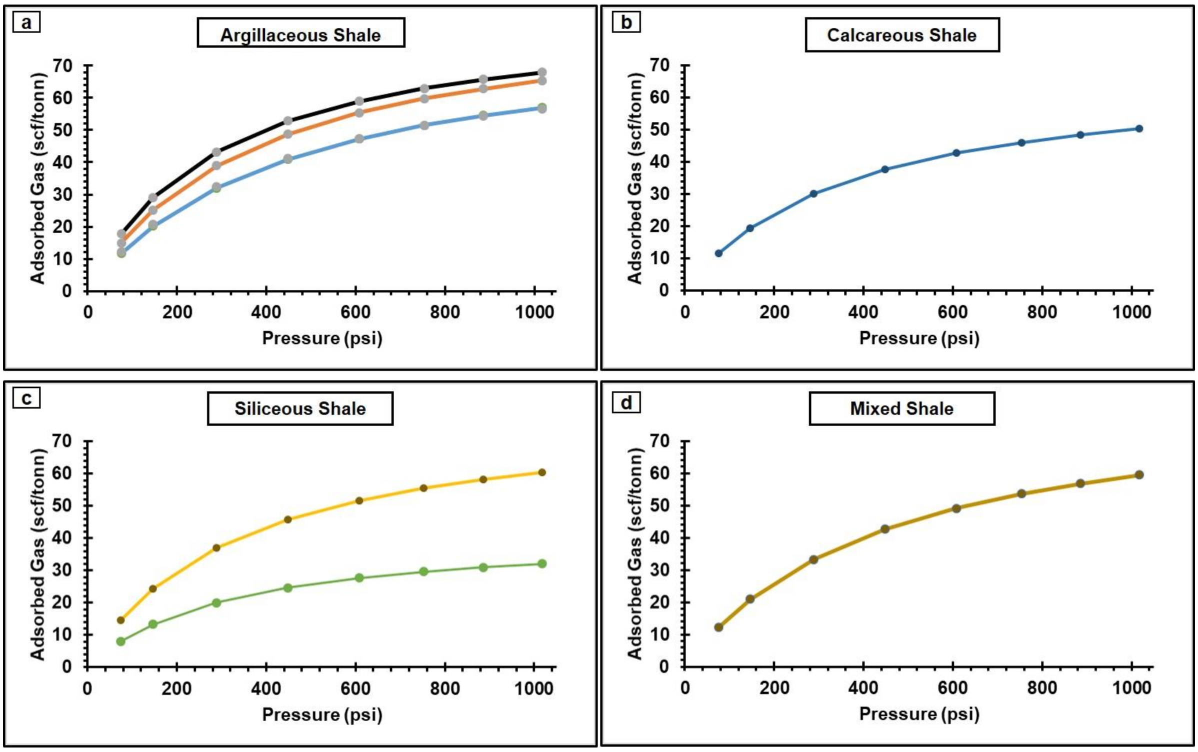

Figure 5.11: Methane adsorption isotherms for Goldwyer-III shale lithofacies based on pressure and adsorbed gas at experimental temperature (25°C). Different coloured lines illustrating different samples from the same lithofacies.

5.3.5 Generation of Synthetic Logs

The density and neutron logs are missing in three of the wells as shown in Table 5.1. Hence, synthetic curves were generated for these logs by applying appropriate algorithms using the methods given in Chapter 5.3 and briefly described below.

5.3.5.1 Synthetic RHOB and NPHI generation

Gamma ray (GR), sonic (DT) and deep resistivity (Log10_LLD) logs were used for the prediction of synthetic density and neutron curves. Three models (ANN, SVM and RF) were applied to get the best results (Table 5.6). The parameters of these models were optimised by using the validation dataset. The relative performance of these models is shown in Table 5.6. Out of three models, the Random Forrest performed well having least MSE and highest R^2 value. In the blind wells (Canopus-1 and Looma-1), the prediction from RF model is closer to the validation dataset which provides higher confidence for selecting this model. The original and predicted RHOB and NPHI curves for some wells with original logs are shown in Figure 5.12 and Figure 5.13.

Table 5.6: MSE and R^2 for each model to show the selection of best model for synthetic curves generation.

Model Description	Training Mean Squared Error	Training R^2 Score	Validation Mean Squared Error	Validation R^2 Score
Artificial Neural Network (ANN)	0.00	0.65	0.00	0.67
Support Vector Machine (SVM)	0.00	0.58	0.00	0.59
Random Forest	0.00	0.95	0.00	0.89

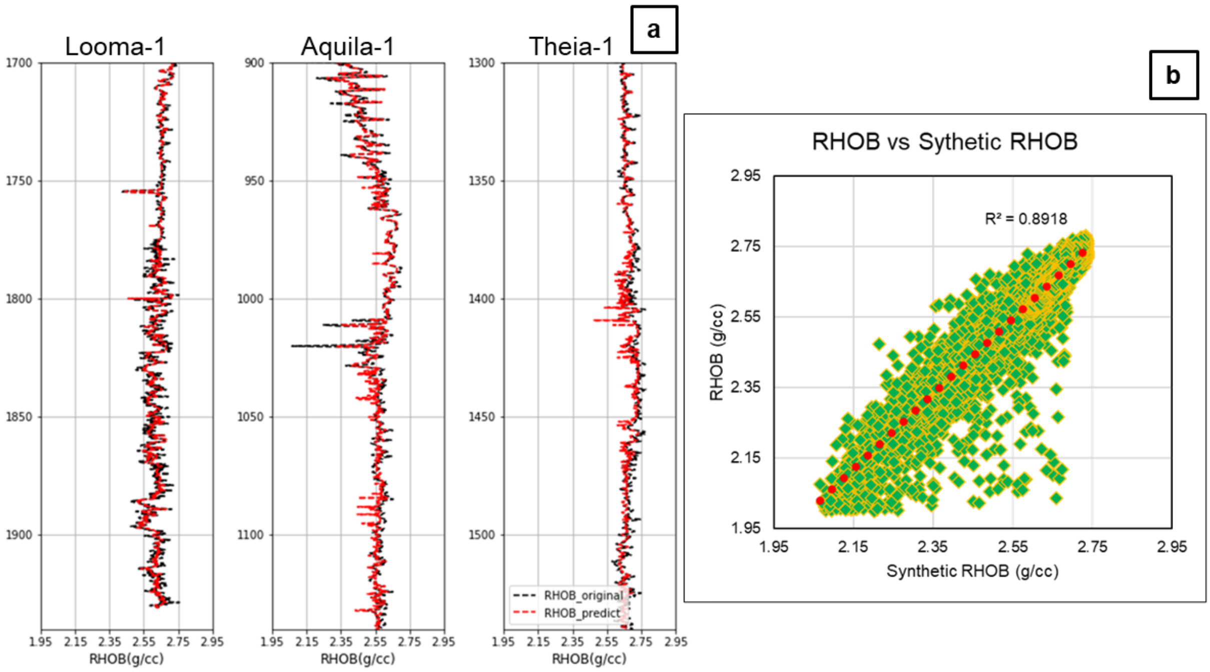

Figure 5.12: Original Vs predicted density curves showing the good performance of the RF model (original black curve; predicted red curve)..

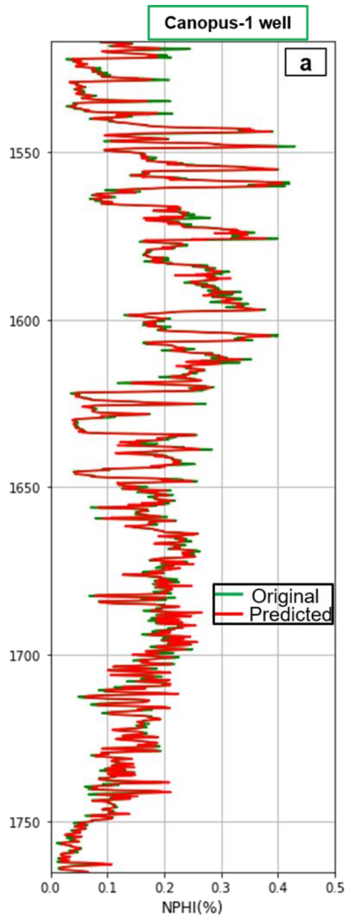

Figure 5.13: NPHI synthetic log generation based on RF model for Canopuse-1 well (original curve green; predicted curve red).

5.3.6 K-means clustering

The K-means clustering method was used to classify the lithofacies from the entire dataset of petrophysical logs, including the synthetic logs, and the petrophysical properties, for all 14 wells as this algorithm was successfully applied in other petrophysics related studies (Abdulaziz et al., 2019; Joshi et al., 2021). The statistical analysis shown in Figure 5.14a-h helped to identify the best input parameters for clustering based on the lowest variance and minimal overlapping. Previous studies (Rebelle & Lalanne, 2014; Schlanser et al., 2016) have relied only on the petrophysical logs for clustering (GR, RHOB, DT, NPHI and LLD). However, improved results have been achieved in this study by selection of additional parameters for clustering, such as TOC, shale volume, total porosity, adsorbed gas content and the geomechanical properties, integrated together with all the logs.

As shown in Figure 5.15a, four clusters were discriminated based on the elbow method in this study. The clustered groups are shown in Figure 5.15b, by integrating clustering with lithofacies (which are defined in Chapter 3). There are two classification schemes defined for Goldwyer-III shale in Chapter 2 and Chapter 3. As the lithofacies defined in Chapter 3 are based on TOC and mineral composition, so we used lithofacies to identify the equivalent cluster and vice versa. It is observed that the cluster-1 corresponds to siliceous shale, cluster-2 corresponds to mixed shale, cluster-3 corresponds to calcareous shale and cluster-4 corresponds to the argillaceous shale. The statistics for the well logs, petrophysical and geomechanical properties are shown in Table 5.7. The vertical distribution of the lithofacies clusters is shown for Theia-1 and the Missing-1 well in Figure 5.16 and Figure 5.17, as examples of the results for the 14 wells. Table 5.7 shows that the siliceous shale (cluster-1) has low shale volume, high TOC, highest porosity, high adsorbed gas and high geomechanical properties. Whereas, the argillaceous shale (cluster-4) has the highest shale volume, highest TOC, lowest porosity, highest adsorbed gas, and lowest geomechanical properties.

Table 5.7: Statistical analysis represents the averaged petrophysical logs, properties and geomechanical properties of Goldwyer-III shale clusters.

Cluster		GR (API)	LLD (ohmm)	NPHI	RHOB (g/cc)	DTC μ/ft)	TOC_Log (wt%)	Vsh_GR (v/v)	Total porosity (v/v)	gc(T) (scf/t)	Edyn (Gpa)	Vdyn (Gpa)	Esta (Gpa)	vsta (Gpa)	S_TCS (Mpa)	fric_i	BI_E (v/v)
Cluster-1	**Mean**	120.00	11.83	1.76	2.61	78.51	1.84	0.46	0.11	45.49	34.42	0.24	15.48	0.24	145.99	0.60	0.70
	Min	95.51	1.46	0.06	2.37	62.07	0.01	0.43	0.00	1.01	19.36	0.16	9.11	0.16	119.70	0.48	0.56
	Max	250.00	285.76	35.8	2.73	96.97	4.43	1.40	0.18	87.60	56.58	0.29	24.85	0.29	184.71	0.77	0.76
	Std	29.75	15.30	5.78	0.05	7.87	0.79	0.11	0.03	11.49	8.02	0.02	3.39	0.02	14.01	0.06	0.04
Cluster-2	**Mean**	135.65	11.47	5.53	2.61	78.49	1.66	0.45	0.10	25.15	34.37	0.24	15.46	0.24	145.92	0.60	0.66
	Min	53.88	1.75	0.03	2.37	63.90	0.01	0.05	0.00	0.01	19.51	0.17	9.17	0.17	119.96	0.49	0.56
	Max	215.61	174.18	50.2	2.75	95.31	4.71	0.76	0.19	56.73	52.65	0.31	23.19	0.31	177.84	0.74	0.74
	Std	32.31	9.84	10.5	0.05	7.73	0.93	0.12	0.03	10.55	7.92	0.02	3.35	0.02	13.84	0.06	0.04
Cluster-3	**Mean**	110.62	15.74	2.04	2.66	62.54	1.43	0.37	0.09	18.27	57.67	0.20	25.31	0.20	186.62	0.78	0.76
	Min	38.68	2.60	0.01	2.53	41.78	0.02	0.05	0.00	0.05	46.46	0.13	20.57	0.13	167.03	0.69	0.72
	Max	214.63	254.68	25.8	2.76	69.20	3.87	0.82	0.17	53.27	132.51	0.25	56.97	0.25	317.36	1.35	0.98
	Std	36.37	12.18	4.55	0.05	3.29	0.76	0.14	0.03	11.88	7.98	0.01	3.38	0.01	13.95	0.06	0.03
Cluster-4	**Mean**	172.00	8.35	18.6	2.52	102.95	2.14	0.70	0.08	50.45	17.06	0.30	8.14	0.30	115.68	0.47	0.54
	Min	42.44	1.49	0.13	2.09	93.04	0.02	0.07	0.00	3.74	5.31	0.28	3.17	0.28	95.15	0.38	0.41
	Max	307.00	49.20	58.7	2.70	144.93	4.55	1.11	0.24	80.88	22.54	0.37	10.45	0.37	125.25	0.51	0.59
	Std	23.11	5.29	18.9	0.11	9.88	0.90	0.13	0.03	10.65	3.47	0.02	1.47	0.02	6.06	0.03	0.03

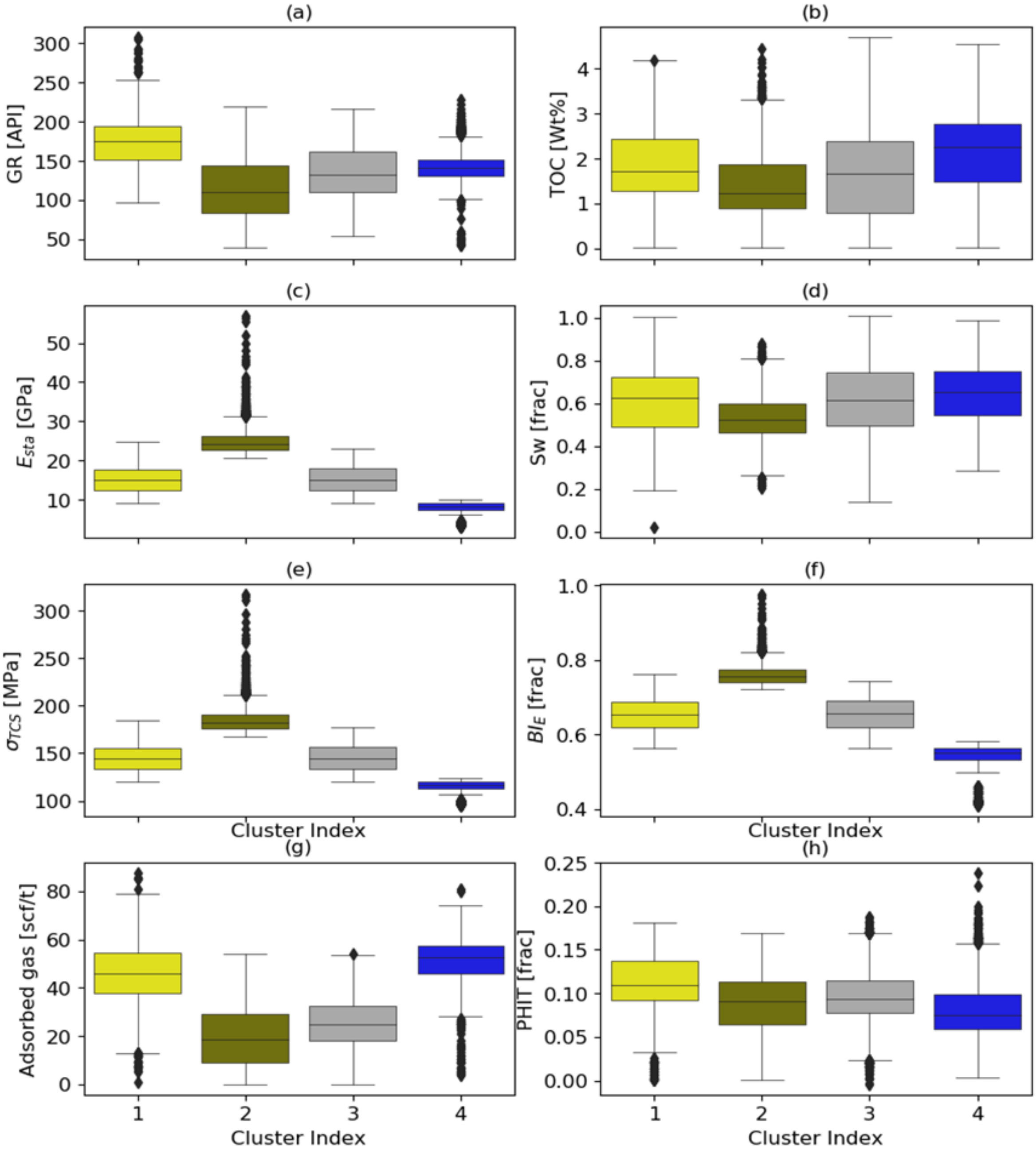

Figure 5.14: Statistical analysis to select the best parameters for clustering based on low variance and minimising overlapping. The colours represent such as yellow colour is cluster-1 equivalent to siliceous shale; green colour is cluster-2 equivalent to mixed shale; blue colour is cluster-3 equivalent to calcareous shale; grey colour is cluster-4 equivalent to argillaceous shale.

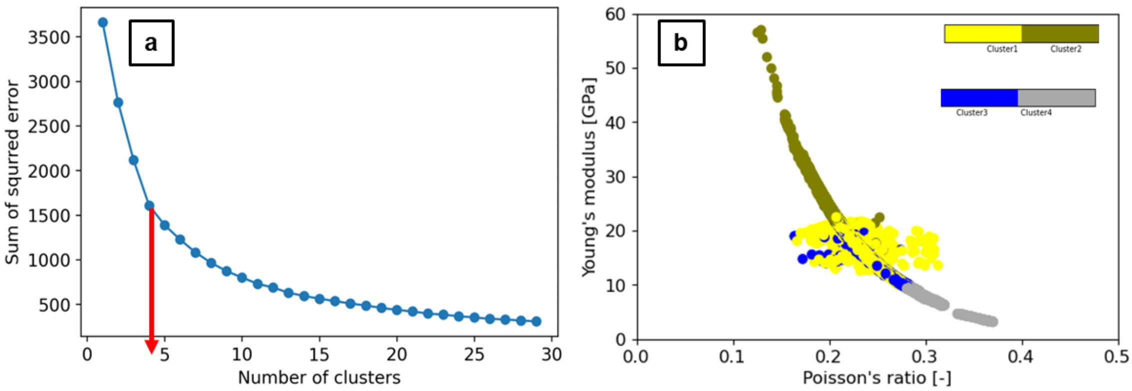

Figure 5.15: (a) Selection of the optimum cluster from the elbow method. (b) Cross-plot of Young's modulus and Poisson's ratio colour coded with cluster groups. The yellow colour is cluster-1 equivalent to siliceous shale; green colour is cluster-2 equivalent to mixed shale; blue colour is cluster-3 equivalent to calcareous shale; grey colour is cluster-4 equivalent to argillaceous shale.

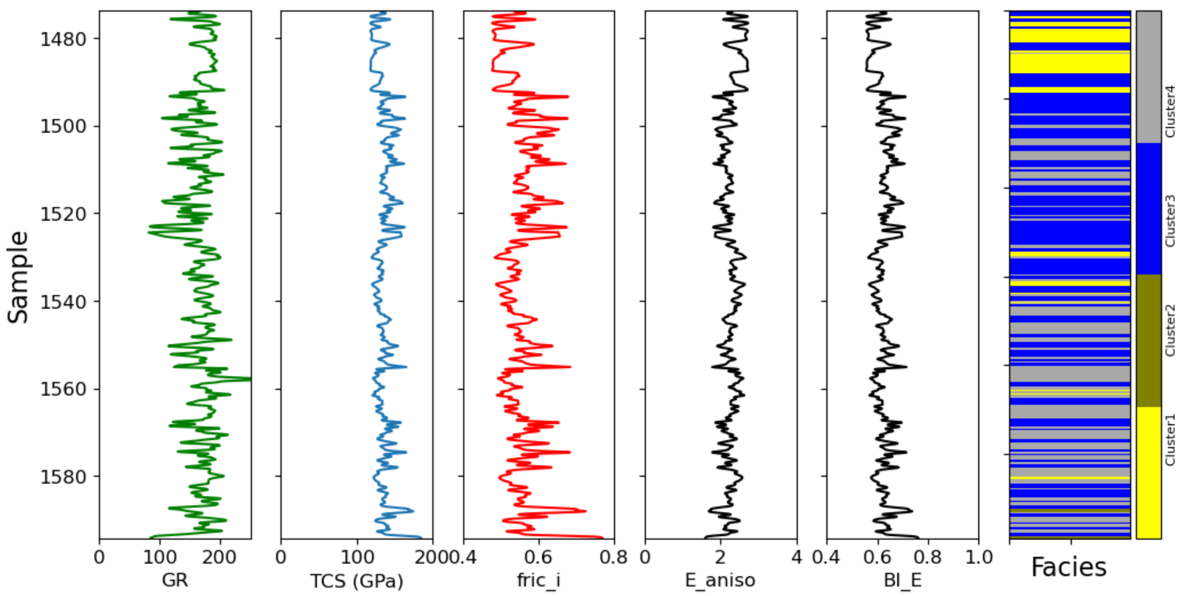

Figure 5.16: Facies identification based on K-means clustering in the Theia-1 well. The yellow colour is cluster-1 equivalent to siliceous shale; green colour is cluster-2 equivalent to mixed shale; blue colour is cluster-3 equivalent to calcareous shale; grey colour is cluster-4 equivalent to argillaceous shale.

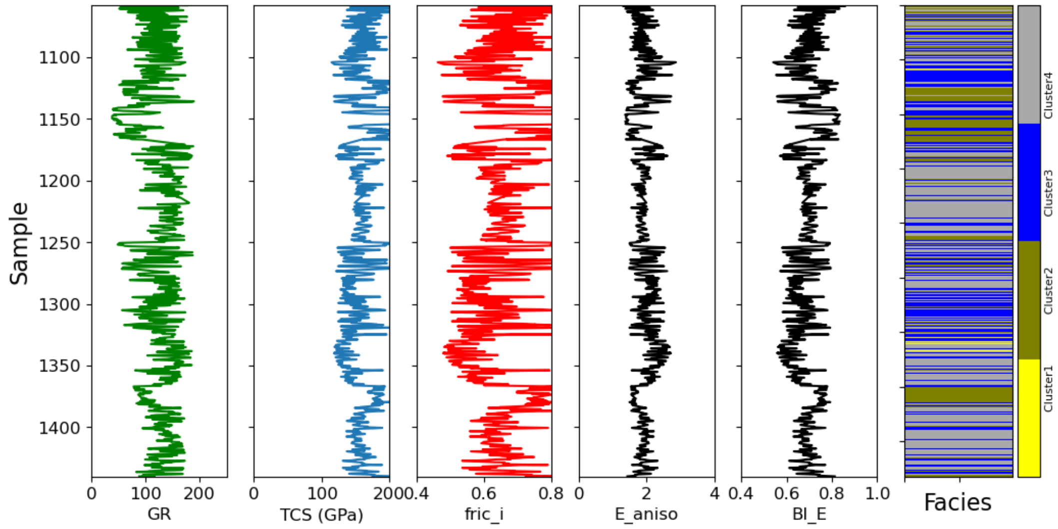

Figure 5.17: Facies identification based on K-means clustering in Missing-1 well.

5.3.7 Goldwyer-III Shale 3-D model results

5.3.7.1 Facies modelling

The lateral distribution of the lithofacies over the Broome Platform to east Crossland Platform was estimated using the Sequential Indicator Simulation method. Maps of the average thickness for each lithofacies are shown in Figure 5.18a-d. A NW-SE well-section through the 3D model is shown in Figure 5.19a-c.

The average thickness of the argillaceous shale varies from 10 to 100m and is thickest in the NW (towards Aquila-1 well), whereas it thins towards the centre and becomes absent in the central and SW wells (Mclarty-1, Looma-1, Canopus-1, Matches Spring-1, Edgar Range-1 and Missing-1) (Figure 5.18a). In contrast, the calcareous shale is the thickest facies and ranges from 50m in the NW to 250m towards the SE, with some local variation in-part possibly due to the lack of well data in some areas such as in the NW north of Aquila-1 (Figure 5.18b).

The siliceous shale is thinner and relatively constant over most of the area typically 20-50m with a range of 5 to 150m. It is thicker in the NE and NW though there may be some edge effects due to lack of data (Figure 5.18c). The thickness of the mixed shale is reasonably even at 10-50m over most of the Broome Platform but thickens to over 150m towards the SE parts into the

Crossland Platform (Figure 5.18d). A local thickening also occurs on the NW edge of the map north of Aquila-1 where there is no well control that is probably an artefact of the gridding as mentioned for the calcareous shale.

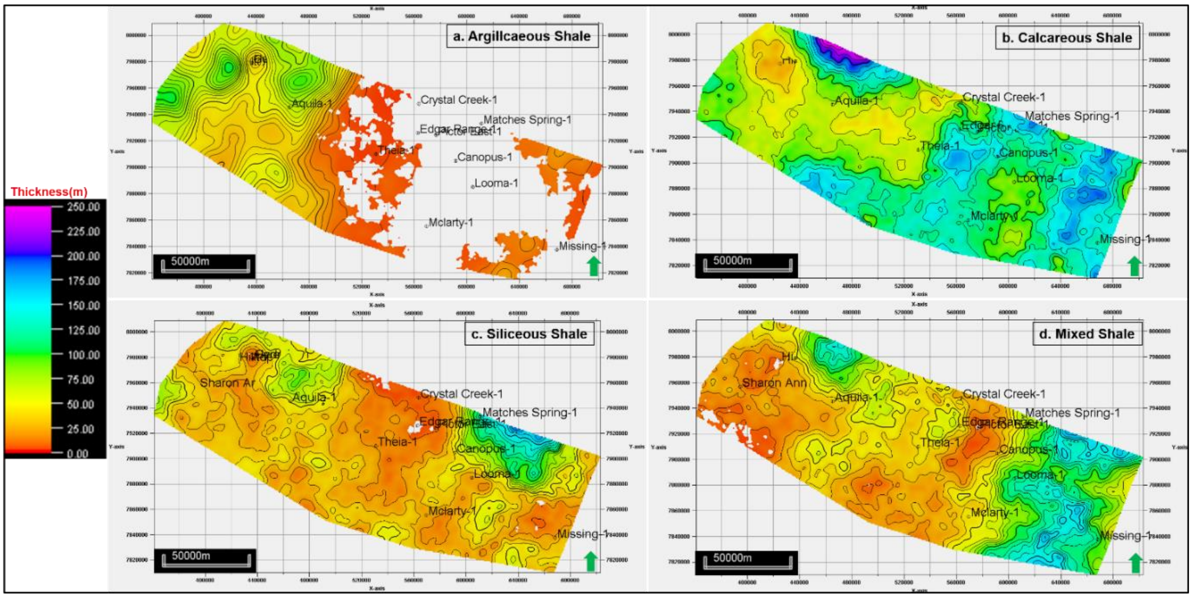

Figure 5.18: Averaged thickness maps of Goldywer-III shale lithofacies.

5.3.7.2 Petrophysical modelling

The lateral distribution of the petrophysical properties over the Broome Platform to the east Crossland Platform was estimated using the Sequential Gaussian Simulation method. Maps of the average properties per lithofacies are described below.

Generating the property average maps is a common and efficient way to simplify the model assessments. Therefore, average maps were generated for each petrophysical property with respect to different lithofacies.

A. TOC average maps

TOC average maps were generated for each of the four lithofacies in the Goldwyer-III shale (Figure 5.20). The averaged TOC for the argillaceous shale ranges from 1.5 to 2.5 wt%, except where it thins to the SE (Figure 5.20a), which is similar to the TOC measured on Goldwyer-III shale samples in Theia-1, although the organic rich high TOC thin beds are not adequately captured in the averaging process.

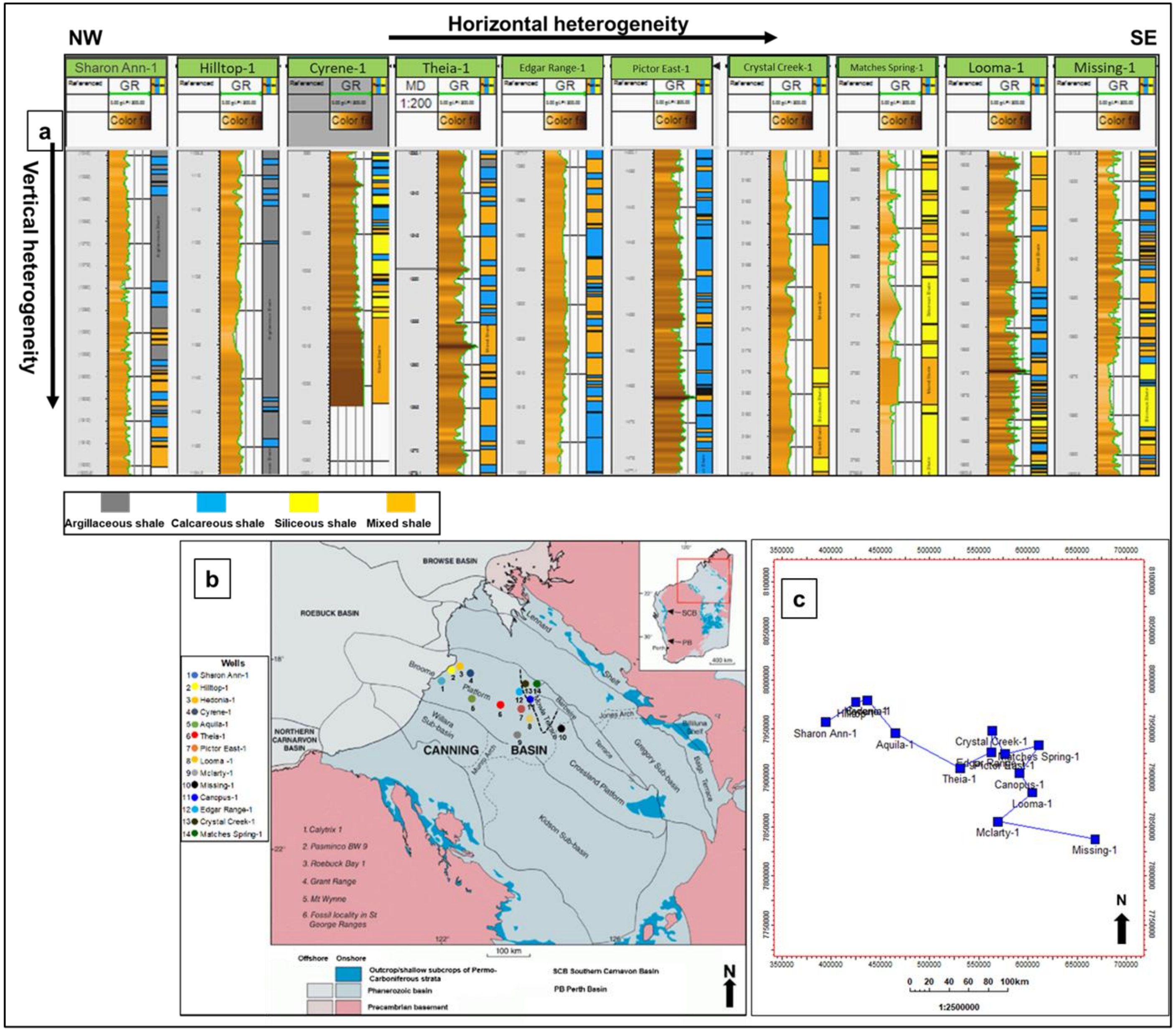

Figure 5.19: a) Well section showing vertical and horizontal heterogeneities in Goldwyer-III shale lithofacies; b) Geographical locations of the wells in Canning Basin; c) Map section showing well to well locations.

The TOC for the calcareous shale mostly ranges from 1 to 2.5 wt% with the highest values towards the NW where it is thin, but decreasing to 1-2% towards the central part of Broome platform where it is thick in the Theia-1 area, and increasing again towards the SE in the Crossland platform (Figure 5.20b). The TOC of the siliceous shale is typically <1% over most of the area with some higher values up to 2.5 % towards SE in Missing-1 (Figure 5.20c). In contrast, the TOC of the mixed shale has a larger range from 1-3 wt% for most of the study area decreasing to the SE where it is mostly 1-2.5% (Figure 5.20d).

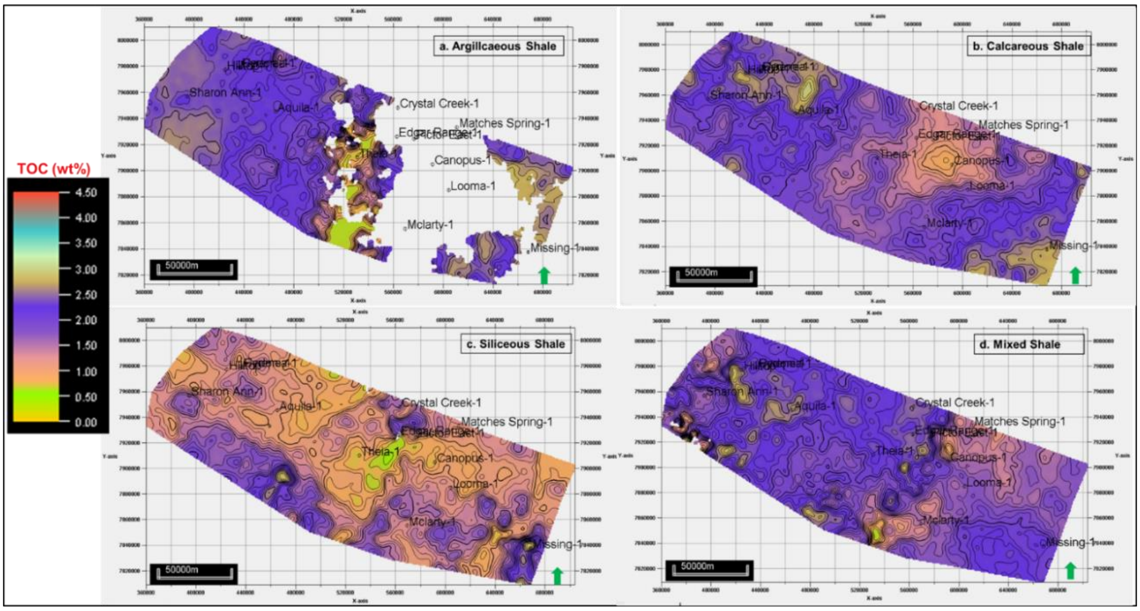

Figure 5.20: TOC distribution maps of Goldwyer-III shale lithofacies based on 3-D modelling across Broome and Crossland platforms.

B. Total porosity average maps

The total porosity (PHIT) average maps generated for the four lithofacies of Goldwyer-III shale are shown in Figure 5.21. Overall, the shale lithofacies have >6 % porosity except for some minor areas in the argillaceous and calcareous shales. The porosity of the argillaceous shale is typically lower than the other lithofacies mostly around 6% and in the range of 7 to 12 %. Some areas in the east have higher porosity probably due to more organic rich layers, such as in the central area at Theia-1 and to the SE at Missing-1. The porosity of the calcareous shale ranges from 7 to 15 %, increasing towards the NW and the SE, and may decrease in the south-central area where there is no well data (Figure 5.21b).

The porosity of the siliceous shale is typically higher around 10% and varies from 8 to 16 % with the highest values towards the SE and NW (Figure 5.21c). Whereas PHIT is decreasing towards centre of Broome platform. The mixed shales have the highest porosity typically around 12-14%, with a range from 9 to 17%. The porosity is highest towards the west and increases towards the SE in the Crossland Platform (Figure 5.21d).

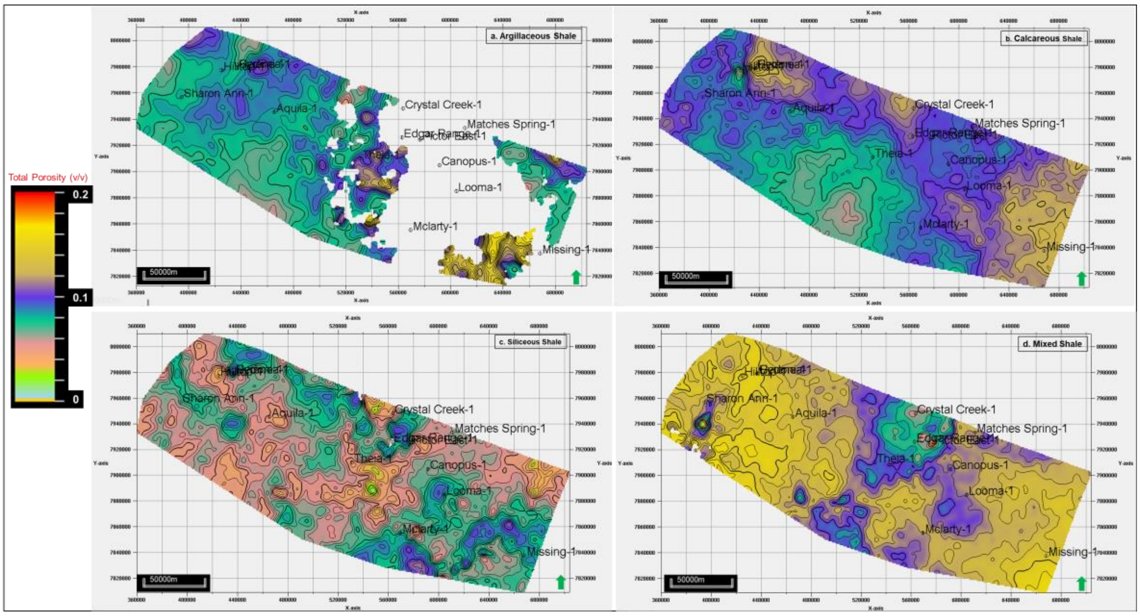

Figure 5.21: Total porosity maps of Goldwyer-III shale lithofacies based on 3-D modelling across Broome and west Crossland platforms.

C. Water saturation average maps

The average water saturation (Sw) maps for the four lithofacies of Goldwyer-III shale are shown in Figure 5.22. The maps show significant differences between each lithofacies. The argillaceous shales have high Sw values typically around 70-80% with some lower values towards the SE (Figure 5.22a). The Sw of the calcareous shales is lower typically 50-70%, with lower values down to 40% in the NW and higher values up to 90% in the NE (Figure 5.22b).

The water saturation of the siliceous shale is the lowest, mostly around 30-60% with some higher values up to 85 % in the central north area around Theia-1 (Figure 5.22c). Similarly, the Sw of the mixed shale ranges from 30 to 60% over most of the central and NW areas but increases to 60-80% in the SE in the Crossland platform (Figure 5.22d).

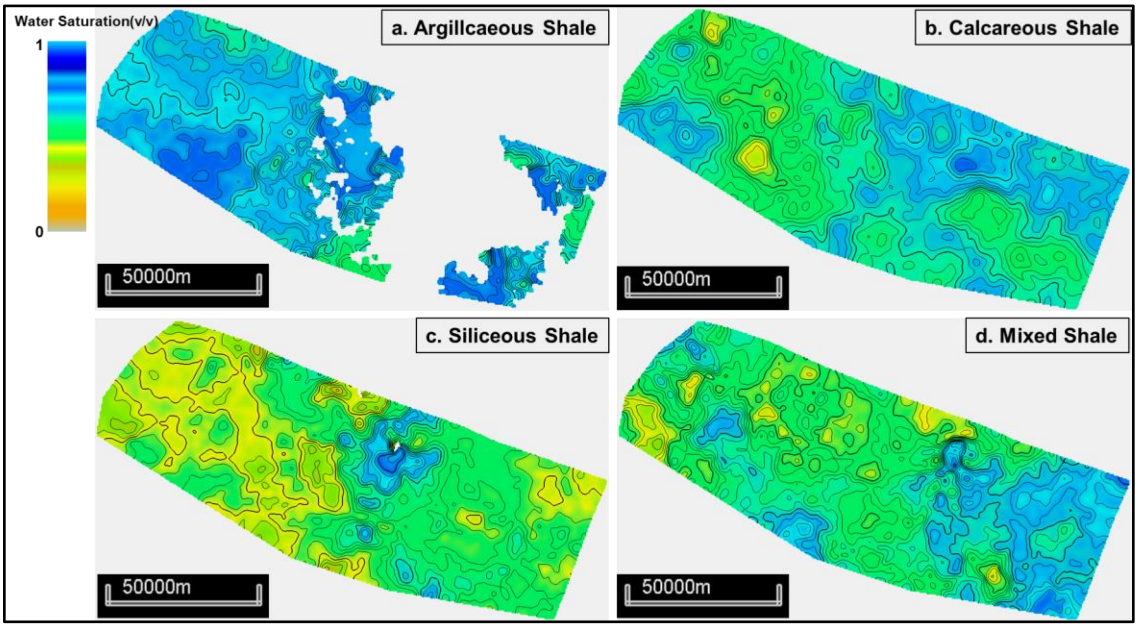

Figure 5.22: Water saturation maps of Goldwyer-III shale lithofacies based on 3-D modelling across Broome and west Crossland platforms.

D. Adsorbed gas average maps

The average adsorbed gas content (gc) maps for the four lithofacies of Goldwyer-III shale are shown in Figure 5.23. The maps show clearly that the argillaceous shales and mixed shales contain substantially more adsorbed gas around 50-60 scf/ton than the siliceous and calcareous shales which contain only 10-30 scf/ton of adsorbed gas. In the argillaceous shale the adsorbed gas mostly ranges from 40 to 60 scf/ton which appears to decrease towards the south (Figure 5.23a).

In the calcareous shale, the adsorbed gas ranges from 10 scf/ton in the SE to 40 scf/ton in the NW (Figure 5.23b). The adsorbed gas is similarly low in the siliceous shale mostly around 10-20 scf/ton, varying from 5 in the SE around Missing-1 up to 35 scf/ton in the central south and decreasing to 10-15 scf/ton in the NW (Figure 5.23c). The adsorbed gas increases in the mixed shale typically around 40-65 scf/ton in the NW and 45-60 in the SE with lower values in the central area around 20-50 scf/ton (Figure 5.23d).

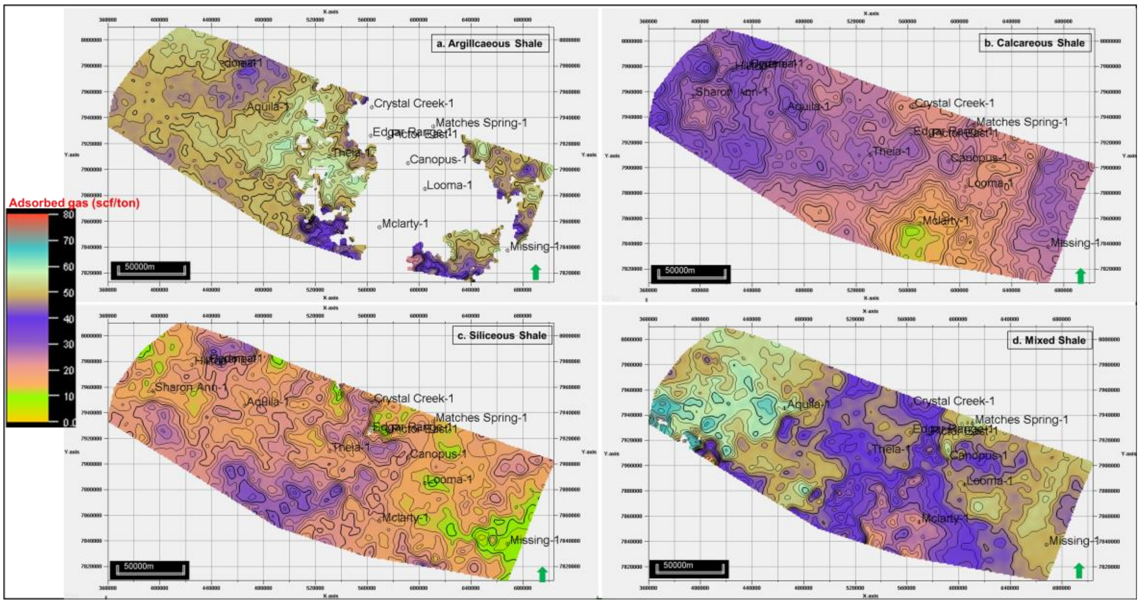

Figure 5.23: Adsorbed gas maps of Goldwyer-III shale lithofacies based on 3-D modelling across Broome and west Crossland platforms.

5.3.7.3 Geomechanical modelling

The geomechanical properties (Poisson's ration, Young's modulus, and Brittleness index), were determined via equations 5.4 to 5.7 and calibrated to core analysis results in Theia-1 well (as described in Chapter 5.3.7.2). A 3-D geomechanical model was generated in Petrel using the Sequential Guassian Simulation (SGS) for each property based on the variogram parameters given in Table 5.3. The lithofacies clusters identified through the K-means clustering were entered into the Petrel as discrete logs for each well. These were then upscaled into the Goldwyer-III shale (the zones and layers). The lithofacies discrete logs were then interpolated through the 3D model of the Goldwyer-III shale constrained by the well tops. An example of Theia-1 well location and well tops are shown in Figure 5.8.

A. Poisson's ratio average maps

The Poisson's ratio (μ) is the ratio of transverse strain to axial strain (expansion or contraction) in directions perpendicular to the direction of stress (loading or extension) and for rocks is controlled by lithology and normally increases with porosity. The average poisson's ratio maps for the Goldwyer-III shale's lithofacies are shown in Figure 5.24. Overall, the poisson's ratio of Goldwyer-III shale varies from low values in the siliceous shales around 0.2, to moderate values of around 0.22-0.25 in the calcareous and mixed shales, up to around 0.3 in the argillaceous shales. In the argillaceous shale the poisson's ratio is reasonably uniform and mainly ranges from 0.28 to 30 with some localised slighly lower values (Figure 5.24a). The poisson's ratio of the calcareous shale is more variable and ranges from about 0.2 over most of the area increasing up to 0.25 in the central south and NW areas (Figure 5.24b).

The Poisson's ratio of the siliceous shale is much lower and uniform varying from about 0.18 increasing locally up to 0.22 (Figure 5.24c). The Poisson's ratio of the mixed shale is higher and variable similar to the calcareous shale, being around 0.2-0.24 in the NW and far SE but higher between about 0.24-0.28 in the central south area (Figure 5.24d).

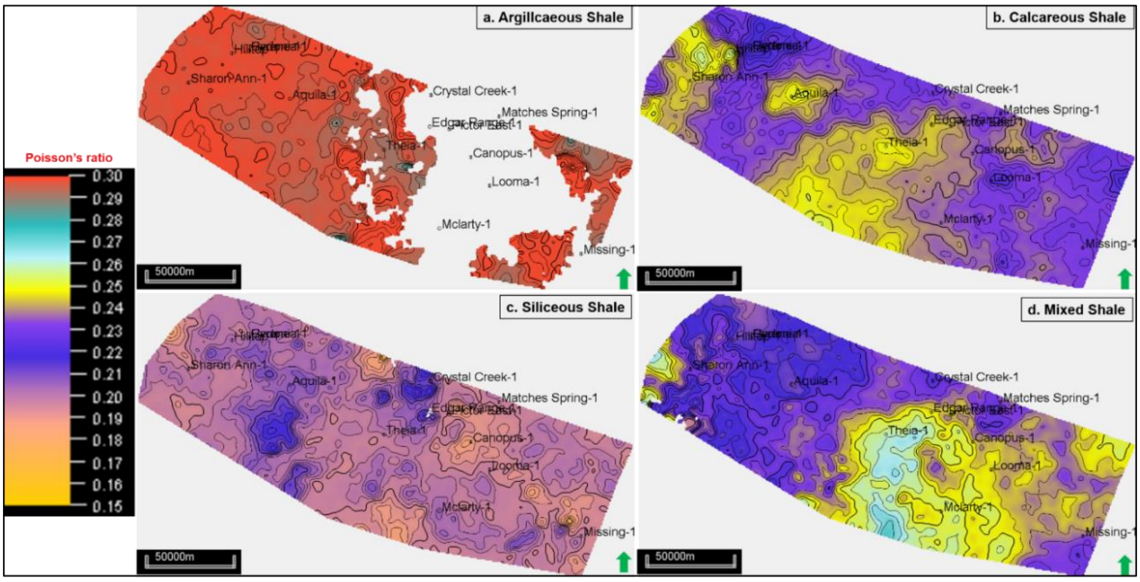

Figure 5.24: Poisson's ratio maps of Goldwyer-III shale lithofacies based on 3-D modelling across Broome and west Crossland platforms.

B. Young's modulus average maps

The Young's modulus (E) is the ratio of tensile stress (σ) to tensile strain (ε). The average maps of Young's modulus for the four lithofacies range from low values of around 7 Gpa in the argillaceous shales up to around 30 Gpa in the siliceous shales and are shown in (Figure 5.25). Young's modulus in the argillaceous shale is uniform mostly about 10 Gpa (Figure 5.25a). The Young's modulus of the calcareous shale is also uniform but higher in the range of 15 to 20 Gpa, decreasing slighly towards the east and in the south central areas (Figure 5.25b).

In contrast, the Young's modulus of the siliceous shale is more variable and ranges from 20 Gpa mainly in the south and SW to 32 Gpa mainly in the NE (Figure 5.25c). The Young's modulus of the mixed shale is low and moderately uniform in the range of 15-20 Gpa over most of the area increasing to up to 25 Gpa locally in the NW near Hedonia-1 (Figure 5.25d).

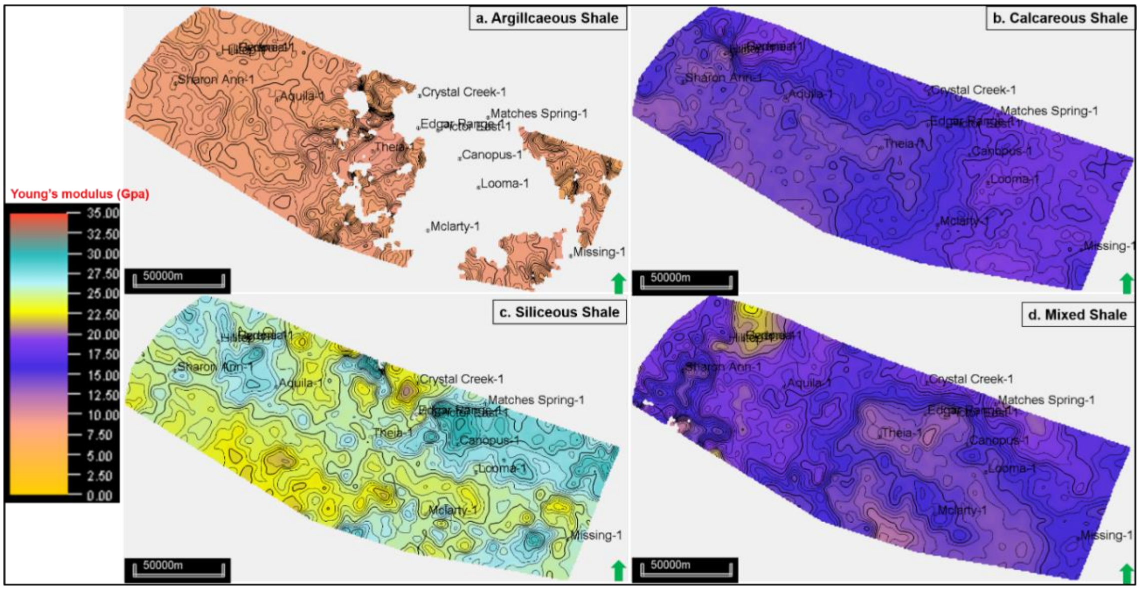

Figure 5.25: Young's modulus maps of Goldwyer-III shale lithofacies based on 3-D modelling across Broome and west Crossland platforms.

C. Brittleness index average maps

The brittleness index (BI) is an important indicator of rock strength for unconventional shales. The maps of average calculated brittleness index for the four Goldwyer-III shale lithofacies show variation almost across the total range from about 0.5 to 0.8 (Figure 5.26). The argillaceous shale has low brittleness indices mostly from 0.53-0.55 decreasing to 0.5 towards the NW (Figure 5.26a). The brittleness index of the calcareous shale ranges from 0.6 to 0.71 which increases towards the east to around 0.7 (Figure 5.26b).

The brittleness index of the siliceous shale is the highest mostly ranging from 0.75 to 0.78 with local values down to 0.72 and approaching 0.8 (Figure 5.26c). The brittleness index of the mixed shale is lower and more variable similar to the calcareous shales, mostly in the range 0.65-0.7, but increasing towards the NW and SE to values around 0.75, and decreasing towards the central Broome Platform to values of 0.6 near Theia-1 (Figure 5.26d).

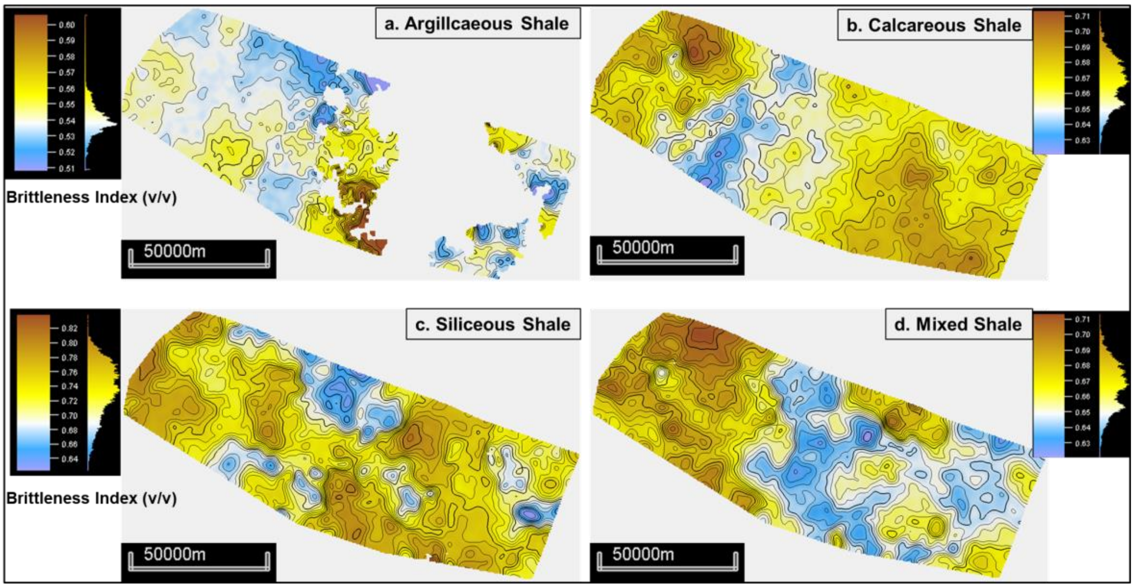

Figure 5.26: Brittleness index maps of Goldwyer-III shale lithofacies based on 3-D modelling across Broome and west Crossland platforms.

5.4 Discussion

5.4.1 Vertical and horizontal heterogeneities of Goldwyer-III shale

In this study, the distribution of lithofacies, petrophysical and geomechanical properties has been used to characterise the heterogeneity in the Goldwyer III shales, aimed at understanding and identifying areas with the highest potential for production of unconventional gas or sweet spots at the basin level. The data from the Theia-1 well provide good examples of the vertical heterogeneity in the Goldwyer-III shale as described in Chapter 2 and in (Iqbal et al., 2022). The regional scaled heterogeneity needs to be modelled in 3D as demonstrated in this chapter to extend the vertical heterogeneity into the horizontal domain, to gain a proper understanding of the variation in and control of depositional facies, on important variables such as the organic, petrophysical and geomechanical properties. This can be used then in well planning, optimum landing strategies and real-time geosteering along the high gas yielding beds.

At the gross regional scale, the variation in lithofacies thickness (refer to Figure 5.18) is linked to the changes in depositional settings over long periods of time, whereas the high resolution short term cyclic sedimentation is best seen on the vertical logs (Figure 5.19) and this figure also shows the variation in lithofacies from the NW to SE. The overall depositional setting was probably a shallow flat ramp beneath a shallow epeiric intracratonic sea (Figure 5.27) similar to that proposed by Ferguson (2016). Proximal lagoonal calcareous muds with thin organic rich muds were deposited inshore and inter-fingered into mid ramp carbonate buildups, with rare oolitic calcareous sands on local shoals, passing into mixed interbedded calcareous muds, organic muds, and siliceous silts in deeper water. Consequently, thick argillaceous shales are dominant in the NW in the shallow water lagoonal and restricted areas where organic content is high (e.g., Sharon Ann-1 to Theia-1 areas, Figure 5.19). These pass into calcareous shales and interbedded mixed shales in the central part of Broome platform where organic content is lower (e.g., Edgar Range-1 and Pictor-1). The mixed shales are thicker in the SE part of the Broome platform, along with the siliceous shales that represent more starved conditions especially during highstands (e.g., Crystal Creek-1 and Matches Springs-1, Figure 5.19). The fluctuations in organic content between the shales probably represent oxic, dysoxic and possibly anoxic fluctuations arising from cyclic changes in relative restriction, water depth and biological activity with time (Bruner et al., 2015; Iqbal et al., 2022; McCollum, 1988; Murphy et al., 2000; Schieber, 1999). The variations in the depositional environments and organic content are recognizable as para-sequences comprising vertically stacked lithofacies in each borehole (Jiang et al., 2015; Taylor & Goldring, 1993) as shown in Figure 5.19.

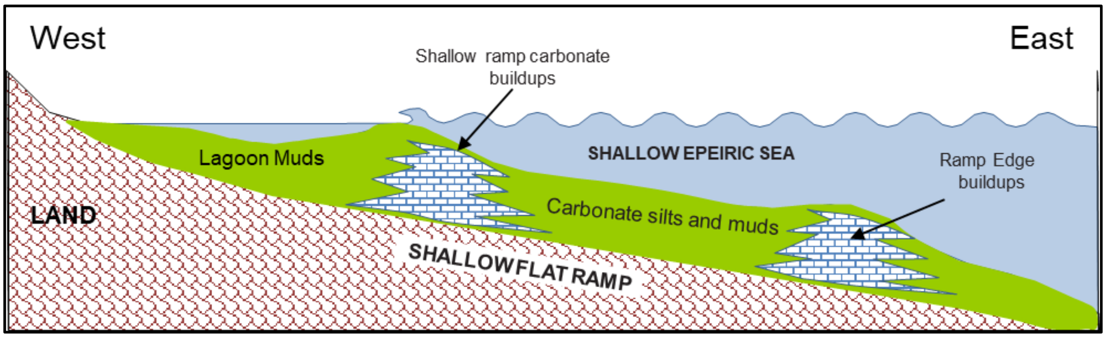

Figure 5.27: Schematic Depositional Facies for the Broome Platform study area.

5.4.2 Mechanical Stratigraphy – A novel approach to Identifying suitable layers

The integration of lithofacies, petrophysical and geomechanical properties with clustering in this study in effect produces a mechanical stratigraphy. The concept of mechanical stratigraphy as introduced here provides the ability for new insights to better understand the distribution of potential gas shale reservoirs across the Canning Basin. The relationship between Poisson's ratio and Young's modulus (Figure 5.28a-d) showed that the mixed shale lithofacies (cluster-2) has the highest brittleness index indicating it is the most suitable for hydraulic fracturing. In contrast the argillaceous shales (cluster-4) are least suitable for hydraulic fracturing. However, high brittleness is not enough on its own for the economic development of gas shale reservoirs, rather a combination of petrophysical and geomechanical properties are necessary (Gholami et al., 2016; Jin et al., 2015; Rezaee, 2015). The mechanical stratigraphy developed here can identify these beds, as shown in Figure 5.28 b-d, in which the mixed shale (cluster-2) has favourably lower water saturation, medium to high total porosity and high adsorbed gas. In contrast, the argillaceous shale (cluster-4), which has the lowest brittleness, has the highest water saturation and low total porosity, even though it has the highest adsorbed gas. The siliceous shales (cluster-1) and calcareous shales (cluster-3) have intermediate moderate to low petrophysical and geomechanical properties. Notably, mixed lithofacies are commonly considered the best rock types for successful development of gas shale reservoirs elsewhere in other worldwide basins (Alvarez & Schechter, 2017; Glorioso & Rattia, 2012; Li et al., 2020; Mandal, 2021; Zhou et al., 2019). It is important to highlight that although argillaceous shale has the highest adsorbed gas due to higher TOC and clay contents, its poor geomechanical properties mean that their development as a gas shale reservoir will be difficult and less likely than for some of the other shales. The mixed shales are the most likely to be developed as a gas shale reservoir due to their higher brittleness index and acceptable petrophysical properties even though they have lower TOC contents.

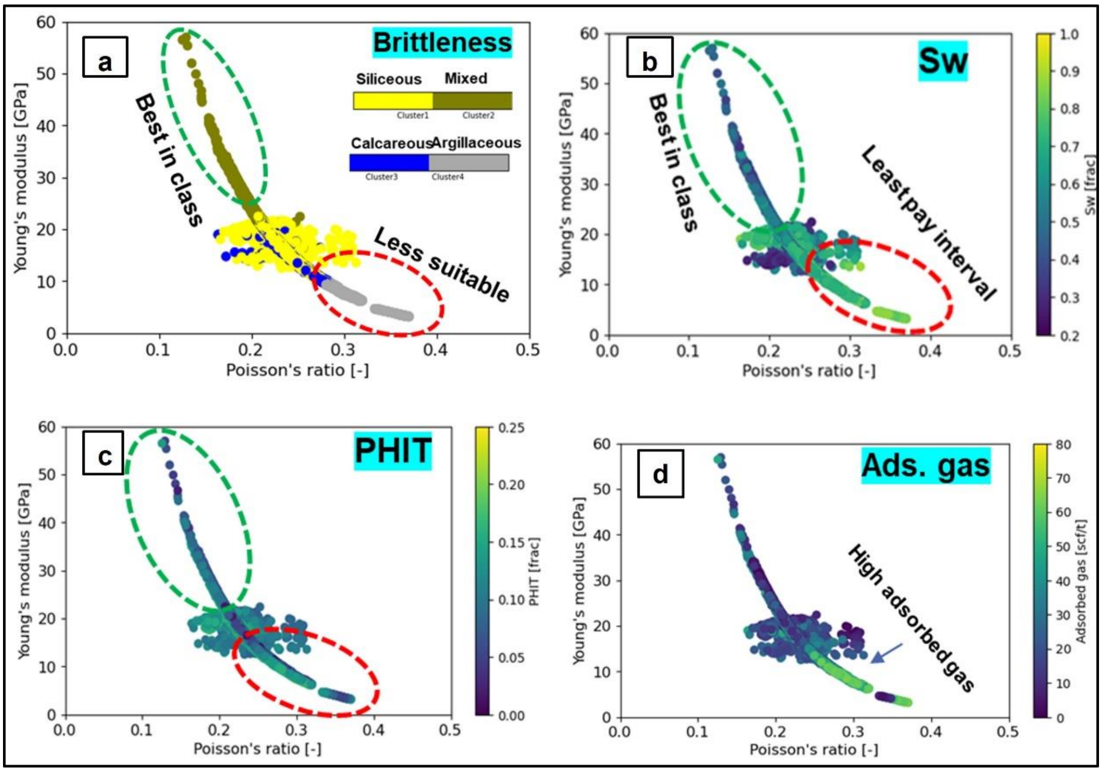

Figure 5.28: Cross plots of Young's modulus and Poisson's ration with variable colour codes based on petrophysical properties to illustrate the best clusters for hydraulic fracturing. The regions of each lithofacies/cluster in b,c,and d are same like a. The region in c (highlighted by green means high porous and red is low porous.

5.4.3 Influence of lithofacies on gas potential of Goldwyer-III shale

The gas shale reservoirs contain free as well as adsorbed gas with the free gas occurring in the pore spaces, whereas the adsorbed gas is sorbed onto the surface of the organic matter and clay minerals (Ekundayo & Rezaee, 2019; Iqbal et al., 2022; L. M. Johnson et al., 2020; Rezaee, 2015). The free gas potential of a shale reservoir mainly depends on porosity and water saturation which can be indicated by estimating the hydrocarbon pore volume (HPV) by using Eq. 5.12:

$$HPV = GRV * \frac{N}{G} * \emptyset * (1 - S_w)$$

(Eq. 5.12)

Where, GRV = Gross rock volume; $\frac{N}{G}$ = Net to gross ratio; $\emptyset$ = Porosity; S_w = Water saturation.

Hence, the hydrocarbon pore volume varies across the Broome and Crossland platforms with the variation in the thickness, porosity, adsorbed gas, and water saturation. The adsorbed gas is related to the organic matter and hence the thickness of the argillaceous shales and the mixed shales. Therefor, it is high in both the NW and SE parts of the basin but not in the central area where the calcareous shales occur. The porosity and water saturation are also related to the TOC of Goldwyer-III shale lithofacies so that the HPV is affected by TOC as well. Overall, the estimated HPV of the Goldwyer-III shale ranges from 100 to 400 scf/ton. The HPV increases towards the east and NE of the Broome and Crossland platforms, mainly resulting from an increase in thickness of producible lithofacies (siliceous and mixed shales), as well as the increasing porosity and Sw towards the east. This variation in HPV is complicated by the variations in the petrophysical characteristics shown by the different lithofacies in the Goldwyer-III shale. The porosity and water saturation of the siliceous and mixed shales are higher than other lithofacies, and the thickness of the mixed shale increases towards the east to become much higher than the argillaceous, calcareous and siliceous shales. Consequently, the HPV of the mixed shale, and to a lesser extent the siliceous shale, increases markedly to the east and NE. The map for HPV and adsorbed gas distribution as shown in Figure 5.29 and Figure 5.30, a high area to the NW but there are no wells in this area, and it results from the thickening of the mixed shale in that area, which is probably an artefact of the gridding process on the edge of the average thickness map (Figure 5.18).

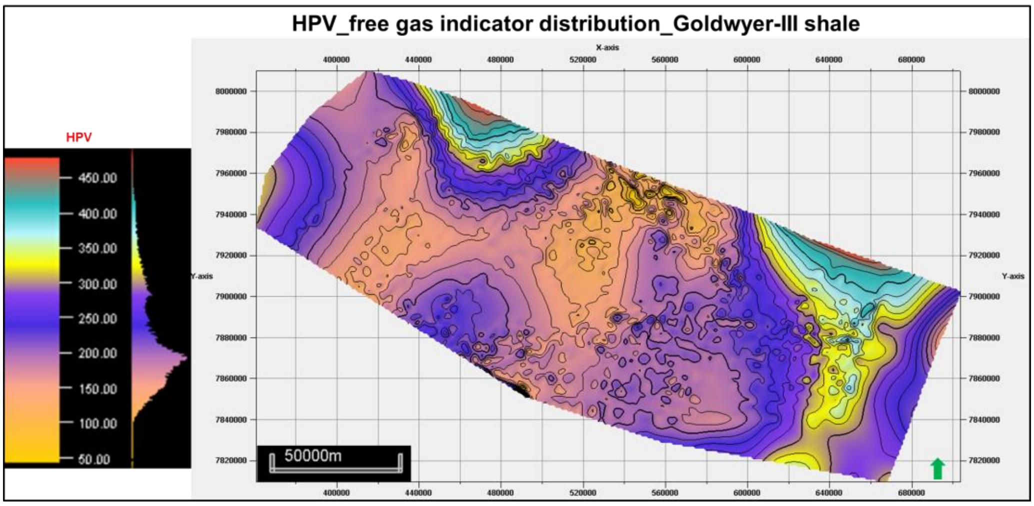

Figure 5.29: Hydrocarbon pore volume distribution of Goldwyer-III shale to indicate free gas potential across Broome and Crossland platforms.

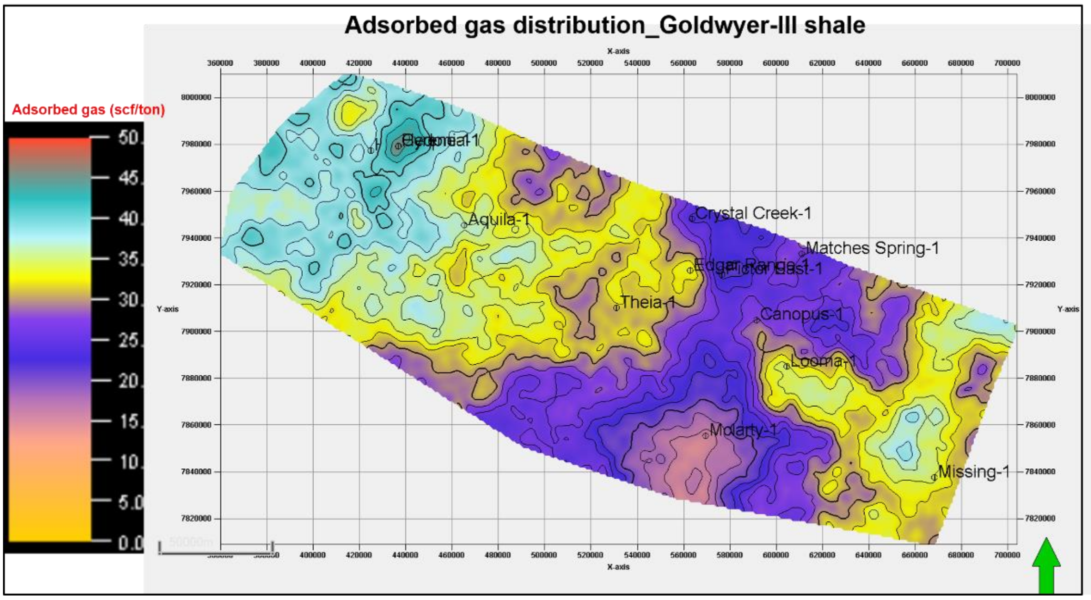

Figure 5.30: Adsorbed gas distribution of Goldwyer-III shale to indicate adsorbed gas potential across Broome and Crossland platforms.

5.4.4 Gas shale potential in Canning Basin

This study has shown that the gas shale potential of Goldwyer-III shale is controlled by the variable and heterogeneous nature of the shales, which can be characterised by integration of a multiscale and multi-variate analytical dataset, and that the occurrence of these lithofacies varies across the Broome Platform. The characteristic parameters for the different rock types in the Goldwyer-III shales are summarised in Table 5.8.

The relative potential for shale gas reservoir development shown by the different rock types (in decreasing order) is: mixed shale > siliceous shale > argillaceous shale > calcareous shale. The mixed shale has the best petrophysical and geomechanical properties of the identified lithofacies for production from these potential shale reservoirs and field development. The mixed shale has inter and intra particle mesopores, highest total porosity, low water saturation, higher adsorbed gas and highest brittleness index. The mixed shale has the best combination of petrophysical (TOC, total porosity, water saturation and adsorbed gas) and geomechanical properties (Poisson's ration, Young's modulus and brittleness index) and is best developed in the SE and central part of the Broome platform. The siliceous shales also have suitable shale reservoir properties and are best developed in the NW and SE parts of the basin. The properties of the mixed and siliceous shales are also within the acceptable range for prospective shale oil plays (Passey et al., 2010).

The argillaceous shale appears to be less suitable as a gas shale reservoir due to its poor petrophysical and geomechanical properties but has the highest TOC and is best developed in the NW of the basin. The argillaceous shales have low brittleness index which is estimated based on log equation. However, the log equation did not take in account the fact about the smectites (swelling clays) are transformed into non-swelling illites due to an increase in burial depth and dehydration of the clays so an increase in brittleness index can be expected. The calcareous shales have the poorest suite of properties.

Consequently, the SE and central parts of Broome platform appear to have the best potential for shale gas reservoir development. This observation is consistent with previous tectonic and gas shale studies of the Goldwyer Formation. Moreover, the detailed study carried out by (Johnson, 2019) for maturation and burial history of Goldwyer Formation also showed that the estimated burial history and temperatures in the central and south-eastern part of the Broome Platform indicates that these areas are in the mid to late mature window for petroleum generation.

Table 5.8: Overall summary of Goldwyer-III shale to illustrate the best rock types for hydrocarbon generation and production potential and their prospects across Broome and west Crossland platforms, Canning Basin, Western Australia.

Rock type	Core image	Mineralogy		TOC	Pore size	Pore type	GR	LLD	NPHI	DEN	DT	Porosity	Sw	Adsorbed gas	BI	Thickness	Prospectivity
Argillaceous shale	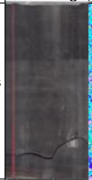	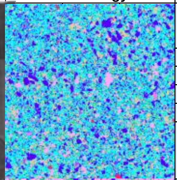	**Average**	2.8	micro and meso	interparticle, slit-like, bottle-neck	165	10	18	2.52	100	7	65	55	54	35m	NW
			std	0.9			23.11	5.2	18.94	0.11	9.88	0.03	0.14	10.65	0.03		
			min	0.5			45	1.5	0.17	2.09	93.04	0.03	0.29	3.74	0.41		
			max	4.5			227	49	45.00	2.70	144.93	0.24	0.99	80.88	0.59		
			Distinctive feature	Low to high			High, serrated & bell shaped	Low to high	High	Low	High	Low	High	High	Low		
Calcareous shale	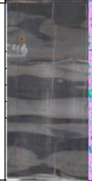	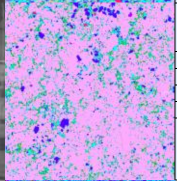	**Average**	1.2	meso	interparticle, wedge shaped	100	15	2	2.68	62	8.5	52	18	65	85m	NW & Centre
			std	0.76			36.37	12.18	4.55	0.05	3.29	0.03	0.11	11.88	0.03		
			min	0.02			38.68	2.60	0.18	2.53	41.78	0.05	0.20	0.05	0.72		
			max	3.87			214.63	254.68	25.83	2.76	69.20	0.17	0.87	53.27	0.82		
			Distinctive feature	Low			Low, funnel shaped, spiky to serrated	Low	Low	High	Low	Moderate	Low	Low	Moderate		
Siliceous shale		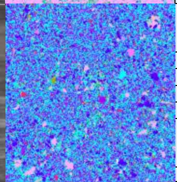	**Average**	2.00	meso and macro	interparticle, slit-like, bottle-neck	120.00	12.00	1.76	2.61	78.00	11.00	55.00	45.00	68.00	55m	NW-SE & Centre
			std	0.79			29.75	15.30	5.78	0.05	7.87	0.03	0.16	11.48	0.04		
			min	0.01			95.51	1.46	0.06	2.37	62.07	0.06	0.02	1.01	0.56		
			max	4.43			307.75	285.76	35.81	2.73	96.97	0.18	1.00	87.60	0.79		
			Distinctive feature	Moderate			Moderate, funnel shaped	Low to moderate	Low	Moderate	Moderate	High	Low	Moderate	High		
Mixed shale	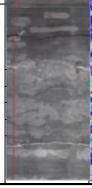	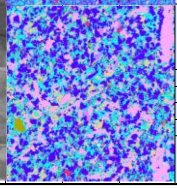	**Average**	2.50	meso	inter&intraparticle, slit-like, bottle-neck	130.00	13.00	5.50	2.61	78.00	12.00	58.00	48.00	72.00	70m	NW-SE & Centre
			std	0.93			32.31	9.84	10.53	0.05	7.73	0.03	0.17	10.54	0.04		
			min	0.01			53.88	1.75	0.03	2.37	63.90	0.07	0.14	0.01	0.56		
			max	4.71			215.61	174.18	45.00	2.75	95.31	0.19	1.01	56.73	0.78		
			Distinctive feature	Moderate to high			Moderate, serrated and bell shaped	Moderate	Moderate	Moderate	Moderate	High	Low to moderate	Moderate	High		

5.5 Conclusions

The integrated multiscale characterisation helped us to conclude that:

i. The vertical or stratal heterogeneity of the Goldwyer-III shales can be measured in terms of mineralogy, total organic carbon, petrophysical and geomechanical properties and classified into four lithofacies: argillaceous shale, calcareous shale, siliceous shale and mixed shale.

ii. Synthetic logs could be generated for wells that did not contain density and neutron logs by using supervised machine learning for which the random forest algorithm worked best with the highest correlation factor.

iii. K-means clustering of the well logs can be used to identify the lithofacies rock types in wells drilled in the study area. The systematic approach of K-means clustering helped to identify four distinct clusters in such a way that cluster-1 corresponds to siliceous shale, cluster-2 to mixed shale, cluster-3 to calcareous shale and cluster-4 to argillaceous shale.

iv. The lateral variation in the lithofacies can be mapped in 3-D Petrel models to identify the distribution of the rock types across the Broome Platform.

v. Sequential Gaussian Simulation (SGS) provided the best results for 3-D modelling of the petrophysical and geomechanical shale properties.

vi. Mechanical stratigraphy was introduced to identify the producible and brittle layers for shale reservoir development. This novel concept involves integrating lithofacies with petrophysical and geomechanical properties. The mechanical stratigraphy showed that the producibility and brittleness of the lithofacies rock types typically decreases from: mixed shale>siliceous shale>argillaceous shale>calcareous shale. That is, the mixed and siliceous shales probably have the best potential for gas shale development in the Goldwyer-III shale.

vii. The 3-D modelling indicated that the mixed shale and siliceous shales are widely distributed across the Broome Platform but are best developed in the SE and central parts of the Broome platform.

Chapter 6 Conclusions and Recommendations

6.1 Conclusions

This thesis presents a multiscale integration of various datasets to characterise the potential of the Goldwyer-III shales for development as a gas shale reservoir. The multiscale approach included core logging, well log analysis, laboratory petrophysical analyses, microscopic analyses, high-resolution mineral mapping, machine learning, and 3-D modelling. The core logging helped to identify the various rock types based on colour, sedimentary features, and lithology. The machine learning approach was able to predict the vertical downhole variation thereby creating the missing well logs and to classify the rock types into different clusters. A 3-D model delineated the lateral variation of the Goldwyer-III shale reservoir and its distribution of facies, petrophysical and geomechanical properties across the Broome Platform.

This research also demonstrated the use of an integrated workflow that can be used elsewhere to understand the heterogeneity of gas shale reservoirs. This included (i) identifying different rock types based on mineralogical, geological, and petrophysical characteristics; (ii) providing corresponding high-resolution mineralogy maps for the main lithofacies to better understand their mineral compositions and lateral distributions; (iii) derived equations for determination of total porosity and water saturation of gas shale reservoirs from well logs; iv) introduced mechanical stratigraphy by incorporating petrophysical and geomechanical data with clustering to identify the best lithofacies for hydraulic fracturing; v) built 3-D model for the lithofacies and petrophysical and geomechanical properties to understand the heterogeneities at the regional level over the Broome Platform.

The key findings of **Chapter 2** were that the Goldwyer-III shale (Goldwyer-III) is significantly heterogeneous as measured at the macro-scale in cores by the integration of HyLogger3 data, FTIR with core linescan, image logs and petrographic data. The results showed that the rock types can be divided into four lithofacies based on colour, lithology and sedimentary features. The identified facies are thinly laminated siliceous shale (TLSh), concretionary-banded calcareous shale (CSh), massive black shale (MBSh) and heterolithic shale (HSh). The core log based sedimentary lithofacies vary with respect to depositional environments and organic content. The HyLogger3 data, FTIR, image logs and petrographic data showed that the Goldwyer III shale is mainly composed of illitic shales, with thin organic-rich, siliceous and calcareous layers, that contain varying amounts of TOC and brittle minerals. The multiscale assessment helped to understand and identify the thin layers and most probable gas reservoir zones which otherwise may have been overlooked. This approach can improve economic decisions when developing gas shale reservoirs.

In **Chapter 3** the lithofacies heterogeneities were evaluated at the micro scale based on mineral composition and TOC allowing sub-division into five lithofacies. The correlation and distribution profile of Goldwyer-III shale facies among the wells from Broome Platform, Canning Basin have shown the vertical and lateral heterogeneities. This understanding of heterogeneities was based on core-scale study. A new workflow was proposed for lithofacies classification of Goldwyer-III shale based on defined mineralogy and TOC cut-off values. The identified lithofacies are named as organic-rich shale, argillaceous shale, siliceous shale, calcareous shale and mixed shale. The impact of different lithofacies on the porosity and pore structure was highlighted to evaluate the storage capacity in different lithofacies.

The pore micro-structure and grain morphology are related to the lithofacies resulting from variations in the organic composition and the mineralogy. The organic-rich shale contains slit-shaped organic pores, whereas the argillaceous and siliceous shales contain bottle-necked slit-shaped inter-particle pores. The calcareous and mixed shales contain predominantly wedge-shaped or narrow slit-like intra-particle pores. These differences in the pore structure and morphology were linked with the total porosity and gas storage capacity of the lithofacies of Goldwyer-III shale. The organic matter and inter-particle pores were the main controlling factor for the porosity in the organic-rich and argillaceous shales. The whole pore aperture analysis indicated that mesopores were the most abundant pores in the Goldwyer-III shale. The lithofacies also controlled the amount of micro and macropores in the Goldwyer-III shale, wherein the organic rich shales have micropores and mixed shales have macropores. The integration of lithofacies with petrophysical properties also suggested that the organic-rich, siliceous and mixed shale lithofacies in Goldwyer-III shale were better for fluid flow via their enhanced pore systems.

The sedimentary facies (classified in Chapter 2) and lithofacies from Chapter 3 are same in terms of composition, however, due to the heterogeneities, extra high-resolution analyses were required to provide cut-offs values to distinguish the different shale lithofacies (as explained in Chapter 3). The reconciliation of these two classifications is as follow numbered to show their corresponcence:

<u>Sedimentary facies</u>

1. Thinly laminated siliceous shale (TLSh),
2. Concretionary-banded calcareous shale (CSh),
3. Massive black shale (MBSh)
4. Heterolithic shale (HSh).

<u>Lithofacies</u>

1. Siliceous shale
2. Calcareous shale
3. Argillaceous shale plus the organic-rich shale,
4. Mixed shale

The classifications above have been shown to correspond and high-resolution analytical work allowed separation of the massive black shale into organic rich and non-organic rich shales. The results demonstrated that the logs could not accurately detect organic matter at low organic matter contents (e.g. TOC<3 wt%) which remains a major challenge for evaluation of the Goldwyer Formation. This is important and it means attempts to use the logs for TOC estimation will struggle in the Canning Basin, whereas this is not a problem in shales with TOC>5 wt% as in the case of Bakken shale.

In **Chapter 4** the gas storage capacity of the lithofacies in the Goldwyer-III shales lithofacies was estimated by carrying out laboratory analyses to estimate porosity and water saturation. However, a continuous profile of total porosity and water saturation for each well were also important to understand the producibility of Goldwyer III shale across the Broome Platform. Therefore, new equations for total porosity and water saturation were proposed for their estimation based on well logs. The proposed equations were corrected for kerogen effects on the density logs to estimate total porosity more accurately. Similarly, the resistivity logs were corrected for the kerogen and shale effects to compute a more accurate water saturation for the shales.

The results indicated that the conventional density log overestimated the total porosity by 8-15%. The new total porosity log based on the density log corrected for kerogen content and kerogen porosity matched very well with the core-based porosity over the range from 5 to 10%. Moreover, the conventional equations overestimated the water saturation with more than 100% in most of the intervals. The new proposed water saturation equation (a modified Archie equation) provided better results and correlation with core-based water saturation over the range from 35 to 80%. Moreover, the introduced modified Archie equation was independent of water resistivity and Archie parameters as these inputs were very difficult to obtain for gas shale reservoirs. This chapter also indicated that the mixed shale and siliceous shale lithofacies have the most gas shale potential in Goldwyer-III shale.

In **Chapter 5** the results from the previous chapters was synthesised into regional interpretations. The earlier chapters focused on identifying the best rock types based on petrophysical properties, TOC and mineral compositions on cores but these results were limited to downhole samples. Moreover, the best rock types should also fulfill the criteria of geomechanical properties to understand the hydraulic fracturing potential. Therefore, Chapter 5 presented an additional workflow incorporating 3-D modelling with geostatistics and the power of machine learning to help address issues specific to development of unconventional energy resources.

First, supervised machine learning allowed prediction of density and neutron logs in wells where they were absent. Several methods were tested which found that the Random Forest algorithm provided the best results, and this provided a complete set of logs that were required for the 14 wells used in this study. The well log suite, augmented by petrophysical and geomechanical measurements, was then used to identify the lithofacies and predict the rock types in all wells, using unsupervised machine learning with K-means clustering. This new approach importantly allowed integration of all the rock type properties for identifying the best rock types with the highest brittleness index: effectively recognizing and defining the mechanical stratigraphy. The mechanical stratigraphy indicated that the producibility and brittleness decreased in the following order: mixed shale>siliceous shale>argillaceous shale>calcareous shale, that is, the mixed shale and siliceous shales probably have the potential for gas shale development in the Goldwyer-III shale.

The lateral and vertical shale distribution of rock types in the Goldwyer III shale over the Broome Platform was then modelled in 3-D using the Petrel software. This included modelling the distribution of facies, TOC, petrophysical and geomechanical properties and good results were achieved using geostatistics and Sequential Gaussian Simulation (SGS). The 3-D modelling showed that the mixed shale and siliceous shales are widely distributed across the Broome Platform with the best development of potential gas shale reservoirs occurring in the south-east and central areas.

Together the chapters in the thesis have provided an integrated method for analysis, evaluation and synthesis of potential shale gas formations in the Broome Platform. The results form a valuable case study that is applicable to many other sedimentary basins throughout the world.

6.2 Limitations and Recommendations

This research followed a series of detailed workflows, to assess and evaluate the heterogeneous shales within the Goldwyer III shale, aimed at identification of the best rock types for possible production of shale gas. However, there are still limitations which can be addressed by considering the recommendations of this thesis.

- The data for research about gas shale reservoirs is still limited so more laboratory-based results should be added by getting more shale samples. The addition of such a dataset would be helpful for validation and training purposes of the machine learning approach. Therefore, more refined and high confidence outputs can be obtained in the future through data analytics.
- 3-D facies, petrophysical and geomechanical models were built based on the available 2-D seismic data in Canning Basin, Western Australia. However, the quality of the open file 2D seismic data is poor which means the modelled location of the main horizons which were used to build and tie the wells for input to the 3-D models is not precise. Clearly it would be advisable to acquire a 3-D seismic dataset prior to production for refinement of the seismic stratigraphy and structure that can be linked with the rock types identified in this study.
- The rock types that were defined using unsupervised clustering were based on the core samples. Some of the dataset is limited, for example TOC, XRD and other mineralogy data, and would benefit from additional samples. This dataset should be expanded for improved validation and revision via supervised machine learning and this should produce better and more detailed rock typing.
- This research showed that HyLogger data is very useful when integrated with laboratory analyses. The HyLogger data are becoming widely available for most wells and should be used with the mineralogical data as in this study. More research is required to investigate how the organic petrography data can be calibrated to define the characteristic spectra for organic matter and similarly other valuable minerals. The biostratigraphic data may be of use for helping to locate the thin organic-rich beds more accurately. If this is pursued then a much better dataset could be obtained to identify the mineralogy and TOC for model refinement.

Multiscale reservoir characterisation of gas shale reservoirs is a key approach for the evaluation of the heterogeneity and potential producibility for unconventional resources. This methodology should lead to more informed decisions with respect to the successful development of shale gas. This study presented some detailed workflows including several novel approaches to achieve the above. Clearly, the methods described in this study can be improved and better results can be achieved by using much larger datasets.

Appendix-A Nomenclature and Tables

Nomenclature

$ØD$	density porosity
ρ_{ma}	matrix density
ρ_b	bulk density
ρ_f	fluid density
ρ_b	bulk density (g/cc)
γ	kerogen conversion factor
ρ_k	kerogen density (g/cc).
ρ_g	grain density
ρ_{bk}	kerogen corrected bulk density
$Ø$	porosity
$Øk$	kerogen porosity
$ØD_{Total}$	total density porosity
a	tortuosity factor
Cc	convertible carbon fraction
C_t	total conductivity
C_w	formation water conductivity
HIp	present hydrogen index
HIo	original hydrogen index
m	cementation exponent
n	saturation exponent
PIp	present production index
PIo	original production index
R_w	formation water resistivity
R_{sh}	resistivity of shale
R_t	true resistivity in ohm-m

R_o the rock resistivity in lean shale interval where water saturation is deemed 100%

R_k Kerogen resistivity

S_w water saturation

TOC total organic carbon content

TOCo original total organic carbon

TR transformation ratio

V_k kerogen volume in fractions

V_{sh} volume of shale

Appendix-A1: Mineralogical compositions of Goldwyer-III shale samples.

Sample ID	Well Name	Depth (m)	Lithofacies	Quartz	Plagioclase	K-feldspar	Mica		Clay						Carbonates	
					Albite	Microcline	Biotite	Muscovite	Illite	Illite+Mica	Kaolinite	Chlorite	Smectite/mixed	Pyrite	Calcite	Dolomite
GS-1		1334.85	Mixed Shale	20.15	4.44	6.58	0.68	5.58	19.68	25.94	0.26	1.29	0.99	0.35	38.6	1.41
GS-2		1336.05	Mixed Shale	17.58	4.67	15	7.39		27.5	34.89	0.15		0.8	2.07	22.63	2.3
GS-3		1473	Argillaceous Shale	20.66	5.13	13.7	4.82		40	44.82	0.44	5.9	0.84	2	5.59	0.94
GS-4		1478	Siliceous Shale	26.14	5.45	10.55	3.3	10.89	24.84	39.03	1.3	5		3.1	10	
GS-5		1478.3	Argillaceous Shale	12.94	4.89	17.27	6.95	20.62	26.1	53.67	0.29		0.89	4.44	5.62	0
GS-6		1479.76	Argillaceous Shale	15	5	3			48	48	1	6	4	1	-	-
GS-8	**Theia 1**	1496.62	Siliceous Shale	18.76	4.66	12.44	4.37	13.83	25.86	44.06	0.16		0.76	3.82	14.48	0.86
GS-9		1499.05	Argillaceous Shale	8.78	1.67	4.56	0.92	7.14	48.94	57	0.1	4.49	0.56	2.59	18.88	1.35
GS-10		1499.56	Calcareous Shale	11	3	2			40	40	-	4	1	1	37	1
GS-11		1506	Argillaceous Shale	16.2			1.5	4.5	47	53	1.6	5.4		2.5	13.5	1.5
GS-12		1508.14	Mixed Shale	14.94	4.1	10.41	4.14	11.84	19.49	35.47	0.14		0.69	2.28	31.96	0.06
GS-13		1508.96	Calcareous Shale	5.32	2.94	4.72	0	0.46	2.02	2.48	0.37	0	1.12	0.73	82.16	0
GS-14		1510.23	Mixed Shale	18.34	4.68	7.81	2.86	11.76	9.72	24.34	0.3	4.38	0.98	2.32	22.69	12.88
GS-15		1514.27	Calcareous Shale	11	3	1			14	14	-	2	1	1	66	1

GS-16		1516	Mixed Shale	17.3		6			48.3	48.3	2.3	3.6			12	1.5
GS-17		1516.55	Argillaceous Shale	10.72	2.77	13.99	2.49		52.55	55.04	0.11		0.6	1.78	13.74	1.25
GS-18		1518.08	Argillaceous Shale	6.05	0.99	7.66	1.02	44.07	28	73.09	0.06		0.33	1.45	9.56	0.81
GS-19		1521	Siliceous Shale	26.58	6	11.44	3.35	10.15	23.88	37.38	1.4	3.7	0.83	4.17	7.19	2.14
GS-20		1521.93	Argillaceous Shale	11.89	8.65	14.11	0.27	23.94	20.06	44.27	0.1	9.88	0.39	0.1	10.13	0.56
GS-21		1523.56	Mixed Shale	16	4	3			42	42	1	6	3	3	21	1
GS-22		1529	Argillaceous Shale	16.5	4.5	3.5		4	49.2	53.2	2.2	4.5		1.5	15	
GS-23		1529.87	Argillaceous Shale	10.71	1.83	13.58	2.54		49.62	52.16	0.1		0.58	2.56	16.76	1.7
GS-24		1530.04	Argillaceous Shale	15.02	3.62	12.17	2.21	20.79	22.18	45.18	0.23	5.83	1.06	2.37	13.78	0.74
GS-25		1531	Mixed Shale	25	3.5	1.5			40	40	2	6		2	20	2
GS-26		1534.73	Organic rich Shale	25.6	5.79	11.94	3.22	13.63	19.21	36.06	0.26	6.25	0.8	4.02	6.93	2.34
GS-27		1538.28	Argillaceous Shale	20	5	4			52	52	1	6	3	3	6	-
GS-28		1541.58	Argillaceous Shale	16	4	3			51	51	-	6	5	4	10	1
GS-29		1543.6	Argillaceous Shale	9.14	2.06	2.74	1.94	17.09	50.11	69.14	0.08	2.81	0.44	1.47	11.18	0.93
GS-30		1543.8	Calcareous Shale	6.02	0.95	5.71	3.48		20.72	24.2	0.28	1.83	0.86	4.33	55.77	0.04
GS-31		1547.07	Mixed Shale	15	3	2			35	35	-	4	2	2	37	-

GS-32		1548.8	Calcareous Shale	6.02	0.95	5.71	3.48		20.72	24.2	0.28	1.83	0.86	4.33	55.77	0.04
GS-33		1550.61	Organic rich Shale	21.61	4.32	11.13	4.42	17.09	31.15	52.66	1.15		1.2	2.42	13.43	0.78
GS-34		1553.59	Organic rich Shale	21	5	3			46	46	-	7	3	6	8	1
GS-35		1559.64	Argillaceous Shale	18	2	10			55	55	1	3	1	3	6	1
GS-36		1572.03	Argillaceous Shale	17.09	6.83	11.42	6.31		52	58.31	0.65			2.25	11.29	1
GS-37		1576.5	Mixed Shale	37	3	5			19	19	-	9	1	3	19	4
GS-38		1582.57	Argillaceous Shale	16	2	4			53	53		5	2	3	12	3
GS-39		1593.76	Siliceous Shale	17.7	4.13	23.35	9.89		30.8	40.69	0.16		0.88	3.33	7.03	2.61
GS-41		1526.67	Mixed Shale	17.53	1.39	9.2	0.87	1.97	18	20.84	5.04	1.5			45	
GS-42		1201	Argillaceous Shale	25			5		52	57	0.5	1.5			15	
GS-43		1400.08	Argillaceous Shale	21	3	9				23	3	14	18	1	5	0
GS-44	**Pictor East 1**	1438.88	Mixed Shale	28	5	5				20	1	8	14	4	9	6
GS-45		1454.54	Argillaceous Shale	26	7	8				23	2	8	15	4	4	1
GS-46		1501.15	Siliceous Shale	50	3	10				8	0	6	4	1	5	6

Appendix-A2: Geochemical properties based on Rock-eval pyrolysis analysis carried out on different Goldwyer-III shale samples, the results for few samples are adapted from Finder Exploration Pty Ltd company report (Finder, 2015).

Sample ID	Well Name	Lithofacies	TOC	S1 - (mg/g)	S2 - (mg/g)	S3 - (mg/g)	PI	Tmax(°C)	HI	OI
GS-1	**Theia 1**	Mixed Shale	0.04	0.03	0.13	0.3	0.2	410	325	750
GS-2		Mixed Shale	0.32	0.05	0.21	0.21	0.18	444	88	88
GS-3		Argillaceous Shale	3.2	2.12	7.55		0.22	454	236	16
GS-4		Siliceous Shale	3.15	1.13	4.05	0.67	0.218147	451.9731	131.9218	21.8241
GS-5		Argillaceous Shale	3.07	1.13	4.05	0.67	0.218147	451.9731	131.9218	21.8241
GS-6		Argillaceous Shale	0.23	0.1	0.22	0.33	0.3125	443.6	92.43697	138.6555
GS-7			0.16	0.12	0.14		0.47	305	88	300
GS-8		Siliceous Shale	3.07							
GS-9		Argillaceous Shale	0.47	0.26	0.28	0.61	0.49	451	57	124
GS-10		Calcareous Shale	1.11	0.59	1.29	0.77	0.31383	441.6	116.2162	69.36937
GS-11		Argillaceous Shale	2.6	1.78	5.62		0.24	453	216	22
GS-12		Mixed Shale	3.15	3.66	4.76	0.43	0.43	441	143	13
GS-13		Calcareous Shale	0.6	1.31	0.69	0.28	0.65	394	101	41
GS-14		Mixed Shale	1.16	1.85	0.74	0.39	0.71	435	76	40
GS-15		Calcareous Shale	1.42	1.37	2.36	0.33	0.367292	432.8	166.1972	23.23944
GS-16		Mixed Shale	2.11							
GS-17		Argillaceous Shale	1.53	1.74	3.41		0.34	441	223	23
GS-18		Argillaceous Shale	1.43	1.64	2.08		0.44	450	141	39
GS-19		Siliceous Shale	2.7	1.43	3.23	0.4	0.31	453	260	32
GS-20		Argillaceous Shale	2.6	3.62	3.74	0.37	0.49	436	133	13
GS-21		Mixed Shale	1.92	1.47	2.94	0.58	0.333333	437.7	153.125	30.20833
GS-22		Argillaceous Shale	2.7	2.33	5.83	0.49	0.29	448	211	18
GS-23		Argillaceous Shale	0.79	2.33	5.83	0.49	0.29	448	211	18
GS-24		Argillaceous Shale	2.19	2.41	2.14	0.41	0.53	448	95	18

GS-25		Mixed Shale	0.71	0.51	0.85		0.37	458	113	55
GS-26		Organic rich Shale	3.26	2.92	5.57		0.34	444	171	11
GS-27		Argillaceous Shale	2.18	1.68	3.25	0.53	0.340771	436.4	149.0826	24.31193
GS-28		Argillaceous Shale	0.625	0.36	0.65	0.81	0.356436	436.2	104	129.6
GS-29		Argillaceous Shale	2.16	2.76	2.31	0.38	0.54	446	94	16
GS-30		Calcareous Shale	0.23	0.27	0.05	0.31	0.84	425	17	107
GS-31		Mixed Shale	3.08	2.6	4.73	0.54	0.354707	435.1	153.5714	17.53247
GS-32		Calcareous Shale	0.23	0.27	0.05	0.31	0.84	425	17	107
GS-33		Organic rich Shale	4.11	6.84	6.63	0.29	0.51	433	148	6
GS-34		Organic rich Shale	3.67	3.68	6.09	0.41	0.376663	432.6	165.9401	11.17166
GS-35		Argillaceous Shale	2.58	2.06	4.49	0.85	0.314504	437.4	174.031	32.94574
GS-36		Argillaceous Shale	2.52	2.34	1.07	0.39	0.69	447	54	20
GS-37		Mixed Shale	0.23	0.06	0	0.65	1	428.5		275.4237
GS-38		Argillaceous Shale	1.16	0.73	1.3	0.77	0.359606	431.6	112.069	66.37931
GS-39		Siliceous Shale	1.21	0.54	0.61	0.38	0.47	468	60	38
GS-40			1.54	1.15	1.48	0.41	0.44	461	96	27
GS-41			0.13	0.17	0.18	0.42	0.48	302	138	323
GS-42		Argillaceous Shale	0.28	0.04	1.1		0.03	442	393	175
GS-43	**Pictor East 1**		0.39	0.06	0.15	1.77	0.29	431	38	454
GS-44			0.39	0.06	0.15	1.62	0.29	436	38	415
GS-45			0.43	0.07	0.17	1.69	0.29	430	40	393
GS-46			0.47	0.04	0.14	1.75	0.22	418	30	372
GS-47			0.9	0.16	0.43	2.14	0.27	419	48	238
GS-48			1.39	0.47	0.98	1.53	0.32	417	71	110
GS-49			1.76	0.57	1.11	2.06	0.34	410	63	117
GS-50			1.91	0.93	1.66	1.55	0.36	414	87	81
GS-51			1.5	0.47	0.85	1.83	0.35	414	57	122
GS-52			1.3	0.44	0.63	1.62	0.41	410	48	125
GS-53			0.59	0.18	0.34	1.24	0.34	410	58	210
GS-54			0.66	0.19	0.34	1.16	0.36	408	52	176
GS-55			0.7	0.19	0.4	1.45	0.32	405	57	207
GS-56			0.4	0.16	0.35	1.3	0.32	409	88	325
GS-57			0.88	0.18	0.42	2.26	0.3	394	48	257

GS-58			0.97	0.27	0.52	1.89	0.34	397	54	195
GS-59			1.12	0.25	0.53	2.5	0.32	399	47	223
GS-60			1.23	0.28	0.59	2.45	0.32	401	48	199
GS-61			0.69	0.13	0.38	1.89	0.26	389	55	274

Appendix-A3: Petrophysical properties (densities, porosity and pore structure parameters) based on gas expansion and adsorption analyses carried out on different Goldwyer-III shale samples.

Sample ID	Lithofacies	Bulk density (g/cc)	Grain density (g/cc)	Total Porosity_He (%)	BET surface area (m^2/g) LPNA	BET surface area (m^2/g) LPCO2	Micropore volume (cm^3/g)	Mesopore volume (cm^3/g)
GS-1	Mixed Shale	N/A	N/A	N/A	1.249	0.5161	0.000805	0.00389
GS-2	Mixed Shale	N/A	N/A	N/A	N/A	N/A	N/A	N/A
GS-3	Argillaceous Shale	N/A	N/A	N/A	12.695	N/A	N/A	0.014796
GS-4	Siliceous Shale	N/A	N/A	N/A	13.6536	2.8649	0.003031	0.017897
GS-5	Argillaceous Shale	N/A	N/A	N/A	N/A	N/A	0.0028	N/A
GS-6	Argillaceous Shale	N/A	N/A	N/A	N/A	N/A	N/A	N/A
GS-7		N/A	N/A	N/A	N/A	N/A	30.67	0.006613
GS-8	Siliceous Shale	N/A	N/A	N/A	18.68	2.6167	0.002683	0.021979
GS-9	Argillaceous Shale	N/A	N/A	N/A	18.5748	1.4084	0.001758	0.046755
GS-10	Calcareous Shale	2.46	2.69	0.082	N/A	N/A	N/A	N/A
GS-11	Argillaceous Shale	2.58	2.66	0.0735	N/A	1.0196	0.00159	N/A
GS-12	Mixed Shale	2.47	2.66	0.11601076	2.137	0.5201	0.001661	0.035956
GS-13	Calcareous Shale	2.65	2.72	0.041274483	1.2889	0.4518	0.0027	0.007374
GS-14	Mixed Shale	2.64	2.79	0.083285229	8.9746	1.1778	0.001598	0.029905

GS-15	Calcareous Shale	2.43	2.72	0.108	N/A	N/A	N/A	N/A
GS-16	Mixed Shale	N/A	N/A	N/A	N/A	1.1169	0.001826	
GS-17	Argillaceous Shale	N/A	N/A	N/A	11.4966	N/A	N/A	0.0389
GS-18	Argillaceous Shale	N/A	N/A	N/A	N/A	N/A	N/A	N/A
GS-19	Siliceous Shale	N/A	N/A	N/A		1.65	0.001826	
GS-20	Argillaceous Shale	2.51	2.68	0.075713393	10.3353	1.66	0.002014	0.038105
GS-21	Mixed Shale	2.45	2.73	0.101	1.55	N/A	N/A	0.021989
GS-22	Argillaceous Shale	N/A	N/A	N/A	N/A	N/A	0.002175	N/A
GS-23	Argillaceous Shale	N/A	N/A	N/A	N/A	N/A	0.002175	N/A
GS-24	Argillaceous Shale	2.57	2.69	0.070808687	13.2989	1.4858	0.001909	0.037433
GS-25	Mixed Shale	N/A	N/A	N/A	21.4	N/A	0.001713	0.024188
GS-26	Organic rich shale	N/A	N/A	N/A	N/A	N/A	0.003405	N/A
GS-27	Argillaceous Shale	2.45	2.73	0.105	N/A	N/A	N/A	N/A
GS-28	Argillaceous Shale	2.54	2.76	0.082	N/A	N/A	N/A	N/A
GS-29	Argillaceous Shale	2.50	2.70	0.118523118	15.4653	2.4826	0.002733	0.055
GS-30	Calcareous Shale	2.70	2.72	0.024012628	8.7512	1.0031	0.001569	0.035845
GS-31	Mixed Shale	2.41	2.69	0.102	N/A	N/A	N/A	N/A
GS-32	Calcareous Shale	N/A	N/A	N/A	N/A	N/A	0.000805	0.00305
GS-33	Organic rich Shale	N/A	N/A	0.128	13.6498	1.8238	0.0032	0.05158
GS-34	Organic rich Shale	2.44	2.65	0.128088523	N/A	N/A	N/A	N/A
GS-35	Argillaceous Shale	2.40	2.68	0.106	N/A	N/A	N/A	N/A
GS-36	Argillaceous Shale	2.46	2.70	0.088	17.2344	2.4934	0.002708	0.05184
GS-37	Mixed Shale	2.57	2.70	0.079939777	N/A	N/A	N/A	N/A
GS-38	Argillaceous Shale	2.62	2.75	0.047	N/A	N/A	N/A	N/A
GS-39	Siliceous Shale	2.48	2.76	0.1	19.6014	1.1505	0.002202	0.053753
GS-40		N/A	N/A	N/A	9.5044	N/A	N/A	0.050874

GS-41		N/A	N/A	N/A	N/A	1.976	0.002093	0.0045
GS-42	Argillaceous Shale	N/A	N/A	N/A	N/A	0.6084	0.00206	0.033

Appendix-B Attributions

Journal Paper: Integrated sedimentary and high-resolution mineralogical characterisation of Ordovician shale from Canning Basin, Western Australia: Implications for facies heterogeneity evaluation. 2021. JPSE. 109347

Muhammad Atif Iqbal[a]*, Reza Rezaee[a], Carsten Laukamp[b], Bobby Pejcic[c], Gregory Smith[d]
[a]Department of Petroleum Engineering, Western Australian School of Mines: Minerals, Energy and Chemical Engineering, Curtin University, 26 Dick Perry Avenue, WA 6151 Kensington, Australia
[b]CSIRO, Mineral Resources, 26 Dick Perry Avenue, Kensington, WA 6151, Australia
[c]CSIRO, Energy, 26 Dick Perry Avenue, Kensington, WA 6151, Australia
[d]Department of Applied Geology, West Australian School of Mines, Curtin University, Perth, Australia

	Conception and Design	Acquisition of Data and Method	Data Conditioning and Manipulation	Analysis and Statistical Method	Interpretation and Discussion
Muhammad Atif Iqbal	x	x	x	x	x
I acknowledge that these represent my contribution to the above research output, and I have approved the final version. Signed:					
Reza Rezaee	x		x		x
I acknowledge that these represent my contribution to the above research output, and I have approved the final version. Signed:					
Carsten Laukamp	x				x
I acknowledge that these represent my contribution to the above research output, and I have approved the final version. Signed:					
Bobby Pejcic					x
I acknowledge that these represent my contribution to the above research output, and I have approved the final version. Signed:					
Gregory Smith	x				x
I acknowledge that these represent my contribution to the above research output, and I have approved the final version. Signed:					

Journal Paper: Shale lithofacies controls on porosity and pore structure: An example from Ordovician Goldwyer Formation, Canning Basin, Western Australia. 2021. JNGSE. 103888.

Muhammad Atif Iqbal[a]*, Reza Rezaee[a], Gregory Smith[b], Jamiu M. Ekundayo[a]
[a]Department of Petroleum Engineering, Western Australian School of Mines: Minerals, Energy and Chemical Engineering, Curtin University, 26 Dick Perry Avenue, WA 6151 Kensington, Australia
[b]Department of Applied Geology, West Australian School of Mines, Curtin University, Perth, Australia

	Conception and Design	Acquisition of Data and Method	Data Conditioning and Manipulation	Analysis and Statistical Method	Interpretation and Discussion
Muhammad Atif Iqbal	x	x	x	x	x
I acknowledge that these represent my contribution to the above research output, and I have approved the final version. Signed:					
Reza Rezaee	x				x
I acknowledge that these represent my contribution to the above research output, and I have approved the final version. Signed:					
Gregory Smith	x				x
I acknowledge that these represent my contribution to the above research output, and I have approved the final version. Signed:					
Jamiu Ekundayo					x
I acknowledge that these represent my contribution to the above research output, and I have approved the final version. Signed:					

Journal Paper: Porosity and Water Saturation Estimation for ShaleReservoirs: An Example from Goldwyer Formation Shale, Canning Basin, Western Australia. 2020. Energies. 13236294

Muhammad Atif Iqbal[a]*, Reza Rezaee[a]
[a]Department of Petroleum Engineering, Western Australian School of Mines: Minerals, Energy and Chemical Engineering, Curtin University, 26 Dick Perry Avenue, WA 6151 Kensington, Australia

	Conception and Design	Acquisition of Data and Method	Data Conditioning and Manipulation	Analysis and Statistical Method	Interpretation and Discussion
Muhammad Atif Iqbal	x	x	x	x	x
I acknowledge that these represent my contribution to the above research output, and I have approved the final version. Signed:					
Reza Rezaee	x			x	x
I acknowledge that these represent my contribution to the above research output, and I have approved the final version. Signed:					

Journal Paper: Implications of thin laminations on pore structure of shale reservoir: Ordovician Goldwyer Formation Case study from Western Australia. APPEA

Muhammad Atif Iqbal[a]*, Reza Rezaee[a], Gregory Smith[b], Partha Pratim Mandal[a]
[a]Department of Petroleum Engineering, Western Australian School of Mines: Minerals, Energy and Chemical Engineering, Curtin University, 26 Dick Perry Avenue, WA 6151 Kensington, Australia
[b]Department of Applied Geology, West Australian School of Mines, Curtin University, Perth, Australia

	Conception and Design	Acquisition of Data and Method	Data Conditioning and Manipulation	Analysis and Statistical Method	Interpretation and Discussion
Muhammad Atif Iqbal	x	x	x	x	x
I acknowledge that these represent my contribution to the above research output, and I have approved the final version. Signed:					
Reza Rezaee	x				x
I acknowledge that these represent my contribution to the above research output, and I have approved the final version. Signed:					
Gregory Smith	x				x
I acknowledge that these represent my contribution to the above research output, and I have approved the final version. Signed:					
Partha Pratim Mandal					x
I acknowledge that these represent my contribution to the above research output, and I have approved the final version. Signed:					

Book Chapter: Well-log Analysis of Shale Gas Reservoirs. Encyclopedia of Petroleum Geoscience, Springer.

Muhammad Atif Iqbal[a]*, Reza Rezaee[a]
[a]Department of Petroleum Engineering, Western Australian School of Mines: Minerals, Energy and Chemical Engineering, Curtin University, 26 Dick Perry Avenue, WA 6151 Kensington, Australia

	Conception and Design	Acquisition of Data and Method	Data Conditioning and Manipulation	Analysis and Statistical Method	Interpretation and Discussion
Muhammad Atif Iqbal	x	x	x	x	x
I acknowledge that these represent my contribution to the above research output, and I have approved the final version. Signed:					
Reza Rezaee	x			x	x
I acknowledge that these represent my contribution to the above research output, and I have approved the final version. Signed:					

Journal Paper: Integration of mechanical stratigraphy with lithofacies in Goldwyer shale for selecting producible and hydraulic fracturing layers. 82nd EAGE Annual Conference & Exhibition, Oct 2021, Volume 2021, p.1 – 5. Published in EarthDoc.

Muhammad Atif Iqbal[1]*, Partha Pratim Mandal[1], Reza Rezaee[1], Joel Sarout[2], Gregory Smith[3]
[1]Curtin University, WASM, Petroleum Engineering, Perth, Australia
[2]CSIRO Energy, Rock Properties Team, Perth, Australia
[2]CSIRO Energy, Geomechanics and Geophysics Laboratory, Perth, Australia
[3]Department of Applied Geology, Curtin University, Perth, Australia
*Corresponding author: m.iqbal14@postgrad.curtin.edu.au

	Conception and Design	Acquisition of Data and Method	Data Conditioning and Manipulation	Analysis and Statistical Method	Interpretation and Discussion
Muhammad Atif Iqbal	x	x	x	x	x
I acknowledge that these represent my contribution to the above research output, and I have approved the final version. Signed:					
Partha Pratim Mandal	x				x
I acknowledge that these represent my contribution to the above research output, and I have approved the final version. Signed:					
Reza Rezaee	x				x
I acknowledge that these represent my contribution to the above research output, and I have approved the final version. Signed:					
Joel Sarout		x			
I acknowledge that these represent my contribution to the above research output, and I have approved the final version. Signed:					
Gregory Smith					x
I acknowledge that these represent my contribution to the above research output, and I have approved the final version. Signed:					

Journal Paper: Integration of high-resolution HyLogger3 spectral scanner and TESCAN Integrated Mineral Analyser for mineralogical characterisation of shale. Australian Exploration Geoscience Conference, 2021.

Muhammad Atif Iqbal[1*], Reza Rezaee[1], Gregory Smith[2], Hasnain Ali Bangash[3]
[1]Curtin University, WASM, Petroleum Engineering, Perth, Australia
[2]Department of Applied Geology, Curtin University, Perth, Australia
[3]Rio Tinto Exploration, Perth, Australia

	Conception and Design	Acquisition of Data and Method	Data Conditioning and Manipulation	Analysis and Statistical Method	Interpretation and Discussion
Muhammad Atif Iqbal	x	x	x	x	x
I acknowledge that these represent my contribution to the above research output, and I have approved the final version. Signed:					
Reza Rezaee	x				x
I acknowledge that these represent my contribution to the above research output, and I have approved the final version. Signed:					
Gregory Smith	x				x
I acknowledge that these represent my contribution to the above research output, and I have approved the final version. Signed:					
Hasnain Ali Bangash					x
I acknowledge that these represent my contribution to the above research output, and I have approved the final version. Signed:					

Appendix-C Copyright Agreement

RightsLink

Home | Help | Email Support | Sign in | Create Account

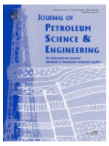

Integrated sedimentary and high-resolution mineralogical characterisation of Ordovician shale from Canning Basin, Western Australia: Implications for facies heterogeneity evaluation

Author: Muhammad Atif Iqbal,Reza Rezaee,Carsten Laukamp,Bobby Pejcic,Gregory Smith

Publication: Journal of Petroleum Science and Engineering

Publisher: Elsevier

Date: January 2022

Journal Author Rights

Please note that, as the author of this Elsevier article, you retain the right to include it in a thesis or dissertation, provided it is not published commercially. Permission is not required, but please ensure that you reference the journal as the original source. For more information on this and on your other retained rights, please visit: https://www.elsevier.com/about/our-business/policies/copyright#Author-rights

BACK | CLOSE WINDOW

RightsLink

Home | Help | Email Support | Sign in | Create Account

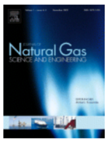

Shale lithofacies controls on porosity and pore structure: An example from Ordovician Goldwyer Formation, Canning Basin, Western Australia

Author: Muhammad Atif Iqbal,Reza Rezaee,Gregory Smith,Jamiu M. Ekundayo

Publication: Journal of Natural Gas Science and Engineering

Publisher: Elsevier

Date: May 2021

Journal Author Rights

Please note that, as the author of this Elsevier article, you retain the right to include it in a thesis or dissertation, provided it is not published commercially. Permission is not required, but please ensure that you reference the journal as the original source. For more information on this and on your other retained rights, please visit: https://www.elsevier.com/about/our-business/policies/copyright#Author-rights

BACK | CLOSE WINDOW

Open Access | Article

Porosity and Water Saturation Estimation for Shale Reservoirs: An Example from Goldwyer Formation Shale, Canning Basin, Western Australia

by Muhammad Atif Iqbal * and Reza Rezaee

Department of Petroleum Engineering, Western Australia School of Mines: Minerals, Energy and Chemical Engineering, Curtin University, 26 Dick Perry Avenue, Kensington, WA 6151, Australia

* Author to whom correspondence should be addressed.

Energies **2020**, *13*(23), 6294; https://doi.org/10.3390/en13236294

Received: 12 November 2020 / Revised: 26 November 2020 / Accepted: 27 November 2020 / Published: 29 November 2020

(This article belongs to the Special Issue Development of Unconventional Reservoirs 2020)

CSIRO PUBLISHING

Licence to Publish

APPEA Limited

The APPEA Journal **Manuscript No.** AJ20025.R1

Title of the paper/presentation (the 'Work') Implications of thin laminations on pore structure of marine shale reservoir: Goldwyer Formation Case study from Western Australia

Author(s) Iqbal, Muhammad; Rezaee, Reza; Smith, Gregory; Mandal, Partha Pratim

The APPEA Journal includes papers submitted to and presented at APPEA Conferences. The purpose of this Licence to Publish is to grant and confirm the grant of exclusive rights to publish the Work in the APPEA Journal.

The APPEA Journal is published by CSIRO Publishing for the Australian Petroleum Production and Exploration Association Limited (APPEA). APPEA Conference papers are made available to delegates to the APPEA Conference and included in the APPEA Journal. The APPEA Journal is a digital, online journal which is sold to subscribers and others.

By submitting this paper, the Author (Authors if a multi-authored paper) represents that they have the right or have obtained authorisation to enter into this Licence and grant the rights granted or contemplated by it.

The Author warrants that:

- Other than as a presentation at an APPEA Conference, the Work (including any abstract) has not been published before.
- The Work is not presently being considered for publication elsewhere.
- The Work does not violate any intellectual property right of any person or entity.
- The Work does not contain any subject matter that contravenes any laws (including defamatory material and misleading and deceptive material.
- The Work meets ethical standards applicable to the research discipline.
- The Work indicates any financial or non-financial interests/relationships that may be interpreted to have influenced the manuscript.
- All Authors have made a significant contribution to the Work and agree to its submission, and
- Permission for any tables or figures or other third party materials included in the Work that have been published elsewhere has been received from the relevant copyright holder and is attributed in the Work.

Terms of the Licence to Publish

1. In consideration for publication of the Work (and without derogating from rights granted in submitting the Work for the Conference), the Author grants to APPEA, through CSIRO Publishing (the 'Publisher'), an exclusive, royalty free, worldwide licence including the right to sub-license, to:
   - Reproduce, publish and communicate the Work, or any part of the Work, to the public in any and all media, whether existing before or after the date of this Licence, for commercial, educational and all other purposes for the full remaining term of the copyright subsisting in the Work in each applicable jurisdiction.
   - Approve fair and reasonable permission requests from third parties to reuse material contained in the Work for the purpose of study, research or subsidiary publication.

   The Author acknowledges that the Publisher is licensed by APPEA to publish and sell the APPEA Journal.

2. In addition to the Author's moral rights in respect of the Work, and subject to third party rights, the Author retains the right to:
   - Use copies of the Work for non-commercial purposes within his/her institution subject to the usual copyright licensing agency arrangements
   - Use the Work for further research and presentations at meetings and conferences
   - Use the illustrations (line art, photographs, figures, plates) and research data in his/her own future works
   - Include the Work in part or in full in a thesis provided it is not published for commercial gain
   - Place his/her pre-publication version of the Work on a pre-print server
   - Place his/her pre-publication version of the Work on a personal website or institutional repository on condition that there is a link to the definitive version on the APPEA Journal site hosted on the Publisher's website.

3. The Author agrees to:
   - Include a link and/or reference to the Work as published by the Publisher on all further uses of the Work or parts of the Work
   - Not reproduce or authorise others to reproduce adaptations of the Work that are substantially identical to the Work for any commercial publication
   - Not permit digital copies of the Work as published by the Publisher to be systematically networked to external users
   - Not use the Work in any way that implies that the Publisher, APPEA, the Journal or the Editors endorse any product or procedure described in the Work.

4. When exercising any of the rights assigned or granted, each party is required to give sufficient acknowledgement of the contribution made by the other party to the published material including a citation to the APPEA Journal.

Works made in the course of employment

5. Where the Work has been made by the Author (or in the case of multiple Authors, by any of them) in the course of employment and their employer owns copyright in the Work, that employer must sign this Licence. The employer has the same rights and obligations and gives the same warranties and licence rights as an Author under this Licence.

Bibliography

Abdulaziz, A. M., Mahdi, H. A., & Sayyouh, M. H. (2019). Prediction of reservoir quality using well logs and seismic attributes analysis with an artificial neural network: A case study from Farrud Reservoir, Al-Ghani Field, Libya. *Journal of Applied Geophysics*, *161*, 239-254.

Administration, U. S. E. I., & Kuuskraa, V. (2011). *World shale gas resources: an initial assessment of 14 regions outside the United States*. US Department of Energy.

Adnan, A., Shukla, U., Verma, A., & Shukla, T. (2015). Lithofacies of transgressive–regressive sequence on a carbonate ramp in Vindhyan basin (Proterozoic): a case of tidal-flat origin from central India. *Arabian Journal of Geosciences*, *8*(9), 6985-7001.

Aghaei, A., Mahboubi, A., Moussavi-Harami, R., Heubeck, C., & Nadjafi, M. (2013). Facies analysis and sequence stratigraphy of an Upper Jurassic carbonate ramp in the Eastern Alborz range and Binalud Mountains, NE Iran. *Facies*, *59*(4), 863-889.

Ahmad, M. (2014). *Petrophysical and mineralogical evaluation of shale gas reservoirs: a Cooper Basin case study*

Akbar, M. N. A., Musu, J. T., & Milad, B. (2018). Water Saturation Interpretation Model for Organic-Rich Shale Reservoir: A Case Study of North Sumatra Basin.

Akinnikawe, O., Lyne, S., & Roberts, J. (2018). Synthetic well log generation using machine learning techniques. SPE/AAPG/SEG Unconventional Resources Technology Conference,

Alfarraj, M., & AlRegib, G. (2019). Semi-supervised learning for acoustic impedance inversion. In *SEG Technical Program Expanded Abstracts 2019* (pp. 2298-2302). Society of Exploration Geophysicists.

Alvarez, J. O., & Schechter, D. S. (2017). Improving oil recovery in the Wolfcamp unconventional liquid reservoir using surfactants in completion fluids. *Journal of Petroleum Science and Engineering*, *157*, 806-815.

Amaefule, J. O., Altunbay, M., Tiab, D., Kersey, D. G., & Keelan, D. K. (1993, 1993/1/1/). *Enhanced Reservoir Description: Using Core and Log Data to Identify Hydraulic (Flow) Units and Predict Permeability in Uncored Intervals/Wells* SPE Annual Technical Conference and Exhibition, Houston, Texas. https://doi.org/10.2118/26436-MS

Ambrose, R. J., Hartman, R. C., Diaz-Campos, M., Akkutlu, I. Y., & Sondergeld, C. H. (2012). Shale gas-in-place calculations part I: new pore-scale considerations. *Spe Journal*, *17*(01), 219-229.

Ambrose, R. J., Hartman, R. C., Diaz Campos, M., Akkutlu, I. Y., & Sondergeld, C. (2010). New pore-scale considerations for shale gas in place calculations. SPE Unconventional Gas Conference,

Apak, S. N., & Carlsen, G. (1997). *A compilation and review of data pertaining to the hydrocarbon prospectivity in the Canning Basin*. Geological Survey of Western Australia, Department of Minerals and Energy.

Archie, G. E. (1942). The electrical resistivity log as an aid in determining some reservoir characteristics. *Transactions of the AIME*, *146*(01), 54-62.

Arredondo-Ramírez, K., Ponce-Ortega, J. M., & El-Halwagi, M. M. (2016). Optimal planning and infrastructure development for shale gas production. *Energy Conversion and Management*, *119*, 91-100.

Arthur, M. A., & Sageman, B. B. (1994). Marine black shales: depositional mechanisms and environments of ancient deposits. *Annual Review of Earth and Planetary Sciences*, *22*(1), 499-551.

Ayling, B., Huntington, J., Smith, B., & Edwards, D. (2016). Hyperspectral logging of middle Cambrian marine sediments with hydrocarbon prospectivity: a case study from the southern Georgina Basin, northern Australia. *Australian Journal of Earth Sciences*, *63*(8), 1069-1085.

Barnaby, R., & Ward, W. (2007). Outcrop analog for mixed siliciclastic–carbonate ramp reservoirs—stratigraphic hierarchy, facies architecture, and geologic heterogeneity: Grayburg Formation, Permian Basin, USA. *Journal of Sedimentary Research*, *77*(1), 34-58.

Basin, M. D., East, N., Hopkins, G., Gippsland, E., Broken, G., Gippsland, W., Rivers, S., East, S., Darling, L. M., & Phillip, P. (2015). South Australian. *Coal Seam, Shale and Tight Gas in Australia: Resources Assessment and Operation Overview 2015*, 23.

Beukes, N. J. (1987). Facies relations, depositional environments and diagenesis in a major early Proterozoic stromatolitic carbonate platform to basinal sequence, Campbellrand Subgroup, Transvaal Supergroup, Southern Africa. *Sedimentary Geology*, *54*(1-2), 1-46.

Bhatt, A. (2002). *Reservoir Properties from Well Logs using neural Networks* Norwegian University of Science and Technology, Trondheim, Norway].

Bhattacharya, S., Carr, T. R., & Pal, M. (2016). Comparison of supervised and unsupervised approaches for mudstone lithofacies classification: Case studies from the Bakken and Mahantango-Marcellus Shale, USA. *Journal of Natural Gas Science and Engineering*, *33*, 1119-1133.

Bjørlykke, K., & Høeg, K. (1997). Effects of burial diagenesis on stresses, compaction and fluid flow in sedimentary basins. *Marine and Petroleum Geology*, *14*(3), 267-276.

Bohacs, K. M., Carroll, A. R., Neal, J. E., & Mankiewicz, P. J. (2000). *Lake-basin type, source potential, and hydrocarbon character*, 3-34.

Boyer, C., Clark, B., Jochen, V., Lewis, R., & Miller, C. (2011). Shale gas: A global resource: Oilfield Review. In: Autumn.

Brown, S., Boserio, I., Jackson, K., & Spence, K. (1984). The geological evolution of the Canning Basin-implications for petroleum exploration.

Bruner, K. R., Walker-Milani, M., & Smosna, R. (2015). Lithofacies of the devonian marcellus shale in the eastern appalachian basin, USA. *Journal of Sedimentary Research*, *85*(8), 937-954.

Bust, V. K., Majid, A. A., Oletu, J. U., & Worthington, P. F. (2013). The petrophysics of shale gas reservoirs: Technical challenges and pragmatic solutions. *Petroleum Geoscience*, *19*(2), 91-103. https://doi.org/10.1144/petgeo2012-031

Bustin, R. M., Bustin, A. M., Cui, A., Ross, D., & Pathi, V. M. (2008). Impact of shale properties on pore structure and storage characteristics. SPE shale gas production conference,

Cadman, S., Pain, L., Vuckovic, V., & Le Poidevin, S. (1993). Canning Basin. *Western Australia: Australian Petroleum Accumulations Report*, *9*, 81.

Carlsen, G., & Ghori, K. A. R. (2005). Canning Basin and global Palaeozoic petroleum systems—a review. *The APPEA Journal*, *45*(1), 349-364.

Carr*, T., Ghahfarokhi, P. K., Carney, B., Hewitt, J., & Vargnetti, R. (2019). Marcellus Shale Energy and Environmental Laboratory (MSEEL) Results and Plans: Improved Subsurface Reservoir Characterization and Engineered Completions. Unconventional Resources Technology Conference, Denver, Colorado, 22-24 July 2019,

Chalmers, G. R., & Bustin, R. M. (2007). The organic matter distribution and methane capacity of the Lower Cretaceous strata of Northeastern British Columbia, Canada. *International Journal of Coal Geology*, *70*(1-3), 223-239.

Chalmers, G. R., Bustin, R. M., & Power, I. M. (2012). Characterization of gas shale pore systems by porosimetry, pycnometry, surface area, and field emission scanning electron microscopy/transmission electron microscopy image analyses: Examples from the Barnett, Woodford, Haynesville, Marcellus, and Doig units. *AAPG Bulletin*, *96*(6), 1099-1119. https://doi.org/10.1306/10171111052

Charsky, A., Pyles, D., & Sonnenberg, S. (2017). Integrating Mineralogy, Process Sedimentology and Geomechanics for Development of a Mechanical Stratigraphy Model of the Bakken Formation. SPE/AAPG/SEG Unconventional Resources Technology Conference,

Chen, F., Lu, S., Ding, X., & He, X. (2018). Shale gas reservoir characterization: A typical case in the Southeast Chongqing of Sichuan Basin, China. *PLoS One*, *13*(6), e0199283. https://doi.org/10.1371/journal.pone.0199283
Chen, L., Jiang, Z., Liu, K., Wang, P., Ji, W., Gao, F., Li, P., Hu, T., Zhang, B., & Huang, H. (2016). Effect of lithofacies on gas storage capacity of marine and continental shales in the Sichuan Basin, China. *Journal of Natural Gas Science and Engineering*, *36*, 773-785.
Chen, L., Lu, Y., Jiang, S., Li, J., Guo, T., & Luo, C. (2015). Heterogeneity of the Lower Silurian Longmaxi marine shale in the southeast Sichuan Basin of China. *Marine and Petroleum Geology*, *65*, 232-246. https://doi.org/https://doi.org/10.1016/j.marpetgeo.2015.04.003
Chen, Y., Lin, Z., Zhao, X., Wang, G., & Gu, Y. (2014). Deep learning-based classification of hyperspectral data. *IEEE Journal of Selected topics in applied earth observations and remote sensing*, *7*(6), 2094-2107.
Christ, N., Immenhauser, A., Amour, F., Mutti, M., Tomas, S., Agar, S. M., Alway, R., & Kabiri, L. (2012). Characterization and interpretation of discontinuity surfaces in a Jurassic ramp setting (High Atlas, Morocco). *Sedimentology*, *59*(1), 249-290.
Clarkson, C. R., Solano, N., Bustin, R. M., Bustin, A. M. M., Chalmers, G. R. L., He, L., Melnichenko, Y. B., Radliński, A. P., & Blach, T. P. (2013). Pore structure characterization of North American shale gas reservoirs using USANS/SANS, gas adsorption, and mercury intrusion. *Fuel*, *103*, 606-616. https://doi.org/https://doi.org/10.1016/j.fuel.2012.06.119
Clavier, C., Coates, G., & Dumanoir, J. (1984). *Theoretical and Experimental Bases forthe Dual-Water Model for the Interpretation of Shaly Sands. SPEJ24 (2): 153-167.*
Colombié, C., & Strasser, A. (2005). Facies, cycles, and controls on the evolution of a keep-up carbonate platform (Kimmeridgian, Swiss Jura). *Sedimentology*, *52*(6), 1207-1227.
Curtis, J. B. (2002). Fractured shale-gas systems. *AAPG Bulletin*, *86*(11), 1921-1938.
Curtis, M. E., Cardott, B. J., Sondergeld, C. H., & Rai, C. S. (2012). Development of organic porosity in the Woodford Shale with increasing thermal maturity. *International Journal of Coal Geology*, *103*, 26-31.
Dawson, W. C. (2000). Shale microfacies: Eagle Ford Group (Cenomanian-Turonian) north-central Texas outcrops and subsurface equivalents.
Day-Stirrat, R. J., Loucks, R. G., Milliken, K. L., Hillier, S., & van der Pluijm, B. A. (2008). Phyllosilicate orientation demonstrates early timing of compactional stabilization in calcite-cemented concretions in the Barnett Shale (Late Mississippian), Fort Worth Basin, Texas (U.S.A). *Sedimentary Geology*, *208*(1), 27-35. https://doi.org/https://doi.org/10.1016/j.sedgeo.2008.04.007
De Silva, P., Simons, S., & Stevens, P. (2016). Economic impact analysis of natural gas development and the policy implications. *Energy Policy*, *88*, 639-651.
De Silva, P., Simons, S., Stevens, P., & Philip, L. (2015). A comparison of North American shale plays with emerging non-marine shale plays in Australia. *Marine and Petroleum Geology*, *67*, 16-29.
De Silva, P. N. K., Simons, S. J. R., Stevens, P., & Philip, L. M. (2015). A comparison of North American shale plays with emerging non-marine shale plays in Australia. *Marine and Petroleum Geology*, *67*, 16-29. https://doi.org/10.1016/j.marpetgeo.2015.04.011
Delle Piane, C., Almqvist, B. S., MacRae, C. M., Torpy, A., Mory, A. J., & Dewhurst, D. N. (2015). Texture and diagenesis of Ordovician shale from the Canning Basin, Western Australia: Implications for elastic anisotropy and geomechanical properties. *Marine and Petroleum Geology*, *59*, 56-71.
Dong, T., Harris, N. B., Ayranci, K., Twemlow, C. E., & Nassichuk, B. R. (2015). Porosity characteristics of the Devonian Horn River shale, Canada: Insights from lithofacies classification and shale composition. *International Journal of Coal Geology*, *141*, 74-90.

Ekundayo, J. M., & Rezaee, R. (2019). Effect of Equation of States on High-Pressure Volumetric Measurements of Methane–Coal Sorption Isotherms—Part 1: Volumes of Free Space and Methane Adsorption Isotherms. *Energy & fuels*, *33*(2), 1029-1036.

Ekundayo, J. M., Rezaee, R., & Fan, C. (2021). Experimental investigation and mathematical modelling of shale gas adsorption and desorption hysteresis. *Journal of Natural Gas Science and Engineering*, *88*, 103761.

Emelyanova, I., Pervukhina, M., Clennell, M. B., & Dewhurst, D. N. (2016). Applications of standard and advanced statistical methods to TOC estimation in the McArthur and Georgina basins, Australia. *The Leading Edge*, *35*(1), 51-57.

Eshkalak, M. O., Mohaghegh, S. D., & Esmaili, S. (2014). Geomechanical properties of unconventional shale reservoirs. *Journal of Petroleum Engineering*, *2014*.

Espitalie, J., Deroo, G., & Marquis, F. (1985). Rock-Eval pyrolysis and its applications. *Revue De L Institut Francais Du Petrole*, *40*(5), 563-579.

Espitalie, J., Madec, M., Tissot, B., Mennig, J., & Leplat, P. (1977). Source rock characterization method for petroleum exploration. Offshore Technology Conference,

Farouk, S., Ahmad, F., Mousa, D., & Simmons, M. (2016). Sequence stratigraphic context and organic geochemistry of Palaeogene oil shales, Jordan. *Marine and Petroleum Geology*, *77*, 1297-1308.

Farouk, S., Ahmad, F., & Powell, J. H. (2017). Cenomanian–Turonian stable isotope signatures and depositional sequences in northeast Egypt and central Jordan. *Journal of Asian Earth Sciences*, *134*, 207-230.

Feng, R., Zhang, Y., Rezagholilou, A., Roshan, H., & Sarmadivaleh, M. (2019). Brittleness Index: From Conventional to Hydraulic Fracturing Energy Model. *Rock Mechanics and Rock Engineering*, 1-15.

Ferguson, D. P. (2016). *The depositional history of the Ordovician lower Goldwyer Formation, Canning Basin, Western Australia* The University of Western Australia].

Finder, E. P. L. (2015). Geochemical Analysis for Goldwyer Shale samples (Theia-1 well). *Private Communication*.

Fitch, P. J., Lovell, M. A., Davies, S. J., Pritchard, T., & Harvey, P. K. (2015). An integrated and quantitative approach to petrophysical heterogeneity. *Marine and Petroleum Geology*, *63*, 82-96.

Flugel, E., & Flügel, E. (2004). *Microfacies of carbonate rocks: analysis, interpretation and application*. Springer Science & Business Media.

Folk, R. L. (1980). *Petrology of sedimentary rocks*. Hemphill publishing company.

Foster, C., O'Brien, G., & Watson, S. (1986). Hydrocarbon source potential of the Goldwyer Formation, Barbwire Terrace, Canning Basin, Western Australia. *The APPEA Journal*, *26*(1), 142-155.

Frykman, P. (2001). Spatial variability in petrophysical properties in Upper Maastrichtian chalk outcrops at Stevns Klint, Denmark. *Marine and Petroleum Geology*, *18*(10), 1041-1062. https://doi.org/https://doi.org/10.1016/S0264-8172(01)00043-5

Fu, H., Wang, X., Zhang, L., Gao, R., Li, Z., Xu, T., Zhu, X., Xu, W., & Li, Q. (2015). Investigation of the factors that control the development of pore structure in lacustrine shale: A case study of block X in the Ordos Basin, China. *Journal of Natural Gas Science and Engineering*, *26*, 1422-1432.

Fu, Q., Horvath, S. C., Potter, E. C., Roberts, F., Tinker, S. W., Ikonnikova, S., Fisher, W. L., & Yan, J. (2015). Log-derived thickness and porosity of the Barnett Shale, Fort Worth basin, Texas: Implications for assessment of gas shale resources. *AAPG Bulletin*, *99*(1), 119-141.

Gao, F., Song, Y., Li, Z., Xiong, F., Chen, L., Zhang, Y., Liang, Z., Zhang, X., Chen, Z., & Joachim, M. (2018). Lithofacies and reservoir characteristics of the Lower Cretaceous continental Shahezi Shale in the Changling Fault Depression of Songliao Basin, NE China. *Marine and petroleum Geology*, *98*, 401-421.

Gardner, G., Gardner, L., & Gregory, A. (1974). Formation velocity and density—The diagnostic basics for stratigraphic traps. *Geophysics*, *39*(6), 770-780.
Gholami, R., Rasouli, V., Sarmadivaleh, M., Minaeian, V., & Fakhari, N. (2016). Brittleness of gas shale reservoirs: A case study from the north Perth basin, Australia. *Journal of Natural Gas Science and Engineering*, *33*, 1244-1259.
Glorioso, J. C., & Rattia, A. (2012). Unconventional reservoirs: basic petrophysical concepts for shale gas. SPE/EAGE European unconventional resources conference & exhibition-from potential to production,
Gou, Q., Xu, S., Hao, F., Zhang, B., Shu, Z., Yang, F., Wang, Y., & Li, Q. (2020). Quantitative calculated shale gas contents with different lithofacies: A case study of Fuling gas shale, Sichuan Basin, China. *Journal of Natural Gas Science and Engineering*, *76*, 103222.
Gunn, S. R. (1998). Support vector machines for classification and regression. *ISIS technical report*, *14*(1), 5-16.
Gunter, G. W., Finneran, J. M., Hartmann, D. J., & Miller, J. D. (1997, 1997/1/1/). *Early Determination of Reservoir Flow Units Using an Integrated Petrophysical Method* SPE Annual Technical Conference and Exhibition, San Antonio, Texas. https://doi.org/10.2118/38679-MS
Guo, J.-C., Luo, B., Zhu, H.-Y., Wang, Y.-H., Lu, Q.-L., & Zhao, X. (2015). Evaluation of fracability and screening of perforation interval for tight sandstone gas reservoir in western Sichuan Basin. *Journal of Natural Gas Science and Engineering*, *25*, 77-87. https://doi.org/https://doi.org/10.1016/j.jngse.2015.04.026
Guo, S., & Peng, Y. (2019). Determination method of shale gas content: A case study in the Ordos Basin, China. *Journal of Petroleum Science and Engineering*, *173*, 95-100.
Guo, W., Hu, Z., Zhang, X., Yu, R., & Wang, L. (2017). Shale gas adsorption and desorption characteristics and its effects on shale permeability. *Energy Exploration & Exploitation*, *35*(4), 463-481. https://doi.org/10.1177/0144598716684306
Guo, X., Li, Y., Liu, R., & Wang, Q. (2014). Characteristics and controlling factors of micropore structures of the Longmaxi Shale in the Jiaoshiba area, Sichuan Basin. *Natural Gas Industry B*, *1*(2), 165-171.
Gupta, I. (2017). Rock Typing in Organic Shales: Eagle Ford, Woodford, Barnett and Wolfcamp Formations.
Gupta, I., Rai, C., Sondergeld, C., & Devegowda, D. (2017). Rock typing in Wolfcamp formation. SPWLA 58th Annual Logging Symposium,
Haines, P. (2004). Depositional facies and regional correlations of the Ordovician Goldwyer and Nita Formations, Canning Basin, Western Australia, with implications for petroleum exploration. *Geological Survey of Western Australia, Record*, *7*.
Hamerly, G., & Elkan, C. (2003). Learning the k in k-means. *Advances in neural information processing systems*, *16*.
Hancock, E., & Huntington, J. F. (2010). *The GSWA NVCL HyLogger: rapid mineralogical analysis for characterizing mineral and petroleum core*. Geological Survey of Western Australia.
Higgs, K., Haese, R., Golding, S., Schacht, U., & Watson, M. (2015). The Pretty Hill Formation as a natural analogue for CO2 storage: an investigation of mineralogical and isotopic changes associated with sandstones exposed to low, intermediate and high CO2 concentrations over geological time. *Chemical Geology*, *399*, 36-64.
Hill, A., & Mauger, A. (2016). HyLogging unconventional petroleum core from the Cooper Basin, South Australia. *Australian Journal of Earth Sciences*, *63*(8), 1087-1097.
Huang, C., Zhang, J., Hua, W., Yue, J., & Lu, Y. (2018). Sedimentology and lithofacies of lacustrine shale: A case study from the Dongpu sag, Bohai Bay Basin, Eastern China. *Journal of Natural Gas Science and Engineering*, *60*, 174-189. https://doi.org/https://doi.org/10.1016/j.jngse.2018.10.014

Huntington, J., Whitbourn, L., Mason, P., Berman, M., & Schodlok, M. C. (2010). HyLogging—Voluminous industrial-scale reflectance spectroscopy of the Earth's subsurface. Proceedings of ASD and IEEE GRS; Art, Science and Applications of Reflectance Spectroscopy Symposium,

Ibach, L. E. J. (1982). Relationship between sedimentation rate and total organic carbon content in ancient marine sediments. *AAPG Bulletin*, *66*(2), 170-188.

Iqbal, M., Mandal, P., Rezaee, R., Sarout, J., & Smith, G. (2021). Integration of mechanical stratigraphy with lithofacies in Goldwyer shale for selecting producible and hydraulic fracturing layers. 82nd EAGE Annual Conference & Exhibition,

Iqbal, M. A., & Rezaee, R. (2020). Porosity and Water Saturation Estimation for Shale Reservoirs: An Example from Goldwyer Formation Shale, Canning Basin, Western Australia. *Energies*, *13*(23), 6294.

Iqbal, M. A., Rezaee, R., Laukamp, C., Pejcic, B., & Smith, G. (2022). Integrated sedimentary and high-resolution mineralogical characterisation of Ordovician shale from Canning Basin, Western Australia: Implications for facies heterogeneity evaluation. *Journal of Petroleum Science and Engineering*, *208*, 109347.

Iqbal, M. A., Rezaee, R., Smith, G., & Ekundayo, J. M. (2021). Shale lithofacies controls on porosity and pore structure: An example from Ordovician Goldwyer Formation, Canning Basin, Western Australia. *Journal of Natural Gas Science and Engineering*, *89*, 103888.

Iqbal, M. A., Salim, A. M. A., Baioumy, H., Gaafar, G. R., & Wahid, A. (2019). Identification and characterization of low resistivity low contrast zones in a clastic outcrop from Sarawak, Malaysia. *Journal of Applied Geophysics*, *160*, 207-217.

Iqbal, O., Ahmad, M., & Kadir, A. a. (2018). Effective evaluation of shale gas reservoirs by means of an integrated approach to petrophysics and geomechanics for the optimization of hydraulic fracturing: A case study of the Permian Roseneath and Murteree Shale Gas reservoirs, Cooper Basin, Australia. *Journal of Natural Gas Science and Engineering*, *58*, 34-58. https://doi.org/10.1016/j.jngse.2018.07.017

Jacobi, D. J., Breig, J. J., LeCompte, B., Kopal, M., Hursan, G., Mendez, F. E., Bliven, S., & Longo, J. (2009). Effective geochemical and geomechanical characterization of shale gas reservoirs from the wellbore environment: Caney and the Woodford shale. SPE annual technical conference and exhibition,

Jadoon, Q. K. (2016). *Unconventional shale gas reservoir characterization and modelling of the Permian Roseneath and Murteree shales in the Cooper Basin, Australia* James Cook University].

Jadoon, Q. K., Roberts, E., Blenkinsop, T., Wust, R. A. J., & Shah, S. A. (2016). Mineralogical modelling and petrophysical parameters in Permian gas shales from the Roseneath and Murteree formations, Cooper Basin, Australia. *Petroleum Exploration and Development*, *43*(2), 277-284. https://doi.org/https://doi.org/10.1016/S1876-3804(16)30031-3

Jadoon, Q. K., Roberts, E. M., Henderson, B., Blenkinsop, T. G., Wüst, R. A., & Mtelela, C. (2017). Lithological and facies analysis of the Roseneath and Murteree shales, Cooper Basin, Australia. *Journal of Natural Gas Science and Engineering*, *37*, 138-168.

Jarvie, D. M., Hill, R. J., Ruble, T. E., & Pollastro, R. M. (2007). Unconventional shale-gas systems: The Mississippian Barnett Shale of north-central Texas as one model for thermogenic shale-gas assessment. *AAPG Bulletin*, *91*(4), 475-499.

Javadpour, F. (2009). Nanopores and apparent permeability of gas flow in mudrocks (shales and siltstone). *Journal of Canadian Petroleum Technology*, *48*(08), 16-21.

Jenner, S., & Lamadrid, A. J. (2013). Shale gas vs. coal: Policy implications from environmental impact comparisons of shale gas, conventional gas, and coal on air, water, and land in the United States. *Energy Policy*, *53*, 442-453.

Jennings, J. W., Jr., & Lucia, F. J. (2003). Predicting Permeability From Well Logs in Carbonates With a Link to Geology for Interwell Permeability Mapping. *SPE Reservoir Evaluation & Engineering*, *6*(04), 215-225. https://doi.org/10.2118/84942-PA
Ji, L., Ma, X., Xia, Y., & Qiu, J. (2014). Relationship between methane adsorption capacity of clay minerals and micropore volume. *Nat. Gas Geosci*, *25*(2), 141-152.
Jia, H., & Sheng, J. J. (2017). Discussion of the feasibility of air injection for enhanced oil recovery in shale oil reservoirs. *Petroleum*, *3*(2), 249-257.
Jiang, S., Xu, Z., Feng, Y., Zhang, J., Cai, D., Chen, L., Wu, Y., Zhou, D., Bao, S., & Long, S. (2016). Geologic characteristics of hydrocarbon-bearing marine, transitional and lacustrine shales in China. *Journal of Asian Earth Sciences*, *115*, 404-418. https://doi.org/10.1016/j.jseaes.2015.10.016
Jiang, Z., Tang, X., Cheng, L., Li, Z., Zhang, Y., Bai, Y., Yuan, Y., & Hao, J. (2015). Characterization and origin of the Silurian Wufeng-Longmaxi Formation shale multiscale heterogeneity in southeastern Sichuan Basin, China. *Interpretation*, *3*(2), SJ61-SJ74.
Jin, H., & Sonnenberg, S. A. (2013). Characterization for source rock potential of the Bakken Shales in the Williston Basin, North Dakota and Montana. Unconventional Resources Technology Conference,
Jin, X., Shah, S. N., Roegiers, J.-C., & Zhang, B. (2014). Fracability evaluation in shale reservoirs-an integrated petrophysics and geomechanics approach. SPE hydraulic fracturing technology conference,
Jin, X., Shah, S. N., Roegiers, J.-C., & Zhang, B. (2015). An integrated petrophysics and geomechanics approach for fracability evaluation in shale reservoirs. *SPE Journal*, *20*(03), 518-526.
Johnson, C., & Boersma, T. (2013). Energy (in) security in Poland the case of shale gas. *Energy Policy*, *53*, 389-399.
Johnson, L., Smith, G., Rezaee, R., & Kadkhodaie, A. (2020). A 3D Model of the Unconventional Play in the Goldwyer Formation: An Integrated Shale Rock Characterisation over the Broome Platform, Canning Basin. Asia Pacific Unconventional Resources Technology Conference, Brisbane, Australia, 18-19 November 2019,
Johnson, L. M. (2019). *Integrated Reservoir Characterization of the Goldwyer Formation, Canning Basin* Curtin University].
Johnson, L. M., Rezaee, R., Kadkhodaie, A., Smith, G., & Yu, H. (2018). Geochemical property modelling of a potential shale reservoir in the Canning Basin (Western Australia), using Artificial Neural Networks and geostatistical tools. *Computers & Geosciences*, *120*, 73-81.
Johnson, L. M., Rezaee, R., Smith, G. C., Mahlstedt, N., Edwards, D. S., Kadkhodaie, A., & Yu, H. (2020). Kinetics of hydrocarbon generation from the marine Ordovician Goldwyer Formation, Canning Basin, Western Australia. *International Journal of Coal Geology*, 103623.
Jordan, C., Barker, G., & Gunn, B. (2013). Evaluating Australian unconventional gas: use and misuse of North American analogues. *The APPEA Journal*, *53*(1), 37-46.
Josh, M., Delle Piane, C., Esteban, L., Bourdet, J., Mayo, S., Pejcic, B., Burgar, I., Luzin, V., Clennell, M. B., & Dewhurst, D. N. (2019). Advanced laboratory techniques characterising solids, fluids and pores in shales. *Journal of Petroleum Science and Engineering*, *180*, 932-949.
Josh, M., Esteban, L., Delle Piane, C., Sarout, J., Dewhurst, D. N., & Clennell, M. B. (2012). Laboratory characterisation of shale properties. *Journal of Petroleum Science and Engineering*, *88-89*, 107-124. https://doi.org/10.1016/j.petrol.2012.01.023
Joshi, D., Patidar, A. K., Mishra, A., Mishra, A., Agarwal, S., Pandey, A., Dewangan, B. K., & Choudhury, T. (2021). Prediction of sonic log and correlation of lithology by comparing geophysical well log data using machine learning principles. *GeoJournal*, 1-22.

Kadkhodaie, A., & Rezaee, R. (2016). A new correlation for water saturation calculation in gas shale reservoirs based on compensation of kerogen-clay conductivity. *Journal of Petroleum Science and Engineering*, *146*, 932-939. https://doi.org/10.1016/j.petrol.2016.08.004
Kale, S., Rai, C., & Sondergeld, C. (2010, 2010/1/1/). *Rock Typing in Gas Shales* SPE Annual Technical Conference and Exhibition, Florence, Italy. https://doi.org/10.2118/134539-MS
Katahara, K. (2008). What is shale to a petrophysicist? *The Leading Edge*, *27*(6), 738-741.
Katsube, T., & Williamson, M. (1994). Effects of diagenesis on shale nano-pore structure and implications for sealing capacity. *Clay minerals*, *29*(4), 451-461.
Kawata, Y., & Fujita, K. (2001). Some predictions of possible unconventional hydrocarbons availability until 2100. SPE Asia Pacific Oil and Gas Conference and Exhibition,
Kecman, V. (2005). Support vector machines–an introduction. In *Support vector machines: theory and applications* (pp. 1-47). Springer.
Kilgore, E., Land, A., Schmidt, A., & Yunker, J. (1972). Applications Of The Coriband Technique To Complex Lithologies. *The Log Analyst*, *13*(01).
Klaja, J., & Dudek, L. (2016). Geological interpretation of spectral gamma ray (SGR) logging in selected boreholes. *Nafta-Gaz*, *72*(1), 3-14.
Klaja, J., Łykowska, G., & Przelaskowska, A. (2015). Helium porosity measurements for rocks from unconventional reservoirs performed on crushed samples. *Nafta-Gaz*, *71*(11), 856-863.
Klaver, J., Desbois, G., Littke, R., & Urai, J. L. (2015). BIB-SEM characterization of pore space morphology and distribution in postmature to overmature samples from the Haynesville and Bossier Shales. *Marine and petroleum Geology*, *59*, 451-466.
Kuila, U., & Prasad, M. (2013). Specific surface area and pore-size distribution in clays and shales. *Geophysical Prospecting*, *61*(2), 341-362.
Kurtoglu, B., Sorensen, J. A., Braunberger, J., Smith, S., & Kazemi, H. (2013). Geologic characterization of a Bakken reservoir for potential CO2 EOR. Unconventional Resources Technology Conference,
Labani, M. M., Rezaee, R., Saeedi, A., & Al Hinai, A. (2013). Evaluation of pore size spectrum of gas shale reservoirs using low pressure nitrogen adsorption, gas expansion and mercury porosimetry: A case study from the Perth and Canning Basins, Western Australia. *Journal of Petroleum Science and Engineering*, *112*, 7-16.
Lastoskie, C., Gubbins, K. E., & Quirke, N. (1993). Pore size distribution analysis of microporous carbons: a density functional theory approach. *The journal of physical chemistry*, *97*(18), 4786-4796.
Lazar, O. R., Bohacs, K. M., Macquaker, J. H., Schieber, J., & Demko, T. M. (2015). Capturing Key Attributes of Fine-Grained Sedimentary Rocks In Outcrops, Cores, and Thin Sections: Nomenclature and Description GuidelinesMUDSTONES: NOMENCLATURE AND DESCRIPTION GUIDELINES. *Journal of Sedimentary Research*, *85*(3), 230-246.
Leather, D. T., Bahadori, A., Nwaoha, C., & Wood, D. A. (2013). A review of Australia's natural gas resources and their exploitation. *Journal of Natural Gas Science and Engineering*, *10*, 68-88.
Lee, Y. I., & Kim, J. C. (1992). Storm-influenced siliciclastic and carbonate ramp deposits, the Lower Ordovician Dumugol Formation, South Korea. *Sedimentology*, *39*(6), 951-969.
Leveaux, J., & Poupon, A. (1971). Evaluation of water saturation in shaly formations. *The Log Analyst*, *12*(04).
Li, W., Cao, J., Shi, C., Xu, T., Zhang, H., & Zhang, Y. (2020). Shale oil in saline lacustrine systems: A perspective of complex lithologies of fine-grained rocks. *Marine and Petroleum Geology*, *116*, 104351.

Liang, C., Jiang, Z., Yiting, Y., & Xiajie, W. (2012). Shale lithofacies and reservoir space of the Wufeng–Longmaxi formation, Sichuan Basin, China. *Petroleum Exploration and Development*, *39*(6), 736-743.
Liaw, A., & Wiener, M. (2002). Classification and regression by randomForest. *R news*, *2*(3), 18-22.
Liu, D., Li, Z., Jiang, Z., Zhang, C., Zhang, Z., Wang, J., Yang, D., Song, Y., & Luo, Q. (2019). Impact of laminae on pore structures of lacustrine shales in the southern Songliao Basin, NE China. *Journal of Asian Earth Sciences*, *182*, 103935.
Loucks, R. G., Reed, R. M., Ruppel, S. C., & Hammes, U. (2012). Spectrum of pore types and networks in mudrocks and a descriptive classification for matrix-related mudrock pores. *AAPG bulletin*, *96*(6), 1071-1098.
Loucks, R. G., Reed, R. M., Ruppel, S. C., & Jarvie, D. M. (2009). Morphology, genesis, and distribution of nanometer-scale pores in siliceous mudstones of the Mississippian Barnett Shale. *Journal of Sedimentary Research*, *79*(12), 848-861.
Luffel, D. L., Guidry, F. K., & Curtis, J. B. (1992). Evaluation of Devonian Shale With New Core and Log Analysis Methods. *Journal of Petroleum Technology*, *44*(11), 1192-1197. https://doi.org/10.2118/21297-PA
Luo, P., & Zhong, N. (2020). The role of residual bitumen on the pore structure of organic-rich shales from low to over mature: Insight from shale and coal samples after the hydrous pyrolysis. *International Journal of Coal Geology*, 103515.
Ma, Y., Zhong, N., Li, D., Pan, Z., Cheng, L., & Liu, K. (2015). Organic matter/clay mineral intergranular pores in the Lower Cambrian Lujiaping Shale in the north-eastern part of the upper Yangtze area, China: A possible microscopic mechanism for gas preservation. *International Journal of Coal Geology*, *137*, 38-54.
Mackie, S. (1987). Cooper/Eromanga basins hydrocarbon potential.
Macquaker, J., & Gawthorpe, R. (1993). Mudstone lithofacies in the Kimmeridge Clay Formation, Wessex Basin, southern England; implications for the origin and controls of the distribution of mudstones. *Journal of Sedimentary Research*, *63*(6), 1129-1143.
Mandal, P. P. (2021). *Integrated Geomechanical Characterization of Anisotropic Gas Shales: Field Appraisal, Laboratory Testing, Viscoelastic Modelling, and Hydraulic Fracture Simulation* Curtin University].
Mandal, P. P., Rezaee, R., & Emelyanova, I. (2021). Ensemble Learning for Predicting TOC from Well-Logs of the Unconventional Goldwyer Shale. *Energies*, *15*(1), 216.
Mandal, P. P., Sarout, J., & Rezaee, R. (2020). Geomechanical appraisal and prospectivity analysis of the Goldwyer shale accounting for stress variation and formation anisotropy. *International Journal of Rock Mechanics and Mining Sciences*, *135*, 104513.
Mastalerz, M., Schimmelmann, A., Drobniak, A., & Chen, Y. (2013). Porosity of Devonian and Mississippian New Albany Shale across a maturation gradient: Insights from organic petrology, gas adsorption, and mercury intrusion. *AAPG Bulletin*, *97*(10), 1621-1643.
Mazzullo, S., & Harris, P. (1992). Mesogenetic dissolution: its role in porosity development in carbonate reservoirs. *AAPG Bulletin*, *76*(5), 607-620.
McCollum, L. (1988). A shallow epeiric sea interpretation for an offshore Middle Devonian black shale facies in eastern North America.
Milliken, K. (2014). A compositional classification for grain assemblages in fine-grained sediments and sedimentary rocks. *Journal of Sedimentary Research*, *84*(12), 1185-1199.
Milliken, K. L., Rudnicki, M., Awwiller, D. N., & Zhang, T. (2013). Organic matter–hosted pore system, Marcellus formation (Devonian), Pennsylvania. *AAPG Bulletin*, *97*(2), 177-200.
Mohammed, I. Q., Farouk, S., Baioumy, H., Lotfy, N. M., & Al-Hadidy, A. H. (2020). Mineralogical and geochemical characteristics of the Paleozoic source rocks, Akkas gas field, Western Desert of Iraq: Implications for their origin, maturation and Ordovician-Silurian transition. *Marine and Petroleum Geology*, *118*, 104432. https://doi.org/https://doi.org/10.1016/j.marpetgeo.2020.104432

Mory, A. (2010). A review of mid-Carboniferous to Triassic stratigraphy, Canning Basin, Western Australia, GS o. W. Australia, Report 107.

Mullen, J. (2010). Petrophysical characterization of the Eagle Ford Shale in south Texas. Canadian Unconventional Resources and International Petroleum Conference,

Murphy, A. E., Sageman, B. B., Hollander, D. J., Lyons, T. W., & Brett, C. E. (2000). Black shale deposition and faunal overturn in the Devonian Appalachian Basin: Clastic starvation, seasonal water-column mixing, and efficient biolimiting nutrient recycling. *Paleoceanography*, *15*(3), 280-291.

Nasira, G., Kumar, S. A., & Kiruba, M. S. (2008). A comparative study of fuzzy logic with artificial neural networks algorithms in clustering. *Journal of Computer Applications*, *1*(4), 6.

North, F. (1985). Petroleum geology: Boston. *Allen amp Unwin*, 253-341.

Olgaard, D. L., Nuesch, R., & Ural, J. (1995). Consolidation of water saturated shales at great depth under drained conditions. 8th ISRM Congress,

Olierook, H. K., Delle Piane, C., Timms, N. E., Esteban, L., Rezaee, R., Mory, A. J., & Hancock, L. (2014). Facies-based rock properties characterization for CO2 sequestration: GSWA Harvey 1 well, Western Australia. *Marine and Petroleum Geology*, *50*, 83-102.

Pashin, J. C., Kopaska-Merkel, D., Arnold, A., & McIntyre, M. (2011). Geological foundation for production of natural gas from diverse shale formations. *RPSEA, Final Report*, *7122*, 156.

Passey, Q., Creaney, S., Kulla, J., Moretti, F., & Stroud, J. (1990). A practical model for organic richness from porosity and resistivity logs. *AAPG Bulletin*, *74*(12), 1777-1794.

Passey, Q. R., Bohacs, K., Esch, W. L., Klimentidis, R., & Sinha, S. (2010). From oil-prone source rock to gas-producing shale reservoir-geologic and petrophysical characterization of unconventional shale gas reservoirs. International oil and gas conference and exhibition in China,

Patel, H., Johanning, J., & Fry, M. (2014). Borehole microseismic, completion and production data analysis to determine future wellbore placement, spacing and vertical connectivity, Eagle Ford shale, South Texas. In *SEG Technical Program Expanded Abstracts 2014* (pp. 4475-4486). Society of Exploration Geophysicists.

Paukert Vankeuren, A. N., Hakala, J. A., Jarvis, K., & Moore, J. E. (2017). Mineral reactions in shale gas reservoirs: barite scale formation from reusing produced water as hydraulic fracturing fluid. *Environmental science & technology*, *51*(16), 9391-9402.

Pawar, G., Meakin, P., & Huang, H. (2017). Reactive Molecular Dynamics Simulation of Kerogen Thermal Maturation and Cross-Linking Pathways. *Energy & Fuels*, *31*(11), 11601-11614. https://doi.org/10.1021/acs.energyfuels.7b01555

Perry, R., Mischler, G., Guo, R., Lee, T., Chang, A., Koul, A., Franz, C., Richard, H., Carmichael, I., & Ablin, P. (2021). mvlearn: Multiview Machine Learning in Python. *J. Mach. Learn. Res.*, *22*, 109:101-109:107.

Peters, K. E., Walters, C., & Moldowan, J. M. (2005). *Biomarkers and isotopes in the environment and human history*. Cambridge University Press.

Poppe, L., Paskevich, V., Hathaway, J., & Blackwood, D. (2001). A laboratory manual for X-ray powder diffraction. *US Geological Survey open-file report*, *1*(041), 1-88.

Pranter, M. J., Hirstius, C. B., & Budd, D. A. (2005). Scales of lateral petrophysical heterogeneity in dolomite lithofacies as determined from outcrop analogs: Implications for 3-D reservoir modeling. *AAPG Bulletin*, *89*(5), 645-662.

Rebelle, M., & Lalanne, B. (2014). Rock-typing in carbonates: A critical review of clustering methods. Abu Dhabi international petroleum exhibition and conference,

Rezaee, M. R., Slatt, R. M., & Sigal, R. F. (2007). Shale gas rock properties prediction using artificial neural network technique and multi regression analysis, an example from a North American shale gas reservoir. *ASEG Extended Abstracts*, *2007*(1), 1-4.

Rezaee, R. (2015). *Fundamentals of gas shale reservoirs*. John Wiley & Sons.

Rogner, H.-H. (1997). An assessment of world hydrocarbon resources. *Annual review of energy and the environment*, *22*(1), 217-262.

Ross, D. J. K., & Bustin, R. M. (2008). Characterizing the shale gas resource potential of Devonian–Mississippian strata in the Western Canada sedimentary basin: Application of an integrated formation evaluation. *AAPG Bulletin*, *92*(1), 87-125. https://doi.org/10.1306/09040707048

Ross, D. J. K., & Marc Bustin, R. (2009). The importance of shale composition and pore structure upon gas storage potential of shale gas reservoirs. *Marine and Petroleum Geology*, *26*(6), 916-927. https://doi.org/10.1016/j.marpetgeo.2008.06.004

Rouquerol, J., Avnir, D., Fairbridge, C., Everett, D., Haynes, J., Pernicone, N., Ramsay, J., Sing, K., & Unger, K. (1994). Recommendations for the characterization of porous solids (Technical Report). *Pure and Applied Chemistry*, *66*(8), 1739-1758.

Rybacki, E., Meier, T., & Dresen, G. (2016). What controls the mechanical properties of shale rocks? – Part II: Brittleness. *Journal of Petroleum Science and Engineering*, *144*, 39-58. https://doi.org/10.1016/j.petrol.2016.02.022

Schieber, J. (1999). Distribution and deposition of mudstone facies in the Upper Devonian Sonyea Group of New York. *Journal of Sedimentary Research*, *69*(4), 909-925.

Schieber, J. (2013). 13 SEM Observations on Ion-milled Samples of Devonian Black Shales from Indiana and New York: The Petrographic Context of Multiple Pore Types.

Schlanser, K., Grana, D., & Campbell-Stone, E. (2016). Lithofacies classification in the Marcellus Shale by applying a statistical clustering algorithm to petrophysical and elastic well logs. *Interpretation*, *4*(2), SE31-SE49.

Schodlok, M., Whitbourn, L., Huntington, J., Mason, P., Green, A., Berman, M., Coward, D., Connor, P., Wright, W., & Jolivet, M. (2016). HyLogger-3, a visible to shortwave and thermal infrared reflectance spectrometer system for drill core logging: functional description. *Australian Journal of Earth Sciences*, *63*(8), 929-940.

Schulz, H., & Horsfield, B. (2010). Rock matrix as reservoir: mineralogy & diagenesis. *DeutschesGeoForschungsZentrumGFZ, Potsdam, University of Cape Town, Rondebosch*, *7701*.

Seaton, N., & Walton, J. (1989). A new analysis method for the determination of the pore size distribution of porous carbons from nitrogen adsorption measurements. *Carbon*, *27*(6), 853-861.

Seyedmehdi, Z., George, A. D., & Tucker, M. E. (2016). Sequence development of a latest Devonian–Tournaisian distally-steepened mixed carbonate–siliciclastic ramp, Canning Basin, Australia. *Sedimentary Geology*, *333*, 164-183.

Shmilovici, A. (2009). Support vector machines. In *Data mining and knowledge discovery handbook* (pp. 231-247). Springer.

Sieminski, A., & Administrator, U. (2016). Energy Information Administration. *International Energy Outlook*.

Simandoux, P. (1963). Dielectric measurements in porous media and application to shaly formation: Revue del'Institut Francais du Petrole. *Supplementary Issue*, 193-215.

Slatt, R. M., & O'Brien, N. R. (2011). Pore types in the Barnett and Woodford gas shales: Contribution to understanding gas storage and migration pathways in fine-grained rocks. *AAPG Bulletin*, *95*(12), 2017-2030.

Sondergeld, C. H., Newsham, K. E., Comisky, J. T., Rice, M. C., & Rai, C. S. (2010, 2010/1/1/). *Petrophysical Considerations in Evaluating and Producing Shale Gas Resources* SPE Unconventional Gas Conference, Pittsburgh, Pennsylvania, USA. https://doi.org/10.2118/131768-MS

Song, D., Ji, X., Li, Y., Zhao, H., Song, B., & He, K. (2020). Heterogeneous development of micropores in medium-high rank coal and its relationship with adsorption capacity. *International Journal of Coal Geology*, 103497.

Spaak, G., Edwards, D. S., Foster, C. B., Pages, A., Summons, R. E., Sherwood, N., & Grice, K. (2017). Environmental conditions and microbial community structure during the Great Ordovician Biodiversification Event; a multi-disciplinary study from the Canning Basin, Western Australia. *Global and Planetary Change*, *159*, 93-112.

Stegent, N. A., Wagner, A. L., Mullen, J., & Borstmayer, R. E. (2010). Engineering a successful fracture-stimulation treatment in the Eagle Ford shale. Tight gas completions conference,

Stow, D. A. V., Huc, A. Y., & Bertrand, P. (2001). Depositional processes of black shales in deep water. *Marine and Petroleum Geology*, *18*(4), 491-498. https://doi.org/https://doi.org/10.1016/S0264-8172(01)00012-5

Strahler, A. N. (1981). *Physical geology*.

Suarez-Rivera, R., Green, S. J., McLennan, J., & Bai, M. (2006). Effect of layered heterogeneity on fracture initiation in tight gas shales. SPE Annual Technical Conference and Exhibition,

Sun, T., Merletti, G., Patel, H., Cadwallader, S., Graff, M. C., Wampler, J., Gil, I. R., Sebastian, H., Spain, D., & Aguirre, O. (2015). Advanced petrophysical, geological, geophysical and geomechanical reservoir characterization-key to the successful implementation of a geo-engineered completion optimization program in the Eagle Ford shale. Unconventional Resources Technology Conference, San Antonio, Texas, 20-22 July 2015,

Svetnik, V., Liaw, A., Tong, C., Culberson, J. C., Sheridan, R. P., & Feuston, B. P. (2003). Random forest: a classification and regression tool for compound classification and QSAR modeling. *Journal of chemical information and computer sciences*, *43*(6), 1947-1958.

Swanson, B. F. (1981). A Simple Correlation Between Permeabilities and Mercury Capillary Pressures. *Journal of Petroleum Technology*, *33*(12), 2498-2504. https://doi.org/10.2118/8234-PA

Tang, X., Jiang, Z., Jiang, S., Cheng, L., & Zhang, Y. (2017). Characteristics and origin of in-situ gas desorption of the Cambrian Shuijingtuo Formation shale gas reservoir in the Sichuan Basin, China. *Fuel*, *187*, 285-295. https://doi.org/https://doi.org/10.1016/j.fuel.2016.09.072

Taylor, A., & Goldring, R. (1993). Description and analysis of bioturbation and ichnofabric. *Journal of the Geological Society*, *150*(1), 141-148.

Taylor, A. R., Harrington, G. A., Clohessy, S., Dawes, W. R., Crosbie, R. S., Doble, R. C., Wohling, D. L., Batlle-Aguilar, J., Davies, P. J., & Thomas, M. (2018). *Hydrogeological assessment of the Grant Group and Poole Sandstone-Fitzroy Catchment, Western Australia*.

Thomeer, J. H. (1983). Air Permeability as a Function of Three Pore-Network Parameters. *Journal of Petroleum Technology*, *35*(04), 809-814. https://doi.org/10.2118/10922-PA

Thomeer, J. H. M. (1960). Introduction of a Pore Geometrical Factor Defined by the Capillary Pressure Curve. *Journal of Petroleum Technology*, *12*(03), 73-77. https://doi.org/10.2118/1324-G

Tissot, B. P., & Welte, D. H. (1984). Diagenesis, catagenesis and metagenesis of organic matter. In *Petroleum formation and occurrence* (pp. 69-73). Springer.

Tissot, B. P., & Welte, D. H. (2013). *Petroleum formation and occurrence*. Springer Science & Business Media.

Torghabeh, A. K., Rezaee, R., Pimentel, N., Johnson, L., & Alshakhs, M. (2019). Petroleum geochemistry, burial history and shale gas potential of the Goldwyer Formation-Canning Basin, Western Australia. *International Journal of Oil, Gas and Coal Technology*, *20*(4), 420-440.

Turner, B. W., Tréanton, J. A., & Slatt, R. M. (2016). The use of chemostratigraphy to refine ambiguous sequence stratigraphic correlations in marine mudrocks. An example from the Woodford Shale, Oklahoma, USA. *Journal of the Geological Society*, *173*(5), 854. https://doi.org/10.1144/jgs2015-125 van Hattum, J., Bond, A., Jablonski, D., & Taylor-Walshe, R. (2019). Exploration of an unconventional petroleum resource through extensive core analysis and basin geology interpretation utilising play element methodology: the Lower Goldwyer Formation, onshore Canning Basin, Western Australia. *The APPEA Journal*, *59*(1), 464-481.

Walderhaug, O. (2000). Modeling quartz cementation and porosity in Middle Jurassic Brent Group sandstones of the Kvitebjørn field, northern North Sea. *AAPG Bulletin*, *84*(9), 1325-1339.

Walls, J. D., & Sinclair, S. W. (2011). Eagle Ford shale reservoir properties from digital rock physics. *First Break*, *29*(6).

Wang, F. P., & Gale, J. F. (2009). Screening criteria for shale-gas systems.

Wang, G., & Carr, T. R. (2012). Marcellus shale lithofacies prediction by multiclass neural network classification in the Appalachian Basin. *Mathematical Geosciences*, *44*, 975-1004.

Wang, G., & Carr, T. R. (2012). Methodology of organic-rich shale lithofacies identification and prediction: A case study from Marcellus Shale in the Appalachian basin. *Computers & Geosciences*, *49*, 151-163. https://doi.org/https://doi.org/10.1016/j.cageo.2012.07.011

Wang, G., & Carr, T. R. (2013). Organic-rich Marcellus Shale lithofacies modeling and distribution pattern analysis in the Appalachian Basin. *AAPG Bulletin*, *97*(12), 2173-2205.

Wang, G., Carr, T. R., Ju, Y., & Li, C. (2014). Identifying organic-rich Marcellus Shale lithofacies by support vector machine classifier in the Appalachian basin. *Computers & Geosciences*, *64*, 52-60.

Wang, P., Jiang, Z., Yin, L., Chen, L., Li, Z., Zhang, C., Li, T., & Huang, P. (2017). Lithofacies classification and its effect on pore structure of the Cambrian marine shale in the Upper Yangtze Platform, South China: Evidence from FE-SEM and gas adsorption analysis. *Journal of Petroleum Science and Engineering*, *156*, 307-321.

Wang, X., Liu, L., Wang, Y., Sheng, Y., Zheng, S., Wu, W., & Luo, Z. (2020). Comparison of the Pore Structures of Lower Silurian Longmaxi Formation Shales with Different Lithofacies in the Southern Sichuan Basin, China. *Journal of Natural Gas Science and Engineering*, 103419.

Wei, W., Zhu, X., Meng, Y., Xiao, L., Xue, M., & Wang, J. (2016). Porosity model and its application in tight gas sandstone reservoir in the southern part of West Depression, Liaohe Basin, China. *Journal of Petroleum Science and Engineering*, *141*, 24-37.

Weijermars, R. (2013). Economic appraisal of shale gas plays in Continental Europe. *Applied Energy*, *106*, 100-115.

Winchester-Seeto, T., Foster, C., & O'Leary, T. (2000). The environmental response of Middle Ordovician large organic walled microfossils from the Goldwyer and Nita Formations, Canning Basin, Western Australia. *Review of Palaeobotany and Palynology*, *113*(1), 197-212. https://doi.org/https://doi.org/10.1016/S0034-6667(00)00060-9

Wu, L., Lu, Y., Jiang, S., Lu, Y., Liu, X., & Hu, H. (2018). Pore structure characterization of different lithofacies in marine shale: A case study of the Upper Ordovician Wufeng-Lower Silurian Longmaxi formation in the Sichuan Basin, SW China. *Journal of Natural Gas Science and Engineering*, *57*, 203-215. https://doi.org/10.1016/j.jngse.2018.07.009

Wu, T., Li, X., Zhao, J., & Zhang, D. (2017). Multiscale pore structure and its effect on gas transport in organic-rich shale. *Water Resources Research*, *53*(7), 5438-5450. https://doi.org/10.1002/2017wr020780

Xue, B., Zhang, J., Tang, X., Yang, C., Chen, Q., Man, X., & Dang, W. (2016). Micro-pore structure and gas accumulation characteristics of shale in the longmaxi formation, northwest guizhou. *Petroleum Research*, *1*(2), 191-204.

Yan, J., Zhang, Q., & Gao, J. (1979). Adsorption and condensation-the surface and pore of solid. *Science, Beijing*, 118-124.

Yang, F., Xu, S., Hao, F., Hu, B., Zhang, B., Shu, Z., & Long, S. (2019). Petrophysical characteristics of shales with different lithofacies in Jiaoshiba area, Sichuan Basin, China: Implications for shale gas accumulation mechanism. *Marine and Petroleum Geology*, *109*, 394-407.

Yang, W., Zuo, R., Jiang, Z., Chen, D., Song, Y., Luo, Q., Wang, Q., & Zhu, H. (2018). Effect of lithofacies on pore structure and new insights into pore-preserving mechanisms of the over-mature Qiongzhusi marine shales in Lower Cambrian of the southern Sichuan Basin, China. *Marine and Petroleum Geology*, *98*, 746-762.

Yang, Y., Wu, K., Zhang, T., & Xue, M. (2015). Characterization of the pore system in an over-mature marine shale reservoir: A case study of a successful shale gas well in Southern Sichuan Basin, China. *Petroleum*, *1*(3), 173-186.

Yu, H., Rezaee, R., Wang, Z., Han, T., Zhang, Y., Arif, M., & Johnson, L. (2017). A new method for TOC estimation in tight shale gas reservoirs. *International Journal of Coal Geology*, *179*, 269-277.

Yu, H., Wang, Z., Rezaee, R., Zhang, Y., Han, T., Arif, M., & Johnson, L. (2018). Porosity estimation in kerogen-bearing shale gas reservoirs. *Journal of Natural Gas Science and Engineering*, *52*, 575-581. https://doi.org/10.1016/j.jngse.2018.02.012

Yuan, Y., Rezaee, R., Al-Khdheeawi, E. A., Hu, S.-Y., Verrall, M., Zou, J., & Liu, K. (2019). Impact of Composition on Pore Structure Properties in Shale: Implications for Micro-/Mesopore Volume and Surface Area Prediction. *Energy & Fuels*, *33*(10), 9619-9628.

Yuan, Y., Rezaee, R., Verrall, M., Hu, S.-Y., Zou, J., & Testmanti, N. (2018). Pore characterization and clay bound water assessment in shale with a combination of NMR and low-pressure nitrogen gas adsorption. *International Journal of Coal Geology*, *194*, 11-21. https://doi.org/10.1016/j.coal.2018.05.003

Zhang, L., He, X., Li, X., Li, K., He, J., Zhang, Z., Guo, J., Chen, Y., & Liu, W. (2022). Shale gas exploration and development in the Sichuan Basin: Progress, challenge and countermeasures. *Natural Gas Industry B*.

Zhang, L., Lu, S., Jiang, S., Xiao, D., Chen, L., Liu, Y., Zhang, Y., Li, B., & Gong, C. (2018). Effect of Shale Lithofacies on Pore Structure of the Wufeng–Longmaxi Shale in Southeast Chongqing, China. *Energy & Fuels*, *32*(6), 6603-6618.

Zhang, T. (2008). Incorporating geological conceptual models and interpretations into reservoir modeling using multiple-point geostatistics. *Earth Science Frontiers*, *15*(1), 26-35.

Zhang, T., Ellis, G. S., Ruppel, S. C., Milliken, K., & Yang, R. (2012). Effect of organic-matter type and thermal maturity on methane adsorption in shale-gas systems. *Organic Geochemistry*, *47*, 120-131. https://doi.org/https://doi.org/10.1016/j.orggeochem.2012.03.012

Zhang, Y., Shao, D., Yan, J., Jia, X., Li, Y., Yu, P., & Zhang, T. (2016). The pore size distribution and its relationship with shale gas capacity in organic-rich mudstone of Wufeng-Longmaxi Formations, Sichuan Basin, China. *Journal of Natural Gas Geoscience*, *1*(3), 213-220.

Zhou, L., Pu, X., Han, W., Jin, F., Xiao, D., Shi, Z., Deng, Y., Zhang, W., & Jiang, W. (2019). Exploration breakthroughs and geological characteristics of continental shale oil: A case study of the Kongdian Formation in the Cangdong Sag, China. *Marine and Petroleum Geology*, *102*, 544-556.

Zou, J., & Rezaee, R. (2019). A Prediction Model for Methane Adsorption Capacity in Shale Gas Reservoirs. *Energies*, *12*(2), 280.